Wind tunnel experiments on a single trailing vortex

van Sommeren, D.D.J.A.

Award date:
2009

TU/e Technische Universiteit Eindhoven University of Technology

Department of Applied Physics
Fluid Dynamics Laboratory
Cascade Building
P.O. Box 513
5600 MB Eindhoven

Title: **Wind tunnel experiments on a single trailing vortex**

Author: D. D. J. A. van Sommeren (Daan)

Report number: R-1762-A

Date: December 2009

Supervisors: dr. ir. R. R. Trieling
ir. A. Elsenaar
prof. dr. ir. B. J. Geurts
prof. dr. ir. G. J. F. van Heijst
Technical Support: ing. A. P. C. Holten

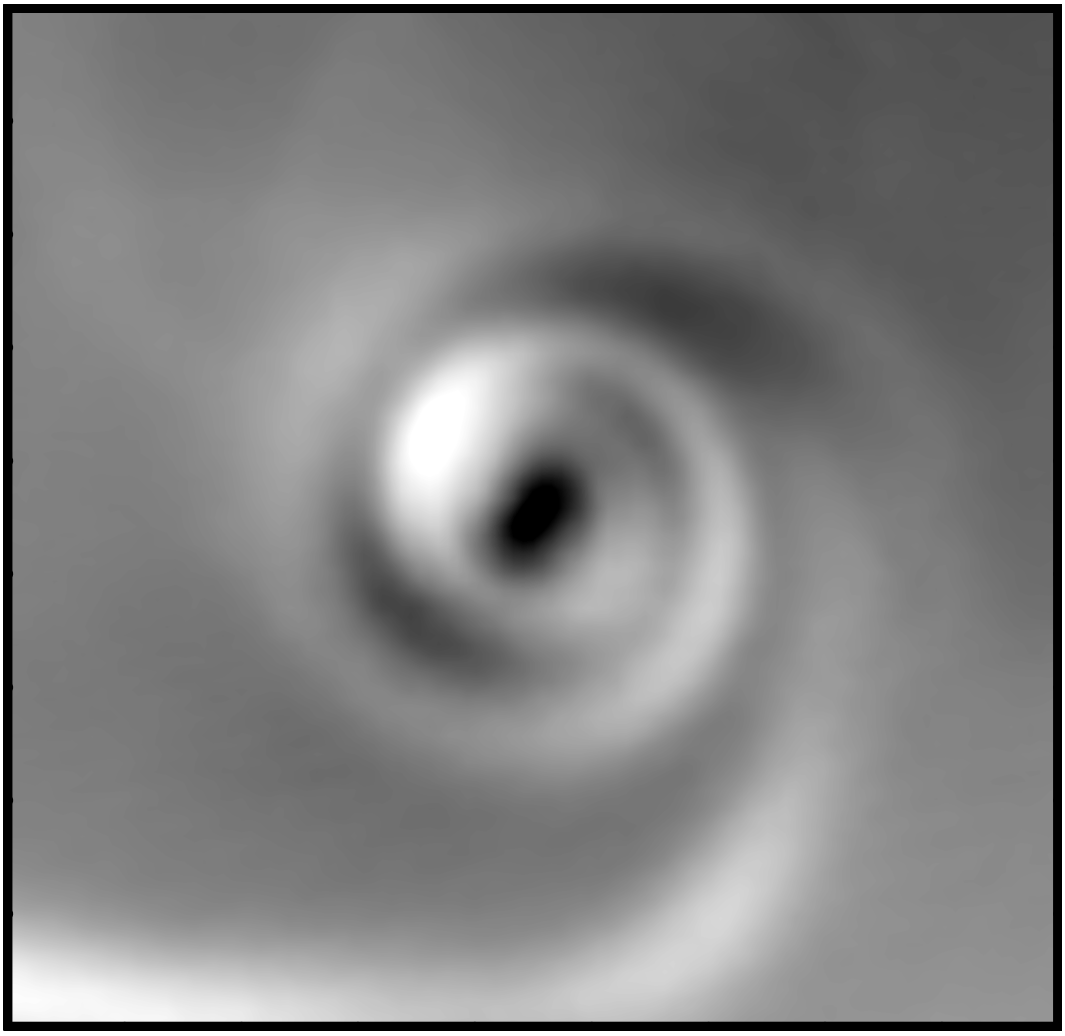

The cover figure shows the distribution of axial velocity in a plane perpendicular to the axis of an airplane trailing vortex. Darker colors indicate higher axial velocities. The concentration of lighter colors corresponds to a remnant of the boundary layer flow over the wing that spirals inwards to the vortex centre. This nicely illustrates the roll-up of a vortex sheet shed from an airplane wing. The wing is located horizontally and to the left side of the vortex centre, and its trailing edge is 1.5 chord lengths upstream.

Abstract

Trailing vortices may pose a severe hazard to an aircraft that closely follows another aircraft. This is especially the case during the landing and take off phases of flight. A detailed knowledge of trailing vortex breakdown is important to reduce the stress on air traffic control spacing rules. Many studies are therefore concentrated on the breakdown of a system of two counter-rotating trailing vortices at large downstream distance. However, to obtain a better understanding of this process, it is believed that the evolution of single trailing vortex needs to be thoroughly analyzed first.

In this work, wind tunnel experiments are performed on a single trailing vortex shed from an airplane wing. We analyzed cases without and with grid-generated turbulence. The 3C-PIV measurement technique is applied to obtain three-components velocity fields in a plane perpendicular to the vortex axis of symmetry. In contrast to the 2C-PIV measurement technique applied by Van Jaarsveld (2008), it was now possible to measure the axial velocity as well. Mean distributions of the azimuthal and axial components of the velocity and vorticity, the circulation, and the kinetic energy of turbulence are determined from an ensemble of 1.000 realizations for each measurement. Special care is taken to determine the vortex centre position for each realization. A frame of reference moving with the fluctuating vortex centre is applied to correct for the effects of vortex wandering. The ensemble of vortex centre positions in the stationary frame of reference is used to determine a probability density function (PDF) for the radial position of the vortex from its mean position.

Flow quantities are retrieved in the vortex core region with a higher accuracy and spatial resolution than Van Jaarsveld (2008). It was therefore possible to capture the roll-up of a trailing vortex in detail. The axial velocity near the vortex centre shows a jet-like structure at a downstream distance close to the wing, but transforms into a wake-like structure further downstream. A good indication is found for the azimuthal and axial velocity being related to each other as suggested by Batchelor (1964). Radial profiles of the circulation show the necessity for a two-length-scales vortex model. The inner length scale characterizes the viscous decay of the vortex core, while the outer length scale characterizes the roll-up of the vortex sheet. The PDFs for the radial position of the vortex from its mean position are in close agreement with those of a Rayleigh distribution characterizing the random-walk process.

Following the definition of Crow and Bate (1976) and making use of a typical distance between two trailing vortices as applied by Van Jaarsveld (2008), the grid-generated turbulence can be characterized as having a weak turbulence intensity. This means that a trailing vortex pair would break-up due to the Crow instability and the subsequent linking of vortex lines. It was found that the influence of weak turbulence is negligible for the decay of a single trailing vortex.

Contents

Chapter 1

Introduction

A trailing vortex is a strongly rotating structure inherent to lift generating bodies. Flying birds, rotating propellers, and boats sailing against the wind are just a few examples of objects leaving such vortical structures behind. Most studies on trailing vortices are concentrated on the vortical structures shed from a lift generating airplane wing. Fascinating manifestations of these kinds of trailing vortices can be seen across the open sky, in which the vortices may be visible by condensation of water vapor inside their cores. The motivation for studies on trailing vortices in aeronautics is twofold. First, an airplane experiences significant drag associated with the energy stored in a trailing vortex system. It is of aeronautical interest to reduce such drag to minimize fuel consumption. Second, trailing vortices can pose a severe hazard to an aircraft that closely follows an other aircraft. This is especially the case during the landing and take off phases of flight so that stringent spacing rules are necessary in air traffic control. It is believed that the stress on air traffic control will only increase with the ever increasing intensity and sizes of airplanes leaving and approaching airports. Many studies are therefore focused on the understanding and the control of trailing vortex breakdown.

The formation of trailing vortices behind an airplane wing was first recognized by Lanchester (1907). This illustrates that trailing vortices were analyzed even shortly after the birth of flight in 1903. Many theoretical and experimental studies have been dedicated to the topic of trailing vortices since then. Numerical simulations of trailing vortices are boosted during the recent decades of increasing computer power. Most of the theoretical, experimental, and numerical studies are motivated by spacing rules in air traffic control. Interestingly, Spalart (1998) notes in his reviewing work on trailing vortices, that the activity of aeronautical trailing vortices research dropped during the 1980s. The air traffic control rules were viewed as satisfactory and much heavier airplanes would not enter service. The recent introduction of the Airbus A380 illustrates that this perspective needed revision, and many studies are focused on aeronautical trailing vortices these days.

Studies motivated by the increasing stress on air traffic control are mostly related to the breakdown of two oppositely rotating trailing vortices. The understanding of this topic is greatly contributed by the work of Crow (1970) and Crow and Bate (1976). Crow (1970) considered the break-up of vortices due to a longwave cooperative instability and the subsequent linking of the vortex lines. The specific longwave cooperative instability that causes two counter rotating vortices to break-down is well known as the Crow instability. Crow and Bate (1976) were the first to derive an asymptotic relation between external turbulence and the lifetime of two oppositely rotating trailing vortices. They distinguished two flow regimes. For the case with weak and moderate turbulence intensity, the break-up is caused by the Crow instability and the subsequent linking of the vortex lines. In the flow regime with strong turbulence intensity, the trailing vortex breaks up due to bodily convection in the turbulent flow field. These break-up mechanisms are recovered and analyzed in many studies, see Tombach (1973), Sarpkaya (1998), Liu (1992),

and Van Jaarsveld (2008). The decay of trailing vortices is not limited by the break-up mechanism described by Crow (1970) and Crow and Bate (1976). Viscous decay and cross-diffusion at the symmetry plane where vorticity of opposite sign cancels, are two other important and well analyzed decay mechanisms. The decay of two oppositely rotating trailing vortices due to cross-diffusion is considered in the work of Cantwell and Rott (1988).

Van Jaarsveld (2008) performed wind tunnel experiments on the decay of a single and two oppositely rotating trailing vortices. Cases with and without grid-generated turbulence were considered in the experiments on the break-down of a trailing vortex pair, the grid-generated turbulence was characterized as having a strong intensity. Note that we use the definition of Crow and Bate (1976) in making a distinction between weak and strong turbulence intensities. The single trailing vortex was observed to consists of a laminar core embedded in region with relatively low vorticity. Van Jaarsveld (2008) found that the radius of the vortex core decays like that of a Lamb-Oseen vortex, while the radius of the outer region stays approximately constant. This behaviour was found to be independent of the external turbulence, which is in contrast to the decay of a vortex pair that strongly depends on the external turbulence. Van Jaarsveld (2008) found that the influence of external turbulence on the decay of two oppositely rotating trailing vortices is twofold. First, the turbulence increases the cross-diffusion of vorticity, and second, it triggers the Crow instability and the subsequent linking of vortex lines. These two decay mechanisms were found to occur at the same time, resulting in a complex break-up process.

This work can be seen as a continuation of the work of Van Jaarsveld (2008). We analyze the evolution of a single trailing vortex without and with grid-generated turbulence. By applying weak instead of strong external turbulence, it is believed that we will contribute to an enhanced understanding of the observations made by Van Jaarsveld (2008). It is illustrated by Devenport et al. (1996) that the flow field of a trailing vortex, even at thirty chord lengths downstream, is greatly influenced by its formation. Therefore, we also analyse the evolution of the trailing vortex from a downstream distance closer to the wing than Van Jaarsveld (2008). It is assumed that this will give more insight in the distinct regions of a trailing vortex as discussed by Van Jaarsveld (2008).

Wind tunnel experiments are performed on a single trailing vortex with and without grid-generated turbulence. The trailing vortex is shed from an airplane wing with a rectangular circulation distribution. Three-components particle image velocimetry (3C-PIV) is applied at four downstream distances. For the case without grid-generated turbulence, a fifth measurement location at a larger downstream distance is considered as well. In contrast to the 2C-PIV measurement technique applied by Van Jaarsveld (2008), it is now possible to measure the axial velocity as well. Every measurement consists of an ensemble with 1.000 realizations. Each realization is a three-components flow field defined in a plane perpendicular to the vortex axis. The mean quantities of the ensemble provide insight in the evolution of the azimuthal and axial velocity and vorticity components, the circulation, and the kinetic energy of turbulence. Special care is taken to determine the trailing vortex centre position for each realization. A statistical analysis of the fluctuating vortex centre position, also known as 'vortex wandering', is therefore found to be possible.

This report is organized as follows. A theoretical introduction of trailing vortices is provided in Chapter 2. The experimental procedure of the trailing vortex measurements and the the post-processing of the measurement data is discussed in Chapter 3 and Chapter 4, respectively. The results of the wind tunnel experiments are presented in Chapter 5. Chapter 6 will end this report with providing the main conclusions together with a brief discussion.

Chapter 2

Theory

There are many theoretical studies concentrated on trailing vortices, see for example Saffman (1992) and Green (1995). Saffman (1992) applies an analytical approach to viscous and laminair vortices. This work is therefore of special interest when the trailing vortex is analyzed at large downstream distances. The formation of a trailing vortex is more extensively discussed by Green (1995). A detailed study on both the azimuthal and axial velocity in a trailing vortex is provided by Batchelor (1964), Moore and Saffman (1973), and Saffman (1992).

We will consider the governing equations relevant to trailing vortices in Section 2.1. Section 2.2 considers the formation of a trailing vortex from the flow over a lift generating wing. As will be discussed in Section 2.3, a trailing vortex contains both strong azimuthal and axial currents near the vortex centre. We will provide the relationship for the evolution of the axial and azimuthal velocity components as derived by Batchelor (1964). We will end this chapter with a brief discussion of representative trailing vortex models.

2.1 Governing equations

In our wind tunnel experiments, the flow is in good approximation incompressible. For an incompressible flow, the divergence theorem holds

$$\vec{\nabla} \cdot \vec{U} = 0, \tag{2.1}$$

with the velocity denoted by $\vec{U}$. The equation of motion for fluid flows was derived by Claude-Louis Navier and George Gabriel Stokes. The equation for incompressible flows is well-known as the Navier-Stokes equation:

$$\frac{\partial \vec{U}}{\partial t} + (\vec{U} \cdot \vec{\nabla})\vec{U} = -\frac{1}{\rho}\vec{\nabla}P + \nu\vec{\nabla}^2\vec{U} + \frac{1}{\rho}\vec{F}. \tag{2.2}$$

Here, the density of the fluid is denoted by ρ and the kinematic viscosity by ν. The terms on the left hand side of Eq. 2.2 form the inertia terms. The partial time derivative gives the local rate of change of $\vec{U}$. The second inertia term is the advective derivative. The first term on the right hand side represents the pressure gradient force, and the second term denotes the viscous or friction force. Contributions other than the pressure and viscous terms are included in $\vec{F}$. From this point on, we will consider $\vec{F} = 0$. The vorticity is given by:

$$\vec{\omega} = \vec{\nabla} \times \vec{U}. \tag{2.3}$$

Because the divergence of a curl vanishes, the vorticity for any flow must satisfy:

$$\vec{\nabla} \cdot \vec{\omega} = 0. \tag{2.4}$$

By taking the the curl of Eq. 2.2, one obtains the equation for the rate of change of vorticity

$$\vec{\nabla} \times \Big\{ \frac{\partial \vec{U}}{\partial t} + (\vec{U} \cdot \vec{\nabla})\vec{U} = -\frac{1}{\rho}\vec{\nabla}P + \nu\vec{\nabla}^2\vec{U} \Big\}, \tag{2.5}$$

which can be simplified to

$$\frac{\partial \vec{\omega}}{\partial t} + (\vec{U} \cdot \vec{\nabla})\vec{\omega} = (\vec{\omega} \cdot \vec{\nabla})\vec{U} + \nu\vec{\nabla}^2\vec{\omega}, \tag{2.6}$$

for the case of a barotropic flow. The two terms on the left hand side of Eq. 2.6 represent the instationary and stationary advection terms, respectively. The rate of change of vorticity due to stretching and tilting of vortex lines is represented by the first term on the right hand side of Eq. 2.6. The second term on the right hand side represents the diffusion of vorticity.

Integrating Eq. 2.4 over a volume and applying Gauss' theorem results in

$$\int_{\mathcal{V}} \vec{\nabla} \cdot \vec{\omega} d\mathcal{V} = \oint \vec{\omega} \cdot \vec{n} d\mathcal{A} = C = 0, \tag{2.7}$$

where $\vec{n}$ is the normal to the surface $\mathcal{A}$ which encloses the volume $\mathcal{V}$. Basically, Eq. 2.7 states that the total flux of vorticity through a surface $\mathcal{A}$ enclosing volume $\mathcal{V}$ is zero in absence of any sources or sinks ($C = 0$).

The flux through a surface $\mathcal{A}'$ bounded by contour $\mathcal{C}'$ is called the circulation and is defined by

$$\Gamma = \int\int_{\mathcal{A}'} \vec{\omega} \cdot \vec{n'} d\mathcal{A}' = \oint_{C'} \vec{U} \cdot d\vec{l'}, \tag{2.8}$$

where $\vec{n'}$ is the normal vector to surface $\mathcal{A}'$, and $d\vec{l'}$ an element of contour $\mathcal{C}'$. Kelvin's theorem states that the circulation around a closed curve moving with the fluid remains constant with time for an inviscid, barotropic flow, with conservative forces only. Since we assumed incompressibility and did not include any body forces, Kelvin's theorem

$$\frac{\partial \Gamma}{\partial t} + (\vec{U} \cdot \vec{\nabla})\Gamma = 0, \tag{2.9}$$

can be applied when viscous effects are neglected. Trailing vortices are often assumed to be slender, which means that the axial component of the vorticity is much larger than the perpendicular components.

2.2 Flow over a wing: the formation of a trailing vortex

The lift generated per unit span in an irrotational flow over a two-dimensional body of arbitrary cross section is given by the Kutta-Zhukhovsky lift theorem:

$$f_L = \rho\Gamma\overline{U}_x. \tag{2.10}$$

Here, the circulation generated by the lifting body is denoted by Γ. The lift force per unit span f_L is directed perpendicularly to the main stream velocity $\overline{U}_x$. According to Eq. 2.10, the flow over a lift generating wing needs to create circulation. This is found to be possible when the trailing edge of a wing is sufficiently sharp such that the Kutta condition holds, see Kuethe and Schetzer (1959). At the initial moment that the circulation is created, a so-called starting vortex is created parallel to the wing. For an illustrative discussion of the creation of circulation by a lift generating body, the reader is referred to Kundu et al. (2008). The starting vortex is inherent to the circulation, i.e. lift, generated by the wing since Eq. 2.7 needs to be satisfied. Note that the

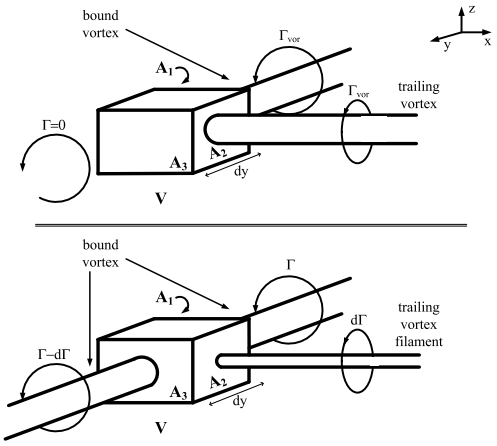

Figure 2.1: Schematic overview of the formation of a trailing vortex shed from a wing with a rectangular circulation distribution (top), and that with a more elliptical circulation distribution (bottom). In case of a wing with a more elliptical circulation distribution, a vortex sheet is formed out of trailing vortex filaments that collectively roll-up into a trailing vortex. The roll-up process stands in contrast with the formation of a trailing vortex shed from a wing with a rectangular circulation distribution. In this case, the trailing vortex has a well defined position and does not form out of a rolled up vortex sheet. The vortex filament emerging from surface A_2 is equal to the difference in vorticity flux through surface A_1 and A_3 such that the total flux through V is zero.

wing generates circulation as long as the lift is nonzero. One can therefore think of the wing as a vortex along its span and with a circulation equal to that generated by the wing. This hypothetical vortex filament replacing the wing is called the bound vortex, with *bound* signifying that it moves with the wing.

With the wing span parallel to the y-axis, and the free-stream velocity directed in the x-direction, the circulation generated by the wing at each position along the wing span is given by $\Gamma(y)$. For most wings, the strength of the circulation is maximum at the center of the wing and zero at the wing tips. In combination with Eq. 2.7, this means that a vortex filament emerges from one of the sides of a box enclosing the wing, see Figure 2.1. The strength $\varsigma(y)$ of the vortex filament emerged from a change in circulation $d\Gamma$ over a length dy is now given by:

$$\varsigma(y) = -\frac{d\Gamma}{dy}dy. \tag{2.11}$$

The Helmholtz vortex theorems state that vortex tubes cannot end within the fluid. Vortex tubes must either end at a solid boundary or form a closed loop. The bound vortex therefore bends downstream and forms a trailing vortex which eventually connects to the the starting vortex. One can think of the vortices with strength given by Eq. 2.11 as filaments from the bound vortex, which collectively roll-up into the trailing vortex.

In this work, a specially designed twisted wing is applied. This wing is characterized by a rectangular lift distribution. This means that the distribution of circulation is constant along the wing

$$\Gamma(y) = \Gamma_w \qquad 0 < y \leqq s \tag{2.12}$$

$$= 0 \qquad y > s, \tag{2.13}$$

in which the wing is located between $0 < y \leqq s$ and $y > 0$. By applying 2.11, it becomes clear that the trailing vortex is located at $y = s$, see also Figure 2.1. In practice, it comes down to the trailing vortex being highly concentrated even close to the wing. For a detail description of the twisted wing design, the reader is referred to Van Jaarsveld (2008).

2.3 Flow field of a trailing vortex

We discussed the origin of a trailing vortex in Section 2.2. Here, it was put forward that a trailing vortex is inevitable to a lift generating body. The flow field of a trailing vortex will now be considered. This flow field is complex nearby the wing due to the roll-up of the vortex sheet. Further downstream, the trailing vortex becomes in good approximation axisymmetric and simplified models can therefore be applied to represent the vortex. We will first discuss the axial flow in a trailing vortex. We will end this section with considering some representative models of a trailing vortex.

Many experimental studies on trailing vortices report a strong axial current near the axis of symmetry of a trailing vortex, see Green (1991) and Chow (1997). In the windtunnel experiments of Chow (1997), such an axial current was observed with a velocity 1.77 times that of the main stream velocity. In this section, we will consider the physical principle behind the axial current in a trailing vortex. For this, we closely follow the work of Batchelor (1964).

In the following, we apply a cylindrical coordinate system r, θ, x. The velocity field of an axisymmetric trailing vortex is given by $\vec{U} = (U_r, U_\theta, U_x)$. For the sake of the argument, we assume that:

$$U_r \ll U_\theta, \tag{2.14}$$

$$\frac{\partial}{\partial x} \ll \frac{\partial}{\partial r}. \tag{2.15}$$

We will validate this boundary layer type approximation in Section 4.1. The radial, azimuthal, and axial components of the equation of motion for a stationary flow are now given by

$$\frac{U_\theta^2}{r} = \frac{1}{\rho}\frac{\partial p}{\partial r}, \tag{2.16}$$

$$U_x \frac{\partial U_\omega}{\partial x} = \nu\big(\nabla^2 U_\omega - \frac{U_\omega}{r^2}\big), \tag{2.17}$$

$$U_x \frac{\partial U_x}{\partial x} = -\frac{1}{\rho}\frac{\partial p}{\partial x} + \nu \nabla^2 U_x, \tag{2.18}$$

respectively. The radial component shows a balance between the centrifugal force and the pressure force. The pressure can be obtained at any point in the trailing vortex by making use of the Bernoulli function. With the pressure p_∞ and main stream velocity $\vec{U} = (0, 0, \overline{U}_x)$ at a large distance upstream from the wing, the Bernoulli equation may be written as

$$\frac{p}{\rho} + \frac{1}{2}(U_x^2 + U_\theta^2) + \triangle H = \frac{p_\infty}{\rho} + \frac{1}{2}\overline{U}_x^2, \tag{2.19}$$

in which the total head loss due to viscous effects is included in $\triangle H \geqq 0$. One can combine Eq. 2.16 and 2.19 in order to obtain a function for the axial velocity at any radial position from the trailing vortex axis of symmetry

$$U_x^2(r) = \overline{U}_x^2 - U_\theta^2(r) + 2\int_r^\infty \frac{U_\theta^2}{r'} dr' - 2\triangle H, \tag{2.20}$$

which can be rewritten with $\Gamma(r) = 2\pi U_\theta(r) r$ as

$$U_x^2(r) = \overline{U}_x^2 + \frac{1}{2\pi}\int_r^\infty \frac{1}{r'^2}\frac{\partial \Gamma(r')}{\partial r'} dr' - 2\triangle H. \tag{2.21}$$

When viscous effects are neglected, Eq. 2.21 reduces to:

$$U_x^2(r) = \overline{U}_x^2 + \frac{1}{2\pi}\int_r^\infty \frac{1}{r'^2}\frac{\partial \Gamma(r')}{\partial r'} dr'. \tag{2.22}$$

The vorticity of a trailing vortex is usually single signed, which means that the radial profile of circulation increases monotonically. The second term on the right hand side of Eq. 2.22 therefore represents the increase in U_x^2. The increase in axial velocity can be thought of as the Bernoulli theorem accompanying for the pressure drop due to the centrifugal force.

The trailing vortex has an axial velocity surplus, often called a jet, near the axis of symmetry. The radial profile of axial velocity is here given by Eq. 2.22. In deriving this equation, we applied an inviscid approach which is valid as long as $\nu t/r_1 \ll 1$, with r_1 approximately the radius of maximum azimuthal velocity and $t = \triangle x/\overline{U}_x$. The downstream distance from the trailing edge to the wing is here denoted by $\triangle x$. The inviscid approach is therefore valid for streamwise distances close to the wing where the trailing vortex has not yet rolled up completely. Batchelor (1964) proved that viscosity becomes important for large downstream distances and showed that the continual slowing-down of the azimuthal motion by viscosity leads to a positive axial pressure gradient and consequently to continual loss of axial momentum. The relation for the viscous decay of the maximum azimuthal velocity with streamwise distance can be derived from Eq. 2.2 and is given by:

$$U_{\theta,max}(\triangle x) \sim \triangle x^{-1/2}. \tag{2.23}$$

An asymptotic analysis revealed that the maximum axial velocity is related to the downstream distance $\triangle x$ from the trailing edge of the wing as:

$$U_{x,max}(\triangle x) \sim \triangle x^{-1} \log(\triangle x). \tag{2.24}$$

Batchelor (1964) showed that the decaying swirling motion increases the pressure in the vortex core and consequently decreases the axial velocity according to $\log(\triangle x)$, while diffuse spreading of the vortex continually diminishes the axial velocity according to $(\triangle x)^{-1}$. The combination of these effects result in Eq. 2.24. According to this relation, the jet can evolve into a wake with an axial velocity defect near the vortex centre. For an extensive discussion on the axial velocity in a trailing vortex, the reader is referred to Saffman (1992).

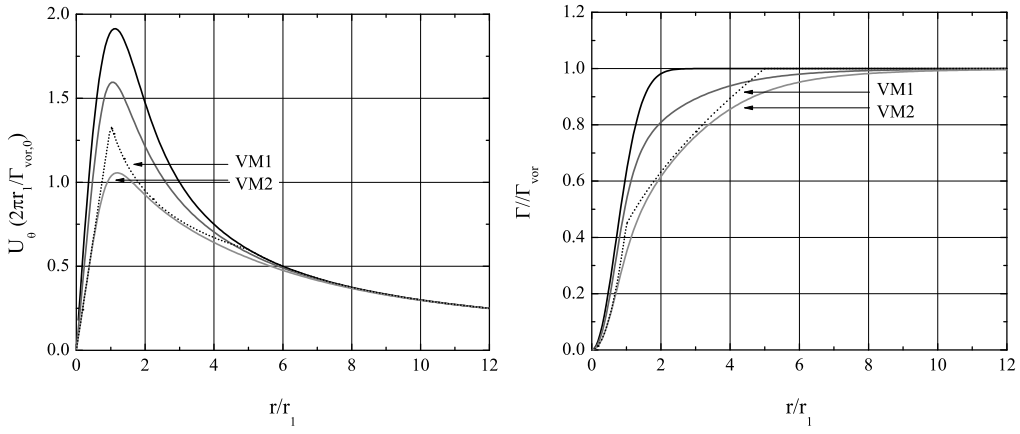

(a) Azimuthal velocity (b) Circulation

Figure 2.2: Radial profiles of the azimuthal velocity (left) and the circulation (right) for the Lamb-Oseen model with $\Gamma_{vor} = 1$, $R = 1$ (dark lines) and the two-length-scales VM2 with $\Gamma_{vor} = 1$, $r_1 = 1$, $r_2 = 5$, $\beta = 0.8$ (dark gray) and $\beta = 0.5$ (gray). The VM1 is applied for the case with $\hat{\beta} = 0.8$ (dotted lines).

2.4 Trailing vortex models

The topic of trailing vortices is the focus for many theoretical, numerical, and experimental studies. Most of these studies apply simplified models to represent a trailing vortex. In this section,

we will discuss two common trailing vortex models. The most simple axisymmetric viscous vortex model is provided by the Lamb-Oseen vortex, see Lamb (1932). It arises as an exact solution of the Navier-Stokes equations for the initial condition

$$\omega_x(r,0) = \Gamma_{vor}\delta_{r=0}, \tag{2.25}$$

with Γ_{vor} the circulation of the vortex, and the delta-function $\delta_{r=0}$ being one for $r = 0$ and zero otherwise. The exact solution is given by

$$U_\theta(r) = \frac{\Gamma_{vor}}{2\pi r}\big(1 - \exp(-r^2/R^2)\big), \tag{2.26}$$

where the vortex core radius is denoted by R and evolves under viscous decay according to:

$$R(t) = \sqrt{4\nu t}. \tag{2.27}$$

The circulation profile is given by:

$$\Gamma(r) = \Gamma_{vor}(1 - \exp(-r^2/R^2)). \tag{2.28}$$

The Lamb-Oseen vortex model is based on the viscous decay of a line vortex, in which the vorticity has initially a delta-function singularity. This is in contrast with the roll-up of a finite sized vortex sheet into a trailing vortex, see Section 2.2. It is believed that due to the roll-up process, a significant amount of vorticity is concentrated in a region around the vortex core. Here, the vortex core is that region in which the flow field can be approximated by a solid-body rotation. More elaborate vortex models are necessary for a more correct description of the region around the vortex core. We will consider the two-length-scales vortex model as first discussed by Jacquin et al. (2001). This vortex model is based on three radial regimes, defined as:

$$U_\theta(r) = \hat{\Omega}_{vor} r \qquad 0 < r \leqq \hat{r}_1, \tag{2.29}$$

$$= \Omega_{vor}\hat{r}_1\Big(\frac{r}{\hat{r}_1}\Big)^{-\hat{\beta}} \qquad \hat{r}_1 < r \leqq \hat{r}_2, \tag{2.30}$$

$$= \frac{\hat{\Gamma_{vor}}}{2\pi r} \qquad r > \hat{r}_2. \tag{2.31}$$

In analogy with Fabre and Jacquin (2004), the vortex model described by Eqs. 2.29-2.31 is referred to as VM1. The more realistic, smooth version of VM1 is referred to as VM2 and is given by

$$U_\theta(r) = \frac{\Omega_{vor} r}{[1 + (r/r_1)^4]^{(1+\beta)/4}[1 + (r/r_2)^4]^{(1-\beta)/4}}, \tag{2.32}$$

and the corresponding circulation profile is specified by

$$\Gamma(r) = \Gamma_{vor}\frac{(r_2/r_1)^{\beta-1}\cdot(r/r_1)^2}{[1 + (r/r_1)^4]^{\frac{1+\beta}{4}}\cdot[1 + (r/r_1)^4]^{\frac{1-\beta}{4}}}, \tag{2.33}$$

in which r_1, r_2, β correspond to the VM1 parameters $\hat{r}_1$ and $\hat{r}_2$, respectively. The radius r_1 defines that region in which the flow field can be approximated by solid-body rotation with angular frequency Ω_{vor}. It has to be remarked, that r_1 is approximately equal to the radius of maximum azimuthal velocity. The radius $r_2 > r_1$ defines the outer region of the vortex in which 97% of the total circulation $\Gamma_{vor} = 2\pi\Omega_{vor}r_1^2(r_2/r_1)^{1-\beta}$ is contained. The angular velocity decays according to $U_\theta(r) \sim r^{-\beta}$ in the region $r_1 \lessapprox r \lessapprox r_2$, and according to $U_\theta(r) \sim r^{-1}$ for $r \gtrapprox r_2$. The values of r_2 and $\beta > 0$ depend on the wing geometry. From now on, the inner vortex region is defined by $0 < r < r_1$ and the outer vortex region by $r_1 < r < r_2$.

Figure 2.2 shows the difference between the Lamb-Oseen vortex model given by Eqs. 2.26-2.28 and the two-length-scales vortex model described by Eqs. 2.29-2.33.

Chapter 3

Experimental Procedure

Trailing vortices are analyzed in many theoretical, numerical, and experimental studies. The experimental studies on a single and a pair of trailing vortices can be divided in experiments performed in a wind tunnel (see Beninati and Marshall (2005), Chow (1997), Devenport et al. (1996)), in a towing tank (Iversen (1976), Sarpkaya and Daly (1987), Liu (1992)), and during flight tests (see Tombach (1973), Sarpkaya (1998)). Wind tunnel studies can be performed with the help of two- (three-)components particle image velocimetry 2C-PIV (3C-SPIV), (multiple) hotwires, and (multiple) pitot tubes. The main difference between these measurement techniques is the spatial and temporal resolution of the measurement. The temporal resolution of hotwire and pitot tube measurements is large and it is often not a problem to cover the smallest time scales present in a (turbulent) flow. On the other hand, the spatial resolution of an instantaneous measurement with multiple hotwires/pitot tubes is limited due to probe interference with the flow. In other words, the spatial resolution is limited by the amount of probes that can be installed without significantly influencing the flow field. The PIV measurement technique makes use of passive tracer particles so that the interference with the flow is negligible. One can provide the flow with a high density of passive particles so that the spatial resolution of PIV is, among other reasons, relatively large. The temporal resolution is limited due to current technological restrictions. The main advantage of PIV above probe measurements is that snapshots of the entire domain of interest can be obtained. On the other hand, hotwire measurements are much more accurate than PIV measurements.

Vortex wandering is a problem encountered in many fixed probe studies on trailing vortices. The coherent low-frequency motion of a trailing vortex can lead to large errors in mean velocity and turbulence measurements made with fixed probes. Devenport et al. (1996) have extensively analyzed and quantified the effects of vortex wandering. They were able to reverse its effects on mean-velocity measurements and spectral decomposition was used to separate its velocity fluctuations from those produced by turbulence. In contrast to fixed-probe measurements, vortex wandering is not that an issue for PIV measurements. The in-plane vortex centre can be defined for every instantaneously obtained flow field, and it is therefore easy to correct for vortex wandering.

For an extensive discussion on the hotwire measurement technique, the reader is referred to Tropea et al. (2007), and the issue of probe interference is discussed by Devenport et al. (1996). This work makes use of the 3C-PIV measurement technique. We will briefly discuss the principle of 3C-PIV in Section 3.1. The method of calibration and experimental parameters are found to be important for the quality of the 3C-PIV measurement results. This will be discussed in Sections 3.1.1 and 3.1.2. We will end this chapter with briefly discussing the experimental setup in Section 3.2.

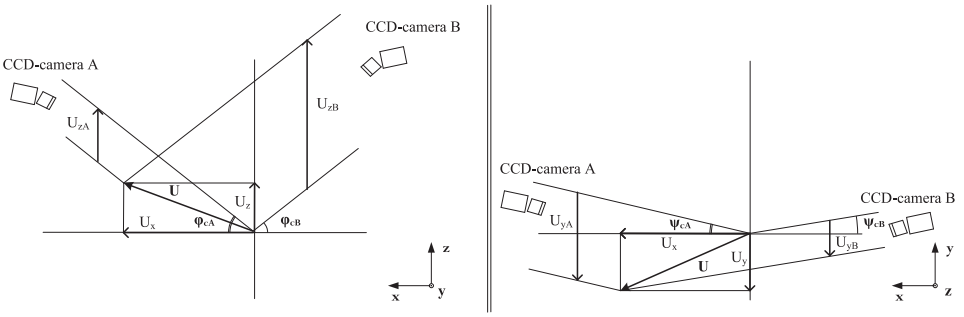

Figure 3.1: Schematic overview of the 3C-PIV experimental setup. The CCD camera A (B) is positioned such that it makes an angle $\varphi_{cA}(\varphi_{cB})$ with the (x, y)-plane, and an angle $\psi_{cA}(\psi_{cB})$ with the (x, z)-plane. By analyzing the recordings of each CCD camera separately, the in-plane velocities U_{yA}, U_{zA}, U_{yB}, and U_{zB} are obtained. General geometrical imaging formulas given by Eqs. 3.1-3.4 are applied to obtain the velocity components U_x, U_y, and U_z.

3.1 Three-Components Particle Image Velocimetry: 3C-PIV

Three-components particle image velocimetry (3C-PIV) is based on determining the displacement of passive tracer particles in three directions. The fluid mechanical properties of the tracer particles are such that they follow the flow accurately and in a passive manner. For each individual 3C-PIV measurement, the tracer particles are illuminated twice by a laser sheet and at each illumination recorded by two cameras. Subsequently, a local displacement in the laser sheet plane is determined by analyzing the two recordings of each CCD camera separately. Note that the displacements are perceived differently for each CCD camera since they are observing the laser sheet at different angles. The displacements are determined by applying the method of autocorrelation, and a measure for the quality of autocorrelation is given by the correlation coefficient. The local displacements can now be divided by the time delay between two subsequent illumination pulses to obtain the local velocity. We will proceed with briefly discussing the procedure with which the three-dimensional velocity is determined from the in-plane velocities obtained by analyzing the recordings of each CCD camera separately. After that, we will describe the most important experimental parameters that determine the quality of the 3C-PIV result.

The CCD camera A (B) is positioned such that it makes an angle $\varphi_{cA}(\varphi_{cB})$ with the (x, y)-plane, and an angle $\psi_{cA}(\psi_{cB})$ with the (x, z)-plane, see Figure 3.1. By analyzing the recordings of each CCD camera separately, the in-plane velocities U_{yA}, U_{zA}, U_{yB}, and U_{zB} are obtained. The actual velocity of the tracer particle is denoted by $\vec{U}$ and consists of components U_x, U_y, and U_z. These velocities can now be obtained from the four measured velocities and angle at which the CCD camera observe the laser sheet

$$U_x = \frac{U_{yA} - U_{yB}}{\tan(\varphi_{cA}) + \tan(\varphi_{cB})} \tag{3.1}$$

$$= \frac{U_{zA} - U_{zB}}{\tan(\psi_{cA}) + \tan(\psi_{cB})}, \tag{3.2}$$

$$U_y = \frac{U_{yA}\tan(\varphi_{cB}) + U_{yB}\tan(\varphi_{cA})}{\tan(\varphi_{cA}) + \tan(\varphi_{cB})} \tag{3.3}$$

$$U_z = \frac{U_{zA}\tan(\psi_{cB}) + U_{xB}\tan(\psi_{cA})}{\tan(\psi_{cA}) + \tan(\psi_{cB})}, \tag{3.4}$$

which are general geometrical imaging formulas. The system of equations 3.1-3.4 is overdetermined and can be solved with a least-squares method. The residual of this least-squares fit can be used as a measure of quality for the three-component measurement result. A high quality result is obtained when the residual is between 0.1 and 0.5 pixels, and a low quality result is obtained

when the residual value is larger than 0.5 pixels. With this, we follow the definition of Raffel et al. (2007). High spatial variations in the flow field and misalignment of the CCD camera views are the most important contributions to significant residuals. Note that the correlation coefficient is indirectly related to the residual value, and that both give a measure for the quality of the 3C-PIV result. However, we use the residual value since it is a more direct measure for the quality of the obtained three-dimensional velocity field. The method of calibration and the setting of experimental parameters are important for the quality of the result. We will briefly discuss the method of calibration and the most important 3C-PIV and experimental parameters.

3.1.1 Method of calibration

In order to reconstruct the local displacement vector, the viewing direction and magnification factor for each CCD camera must be known at each point in the respective PIV recording. Therefore, a sophisticated method of calibration is applied. For each camera, recordings are made of a calibration target placed parallel to the laser sheet at five different x-positions. The calibration target consists of a mesh of dots which are equally spaced with a known distance. This distance is set such that approximately 15^2 dots are contained in the CCD camera view. The x-positions of the calibration target are set to -2, -1, 0, 1, and 2 mm with respect to the estimated x-position of the laser sheet. The x-position of the laser sheet cannot be determined accurately since the sheet thickness varies with the position in the laser sheet. The relative x-locations of the calibration target are determined by a micrometer and with an accuracy of 0.005 mm. The variations in x-positions are large enough to extract the relative (y, z)-position of the cameras accurately, while small enough for the calibration target to be still in focus at every x-position. Digital image processing techniques are applied to acquire the (y_c, z_c) coordinates of each dot in the calibration target as perceived by each camera. The (y_c, z_c) coordinates of the dots can be transformed to (y, z) with the help of a second-order polynomial fit

$$x = a_0 x_c + a_1 y_c + a_2 x_c^2 + a_3 x_c y_c + a_4 y_c^2, \tag{3.5}$$

$$y = b_0 x_c + b_1 y_c + b_2 x_c^2 + b_3 x_c y_c + b_4 y_c^2, \tag{3.6}$$

in which the twelve unknown projection parameters are determined by a least-squares fit of at least six (y_c, z_c) coordinates. The mapping procedure as based on these projection equations is found to be very robust since it accounts for lens distortions and other image nonlinearities. The viewing direction and the magnification of each CCD camera can now be determined from the mapping equation obtained at each of the five x-positions.

The described calibration method provides the essential information needed for the reconstruction of a three-dimensional displacement vector from two separate two-dimensional displacement vectors as obtained at the same instant but from two CCD camera recordings. However, this reconstruction approach assumes that the calibration target is perfectly aligned with the center of the laser sheet. As already mentioned above, this is very difficult to achieve since the x-position of the laser sheet cannot be determined accurately. It was found that a slight out-of-plane position and/or minor rotation of the calibration target results in high values of the residual, i.e. the quality of the result is low. The problem of misalignment is solved with the help of a disparity correction. The disparity correction as applied in this work, is based on the actual PIV recordings from both cameras at the same instant. These images are dewarped according to their projection equations and a cross-correlation is performed between the views. In this way, a displacement field is obtained which represents the disparity of the views with respect to each other. The information from the displacement field can now be used to reposition the laser sheet. With the laser sheet being repositioned, the displacement field is still nonzero due to minor rotation of the calibration target. The displacement field is now used to modify the projection parameters. For this, the displacement field is least-squares fitted with a fourth order polynomial. The procedure described above is called the disparity correction and is performed

for every pair of 3C-PIV recordings. The quality of the three-dimensional velocity fieldwas found to be significantly higher when a disparity correction was applied.

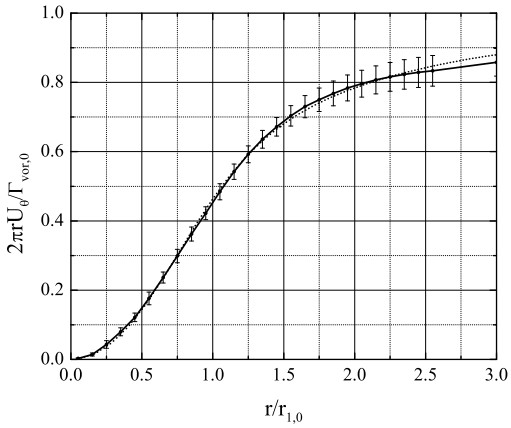

Figure 3.2: The inner (———) and outer region (·····) measurement results for radial profile of circulation. The inner region measurements are performed with a time delay of 25 *and* 75 μs*, respectively. In contrast to Van Jaarsveld (2008), it becomes clear that the inner and outer region measurement results nicely overlap. The circulation is made dimensionless with a typical value for the total circulation of the trailing vortex.*

3.1.2 3C-PIV processing and experimental parameters

For evaluation of the tracer particles displacement, the digital PIV recording is divided in small subareas called interrogation areas. It is hereby assumed that all particles within one interrogation area move homogeneously between the two illuminations. The size of the interrogation areas during evaluation must therefore be small enough to resolve the velocity gradients, but large enough to contain a sufficient amount of tracer particles. The interrogation areas are set to 16 by 16 pixels to obtain sufficient quality results even at small distances from the vortex centre where the velocity gradients are high. Low quality results are obtained for $r/r_{1,0} \lessapprox 1/8$ with $r_{1,0}$ a typical value for r_1. This region of low quality results approximately corresponds to the region in which interrogation areas closest to the vortex centre are located.

The time delay between two illumination pulses and the laser sheet thickness are important parameter and need to be set according to the characteristics of the flow. The time delay must be long enough to obtain a sufficient large displacement of the tracer particles, but short enough to avoid particles leaving the laser sheet between subsequent illuminations. For the same reason, the laser sheet has to be sufficiently thick but not too thick to avoid loss of the required intensity of particle illumination.

3C-PIV measurements are performed that capture both the inner and outer region of the trailing, and there are 3C-PIV measurements performed that capture the inner vortex region only. The experimental parameters are set for each measurement region according to the corresponding flow characteristics. We will continue with discussing the inner and outer region measurements and the most important experimental parameters.

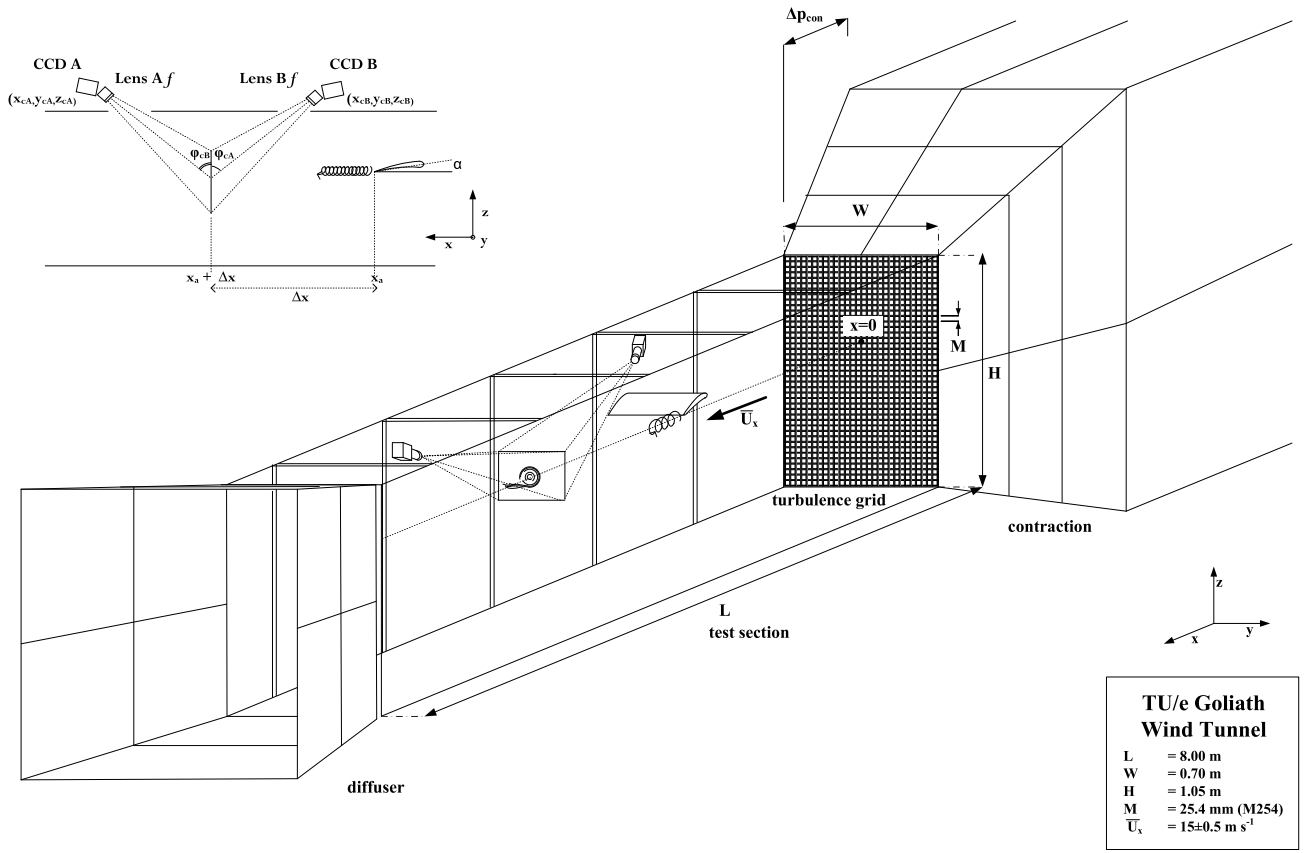

Figure 3.3: Schematic view of the TU/e Goliath Windtunnel with the turbulence grid. The dimensions of the wind tunnel are given by L×H×W= 8.00×1.05×0.70 m^3. The contraction is characterized by an area decrease from 18.38 to 0.74 m^2 over a distance of 5.30 m, the relating pressure drop is given by $\triangle p_{con}$. The main stream velocity $\overline{U}_x$ is set by the pressure drop over the contraction. The trailing edge of the wing corresponds to the streamwise position x_a. The streamwise measurement location, that location where the laser sheet is located, is given by $x_a + \triangle x$.

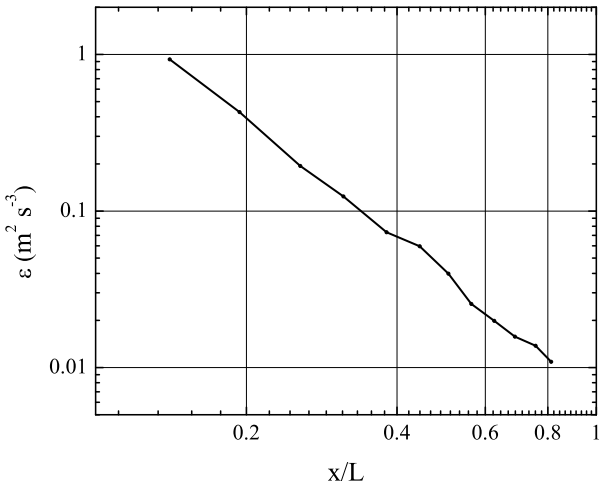

Figure 3.4: The streamwise profile of the turbulence dissipation rate for the wind tunnel flow with grid-generated turbulence. The streamwise location of the wing is $x_a = 3.45$ m, see Table 3.1.

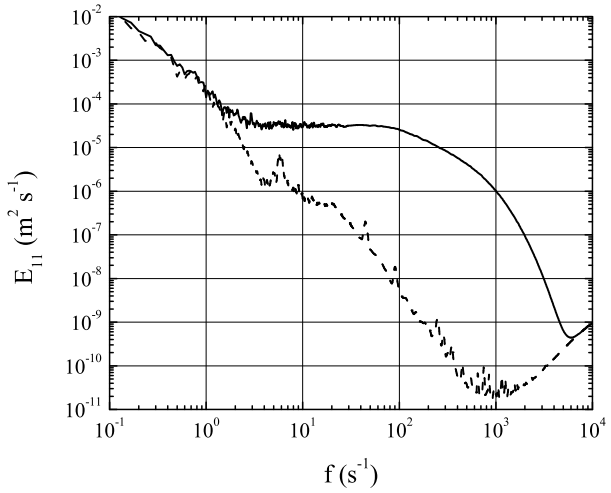

Figure 3.5: The longitudinal energy spectrum for the wind tunnel flow without (———) and with (·····) grid-generated turbulence. The temporal detaching of the boundary layer in the diffuser is believed to responsible for the peak around $f = 4\ s^{-1}$. For a more detailed discussion of the energy spectrum, the reader is referred to Appendix C.

3.1.3 Inner and outer region measurements

Measurements have been performed for the inner and outer region of the trailing vortex. Both kind of measurements have the vortex centre as midpoint. The sides of the inner region measurements are about $3.5 \cdot 10^{-2}$ m, and that of the outer region measurements $14.0 \cdot 10^{-2}$ m. In this way, the region of the trailing vortex $r/r_{1,0} < 3$ is covered with high quality by the inner region measurements, while $3 < r/r_{1,0} < 12$ is covered with high quality by the outer region measurements. In other words, the inner and outer region measurements cover the region around the vortex with a radius approximately three and twelve times that of maximum azimuthal velocity, respectively. The velocities and velocity gradients are larger in the inner region than in the outer region. This means that the time delay between two illumination pulses and the laser sheet thickness needs

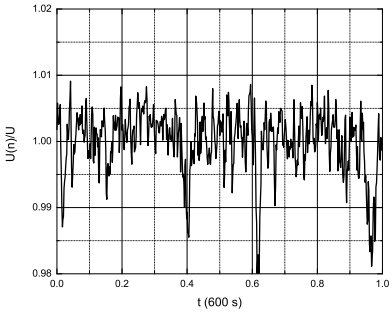

(a) main stream velocity

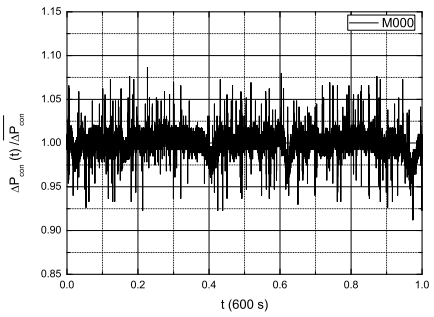

(b) pressure drop over contraction

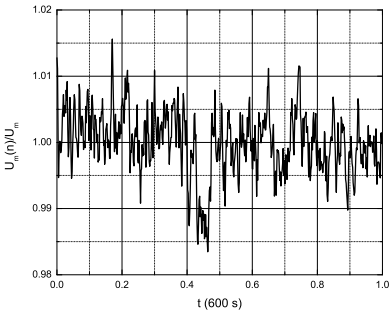

(c) main stream velocity

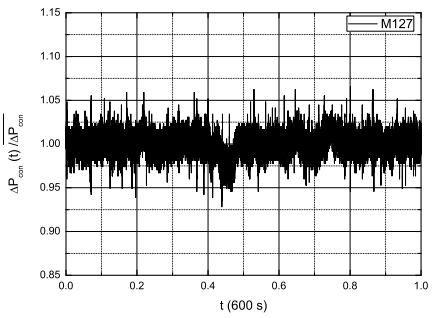

(d) pressure drop over contraction

Figure 3.6: The main stream velocity $U_x(t)/\overline{U}_x$ (left) and the pressure drop over the contraction $\triangle p_{cont}(t)/\overline{\triangle p_{cont}}$ (right) are shown for a measurement of 600 s for the case without (top, denoted by $M000$) and with grid-generated turbulence (bottom, denoted by $M254$). The temporal detaching of the boundary layer in the diffuser is believed to occur at a frequency around $f = 4\ s^{-1}$. It can be seen that sudden changes of 1-2% in the main stream velocity take place and it is believed that these sudden changes are related to unsteady the flow field in the diffuser. The sudden changes in the main stream velocity last about 10 s, and they occur more frequently in the case without than with grid-generated turbulence.

to be set differently. It was found more practical to adapt the time delay while leaving the laser sheet thickness at approximately 3 mm. The time delay is set to 25 and 75 μs for the inner and outer region measurements, respectively. The measurement results of the inner region and outer region are validated with those obtained with a time delay of 75 and 100 μs, respectively. The overlap between the inner and outer region measurement is shown in Figure 3.2.

The tracer particles have a diameter of approximately 4μm, see Raffel et al. (2007), which is both in the inner and outer region measurements smaller than covered by one pixel. This means that the exact position, and therefore the displacements, of tracer particles cannot be determined exactly. As a result, the displacements can be biased toward integral pixel values. This effect is called peak locking, and is discussed by Van Jaarsveld (2008) and Raffel et al. (2007). It was found by Van Jaarsveld (2008) that the effect of peak locking reduces when the seeding density of tracer particles is sufficiently high. With this in mind, the seeding density is controlled by visual inspection. The tracer particles are illuminated by a laser sheet produced by a double pulses Nd:YAG laser. Every pulse is approximately 2 ns which is sufficiently short to avoid streaks. The flow is monitored with an externally triggered 10-bit CCD camera. The CCD has a resolution of 1600 by 1200 pixels and may store image pairs with a frequency of 15 Hz. Sophisticated post-processing software is applied to handle the great amount of data. Both cameras are equipped with a 105

mm and 28 mm lens for the inner and outer region measurements, respectively. The cameras are mounted according to the Scheimpflug condition so that the field of depth is sufficiently large.

Table 3.1: The wing locations x_a and the measurement locations $\triangle x$. Here, x_a is measured from the entrance of the wind tunnel test section, and $\triangle x$ is measured from the trailing edge of the wing. The values of $\triangle x$ are made dimensionless with the chord length of the wing $c = 7.5 \cdot 10^{-2}$ m. The time $t = \triangle x / \overline{U}_x$ is made dimensionless with the advection time scale $\Gamma_{vor,0}/(2\pi r_{1,0}^2) \approx 4.28 \cdot 10^{-4}$ s. Here, $t(\Gamma_{vor,0}/2\pi r_{1,0}^2) = 0$ corresponds to the trailing edge of the wing. We only performed measurements with $t(\Gamma_{vor,0}/2\pi r_{1,0}^2) = 662.5$ for the cases without grid-generated turbulence. It was not possible to consider the same time for the cases with grid-generated turbulence. The turbulence intensity at the location of the wing namely changes since the wing needed to be replaced from $x_a = 3.45$ towards 1.45 m to obtain $t(\Gamma_{vor,0}/2\pi r_{1,0}^2) = 662.5$ still within the wind tunnel test section.

x_a (m)	$\triangle x(m)$	$\triangle x/c$	$t(\Gamma_{vor,0}/2\pi r_{1,0}^2)$
3.45	0.11	1.5	17.5
3.45	0.56	7.5	87.5
3.45	1.13	15.0	175.5
3.45	2.25	30.0	350.0
1.45	4.25	56.7	662.5

3.2 Experimental setup

An overview of the experimental setup is presented in Figure 3.3. The test section of the TU/e Goliath Windtunnel is 8.00 m long, and has a cross section of 1.05 by 0.70 m. Measurements are performed for the case with and without grid-generated turbulence. The turbulence grid is characterized by a mesh size $M \approx 2.54 \cdot 10^{-2}$ and solidity $\sigma = 0.26$. This turbulence grid is especially designed to generate weak turbulence, see Appendix B and Crow and Bate (1976) for the definition of weak turbulence. It has to be remarked that the definition of weak or strong turbulence depends on the distance between the two trailing vortices, and that we use typical values for these as applied by Van Jaarsveld (2008). The wind tunnel flow with and without grid-generated turbulence is extensively studied in Appendix C. The main stream velocity is denoted by $\overline{U}_x$ and is set to 15±0.5 m s^{-1} for all measurements. The main stream velocity is controlled by the pressure drop over the contraction $\triangle p_{con}$. In this way, no velocity measurement device has to be installed inside the test section such that it can interfere with the flow. The streamwise profile of the turbulence dissipation rate for the wind tunnel flow with grid-generated turbulence is presented in Figure 3.4. For this case, the Taylor Reynolds number decays from 55±8 to 45±5 at the end of the test section. The wind tunnel flow field was found to be in good approximation homogeneous and isotropic. However, a fluctuation is caused by a temporal detaching of the boundary layer in the diffuser. The temporal detaching of the boundary layer in the diffuser is believed to occur at a frequency around $f = 4$ s^{-1}, see Figure 3.5. From Figure 3.6, it becomes clear that the main stream velocity can suddenly change 1-2%. It is believed that these sudden changes are related to the unsteady flow field in the diffuser. The sudden changes in the main stream velocity last about 10 s, and they occur more frequently in the case without than with grid-generated turbulence.

A specially designed wing with a rectangular lift distribution, see Chapter 2, is located at streamwise position x_a. Here, x_a is defined as the streamwise distance from the entrance of the wind tunnel test section towards the trailing edge of the wing. The wing has a chord length of $c = 7.50 \cdot 10^{-2}$ m and the angle of attack is set to $\alpha = 7.5°$ for every measurement. In this way, the flight Reynolds number

$$Re_f = \frac{\Gamma_w}{\nu} \tag{3.7}$$

is approximately 40.000. The measurement location, that is the streamwise position at which the laser sheet is located, is denoted by $x_a + \triangle x$. The streamwise distance from the trailing edge of the wing towards the laser sheet is then given by $\triangle x$.

We discussed in Section 2.2 that a vortex sheet rolls up into a trailing vortex. Green (1995) reported that the inner region of the vortex becomes approximately axisymmetric within three chord lengths from the trailing edge of the wing. To capture the roll-up of the vortex, we set our first measurement location at 1.5 chord lengths from the trailing edge of the wing. The measurement location farthest away from the wing is defined by practical reasons. The measurement locations are shown in Table 3.1.

The CCD cameras A and B are placed on top of the test section at positions x_{cA} and x_{cB}. The positions are set such that the angles φ_{cA} and φ_{cB} are close to 45 degrees. In this way, the measurement precision of the out-of-plane component is optimal, see Raffel et al. (2007). The angles ψ_{cA} and ψ_{cB}, see Figure 3.1, are very close to zero.

3.3 Nondimensional quantities

The quantities reported in this work are made dimensionless with the radius r_1 of the inner region and the total circulation Γ_{vor} of the trailing vortex. The values are given by $r_{1,0} = 5.85 \cdot 10^{-3}$ m and $\Gamma_{vor,0} = 0.50$ m^2 s^{-1}, where the subscript 0 refers to the flow quantity obtained at $t(\Gamma_{vor,0}/2\pi r_{1,0}^2) = 350.0$ behind the wing. The time is made dimensionless with the advection time scale $(2\pi r_{1,0}^2)/\Gamma_{vor,0} \approx 4.28 \cdot 10^{-4}$ s.

We will describe the evolution of the trailing vortex in terms of time $\triangle x/\overline{U}_x$ instead of distance $\triangle x$ behind the wing. It is more convenient to make the time dimensionless with parameters of the trailing vortex, than it is for the distance behind the wing. The measurement locations are made dimensionless in Table 3.1.

3.4 Acquisition of experimental data set

An ensemble $\mathcal{P}$ with 1.000 realizations is acquired for every measurement. The realizations $\mathrm{p} \in \mathcal{P}$ are obtained with a frequency of 15 Hz, which is approximately equal to $6.5 \cdot 10^{-3}\Gamma_{vor,0}/(2\pi r_{1,0}^2)$. This means that about every $1.5 \cdot 10^2 2\pi r_{1,0}^2/\Gamma_{vor,0}$ a snapshot of the trailing vortex is obtained. A measurement in which $\mathrm{P} = 1.000$ realizations are obtained, takes then approximately $1.5 \cdot 10^5 2\pi r_{1,0}^2/\Gamma_{vor,0})$. In this way, low-frequency events such as vortex wandering, and more importantly, the sudden changes in main stream velocity are believed to be sufficiently resolved. The typical time of the former is provided by Devenport et al. (1996) and is given by $\mathcal{O}(\cdot 2\pi r_{1,0}^2/\Gamma_{vor,0})$, and that of the latter results from Figure 3.6 and is given by $\mathcal{O}(10^4 \cdot 2\pi r_{1,0}^2/\Gamma_{vor,0})$. We may conclude that one measurement of $\mathcal{P}$ realizations approaches ergodicity.

Chapter 4

Postprocessing of Data

We will discuss the postprocessing of the experimentally obtained three-components velocity field in a plane perpendicular to the trailing vortex axis. Great care is taken to accurately determine the position of the vortex centre for each pair of PIV-recordings. This will be discussed in the first section. Subsequently, a distinction is made between the stationary and two kinds of co-moving frames of reference. In Section 4.2, we will describe the method in which statistical data is derived from an ensemble of vortex centre positions. The calculation of the azimuthal and axial velocity and vorticity components, the circulation, and the kinetic energy of turbulence is elaborated in Section 4.3.

The x-, y-, and z-components of the velocity obtained at the j_s^{th} grid point in the y-direction and the k_s^{th} grid point in the z-direction is denoted by

$$U^{\mathrm{p}}_{s,\zeta}(j_s,k_s) \qquad \zeta = x,y,z \quad j_s = 1..N_{s,j}, k = 1..N_{s,k}, \tag{4.1}$$

in which $N_{s,j}$ and $N_{s,k}$ represent the number of grid points in the y- and z- direction, respectively. The y_s- and z_s- positions corresponding to grid point (j_s,k_s) are denoted by $y_s(j_s,k_s)$ and $z_s(j_s,k_s)$. The subscript s refers to quantities as obtained from the stationary frame of reference. The superscript p refers to the quantities obtained in the p^{th} realization with $\mathrm{p} = 1..\mathrm{P}$ inside the ensemble $\mathcal{P}$.

4.1 Stationary and co-moving frame of reference

The position of the vortex centre is determined by means of an interpolated extremum in the two-dimensional streamfunction. The streamfunction is obtained by integration of the in-plane velocity components $U^{\mathrm{p}}_{s,y}(j_s,k_s)$ and $U^{\mathrm{p}}_{s,z}(j_s,k_s)$. In doing this, we assume that the in-plane flow field is incompressible and divergence free:

$$\frac{\partial U^{\mathrm{p}}_{s,y}}{\partial y_s} + \frac{\partial U^{\mathrm{p}}_{s,z}}{\partial z_s} = 0. \tag{4.2}$$

This two-dimensional approximation of the flow field is based on similar assumptions as used in boundary layer theory. In analogy with the boundary layer approximation, we can define $r_{1,0}$ as a characteristic length scale of the in-plane variation of $U^{\mathrm{p}}_{s,y}(j_s,k_s)$ and $U^{\mathrm{p}}_{s,z}(j_s,k_s)$, and $(\nu r_{1,0}^2/\Gamma_{vor,0})^{1/2}$ as a characteristic length scale of the streamwise variation of $U^{\mathrm{p}}_{s,x}(j_s,k_s)$ due to viscous decay. The assumption of a two-dimensional flow

$$\frac{\partial}{\partial y_s}, \frac{\partial}{\partial z_s} \gg \frac{\partial}{\partial x_s} \tag{4.3}$$

is now validated since:

$$\frac{1}{r_{1,0}} \gg \frac{1}{(\nu r_{1,0}^2/\Gamma_{vor,0})^{1/2}}. \tag{4.4}$$

Note that Eq. 4.4 can be rewritten as $Re_{vor} = \Gamma_{vor,0}/\nu \gg 1$, with Re_{vor} representing the Reynolds number based on the total circulation of the trailing vortex.

The numerical integration of the in-plane velocity field is based on the Gauss-Seidel iteration method. This is a method of successive corrections, in which at every instant all of the latest known components of the streamfunction are used, see Kreyszig (1978). The starting point of the numerical integration process is set arbitrarily at a grid point in the region $r_{1,0}$ around the vortex centre as defined by visual inspection.

The streamfunction is determined at every grid point (j_s, k_s). The grid-point vortex centre is now defined as that grid point at which the streamfunction has an extremum. To define a position of the vortex centre which is not limited to a grid point, we apply an interpolation of the streamfunction in the region $r_{1,0}/2$ around the grid-point vortex centre. In this region, the vortex is approximately in solid-body rotation so that the streamfunction can be fitted with a second-order polynomial function

$$\Psi_{fit}^{\mathrm{p}}(y_s, z_s) = c_1 y_s^2 + c_2 z_s^2 + c_3 y_s z_s + c_4 y_s + c_5 z_s + c_6, \tag{4.5}$$

with $c_1 - c_6$ the fitting parameters to be determined. The least-squares fit is based on approximately 70 grid points in the region $r_{1,0}/2$ around the grid-point vortex centre. The maximum of this second-order polynomial fit is defined as the vortex centre $(y_{s,c}, z_{s,c})$ and deviates on average $r_{1,0}/4$ from the grid-point vortex centre. The difference between the grid-point vortex centre and the vortex centre determined by a least-squares fit of a second-order polynomial through the streamfunction for $r/r_{1,0} < 0.5$ is illustrated in Figure 4.1. Clearly, the vortex centre is not bounded to a grid point when it is determined by a least-squares fit of the streamfunction.

Now that the vortex centre position is known, a new square grid is applied such that the vortex centre $(y_{s,c}, z_{s,c})$ corresponds to a grid point. The new grid has the same spatial resolution as the original grid, but the centre of this grid $(y(((N_j-1)/2), ((N_k-1)/2)), z(((N_j-1)/2), ((N_k-1)/2))) = (0,0)$ corresponds to the vortex centre:

$$(y_{s,c}, z_{s,c}) \Rightarrow (y((N_j-1)/2, (N_k-1)/2), z((N_j-1)/2, (N_k-1)/2)) = (0,0). \tag{4.6}$$

We define (y, z) as the in-plane coordinates in the frame co-moving with the vortex centre, while (y_s, z_s) are those in the stationary frame. Unless stated otherwise, we define the co-moving frame of reference as that co-moving with the vortex centre and not with the grid-point vortex centre. The number of grid points in the frame moving the vortex centre, that is $N_j(= N_k)$, is reduced to an extent determined by the variation in the vortex centre position. The velocity field at the grid moving with the vortex centre is determined by bilinear interpolation.

With an experimentally obtained set of three-components velocity fields in the (y_s, z_s)-plane, it is possible to determine mean flow quantities in the stationary and the co-moving frame of reference. Information about vortex wandering can be obtained by analyzing the ensemble of vortex centre positions in the stationary frame. However, the co-moving frame is more suitable for analyzing the vortex dynamics, because the trailing vortex is believed to be a passive tracer in an unsteady wind tunnel flow, see Van Jaarsveld (2008). It is therefore common practice in experimental studies on trailing vortices to correct for vortex wandering, see Van Jaarsveld (2008), Devenport et al. (1996), Green and Acosta (1991).

We will proceed with discussing the data postprocessing for the analysis of vortex wandering, vortex dynamics, and the turbulence in the vortex.

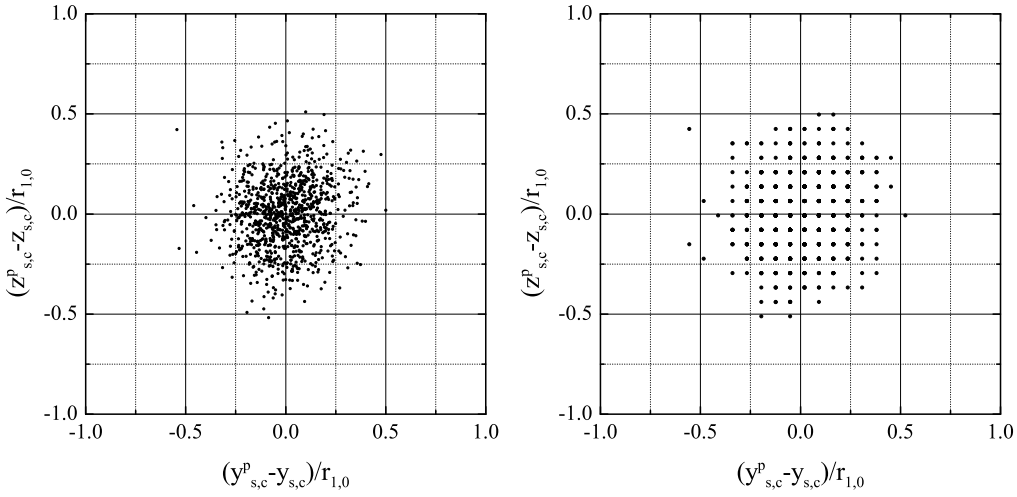

(a) vortex centre position (b) grid-point vortex centre

Figure 4.1: The grid-point vortex centre and the vortex centre determined by a least-squares fit of a second-order polynomial through the streamfunction for $r/r_{1,0} < 0.5$ are shown for $t(\Gamma_{vor,0}/2\pi r_{1,0}^2) = 350.0$ and the case without grid-generated turbulence.

4.2 Vortex wandering: vortex centre position

The analysis of vortex wandering is based on the spatial distribution of the vortex centre positions in the stationary frame of reference. The mean vortex centre position is determined by

$$y_{s,c} = \frac{\sum_{p=1}^{\mathrm{P}} y_{s,c}^{\mathrm{p}}}{\mathrm{P}}, \tag{4.7}$$

$$z_{s,c} = \frac{\sum_{p=1}^{\mathrm{P}} z_{s,c}^{\mathrm{p}}}{\mathrm{P}}, \tag{4.8}$$

in which $(y_{s,c}^{\mathrm{p}}, z_{s,c}^{\mathrm{p}})$ is the vortex centre position of realization $\mathrm{p} \in \mathcal{P}$ in the ensemble of P realizations, as conceived in the stationary frame. For every realization $\mathrm{p} \in \mathcal{P}$, the radial position of the vortex centre position with respect to the mean vortex centre position is given by:

$$r_{s,c}^{\mathrm{p}} = \sqrt{(y_{s,c}^{\mathrm{p}} - y_{s,c})^2 + (z_{s,c}^{\mathrm{p}} - z_{s,c})^2}. \tag{4.9}$$

A probability density function (PDF) is determined for the probability of $r_{s,c}^{\mathrm{p}}$ being in a region $(i-1)\triangle r_{s,c} \leqq r_{s,c}^{\mathrm{p}} < i\triangle r_{s,c}$ with $\triangle r_{s,c} = 2r_{1,0}/25$ and $i = 1, 2, 3....$ The width of the bin $\triangle r_{s,c}$ is set in such a way that a smooth PDF is obtained. The PDF is defined according to

$$Pr(a\triangle r_{s,c} \leqq r_{s,c}^{\mathrm{p}} < b\triangle r_{s,c}) = \sum_{i=a}^{b} PDF\triangle r_{s,c} \qquad b > a; \quad a, b = 1, 2, 3... \tag{4.10}$$

with $Pr(a\triangle r_{s,c} \leqq r_{s,c}^{\mathrm{p}} < b\triangle r_{s,c})$ the probability of $r_{s,c}^{\mathrm{p}}$ to be in the interval $a\triangle r_{s,c} \leqq r_{s,c}^{\mathrm{p}} < b\triangle r_{s,c}$. The PDF is now determined by:

$$PDF = \frac{1}{\triangle r_{s,c}} \frac{\sum_{p=1}^{\mathrm{P}} \delta_{(i-1)\triangle r_{s,c} \leqq r_{s,c}^{\mathrm{p}} < i\triangle r_{s,c}}}{\sum_{l=1}^{N_{\triangle r_{s,c}}} \sum_{p=1}^{\mathrm{P}} \delta_{(l-1)\triangle r_{s,c} \leqq r_{s,c}^{\mathrm{p}} < l\triangle r_{s,c}}}, \qquad i = 1, 2, 3...N_{\triangle r_{s,c}}. \tag{4.11}$$

The delta-function $\delta_{(i-1)\triangle r_{s,c} \leqq r_{s,c}^{\mathrm{p}} < i\triangle r_{s,c}}$ is defined to be 1 if $(i-1)\triangle r_{s,c} \leqq r_{s,c}^{\mathrm{p}} < i\triangle r_{s,c}$ holds, and zero if not. The maximum radius to which the PDF is determined is given by $N_{\triangle r_{s,c}}\triangle r_{s,c}$ and is set sufficiently large such that $\lim_{i\triangle r_{s,c} \to N_{\triangle r_{s,c}}\triangle r_{s,c}} PDF = 0$.

4.3 Vortex dynamics: velocity, vorticity, and circulation

The dynamics of the trailing vortex is analyzed by means of the radial, azimuthal, and axial velocity as well as the circulation and the axial and azimuthal vorticity. The analysis of turbulence quantities is restricted to the kinetic energy of the turbulence and the azimuthal-radial Reynolds shear stress. We will continue with discussing the method in which these flow quantities are obtained from the ensemble of three-components velocity fields in the (y, z)-plane of the co-moving frame of reference. The distribution of these flow quantities will be considered both in the (y, z)-plane and the radial direction.

With the vortex centre position as the origin in the co-moving frame of reference, the radial velocity at every position $y = y(j, k)$ and $z = z(j, k)$ is determined by

$$U_r^{\mathrm{p}}(y, z) = U_y^{\mathrm{p}}(y, z)\cos\theta + U_z^{\mathrm{p}}(y, z)\sin\theta, \tag{4.12}$$

with θ the azimuthal angle with respect to the y-axis. Likewise, the azimuthal velocity is determined by

$$U_\theta^{\mathrm{p}}(y, z) = U_z^{\mathrm{p}}(y, z)\cos\theta - U_y^{\mathrm{p}}(y, z)\sin\theta. \tag{4.13}$$

The axial velocity is simply given by $U_x^{\mathrm{p}}(y, z)$, and the circulation Γ^{p} is approximated for every position as

$$\Gamma^{\mathrm{p}}(y, z) = 2\pi r U_\theta^{\mathrm{p}}(y, z), \tag{4.14}$$

with $r = \sqrt{y^2 + z^2}$. Note that the circulation is an integral quantity, and that therefore the value of the circulation distribution defined by Eq. 4.14 is limited to axisymmetric vortices. The reason for defining the circulation distribution will become clear later on. The axial vorticity distribution $\omega^{\mathrm{p}}(y, z) = \partial U_z^{\mathrm{p}}/\partial y - \partial U_y^{\mathrm{p}}/\partial z$ is determined by

$$\begin{aligned}\omega_x^{\mathrm{p}}(y(j,k), z(j,k)) = \frac{U_z^{\mathrm{p}}(y(j+1,k), z(j+1,k)) - U_z^{\mathrm{p}}(y(j-1,k), z(j-1,k))}{y(j+1,k) - y(j-1,k)} - \\ \frac{U_y^{\mathrm{p}}(y(j,k+1), z(j,k+1)) - U_y^{\mathrm{p}}(y(j,k-1), z(j,k-1))}{z(j,k+1) - z(j,k-1)},\end{aligned} \tag{4.15}$$

in which the central difference method is applied. The azimuthal vorticity distribution $\omega_\theta^{\mathrm{p}}(y, z) = \partial U_r^{\mathrm{p}}/\partial x - (\partial U_x^{\mathrm{p}}/\partial y)\cos\theta - (\partial U_y^{\mathrm{p}}/\partial z)\sin\theta$ is approximated likewise by

$$\begin{aligned}\omega_\theta^{\mathrm{p}}(y(j,k), z(j,k)) = -\frac{U_x^{\mathrm{p}}(y(j+1,k), z(j+1,k)) - U_x^{\mathrm{p}}(y(j-1,k), z(j-1,k))}{y(j+1,k) - y(j-1,k)}\cos\theta - \\ \frac{U_x^{\mathrm{p}}(y(j,k+1), z(j,k+1)) - U_x^{\mathrm{p}}(y(j,k-1), z(j,k-1))}{z(j,k+1) - z(j,k-1)}\sin\theta,\end{aligned} \tag{4.16}$$

in which we assume that the flow is two-dimensional and that the term $\partial U_r^{\mathrm{p}}/\partial x$ is therefore negligible small, see the boundary layer approximation as stated by Eqs. 4.2-4.4.

With the velocities, circulation, and vorticities determined for every realization $\mathrm{p} \in \mathcal{P}$, it is now possible to determine the ensemble mean quantities for every position (y, z)

$$U_r(y, z) = \frac{\sum_{i=1}^{\mathrm{P}} U_r^{\mathrm{p}}(y, z)}{\mathrm{P}}, \tag{4.17}$$

and likewise for $U_\theta(y, z)$, $U_x(y, z)$, $\Gamma(y, z)$, $\omega_x(y, z)$, and $\omega_\theta(y, z)$. In this work, we assume that the local standard deviation of the velocity is a good approximation of the kinetic energy of

turbulence. We are therefore interested in the following quantities:

$$u^2_{rms,r}(y,z) = \frac{\sum_{i=1}^{\mathrm{P}}(U_r^{\mathrm{p}}(y,z) - U_r(y,z))^2}{\mathrm{P}}, \tag{4.18}$$

$$u^2_{rms,\theta}(y,z) = \frac{\sum_{i=1}^{\mathrm{P}}(U_\theta^{\mathrm{p}}(y,z) - U_\theta(y,z))^2}{\mathrm{P}}, \tag{4.19}$$

$$u^2_{rms,x}(y,z) = \frac{\sum_{i=1}^{\mathrm{P}}(U_x^{\mathrm{p}}(y,z) - U_x(y,z))^2}{\mathrm{P}}. \tag{4.20}$$

The kinetic energy of turbulence q can now be determined by:

$$q(y,z) = \frac{1}{2}(u^2_{rms,r}(y,z) + u^2_{rms,\theta}(y,z) + u^2_{rms,x}(y,z)). \tag{4.21}$$

At this stage, the ensemble averaged velocities, circulation, and vorticities are known for every position (y,z) in the co-moving frame of reference. The kinetic energy of the turbulence is derived from the ensemble quantities, and is likewise defined for every position (y,z) in the co-moving frame of reference. Radial profiles of the flow quantities are now obtained by defining annular regions $(i-1)\triangle r \leqq r < i\triangle r$ ($i = 1,2,3...$), also called annular bins, in which flow quantities will be averaged. The width of the annular regions is determined by the spatial resolution of the (y,z)-plane. The smallest number of grid points (j,k) is found in the annular region closest to the origin: $0 \leqq r < \triangle r$. In practice, the width of the annular regions $\triangle r$ is set in such a way that the eight grid points closest to centre $(y,z) = (0,0)$ are still in the first annular bin. The flow is highly axisymmetric near the vortex centre and it is therefore sufficient to enclose only the eight nearest grid points to the first annular bin. In this way, the annular bins are wide enough to perform reliable statistics even close to the vortex core, while a sufficient high radial resolution is maintained to cover the vortex core region accurately. The radial profiles of the mean flow quantities are now determined by

$$U_r(r = i\triangle r) = \frac{\sum_{j=1}^{N_y}\sum_{k=1}^{N_z} U_r(y,z)\delta_{(i-1)\triangle r \leqq r < i\triangle r}}{\sum_{j=1}^{N_y}\sum_{k=1}^{N_z}\delta_{(i-1)\triangle r \leqq r < i\triangle r}}, \tag{4.22}$$

and likewise for U_θ, U_x, Γ, ω_x, ω_θ, and q. The delta-function $\delta_{(i-1)\triangle r \leqq r < i\triangle r}$ defined to be 1 if $(i-1)\triangle r \leqq r < i\triangle r$ holds, and zero if not. The maximum radius to which the radial profiles are determined is set such that $N_{\triangle r}\triangle r = y(N_y, 0) = z(0, N_k)$. In other words, that is half the side of the square (y,z)-plane in the co-moving frame of reference. Erroneous azimuthal averaging is herewith prevented in case of a vortex that is not symmetric, for example during the roll-up process of a trailing vortex. The standard deviation of the mean flow quantities is given by

$$\widehat{U_r}(r = i\triangle r) = \sqrt{\frac{\sum_{j=1}^{N_y}\sum_{k=1}^{N_z}\delta_{(i-1)\triangle r \leqq r < i\triangle r}(U_r(y,z) - U_r(r = i\triangle r))^2}{\sum_{j=1}^{N_y}\sum_{k=1}^{N_z}\delta_{(i-1)\triangle r \leqq r < i\triangle r}}}, \tag{4.23}$$

and likewise for U_θ, U_x, Γ, ω_x, ω_θ, and q. The standard deviation is now defined to be the measurement accuracy. The uncertainty consists of both the measurement accuracy, and the intrinsic variation of the flow quantities inside an annular bin. In practice, it was found that the latter is the most important contribution to the uncertainty. This means that the uncertainty increases when the annular bins become larger.

It was already mentioned that the value of circulation distribution as defined by Eq. 4.14 is limited to axisymmetric vortices. By averaging the circulation distribution according to Eq. 4.22, we correctly approach the integral:

$$\Gamma = \int_0^{2\pi} U_\theta r d\theta. \tag{4.24}$$

The value of Eq. 4.22 is therefore not limited to axisymmetric vortices.

Chapter 5

Results

We will first discuss the evolution of the azimuthal and axial velocity and vorticity components in terms of radial profiles and distribution in the (y, z)-plane. It will become clear that in the first stage of the evolution, the vortex is not symmetric, but that it becomes more axisymmetric at later times. The initial trailing vortex is not axisymmetric since it has yet not rolled up completely. After that, we will consider the radial profiles of the circulation and the energy in the root-mean-square variations of the velocity. The root-mean-square variations of the velocity are used to approximate the kinetic energy of the turbulence. This chapter will be concluded with an analysis of vortex wandering. The vortex centre positions are plotted in the stationary frame of reference, and a probability distribution function (PDF) is determined for the radial position of the vortex centre.

For the conversion between time and location behind the wing, the reader is referred to Table 3.1. All the presented quantities are determined as discussed in Chapter 4 and are made dimensionless as described in Chapter 3.

5.1 Evolution of velocity and vorticity

Radial profiles of the azimuthal and axial velocity are shown in Figure 5.1. The profiles are shown for the cases without and with grid-generated turbulence. Here, we only show the inner region measurement data. The outer region measurement data will be considered later on. For the azimuthal velocity, one can see that the peak value of the azimuthal velocity decreases and that the corresponding radius increases. The axial velocity peaks are located at the vortex centre. While the axial velocity is positive in the region $r/r_{1,0} \lessapprox 0.5$ at $t(\Gamma_{vor,0}/2\pi r_{1,0}^2) = 17.5$, it is negative for $r/r_{1,0} \lessapprox 1.5$ at later times. The maximum axial velocity surplus and deficit are found to be 1.12 and 0.72 times the main stream velocity, respectively. Note that $\overline{U}_x(2\pi r_{1,0}/\Gamma_{vor,0}) = 1.1$. The evolution of the maximum azimuthal velocity and the axial velocity at the vortex centre for the case without and with grid-generated turbulence is shown in Figure 5.2. The evolution of the maximum azimuthal velocity is fitted with $c_1(t-c_2)^{-1/2}+c_3$ and the maximum axial velocity with $c_1'(t-c_2')^{-1}\log(t-c_2')+c_3'$. In this way, we try to retrieve the relation for $U_{\theta,max}$ and $U_{x,max}-\overline{U}_x$ with $U_{x,max} = U_{x,r=\triangle r}$ as suggested by Batchelor (1964), see Eqs. 2.23-2.24. The relations are in good approximation recovered, but a more thorough analysis with more data points is necessary to draw firm conclusions. The evolution of the swirl number defined by

$$s \equiv \frac{U_{\theta,max}}{U_{x,r=\triangle r} - \overline{U}_x}, \tag{5.1}$$

is shown in Figure 5.3. It becomes clear that the swirl number initially switches from a positive to negative value. The swirl numbers reaches an approximate constant value of -2 for $t(\Gamma_{vor,0}/2\pi r_{1,0}^2) \gtrapprox 150$.

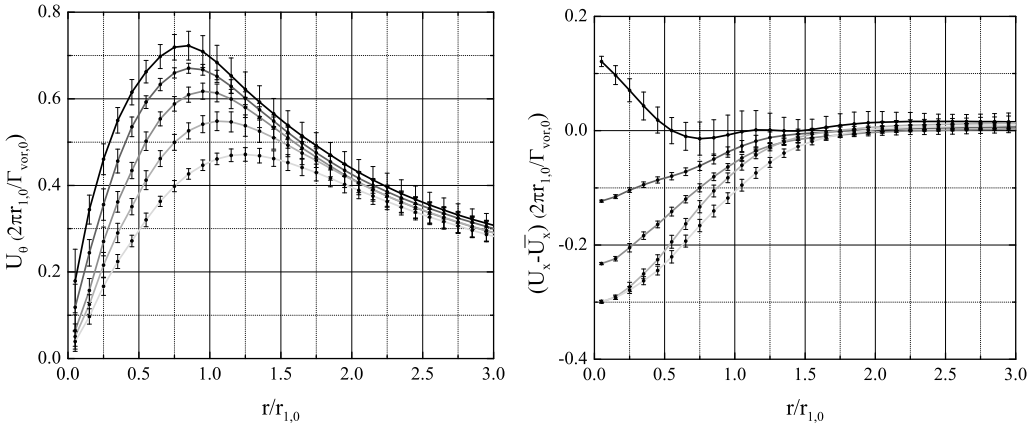

(a) without grid-generated turbulence (b) without grid-generated turbulence

(c) with grid-generated turbulence (d) with grid-generated turbulence

Figure 5.1: Radial profiles of the azimuthal (left) and axial (right) velocity profiles for the case without (top) and with (bottom) grid-generated turbulence. From black to light gray: $t(\Gamma_{vor,0}/2\pi r_{1,0}^2) = 17.5; 87.5; 175.5; 350.0; 662.5$ *(the last time only for the case without grid-generated turbulence).*

The axial velocity profile at $t(\Gamma_{vor,0}/2\pi r_{1,0}^2) = 17.5$ is compared with the theoretically derived profile from Eq. 2.21, see Figure 5.4. Note the theoretical profile involves integration of the azimuthal velocity profile. For this, we numerically integrated the azimuthal velocity profile as obtained in the region $0 < r/r_{1,0} \leqq 12$. Note that we approximate the infinite outer integration limit by $r/r_{1,0} = 12$. This approximation is valid since the difference between the axial velocity profile of a Lamb-Oseen vortex determined with an infinite outer integration limit and that with $r/R = 12$ is found to be negligible. The inner and outer region measurement data are linked to each other, as will be discussed in Section 5.2. Apparently, the axial velocity is lower than the theoretical profile in the region $0 < r/r_{1,0} \lessapprox 2$. This is most likely caused by nonzero viscous contributions which are neglected in the theoretical profile.

One may conclude from the analyses shown above that the difference between the cases without and with grid-generated turbulence is negligible on the axial and azimuthal velocity profiles in the region $0 < r/r_{1,0} \leqq 3$.

Radial profiles of the axial and azimuthal vorticity are shown in Figure 5.5, the axial vorticity is positive and shows a maximum at $r/r_{1,0} = \triangle r$ for all the analyzed times. The profile is sharply

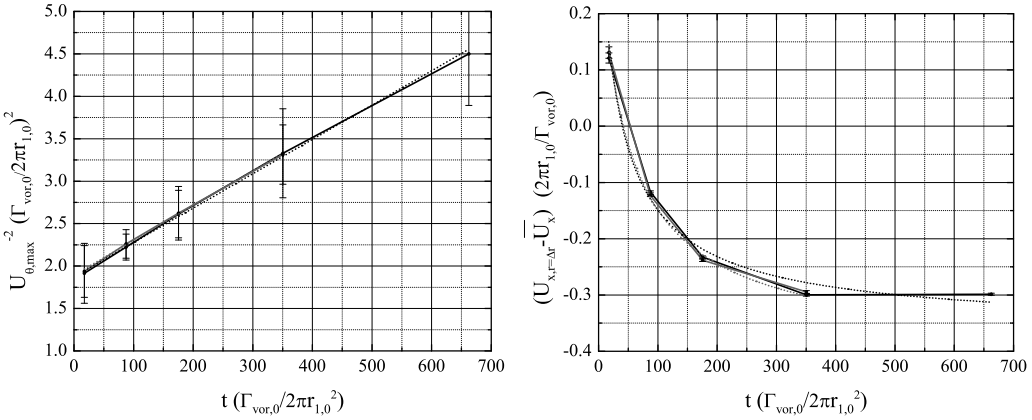

(a) Streamwise evolution of $U_{\theta,max}^{-2}$

(b) Streamwise evolution of $(U_{x,max} - \overline{U}_x)$

Figure 5.2: The evolution of the maximum azimuthal velocity and the axial velocity at $r/r_{1,0} = \triangle x$ for the case with (black lines) and without grid-generated turbulence (dark gray lines). Apparently, the grid-generated turbulence has negligible influence on the evolution of the azimuthal and axial velocity profiles in the vortex inner region $r/r_1 \lessapprox 1$. The evolution of the maximum azimuthal and axial velocity is fitted (dotted lines) with profiles suggested by Batchelor (1964), see Eqs. 2.23-2.24 with $\triangle x \sim t$.

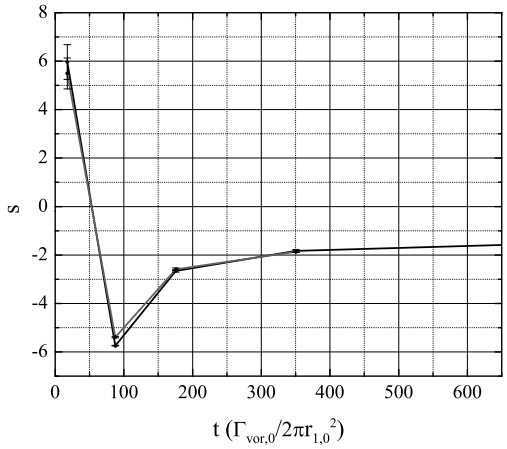

Figure 5.3: Evolution of the swirl number $s = U_{\theta,max}/(U_{x,max} - \overline{U}_x)$ for the case without (black lines) and with grid-generated turbulence (dark gray lines). The swirl numbers reaches an approximate constant value of -2 for $t(\Gamma_{vor,0}/2\pi r_{1,0}^2) \gtrapprox 150$.

peaked at the vortex centre for $t(\Gamma_{vor,0}/2\pi r_{1,0}^2) = 17.5$, but the profiles become smoother at later times. The peak in the axial vorticity decreases in time. At $t(\Gamma_{vor,0}/2\pi r_{1,0}^2) = 17.5$, the azimuthal vorticity has a maximum at the vortex centre. The profile shows a transient profile for the subsequent time $t(\Gamma_{vor,0}/2\pi r_{1,0}^2) = 87.5$. For later times, the azimuthal vorticity has a minimum in the region $0.25 < r/r_{1,0} < 0.75$. As is the case for the radial profiles of azimuthal and axial velocity, the difference between the cases without and with grid-generated turbulence is negligible.

The error bars of the axial velocity and azimuthal vorticity are for $t(\Gamma_{vor,0}/2\pi r_{1,0}^2) = 17.5$ significantly larger than those for subsequent times. Apparently, there is a relatively large azimuthal variation in the axial flow at this stage. This is elucidated by visualizing the distribution of axial velocity and azimuthal vorticity in the (y, z)-plane of the co-moving frame of reference, see Figures 5.6-5.7. Clearly, the distribution of axial velocity and azimuthal vorticity is not axisym-

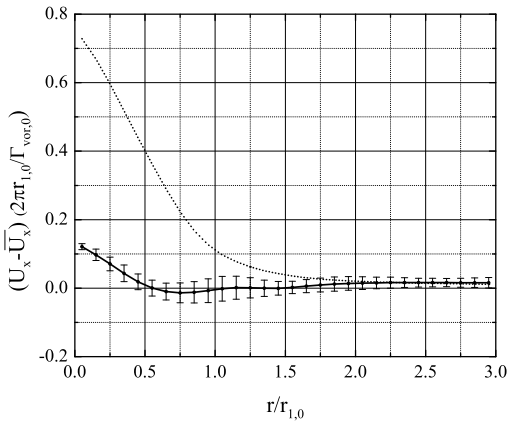

Figure 5.4: The radial profile of the axial velocity for the case without grid-generated turbulence and $t(\Gamma_{vor,0}/2\pi r_{1,0}^2) = 17.5$ is compared to the theoretical profile determined from Eq. 2.22. It becomes clear that the axial velocity is lower in the region $0 < r/r_{1,0} \lessapprox 2$. This is most likely caused by viscous contributions that are neglected in the theoretical profile.

metric at $t(\Gamma_{vor,0}/2\pi r_{1,0}^2) = 17.5$. At this time the distribution of axial velocity shows streaks of positive and negative values around the vortex centre. The streak of negative axial velocity starts in the bottom left side from where it winds around the vortex centre. This streak of negative axial velocity is believed to be a remnant of the boundary layer flow over the wing. In accordance with the radial profile shown in Figure 5.1, the axial velocity has a positive maximum at the vortex centre. At $t(\Gamma_{vor,0}/2\pi r_{1,0}^2) = 87.5$, the concentration of negative axial velocity around the vortex centre is slightly tilted at about an angle of 30° degrees with respect to the vertical z-axis. This antisymmetry may be a result of the winding boundary layer remnant around the vortex centre. It is moreover believed that the initial positive axial velocity in the vortex cores, is brought to a negative axial velocity due that same boundary layer flow spiralling inwards. At $t(\Gamma_{vor,0}/2\pi r_{1,0}^2) \geqq 87.5$, the distribution of azimuthal vorticity shows an annular region around $r/r_{1,0} \approx 0.5$ with less negative vorticity than that in the region enclosed by it. This may also be a product of the boundary layer remnant winding around the vortex centre. For the analyzed times $t(\Gamma_{vor,0}/2\pi r_{1,0}^2) \geqq 175.5$, the distribution of axial velocity and azimuthal vorticity was found to be axisymmetric in the region $r/r_1 \lessapprox 1$. It is therefore believed that distribution of axial velocity and azimuthal vorticity can be conceived as transient.

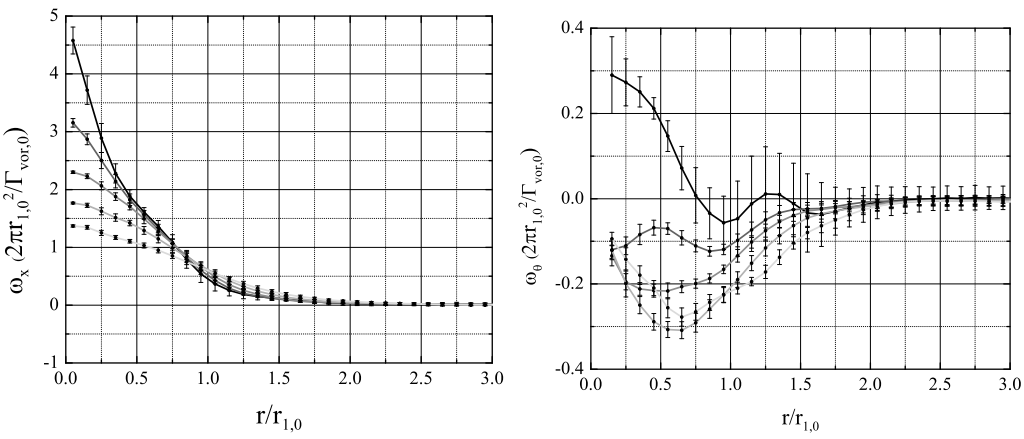

(a) without grid-generated turbulence (b) without grid-generated turbulence

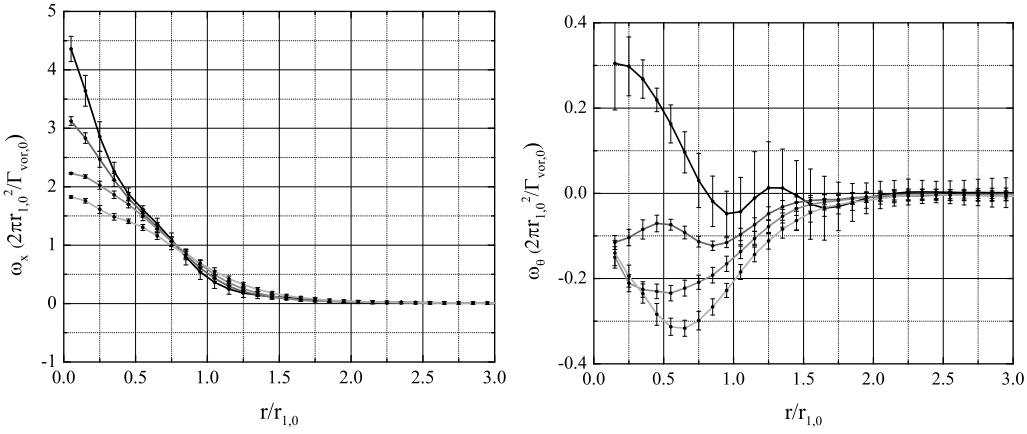

(c) with grid-generated turbulence (d) with grid-generated turbulence

Figure 5.5: Radial profiles of the axial (left) and azimuthal (right) vorticity profiles for the case without (top) and with (bottom) grid-generated turbulence. From black to light gray: $t(\Gamma_{vor,0}/2\pi r_{1,0}^2) = 17.5; 87.5; 175.5; 350.0; (662.5;$ *only for the case without grid-generated turbulence).*

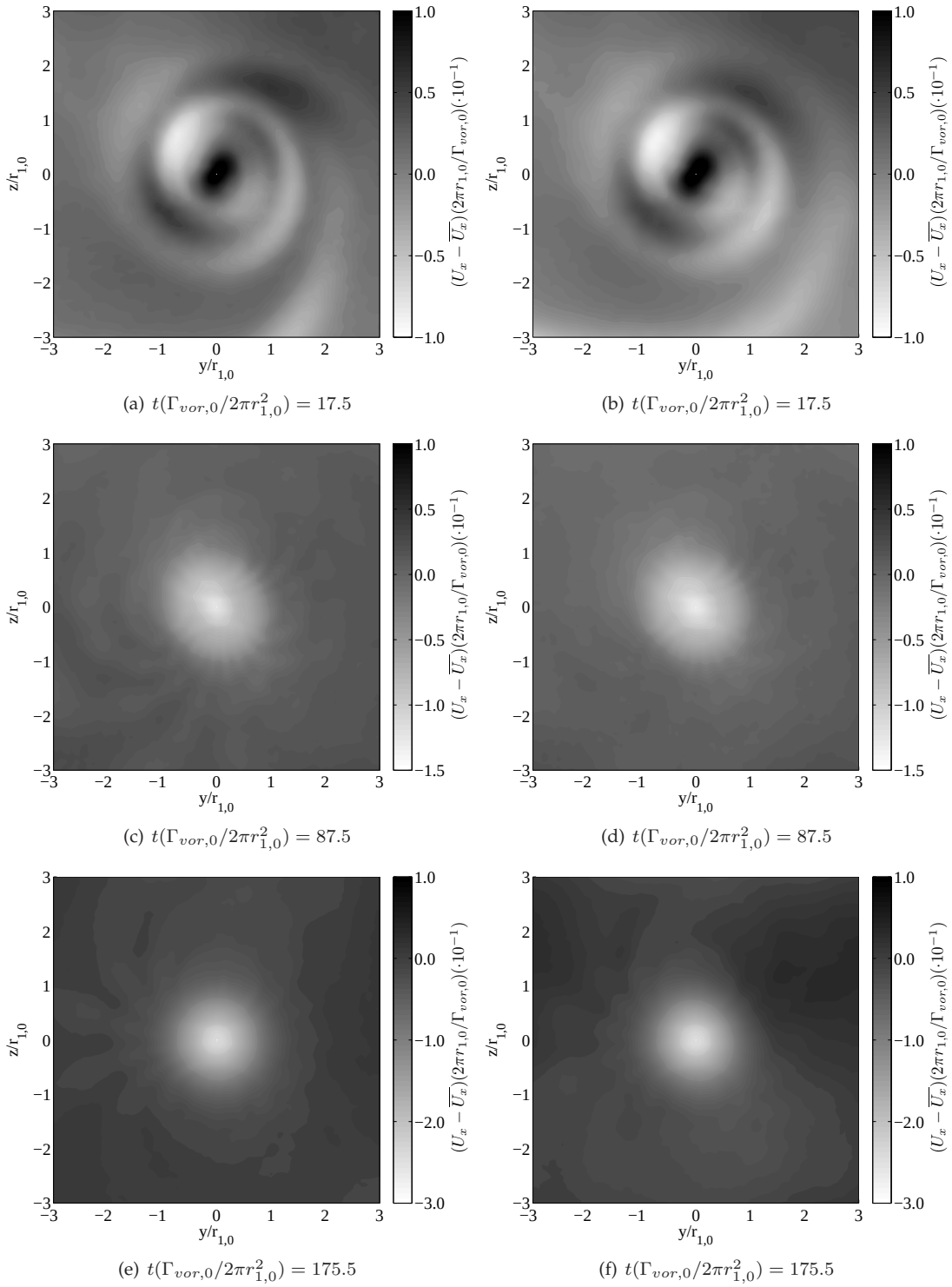

(a) $t(\Gamma_{vor,0}/2\pi r_{1,0}^2) = 17.5$

(b) $t(\Gamma_{vor,0}/2\pi r_{1,0}^2) = 17.5$

(c) $t(\Gamma_{vor,0}/2\pi r_{1,0}^2) = 87.5$

(d) $t(\Gamma_{vor,0}/2\pi r_{1,0}^2) = 87.5$

(e) $t(\Gamma_{vor,0}/2\pi r_{1,0}^2) = 175.5$

(f) $t(\Gamma_{vor,0}/2\pi r_{1,0}^2) = 175.5$

Figure 5.6: Distributions of the axial velocity $U_x - \overline{U}_x$ in the (y, z)-plane for the cases without (left) and with grid-generated turbulence (right). At $t(\Gamma_{vor,0}/2\pi r_{1,0}^2) = 17.5$, there is a jet $(U_x - \overline{U}_x) > 0$ in the the region $r/r_{1,0} \lessapprox 0.5$. This jet is surrounded by both positive and negative streaks of $(U_x - \overline{U}_x)$. For $t(\Gamma_{vor,0}/2\pi r_{1,0}^2) \gtrsim 87.5$, the jet has been transformed to a wake $(U_x - \overline{U}_x) < 0$ which is in good approximation symmetric.

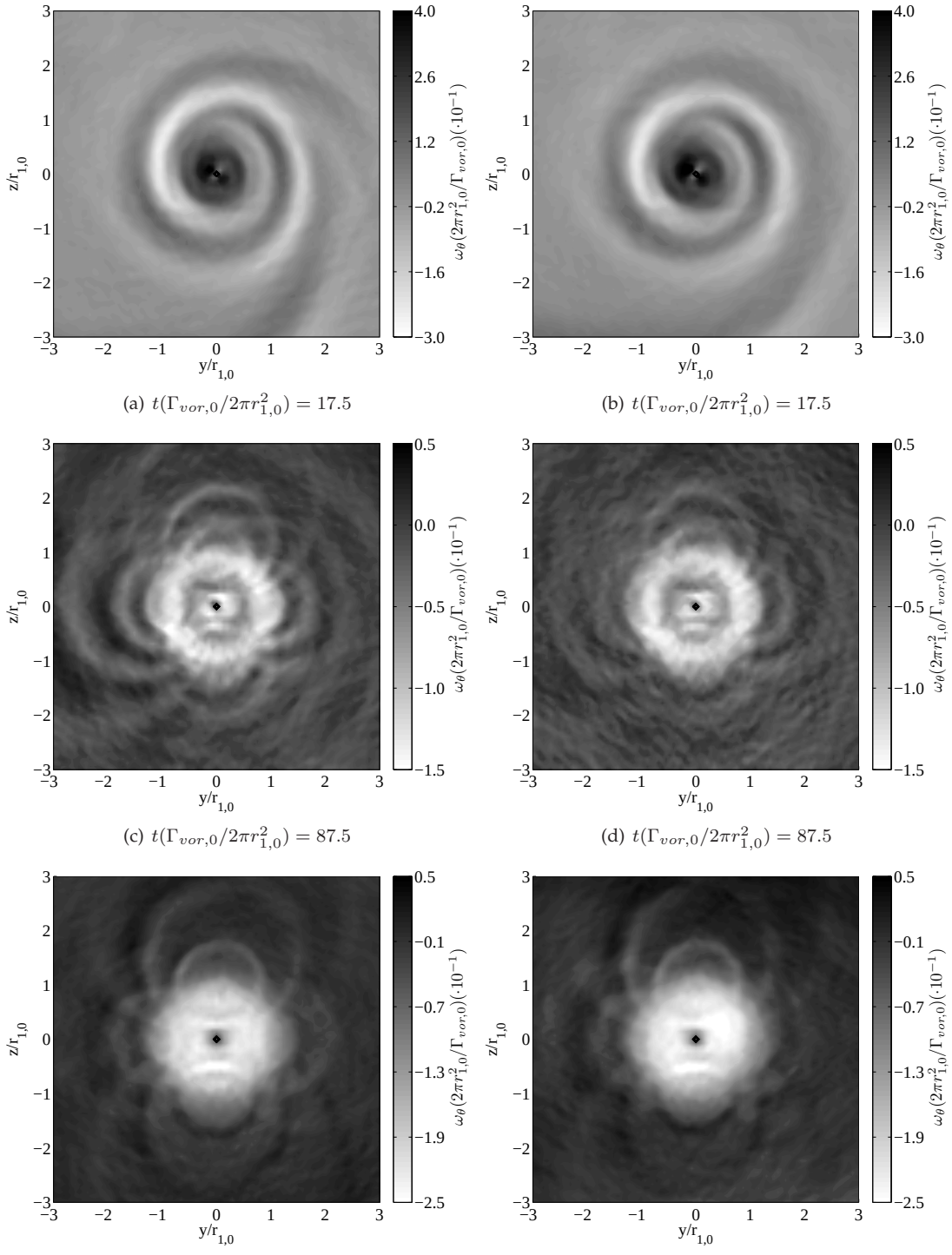

(a) $t(\Gamma_{vor,0}/2\pi r_{1,0}^2) = 17.5$

(b) $t(\Gamma_{vor,0}/2\pi r_{1,0}^2) = 17.5$

(c) $t(\Gamma_{vor,0}/2\pi r_{1,0}^2) = 87.5$

(d) $t(\Gamma_{vor,0}/2\pi r_{1,0}^2) = 87.5$

(e) $t(\Gamma_{vor,0}/2\pi r_{1,0}^2) = 175.5$

(f) $t(\Gamma_{vor,0}/2\pi r_{1,0}^2) = 175.5$

Figure 5.7: Distributions of the azimuthal vorticity as determined by the ensemble average of Eq. 4.16 for the case without (left) and with grid-generated turbulence (right). At $t(\Gamma_{vor,0}/2\pi r_{1,0}^2) = 17.5$, the distribution contains both negative and positive streaks of azimuthal vorticity. The distribution becomes in good approximation axisymmetric for $t(\Gamma_{vor,0}/2\pi r_{1,0}^2) \geqq 87.5$. Note that the artificial shapes in the outer region of the vortex are caused by the measurement limitations, see Appendix G. The non-physical shapes around the vortex centre are believed to be due to the PIV process.

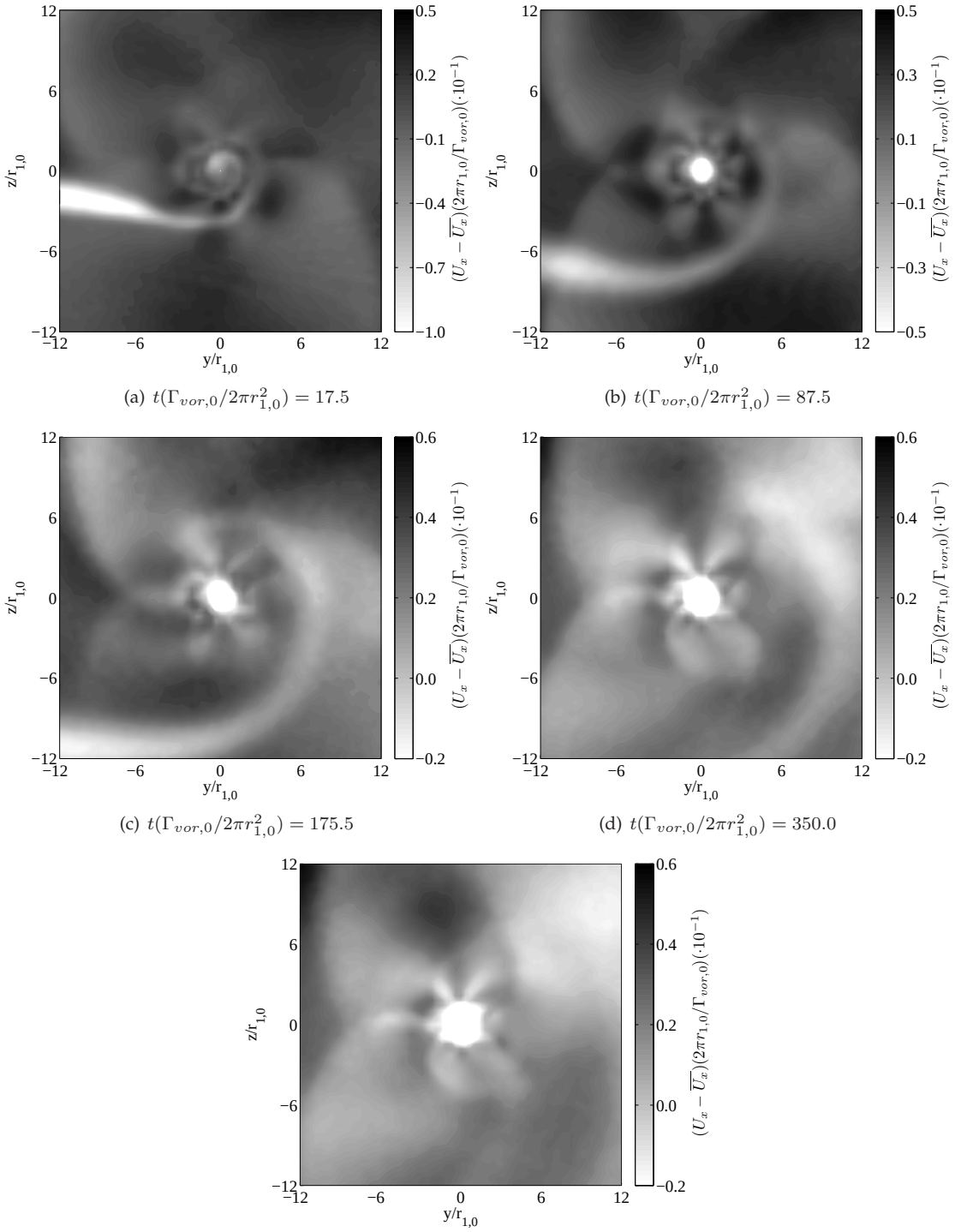

(a) $t(\Gamma_{vor,0}/2\pi r_{1,0}^2) = 17.5$

(b) $t(\Gamma_{vor,0}/2\pi r_{1,0}^2) = 87.5$

(c) $t(\Gamma_{vor,0}/2\pi r_{1,0}^2) = 175.5$

(d) $t(\Gamma_{vor,0}/2\pi r_{1,0}^2) = 350.0$

(e) $t(\Gamma_{vor,0}/2\pi r_{1,0}^2) = 662.5$

Figure 5.8: Distributions of the axial velocity $U_x - \overline{U}_x$ for the case without grid-generated turbulence. It becomes clear that a remnant of the boundary rolls up around the vortex, which is even still visible at $t(\Gamma_{vor,0}/2\pi r_{1,0}^2) = 350.0$. Note that the artificial shapes in the outer region of the vortex are caused by the measurement limitations, see Appendix G. The non-physical shapes around the vortex centre are believed to be due to the PIV process.

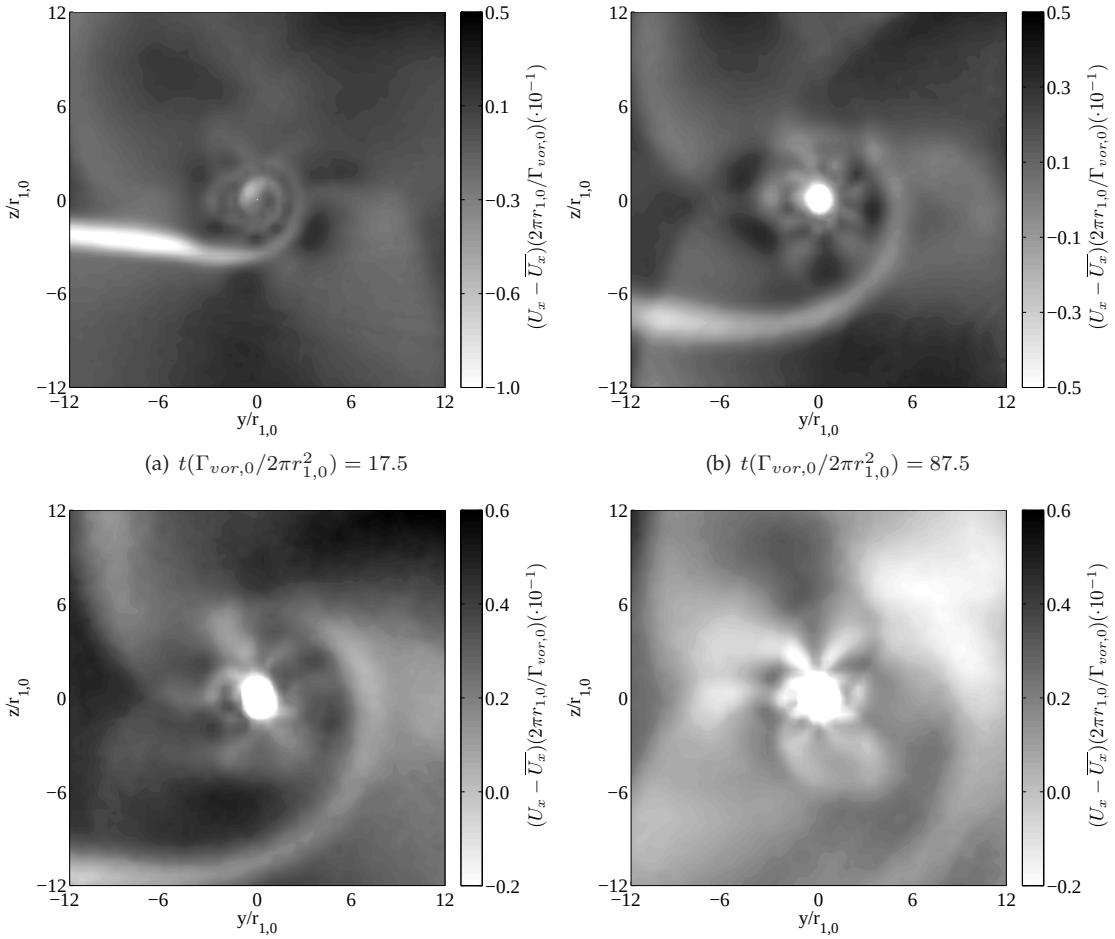

(a) $t(\Gamma_{vor,0}/2\pi r_{1,0}^2) = 17.5$

(b) $t(\Gamma_{vor,0}/2\pi r_{1,0}^2) = 87.5$

(c) $t(\Gamma_{vor,0}/2\pi r_{1,0}^2) = 175.5$

(d) $t(\Gamma_{vor,0}/2\pi r_{1,0}^2) = 350.0$

Figure 5.9: Distributions of the axial velocity $U_x - \overline{U}_x$ for the case with grid-generated turbulence. It becomes clear that a remnant of the boundary rolls up around the vortex, which is even at $t(\Gamma_{vor,0}/2\pi r_{1,0}^2) = 350.0$ still visible. Note that the artificial shapes in the outer region of the vortex are caused by the measurement limitations, see Appendix G. The non-physical shapes around the vortex centre are believed to be due to the PIV process.

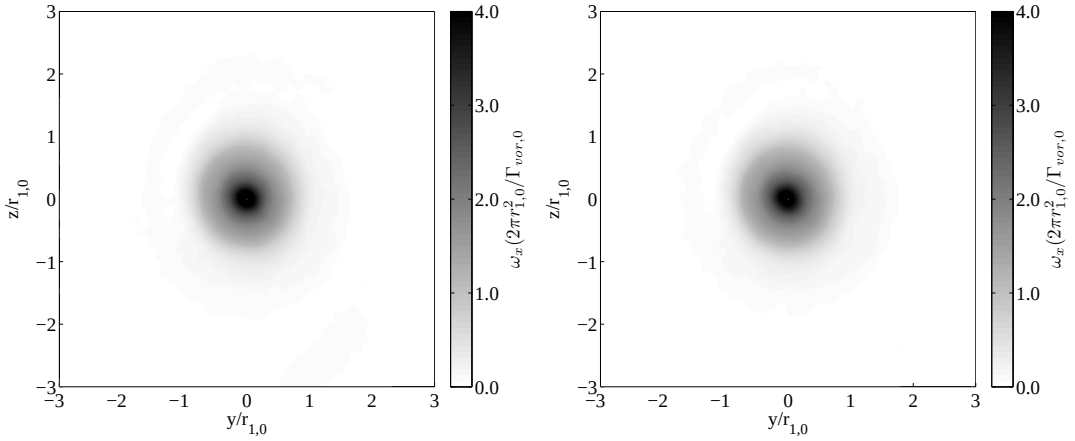

(a) $t(\Gamma_{vor,0}/2\pi r_{1,0}^2) = 17.5$

(b) $t(\Gamma_{vor,0}/2\pi r_{1,0}^2) = 17.5$

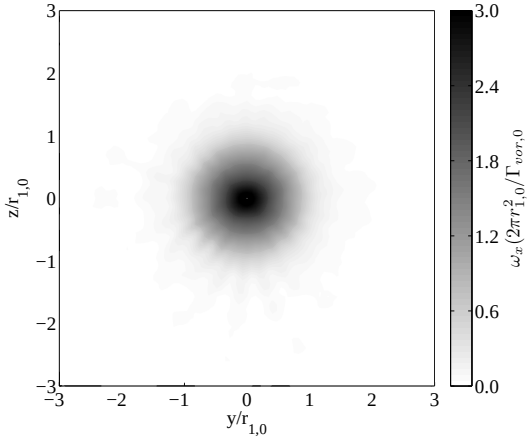

(c) $t(\Gamma_{vor,0}/2\pi r_{1,0}^2) = 87.5$

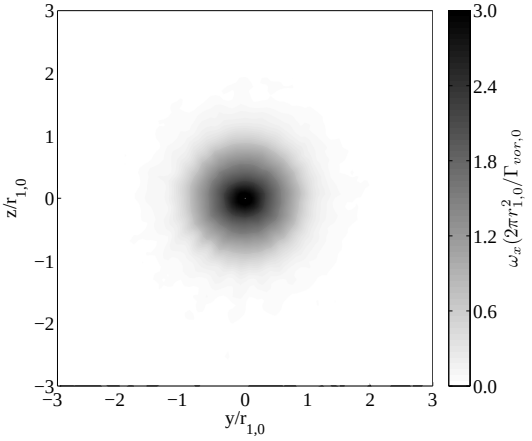

(d) $t(\Gamma_{vor,0}/2\pi r_{1,0}^2) = 87.5$

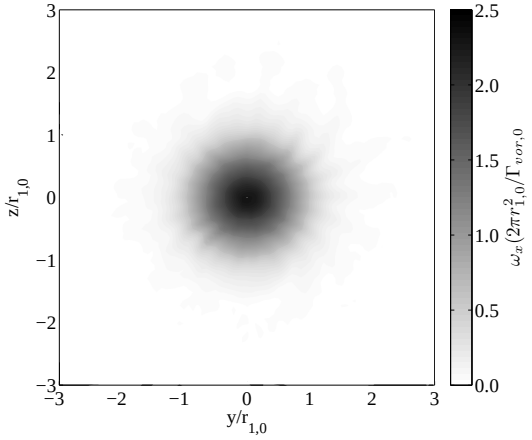

(e) $t(\Gamma_{vor,0}/2\pi r_{1,0}^2) = 175.5$

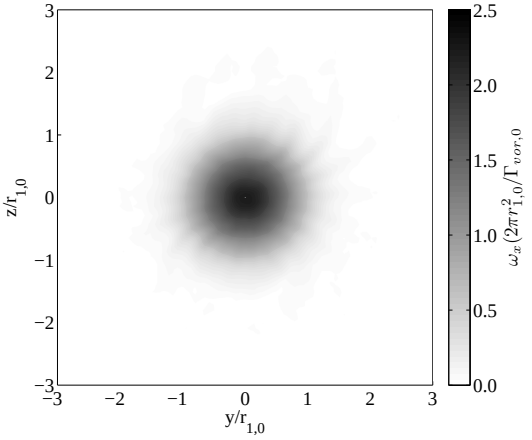

(f) $t(\Gamma_{vor,0}/2\pi r_{1,0}^2) = 175.5$

Figure 5.10: Distributions of the axial vorticity as determined by the ensemble average of Eq. 4.15 for the case without (left) and with grid-generated turbulence (right). From $t(\Gamma_{vor,0}/2\pi r_{1,0}^2) = 17.5$, the distribution is in good approximation symmetric.

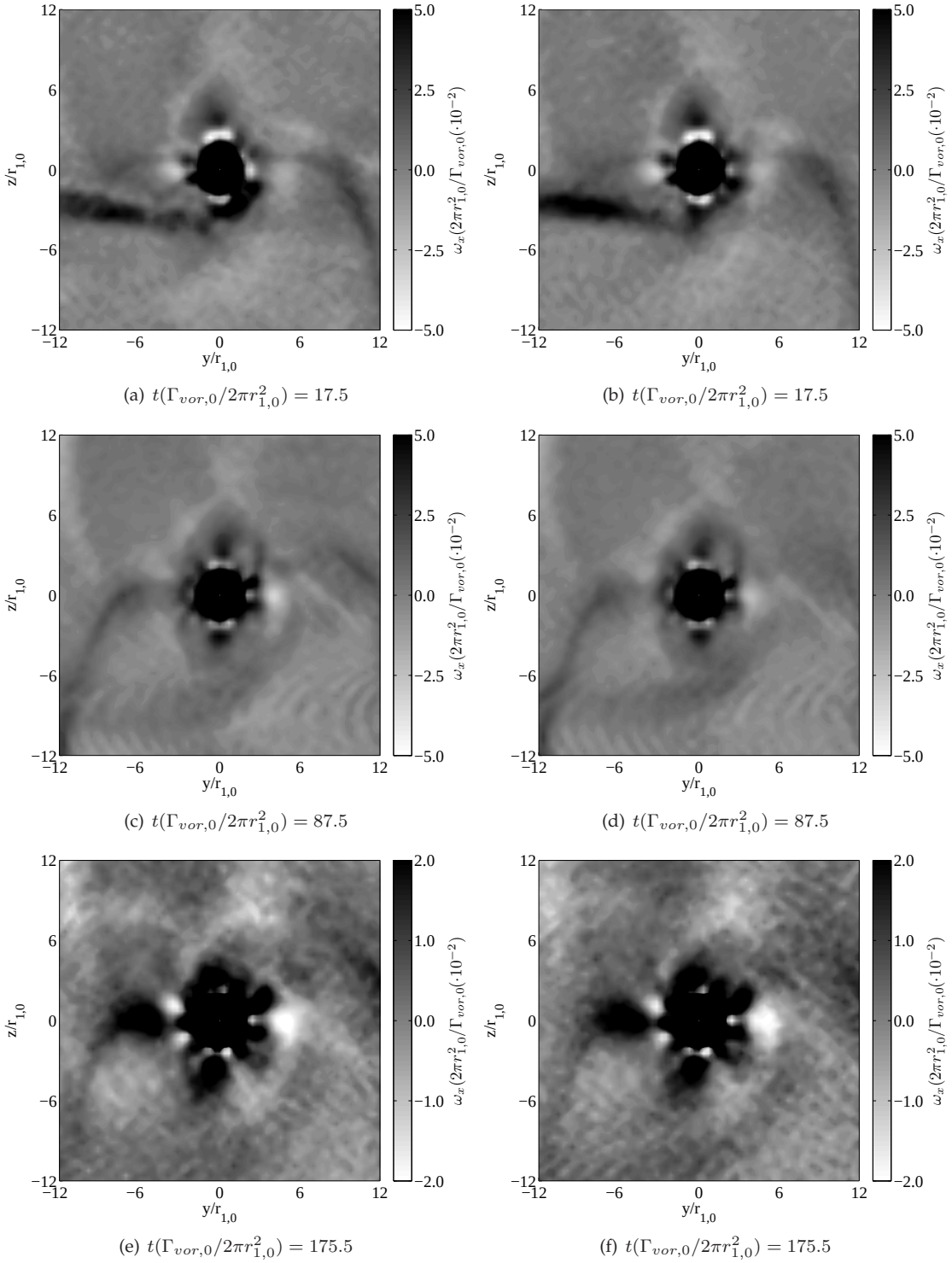

(a) $t(\Gamma_{vor,0}/2\pi r_{1,0}^2) = 17.5$

(b) $t(\Gamma_{vor,0}/2\pi r_{1,0}^2) = 17.5$

(c) $t(\Gamma_{vor,0}/2\pi r_{1,0}^2) = 87.5$

(d) $t(\Gamma_{vor,0}/2\pi r_{1,0}^2) = 87.5$

(e) $t(\Gamma_{vor,0}/2\pi r_{1,0}^2) = 175.5$

(f) $t(\Gamma_{vor,0}/2\pi r_{1,0}^2) = 175.5$

Figure 5.11: Distributions of the axial vorticity as determined by the ensemble average of Eq. 4.15 for the case without (left) and with grid-generated turbulence (right). Low levels of axial vorticity are presented to visualize that part of the trailing vortex that has not yet rolled up completely. A concentration of axial vorticity is present in the lower left side of the domain at $t(\Gamma_{vor,0}/2\pi r_{1,0}^2) = 17.5$, which represents that part of the vortex that has not yet rolled up. Clearly, the distribution of axial vorticity is not axisymmetric for $t(\Gamma_{vor,0}/2\pi r_{1,0}^2) = 17.5$. Note that the artificial shapes in the outer region of the vortex are caused by the measurement limitations, see Appendix G. The non-physical shapes around the vortex centre are believed to be due to PIV process.

We considered the axial velocity and azimuthal vorticity in the region $r/r_{1,0} \leqq 3$. The distribution of these quantities was found to be initially asymmetric due to a remnant of the boundary layer flow spiraling inwards to the vortex centre. This remnant of the boundary layer flow is believed to be extended to the region $r/r_{1,0} > 3$, since the dimensions of this flow are related to those of the wing. The distribution of the axial velocity as obtained from the outer region measurements are therefore shown in Figure 5.8 and 5.9, for the case without and with grid-generated turbulence, respectively. The levels of the axial velocity are limited to low levels such that the boundary layer remnant are visible. Note that the artificial shapes in the outer region of the vortex are caused by the measurement limitations, see Appendix G. The non-physical shapes around the vortex centre are believed to be due to the PIV process.

The distribution of axial velocity at $t(\Gamma_{vor,0}/2\pi r_{1,0}^2) = 17.5$ shows a concentration of negative axial velocity in the left side of the (y, z)-plane. The orientation of this concentration corresponds to that of the wing, which is placed horizontally in the left side $-60 \lessapprox y/r_{1,0} \lessapprox 0$ at height $z/r_{1,0} \approx 1$. This validates our belief that the streak of negative axial velocity spiraling inwards to the vortex centre is a remnant of the boundary layer flow over the wing.

By inspection of the distributions for $t(\Gamma_{vor,0}/2\pi r_{1,0}^2) \geqq 17.5$, it becomes clear that the remnant of the boundary layer flow spirals around the vortex centre. The boundary layer remnant is advected in the flow field of the vortex sheet rolling up into the trailing vortex. The streak of negative axial velocity is contained in the complete domain covered by the outer region measurements. The distributions suggest that the remnant of the boundary layer flow extends even outside the area covered by the outer region measurements. The negative axial velocity contained in the remnant of the boundary layer increases towards zero.

We will now proceed with a brief consideration of the distribution of axial vorticity in the (y, z)-plane. The distributions as obtained from the inner region measurements are shown for the case without and with grid-generated turbulence in Figure 5.10. In contrast to the distributions of axial velocity and azimuthal vorticity, the distribution of axial vorticity is in good approximation axisymmetric for $t(\Gamma_{vor,0}/2\pi r_{1,0}^2) \geqq 17.5$. In accordance with the radial profiles shown in Figure 5.5, the distributions show an axial vorticity evolving from a distribution sharply peaked at the vortex centre, towards one that is smoother.

It was shown by the analysis of the outer region measurements of axial velocity, that a remnant of the boundary layer flow over the wing spirals around the trailing vortex. This streak of negative axial velocity is contained in the complete domain covered by the outer region measurements. Clearly, the influence of the flow over the wing is still noticeable in the distribution of axial velocity in the region $r/r_{1,0} \lessapprox 12$, and for $t(\Gamma_{vor,0}/2\pi r_{1,0}^2) = \mathcal{O}(10^2)$ behind the wing. Since axial vorticity is a result of the flow over the wing, it is equally well believed that axial vorticity is locally concentrated in $r/r_{1,0} \lessapprox 12$ for $t(\Gamma_{vor,0}/2\pi r_{1,0}^2) = \mathcal{O}(10^2)$ after creation of the trailing vortex. The distribution of low level axial vorticity as obtained from the outer region measurements is therefore shown in Figure 5.11 for the case without and with grid-generated turbulence. The artificial shapes are caused by the measurement limitations, see Appendix G. The distribution of axial vorticty is not axisymmetric and the same shapes found for the streaks of negative axial velocity, see Figures 5.8 and 5.9, can be retrieved in the distribution of axial vorticity. It becomes clear that axial vorticity is contained in the region $r/r_{1,0} \lessapprox 12$ for $t(\Gamma_{vor,0}/2\pi r_{1,0}^2) = \mathcal{O}(10^2)$ after creation of the trailing vortex. This can be considered as that part of the trailing vortex that has not yet rolled up completely. Note that for increasing time, the level of axial vorticity approaches the measurement limitation and for that reason it is difficult to visualize the distribution of axial vorticity properly.

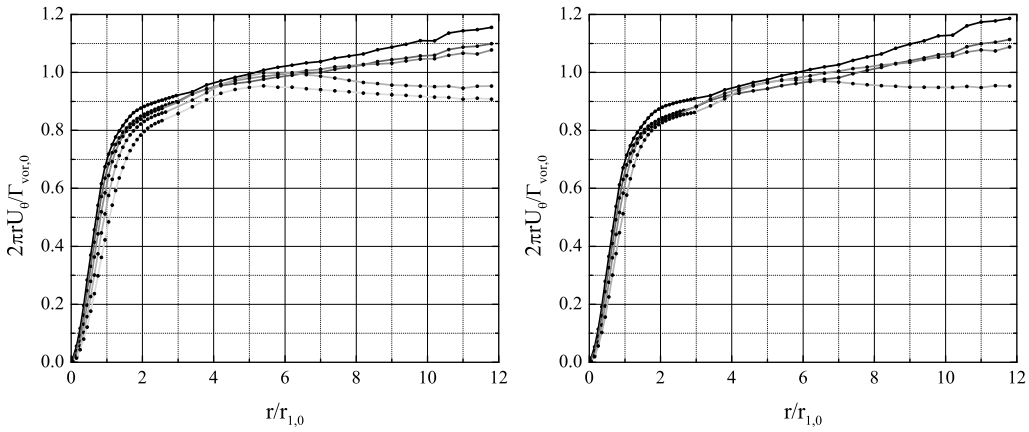

(a) without grid-generated turbulence (b) with grid-generated turbulence

Figure 5.12: Radial profiles of the circulation for the case without grid-generated turbulence (left) and with grid-generated turbulence (right). The profiles show a trend of increasing circulation with increasing radial distance for $t(\Gamma_{vor,0}/2\pi r_{1,0}^2) = -332; 87.5,$ *and* $175.5.$ *For the time* $t(\Gamma_{vor,0}/2\pi r_{1,0}^2) = 0$ *and* 662.5 *(only for the case without grid-generated turbulence) the circulation reaches a maximum after which it starts to decrease. From black to light gray:* $t(\Gamma_{vor,0}/2\pi r_{1,0}^2) = 17.5; 87.5; 175.5; 350.0; 662.5$ *(the last time only for the case without grid-generated turbulence).*

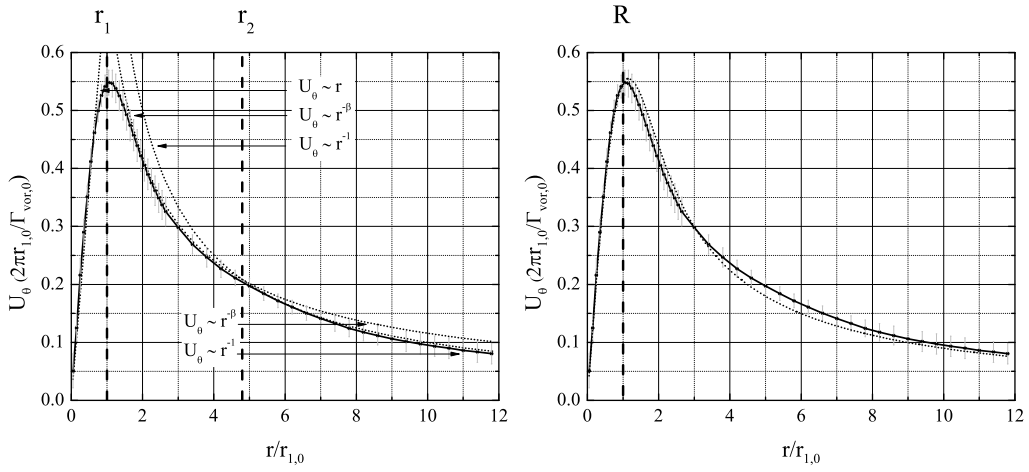

(a) VM1 fit of U_θ (b) Lamb-Oseen fit of U_θ

Figure 5.13: Radial profiles of the azimuthal velocity for $t(\Gamma_{vor,0}/2\pi r_{1,0}^2) = 350.0$ *and the case without grid-generated turbulence. The azimuthal velocity profile is fitted (dotted lines) with the two-length-scales Vortex Model 1 -VM1- (left) and the Lamb-Oseen velocity profile, see Chapter 2. It becomes clear that the Lamb-Oseen velocity profile falls short in the region* $3 \lessapprox r_{1,0} \lessapprox 12$*, and that the velocity profile can only be described correctly with a two-length-scales model. VM1 instead of VM2 is applied to illustrate the different regions of the two-length-scales model mores clearly.*

5.2 Evolution of circulation

The distribution of the axial vorticity is closely related to the distribution of circulation, see Eq. 2.8. We will now continue with discussing the circulation. This will give us a better understanding of the distribution of axial vorticity, i.e. circulation, and the influence of the trailing vortex roll-up process on this distribution.

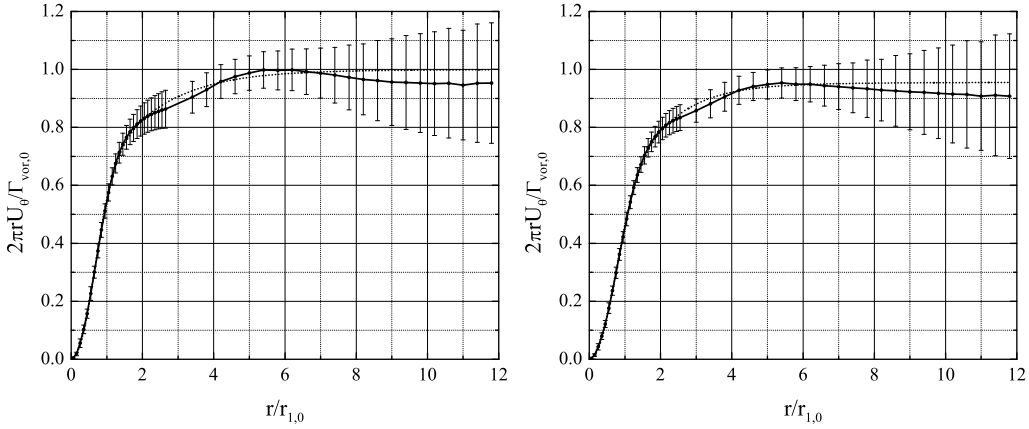

(a) $t(\Gamma_{vor,0}/2\pi r_{1,0}^2) = 350.0$, without grid-generated turbulence

(b) $t(\Gamma_{vor,0}/2\pi r_{1,0}^2) = 662.5$, without grid-generated turbulence

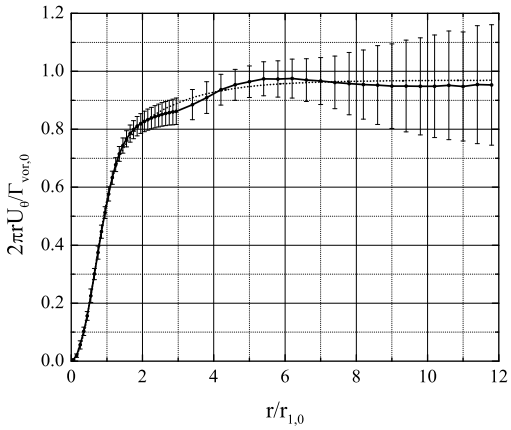

(c) $t(\Gamma_{vor,0}/2\pi r_{1,0}^2) = 350.0$, with grid-generated turbulence

Figure 5.14: The radial profiles of the circulation and their fitted profiles based on VM2. The parameters of the fitted profiles are shown in Table 5.1.

Radial profiles of the circulation are shown in Figure 5.12 for the case without and with grid-generated turbulence. The circulation profiles as obtained with inner and outer region measurements are connected to each other as motivated in Appendix E. The circulation profiles are determined by path integration of the azimuthal velocity, see Eq. 4.22, and are validated by area integration of the axial vorticity, see Appendix F.

For $t(\Gamma_{vor,0}/2\pi r_{1,0}^2) = 17.5, 87.5$, and 175.5, the circulation increases with increasing radius. Approximately 80% of the circulation at $r/r_{1,0} = 12$ is contained in the region $r/r_{1,0} \leqq 2$, and the remaining 20% is evenly distributed in the region $2 < r/r_{1,0} \leqq 12$. For $t(\Gamma_{vor,0}/2\pi r_{1,0}^2) = 350.0$ the circulation profile diverts at $r/r_{1,0} \approx 6$ from the increasing trend observed for earlier times. The circulation even decreases about 0.05 $\Gamma_{vor,0}$ after which it converges to 0.95 $\Gamma_{vor,0}$ in the region $10 < r/r_{1,0} \leqq 12$. The circulation profile for $t(\Gamma_{vor,0}/2\pi r_{1,0}^2) = 662.5$ starts to decrease at $r/r_{1,0} \approx 7$. From that radius, the circulation decreases at a constant slope from approximately 0.95 $\Gamma_{vor,0}$ towards 0.90 $\Gamma_{vor,0}$ at $r/r_{1,0} = 12$. There is no significant difference in the radial profiles of circulation for the case without and with grid-generated turbulence.

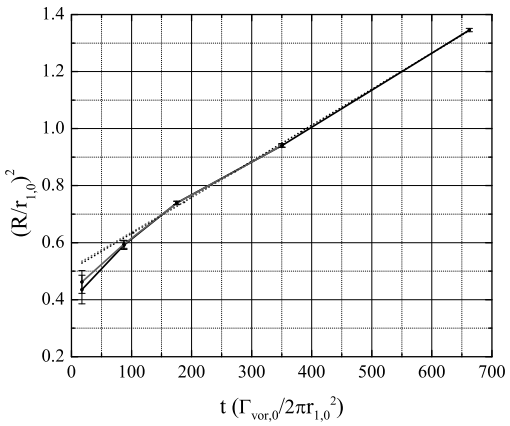

Figure 5.15: The evolution of $(R/r_{1,0})^2$ is shown for the case without (black lines) and with grid-generated turbulence (dark gray lines) to retrieve Eq. 2.27. One may conclude that the vortex inner region is subjected to viscous decay similar to that of a Lamb-Oseen vortex for $t(\Gamma_{vor,0}/2\pi r_{1,0}^2) \gtrapprox 150$.

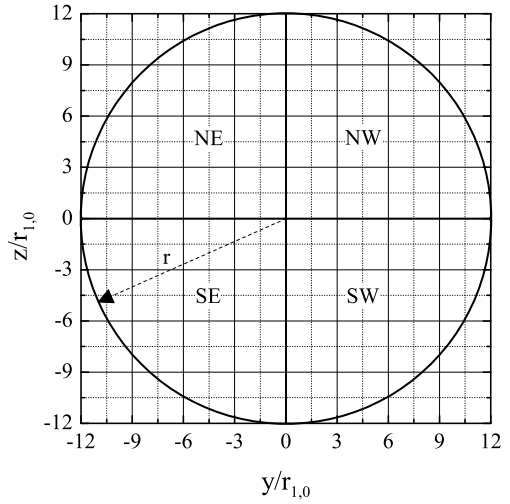

Figure 5.16: Radial profiles of the circulation are for every quadrant determined following Eq. 5.3-5.4. The quadrants are denoted by South West (SW), South East (SE), North East (NE), and North West (NW). The integration area is shown for determining the circulation of quadrant SW till radius $r/r_{1,0} = 12$.

The radial profile of the circulation at $t(\Gamma_{vor,0}/2\pi r_{1,0}^2) = 350.0$ for the case without grid-generated turbulence is fitted with the two-length-scales Jacquin Vortex Model VM2, see Eq. 2.32 and Fabre and Jacquin (2004). The necessity for describing the azimuthal velocity profile with such a two-length-scales model is elucidated in Figure 5.13. Here, the azimuthal velocity profile is fitted with the two-length-scales VM1 and the Lamb-Oseen velocity profile, see Chapter 2. VM1 instead of VM2 is applied to illustrate the different regions of the two-length-scales model mores clearly. It becomes clear that the Lamb-Oseen velocity profile falls short in the region $3 \lessapprox r_{1,0} \lessapprox 12$, and that the velocity profile can only be described correctly with a two-length-scales model.

For $t(\Gamma_{vor,0}/2\pi r_{1,0}^2) = 350.0$, the axial vorticity of the trailing vortex is believed to be fully contained in the measurement region. In other words, the circulation reaches a constant value inside the region $r/r_{1,0} \leqq 12$. This is the reason why $t(\Gamma_{vor,0}/2\pi r_{1,0}^2) = 350.0$ is used for determining the parameters $\Gamma_{vor,0}$ and $r_{1,0}$ that make flow quantities dimensionless.

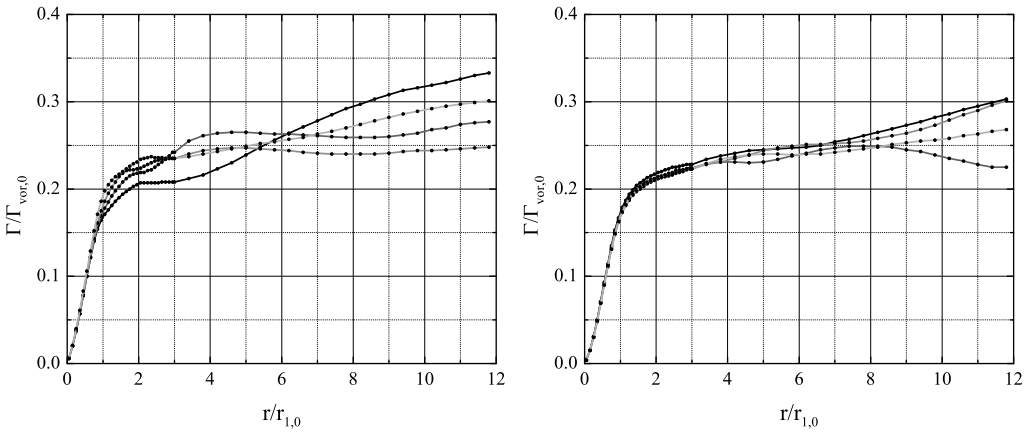

(a) $t(\Gamma_{vor,0}/2\pi r_{1,0}^2) = 17.5$

(b) $t(\Gamma_{vor,0}/2\pi r_{1,0}^2) = 87.5$

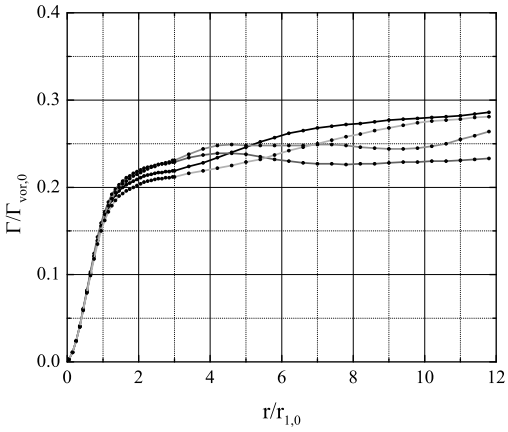

(c) $t(\Gamma_{vor,0}/2\pi r_{1,0}^2) = 175.5$

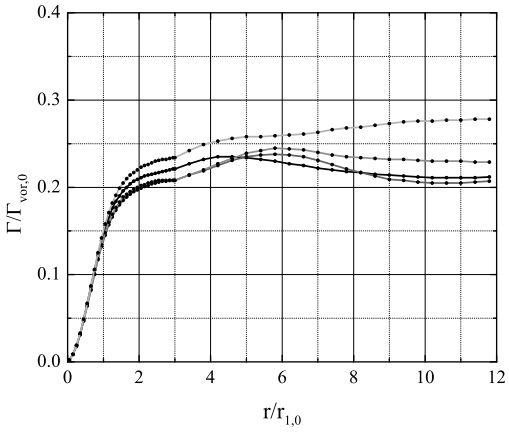

(d) $t(\Gamma_{vor,0}/2\pi r_{1,0}^2) = 350.0$

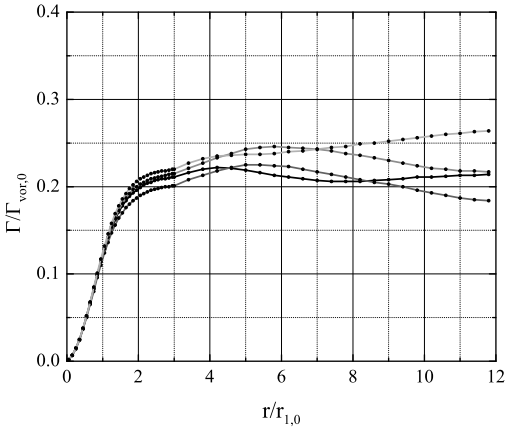

(e) $t(\Gamma_{vor,0}/2\pi r_{1,0}^2) = 662.5$

Figure 5.17: Radial profiles of the circulation for every quadrant as determined by Eqs. 5.3-5.4, see also Figure 5.16. These profiles correspond to cases without grid-generated turbulence. The distribution of circulation, i.e. axial vorticity, is not axisymmetric for the analyzed times $t(\Gamma_{vor,0}/2\pi r_{1,0}^2) = 17.5$ *till* 662.5. *At* $t(\Gamma_{vor,0}/2\pi r_{1,0}^2) = 17.5$ *the North West (NW) and South West (SW) contain the most circulation, i.e. axial vorticity. From black to lightgray: SE; SW; NW; NE.*

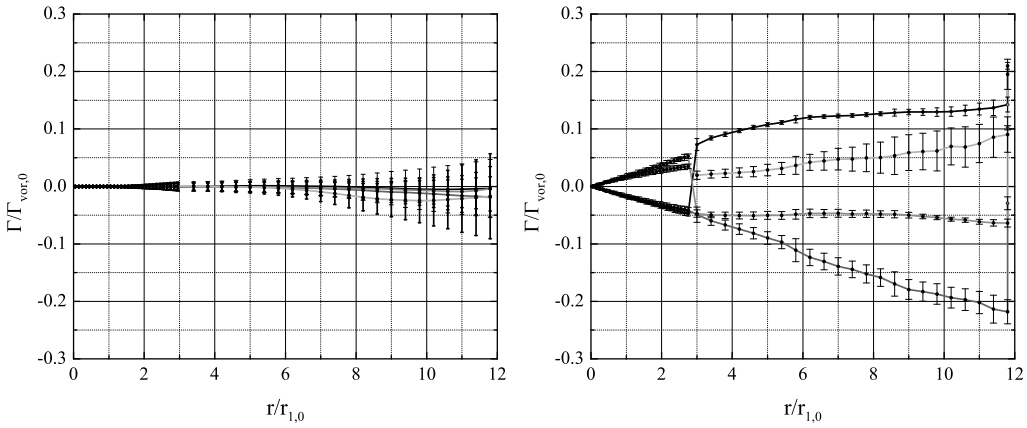

(a) area integration of axial vorticity

(b) path integration of velocity

Figure 5.18: Radial profiles of the circulation as determined by area integration of the axial vorticity (left) and by path integration of the velocity (right) in an empty wind tunnel. An empty wind tunnel flow is defined to be the flow without the wing and turbulence grid installed. Apparently, area integration of axial vorticity is more reliable than path integration. At this stage, it is now known what the reason for this difference is. From black to lightgray: SE; SW; NW; NE.

The VM2 profile contains four fit parameters: the total circulation Γ_{vor}; the inner vortex core radius r_1 characterizing the region $r \lessapprox r_1$ in which the approximation of solid-body rotation is valid; the outer vortex core radius r_2 characterizing the region $r_1 \lessapprox r \lessapprox r_2$ in which the azimuthal velocity behaves to a good approximation as $U_\theta \sim r^{-\beta}$, with β being the last parameter. The total circulation Γ_{vor} is set as a typical value determined from visual inspection of the circulation profile in the region $4 \lessapprox r/r_{1,0} \lessapprox 12$. The value for β is determined by the slope of $\log(U_\theta)$ against $\log(r)$ in the region $2.5 \lessapprox r/r_{1,0} \lessapprox 5$. This region is defined such that it lies in the middle between the estimated values of r_1 and r_2. With Γ_{vor} and β defined, we determine r_1 and r_2 by a least-squares fit method. We believe that r_1 and r_2 are appropriate fit parameters since they are more independent from each other than for example r_2 and Γ_{vor}. The VM2 parameters at $t(\Gamma_{vor,0}/2\pi r_{1,0}^2) = 350.0$ for the case without grid-generated turbulence are found to be $\Gamma_{vor} = 0.50\,\mathrm{m}^2\,\mathrm{s}^{-1}$, $\beta = 0.81$, $r_1 = (5.85\pm0.04)\cdot10^{-3}$ m, and $r_2 = (4.7\pm0.1)r_1 = (2.75\pm0.06)\cdot10^{-2}$ m. These parameters are defined to be $\Gamma_{vor,0}, \beta_0, r_{1,0}$, and $r_{2,0}$, and are used to make flow quantities dimensionless. The VM2 parameters at $t(\Gamma_{vor,0}/2\pi r_{1,0}^2) = 662.5$ for the case without grid-generated turbulence, and those at $t(\Gamma_{vor,0}/2\pi r_{1,0}^2) = 350.0$ for the case with grid-generated turbulence are presented in Table 5.1. The fitted VM2 profiles are shown in Figure 5.14. The circulation profiles for $t(\Gamma_{vor,0}/2\pi r_{1,0}^2) < 350.0$ are not fitted. However, based on visual inspection, we believe that r_2 is larger than $12r_{1,0}$.

The viscous behaviour of the inner vortex region is analyzed by fitting the circulation profiles in the region $0 < r/r_{1,0} \leqq 1.5 \cdot r_{U_{\theta,max}}/r_{1,0}$ with a Lamb-Oseen vortex model. The radius of maximum azimuthal velocity is denoted by $r_{U_{\theta,max}}$, and the region $0 < r/r_{1,0} \leqq 1.5 \cdot r_{U_{\theta,max}}/r_{1,0}$ is believed to be large enough to contain sufficient fitting data, but small enough to represent the inner vortex region. The evolution of vortex core radius is shown in Figure 5.15. From this, one may conclude that the vortex inner region is subjected to viscous decay similar to that of a Lamb-Oseen vortex for $t(\Gamma_{vor,0}/2\pi r_{1,0}^2) \gtrapprox 150$.

The distribution of axial vorticity in the (y, z)-plane, shown in Figure 5.11, is not axisymmetric for $t(\Gamma_{vor,0}/2\pi r_{1,0}^2) = 17.5$ and 87.5. This means that the distribution of circulation is neither symmetric. As suggested in Section 5.1, the antisymmetry is caused by that part of the trailing vortex that has not yet rolled up completely. As a result, a streak of axial vorticity winds around

Table 5.1: The VM2 parameters are presented for the cases without ($M000$) and with grid-generated turbulence ($M254$). Note that Γ_{vor} and β are set, and that both r_1 and r_2 are determined from a least-squares fit.

	M000	M000	M254
$t(\Gamma_{vor,0}/2\pi r_{1,0}^2)$	350.0	662.5	350.0
$\Gamma_{vor}/\Gamma_{vor,0}$	1	0.96	0.97
β	0.81	0.74	0.83
$r_1/r_{1,0}$	1.000±0.007	1.123±0.008	1.013±0.004
$r_2/r_{1,0}$	4.7±0.1	3.8±0.1	4.7±0.1

the vortex centre due to advection. To obtain a better insight in the distribution of circulation, we determine radial profiles of the circulation for every quadrant in the (y,z)-plane, see Figure 5.16. The circulation profiles are now not obtained by path integration of the velocity, but by area integration of the axial vorticity. Both methods are applied for the case with an empty wind tunnel, see Figure 5.18, and the method of area integration of axial vorticity was found to be most reliable. At this stage, the reason for this discrepancy is not known.

We will briefly discuss the method in which the circulation profiles are obtained. Radial profiles of the axial vorticity are determined for both the inner region and the outer region measurements, and for every quadrant by

$$\omega_x(r = i\triangle r) = \frac{\sum_j \sum_k \omega_x(y,z)\delta_{(i-1)\triangle r \leqq r < i\triangle r}}{\sum_j \sum_k \delta_{(i-1)\triangle r \leqq r < i\triangle r}} \quad i = 1,2,3...N_{\triangle r}, \tag{5.2}$$

in which the summation over j and k is defined for each quadrants as:

$$\begin{aligned}
SW \quad & 1 \leqq j \leqq (N_y+1)/2 \quad 1 \leqq k \leqq (N_z+1)/2, \\
SE \quad & (N_y+1)/2 \leqq j \leqq N_y \quad 1 \leqq k \leqq (N_z+1)/2, \\
NE \quad & (N_y+1)/2 \leqq j \leqq N_y \quad (N_z+1)/2 \leqq k \leqq N_z, \\
NW \quad & 1 \leqq j \leqq (N_y+1)/2 \quad (N_z+1)/2 \leqq k \leqq N_z.
\end{aligned}$$

The circulation profile is now determined by

$$\Gamma(r = i\triangle r \leqq r_{con}/\triangle r) = \sum_{l=1}^{l=i} \omega_x(r = l\triangle r) 2\pi l(\triangle r)^2 \quad i = 1,2,3...r_{con}/\triangle r, \tag{5.3}$$

for the inner measurement region, combined with

$$\Gamma(r = i\triangle r > r_{con}/\triangle r) = \sum_{l=r_{con}/\triangle r+1}^{l=i} \omega_x(r = l\triangle r) 2\pi l(\triangle r)^2 + \Gamma(r_{con}); \tag{5.4}$$
$$i - r_{con}/\triangle r = 1,2,3...N_{\triangle r} - r_{con}/\triangle r$$

for the outer measurement region. The circulation profiles are connected to each other at position r_{con} as motivated in Appendix E. The radial profiles of the circulation as determined for every quadrant SouthWest (SW), South East (SE), North East (NE), and North West (NW) are shown in Figure 5.17. We only consider the case without grid-generated turbulence, since we believe that the difference is insignificant for this discussion. For $t(\Gamma_{vor,0}/2\pi r_{1,0}^2) = 17.5$, the trend of increasing circulation for increasing radius as found for the circulation determined for the four quadrants together, see Figure 5.12, is also retrieved for that in every quadrant separately. For $r/r_{1,0} \gtrapprox 8$, the amount of circulation is different for every quadrant. The most circulation is concentrated in the SW quadrant, which is followed by the NW, SE, and NE quadrants, respectively. The amount of circulation in between subsequent quadrants differs approximately 0.025

$\Gamma_{vor,0}$ from each other. It has to be remarked, that great care is necessary for drawing conclusion for the region $r/r_{1,0} \gtrapprox 8$ since the distribution of circulation was found to be asymmetric in the empty wind tunnel measurements, see Figure 5.18. Nevertheless, we believe that the specific shape of the circulation profiles for $r/r_{1,0} \lessapprox 8$ can be explained by a streak of axial vorticity winding around the vortex centre. As discussed in Section 5.1, this streak of axial vorticity is part of the trailing vortex that had not yet rolled up completely. The circulation profiles show a sudden increase in its slope at $r/r_{1,0} \approx 3$, $r/r_{1,0} \approx 2.5$, $r/r_{1,0} \approx 2$, $r/r_{1,0} \approx 3$ for the SW, SE, NE, and NW quadrants, respectively. It is believed that from these radii, the streak of axial vorticity becomes part of the corresponding region in which the circulation is determined. The wing is placed horizontally in the left side $-60 \lessapprox y/r_{1,0} \lessapprox 0$ at height $z/r_{1,0} \approx 1$. The streak of axial vorticity originates from the wing and spirals inwards to the vortex centre. The streak of axial vorticity is therefore for the SE and NE quadrants closer to the vortex centre than for the other quadrants. This is in accordance with the radius at which the slope of the circulation profile increases, being smaller for the SE and NE quadrants than that for the SW and NW quadrants. For $t(\Gamma_{vor,0}/2\pi r_{1,0}^2) = 87.5$, the circulation profile suggests a axisymmetric distribution of circulation in the region $r/r_{1,0} \lessapprox 8$. Apparently, axial vorticity is evenly distributed over the four quadrants such that the circulation profile for each separate quadrant increases at a constant slope for $3 \lessapprox r/r_{1,0} \lessapprox 8$. For $r/r_{1,0} \gtrapprox 8$, the circulation profiles diverge from each other. However, it has to be remarked that measurement limitations may become important here and that it is therefore very difficult to give a physical explanation of the observation.

For $t(\Gamma_{vor,0}/2\pi r_{1,0}^2) = 175.5, 350.0$, and 662.5, the circulation profiles in the region $r/r_{1,0} \lessapprox 8$ differ as much as $0.05\Gamma_{vor}$ between each quadrant. This is believed to be a result of the streak of axial vorticity winding around the vortex centre. From this point of view, one may conclude that the antisymmetry holds on for $t(\Gamma_{vor,0}/2\pi r_{1,0}^2) = \mathcal{O}(10^2)$ after creation of the trailing vortex.

We discussed the evolution of the velocity, vorticity and circulation. For that, we considered radial profiles and the distribution of these flow quantities in the (y, z)-plane. It has become clear, that remnants of the flow over the wing are still observable for $t(\Gamma_{vor,0}/2\pi r_{1,0}^2) = \mathcal{O}(10^2)$ after creation of the trailing vortex. The boundary layer of the flow over the wing spirals as a streak of negative axial velocity around the vortex centre. Likewise, positive axial vorticity that has not yet rolled up into the trailing vortex, winds around the vortex centre. We will now proceed with discussing the kinetic energy of the turbulence in the region $r/r_{1,0} \leqq 3$.

5.3 Evolution of kinetic energy of turbulence

It is assumed that the root-mean-square variations of the velocity are a good approximation for the turbulence velocities. The kinetic energy of the turbulence is determined by Eq. 4.22 and its radial distribution is shown for the case without and with grid-generated turbulence in Figure 5.19. Except at $t(\Gamma_{vor,0}/2\pi r_{1,0}^2) = 350.0$, the kinetic energy of the turbulence has a maximum at the vortex centre for all cases. For $t(\Gamma_{vor,0}/2\pi r_{1,0}^2) = 350.0$, the maximum is slightly out of the vortex centre at $r/r_{1,0} = 0.25$. The maximum kinetic energy of turbulence is $q(2\pi r_{1,0}/\Gamma_{vor,0})^2 \approx 0.7$ for $t(\Gamma_{vor,0}/2\pi r_{1,0}^2) = 17.5$, after which it decreases to $q(2\pi r_{1,0}/\Gamma_{vor,0})^2 \approx 0.3$ for $t(\Gamma_{vor,0}/2\pi r_{1,0}^2) = 87.5$, and it stabilizes at a constant value of $q(2\pi r_{1,0}/\Gamma_{vor,0})^2 \approx 0.12$ for subsequent times. Clearly, the trailing vortex contains a lot of velocity fluctuations after its creation. These velocity fluctuations are believed to be inherent to the asymmetric trailing vortex roll-up. The velocity fluctuations reduce to constant level for $t(\Gamma_{vor,0}/2\pi r_{1,0}^2) = \mathcal{O}(10^2)$ after creation of the trailing vortex.

The influence of the grid-generated turbulence is insignificant for the kinetic energy of turbulence in the region $r/r_{1,0} \lessapprox 1$. For the analyzed times after $t(\Gamma_{vor,0}/2\pi r_{1,0}^2) = 87.5$, the influence of grid-generated turbulence is visible for $r/r_{1,0} \gtrapprox 1$. Higher levels of constant q are obtained than those for the cases without grid-generated turbulence. At $t(\Gamma_{vor,0}/2\pi r_{1,0}^2) = 87.5$, the value

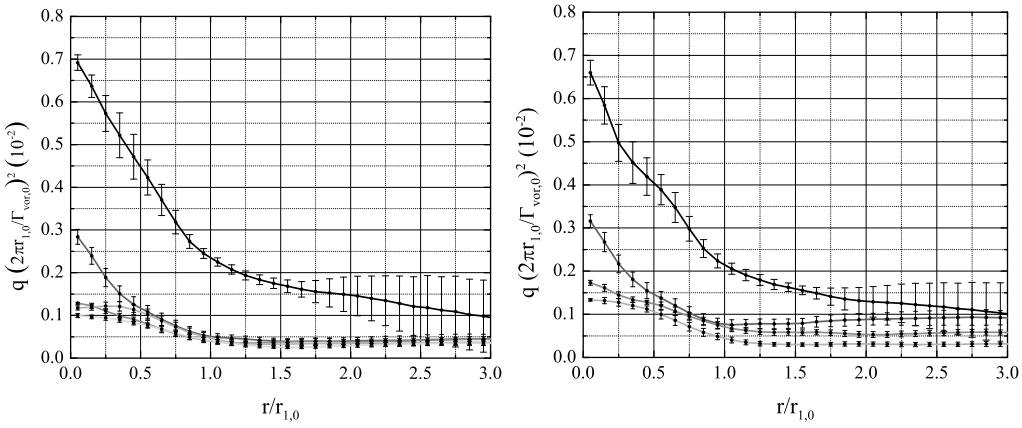

(a) without grid-generated turbulence (b) with grid-generated turbulence

Figure 5.19: Kinetic energy of the turbulence as defined by the ensemble average of Eq. 4.21. The amount of kinetic energy in the inner vortex region decreases from $q(2\pi r_{1,0}/\Gamma_{vor,0})^2 \approx 0.7$ *at* $t(\Gamma_{vor,0}/2\pi r_{1,0}^2) = 17.5$ *to* $q(2\pi r_{1,0}/\Gamma_{vor,0})^2 \approx 0.1$ *for* $t(\Gamma_{vor,0}/2\pi r_{1,0}^2) = 175.5$ *till* $t(\Gamma_{vor,0}/2\pi r_{1,0}^2) = 350.0$ *(*662.5 *for the case without grid-generated turbulence). From black to light gray:* $t(\Gamma_{vor,0}/2\pi r_{1,0}^2) = 17.5; 87.5; 175.5; 350.0; 662.5$ *(the last time only for the case without grid-generated turbulence).*

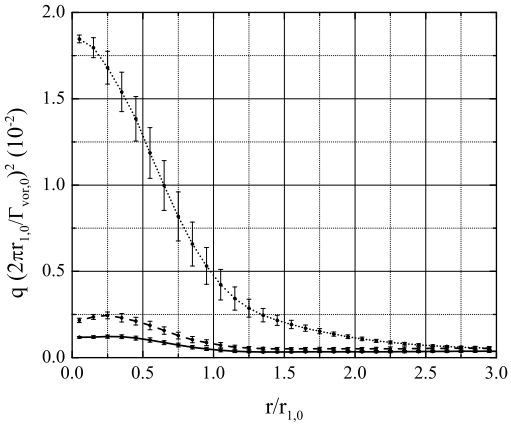

Figure 5.20: Kinetic energy of the turbulence as defined by the ensemble average of Eq. 4.21 in the frame of reference co-moving with the vortex centre (———), co-moving with the grid-point vortex centre frame (- - - -), and that in the stationary frame of reference (·····). The profiles are obtained at $t(\Gamma_{vor,0}/2\pi r_{1,0}^2) = 350.0$ *and for the case without grid-generated turbulence.*

of this constant level of kinetic turbulence is found to be $q(2\pi r_{1,0}/\Gamma_{vor,0})^2 \approx 0.1$. This value is of the same order as that found in our study on the grid-generated turbulence characteristics, see Chapter C.

We assume that the vortex centre position is determined correctly by the method described in Section 4.2. An incorrect vortex centre position would mean that large fluctuations in the velocity are inherent to large velocity gradients. This can be illustrated by determining Eq. 4.21 in the stationary frame of reference, and the frame of reference co-moving with the vortex centre and the grid-point vortex centre. In case of the frame of reference co-moving with the grid-point vortex centre, the vortex centre positions are pinned down to a grid point, see Section 4.2. Figure 5.20 shows the kinetic energy of turbulence as determined by Eq. 4.21 for the stationary frame of reference, and the frame of reference co-moving with the vortex centre and the grid-

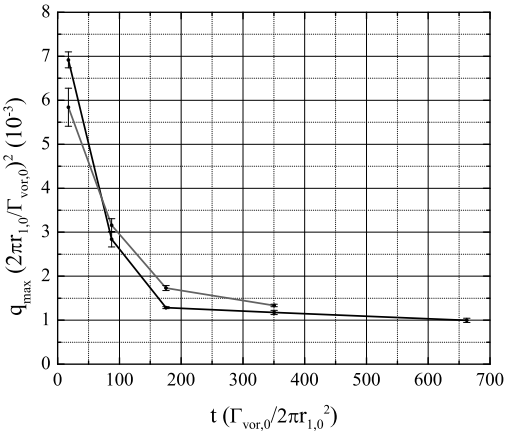

Figure 5.21: The evolution of the maximum kinetic energy of the turbulence is shown for the case without (black line) and with grid-generated turbulence (dark gray line). This maximum decays within $\mathcal{O}(10^2 2\pi r_{1,0}^2/\Gamma_{vor,0})$ towards a constant 15% of its value found closest behind the wing.

point vortex centre. The profiles are obtained at $t(\Gamma_{vor,0}/2\pi r_{1,0}^2) = 350.0$ and for the case without grid-generated turbulence. Apparently, the kinetic energy of turbulence as obtained in the stationary frame of reference is about 15 times, and in the frame of reference co-moving with the grid-point vortex centre 2 times that obtained in the frame of reference co-moving with the vortex centre position. Clearly, high levels of velocity fluctuations are inherent to the combination of an incorrect vortex centre position and large velocity gradients as found in the vortex core region. The same analysis is performed for the azimuthal and axial velocity and vorticity components, and is considered in Appendix H.

5.4 Evolution of vortex centre positions

The vortex centre is determined by a least-squares fit of a second-order polynomial through the streamfunction for $r/r_{1,0} < 0.5$. The vortex centre position $r_{s,c}^{\mathrm{p}}$ is determined for every realization $\mathrm{p} \in \mathcal{P}$ and is shown in the stationary frame in Figures 5.22 and 5.23. Apparently, the vortex centre position fluctuates with increasing intensity for increasing times. The distribution of vortex centre positions is found to be axisymmetric at $t(\Gamma_{vor,0}/2\pi r_{1,0}^2) = 17.5$ for both the case with and without grid-generated turbulence. However, at $t(\Gamma_{vor,0}/2\pi r_{1,0}^2) = 87.5$ and 175.5, this distribution is found to be axisymmetric for the case with grid-generated turbulence, but not for the case without grid-generated turbulence. For the case without grid-generated turbulence at $t(\Gamma_{vor,0}/2\pi r_{1,0}^2) = 87.5$, the distribution is slightly tilted at an angle of about 10 degrees with respect to the vertical axis. At $t(\Gamma_{vor,0}/2\pi r_{1,0}^2) = 175.5$, this distribution is slightly tilted at an angle of about 45 degrees from the vertical axis. The distribution is found to be in good approximation axisymmetric for the times analyzed after $t(\Gamma_{vor,0}/2\pi r_{1,0}^2) = 175.5$.

A probability density function (PDF) is determined for the probability of $r_{s,c}^{\mathrm{p}}$ being in a region $(i-1)\triangle r_{s,c} \leqq r_{s,c}^{\mathrm{p}} < i\triangle r_{s,c}$ with $\triangle r_{s,c} = 2r_{1,0}/25$ and $i = 1, 2, 3...$, see Eq. 4.11. The PDFs are shown in Figure 5.24. The PDFs are at $t(\Gamma_{vor,0}/2\pi r_{1,0}^2) = 17.5$ sharply peaked around $r_s/r_{1,0} = 0.05$, but they evolve into a smoother distribution for later times. In the case without grid-generated turbulence, the PDF peaks around $r_s/r_{1,0} = 0.25$ for $t(\Gamma_{vor,0}/2\pi r_{1,0}^2) = 662.5$. Except at $t(\Gamma_{vor,0}/2\pi r_{1,0}^2) = 350.0$, the PDFs for the cases with grid-generated turbulence are broader than those for the same cases without grid-generated turbulence. One may conclude that the vortex wandering is more intense with grid-generated turbulence for the analyzed cases at $t(\Gamma_{vor,0}/2\pi r_{1,0}^2) < 350.0$. This means that the vortex wandering is less intense with grid-generated turbulence for $t(\Gamma_{vor,0}/2\pi r_{1,0}^2) = 350.0$.

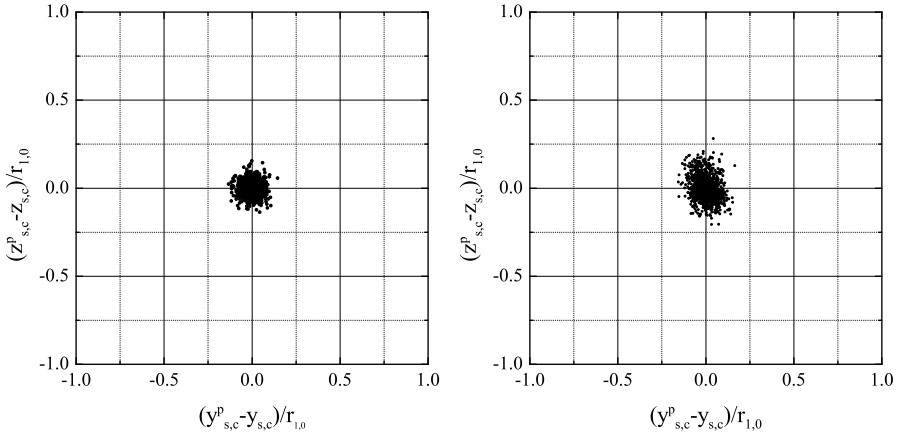

(a) $t(\Gamma_{vor,0}/2\pi r_{1,0}^2) = 17.5$ (b) $t(\Gamma_{vor,0}/2\pi r_{1,0}^2) = 87.5$

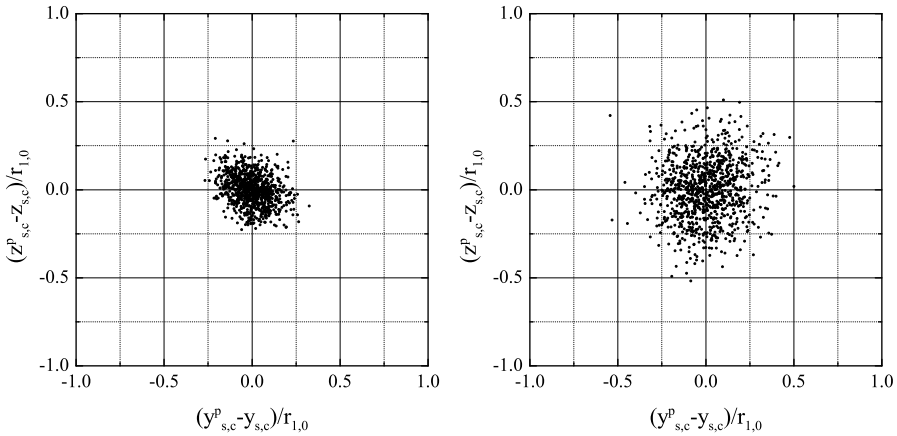

(c) $t(\Gamma_{vor,0}/2\pi r_{1,0}^2) = 175.5$ (d) $t(\Gamma_{vor,0}/2\pi r_{1,0}^2) = 350.0$

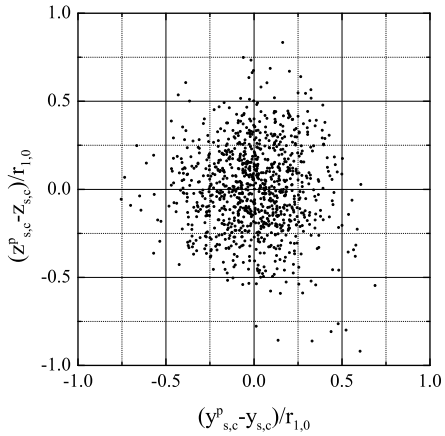

(e) $t(\Gamma_{vor,0}/2\pi r_{1,0}^2) = 662.5$

Figure 5.22: The vortex centre positions in the stationary frame for the the case without grid-generated turbulence. The region in which the vortex centre positions are located becomes larger with time.

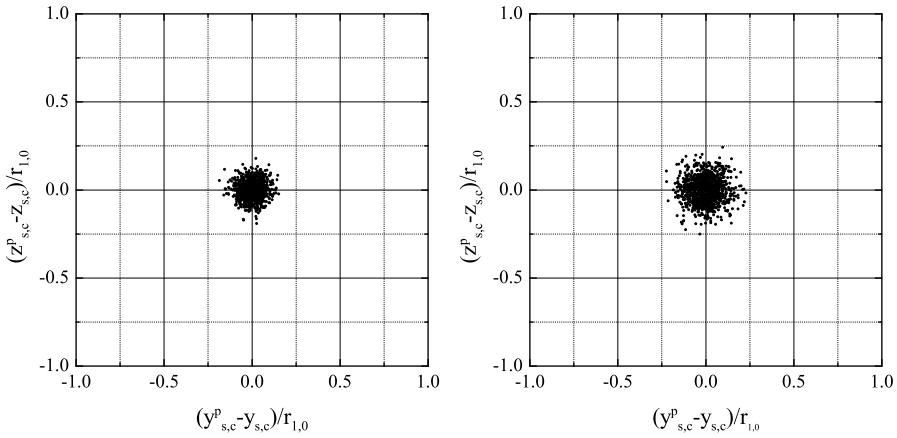

(a) $t(\Gamma_{vor,0}/2\pi r_{1,0}^2) = 17.5$

(b) $t(\Gamma_{vor,0}/2\pi r_{1,0}^2) = 87.5$

(c) $t(\Gamma_{vor,0}/2\pi r_{1,0}^2) = 175.5$

(d) $t(\Gamma_{vor,0}/2\pi r_{1,0}^2) = 350.0$

Figure 5.23: The vortex centre positions in the stationary frame for the the case with grid-generated turbulence. The region in which the vortex centre positions are located becomes larger with time.

Following Devenport et al. (1996), it is assumed that the vortex centre is subjected to Gaussian isotropic wandering. This assumptions implies that the radial position of the vortex centre can be compared to the distance from the origin for a random walk in two dimensions. The PDF is therefore fitted with the Rayleigh distribution defined by

$$PDF(r) = \frac{r}{\chi^2} \exp(\frac{-r^2}{2\chi^2}) \quad \chi > 0; r \geqq 0 \tag{5.5}$$

with $\chi\sqrt{\pi/2}$ the mean of the distribution. The evolution of $\chi\sqrt{\pi/2}$ for increasing time is shown in Figure 5.25. The mean radial position increases approximately linearly with time. This means that a direct analogy with the random walk is not possible. The distance from the origin for a random walk in two dimensions evolves namely with the square root of the duration when constant step sizes are assumed. This relation is not retrieved in Figure 5.25.

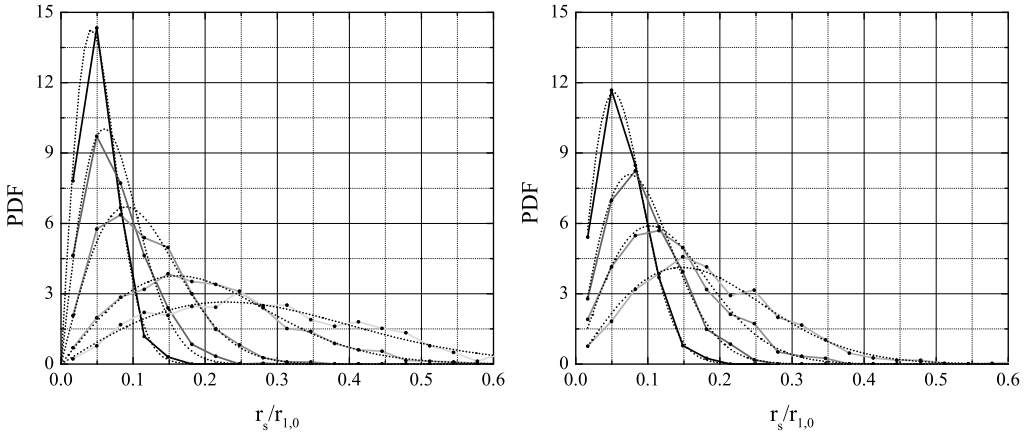

(a) without grid-generated turbulence (b) with grid-generated turbulence

Figure 5.24: Probability Density Function (PDF) as determined by Eq. 4.11. The probability Pr for the vortex centre position $r^{\mathrm{p}}_{c,s}$ to be in the interval $a\triangle r_{s,c} \leqq r^{\mathrm{p}}_{c,s} < b\triangle r_{s,c}$ with $a, b = 1, 2, 3...$ and $b > a$ is given by $Pr(a\triangle r_{s,c} \leqq r^{\mathrm{p}}_{c,s} < b\triangle r_{s,c}) = \sum_{i=a}^{b} PDF\triangle r_{s,c}$. The PDF function is fitted with a Rayleigh distribution, see Eq. 5.5. From black to light gray: $t(\Gamma_{vor,0}/2\pi r^2_{1,0}) = 17.5; 87.5; 175.5; 350.0; 662.5$ (the last time only for the case without grid-generated turbulence).

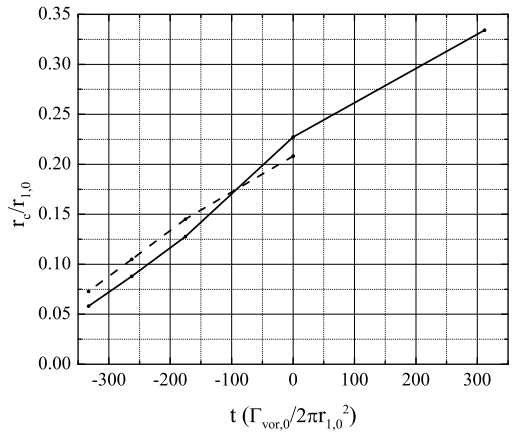

Figure 5.25: Mean radial position $r_{s,c}$ as determined from fitting PDF with a Rayleigh distribution, see Figure 5.24. The data is presented for the case without grid-generated turbulence (black lines), and the case without grid-generated turbulence (dark gray lines). The error bars are determined by the standard error of the fitting procedure. For $t(\Gamma_{vor,0}/2\pi r_{1,0}^2) \lessapprox 250$, the mean radial position of the vortex centre is about $0.025 r_{1,0}$ larger for the case with than that without grid-generated turbulence. After this time, the mean radial position for the case without grid-generated turbulence is larger.

+

Chapter 6

Conclusions and Discussion

Wind tunnel experiments were performed for a single trailing vortex without and with grid-generated turbulence. This work can be seen as a continuation of the work of Van Jaarsveld (2008). The 3C-PIV measurement technique was applied to obtain a three-components velocity field in planes perpendicular to the trailing vortex axis. With respect to the 2C-PIV measurements of Van Jaarsveld (2008), it was now possible to measure the axial velocity as well. Inner and outer region measurements covered the region around the vortex with a radius approximately three and twelve times that of maximum azimuthal velocity, respectively. The inner region measurements captured the vortex with a higher spatial resolution and accuracy than obtained by Van Jaarsveld (2008). Every measurement consisted of an ensemble with 1.000 realizations. Special care was taken to determine the trailing vortex centre position for each realization separately. A frame of reference co-moving with the vortex centre was applied to correct for vortex wandering.

The mean quantities of the ensemble provide insight in the evolution of the azimuthal and axial velocity and vorticity components, the circulation, and the kinetic energy of turbulence. The differences between these flow quantities for the cases with and without grid-generated turbulence are found to be negligible. Following the definition of Crow and Bate (1976) and making use of a typical distance between two trailing vortices as applied by Van Jaarsveld (2008), the grid-generated turbulence can be characterized as having a weak turbulence intensity. This means that a trailing vortex pair would break-up due to the Crow-instability and the subsequent linking of vortex lines. Apparently, the influence of weak turbulence is negligible for the decay of a single trailing vortex but significant for that of a vortex pair.

The axial velocity near the vortex centre transforms from a jet- to a wake-like structure. The jet-like structure near the vortex centre is consistent with the Bernoulli theorem relating the pressure to the azimuthal velocity. The distribution of axial velocities suggests that a sheet of negative axial velocity winds around the vortex centre. In this way, streamlines that have passed the viscous boundary layer of the wing flow entrain the region of high axial velocity. The viscous contribution of $\triangle H$ in

$$U_x^2(r) = \overline{U}_x^2 - U_\theta^2(r) + 2\int_r^\infty \frac{U_\theta^2}{r'}dr' - 2\triangle H, \tag{6.1}$$

cannot be neglected anymore and, as a result, the axial velocity decreases. The number of turns of the viscous boundary layers wrapped around the vortex centre increases as the roll-up evolves. Ultimately, the neighboring turns of the spiral are believed to be close enough for viscous spreading to make a continuous distribution of flow quantities. This evolution is nicely illustrated in Figure 5.6.

The transformation from a surplus towards a deficit of velocity near the vortex centre is not only caused by the entrainment of the viscous boundary layer flow. It is namely discussed by Batchelor (1964) that the continual slowing-down of the azimuthal motion due to viscosity leads to a positive axial pressure gradient and consequently to a continual loss of axial momentum. The velocity defect arising from this conversion of azimuthal motion increases, but is continually diminished by diffusive spreading. Batchelor (1964) derived in an asymptotic analysis a relation for this process. We have tried to recover this relation, but a more thorough analysis is necessary to fully understand the observed evolution of axial velocity near the vortex centre. As reported by Green (1995), the complexity of the axial velocity is caused by its dependence on the tangential velocity distribution, the wing boundary layer and details of the roll-up phase, and the dissipation in the vortex.

The maximum axial velocity surplus (jet) and deficit (wake) are found to be 1.12 and 0.72 $\overline{U}_x$, respectively. Higher axial velocities were observed by Chow (1997) and Green and Acosta (1991) who reported axial currents near the vortex centre with a maximum velocity of 1.77 and 1.62 $\overline{U}_x$, respectively. These higher maximum velocities were obtained within two chords lengths from the trailing edge of the wing. Further downstream, the axial velocity is usually found to have a wake-like structure. Beninati and Marshall (2005) and Devenport et al. (1996) reported an axial velocity deficit of 0.86 and 0.80 $\overline{U}_x$, repectively. These values were found to stay approximately constant between about five and thirty chord lengths from the wing.

It is assumed that the root-mean-square variations of the velocity are a good approximation for the turbulence velocities. The kinetic energy of the turbulence is found to be maximum at or closely near the vortex centre. This maximum decays within $\mathcal{O}(10^2 2\pi r_{1,0}^2/\Gamma_{vor,0})$ towards a constant 15% of its value found closest behind the wing. Apparently, the flow field in the inner region of the trailing vortex rapidly laminarizes towards that with a rather constant turbulence intensity. This supports the findings of both Devenport et al. (1996) and Chow (1997). Devenport et al. (1996) also concluded that the remaining velocity fluctuations are inactive motions produced as the core is buffeted by turbulence from the surrounding wake. The high kinetic energy of the turbulence for the trailing vortex close behind the wing is thought to be inherent to the roll-up process.

The roll-up of the vortex sheet is illustrated by the distributions of axial velocity. The trailing vortex becomes approximately axisymmetric at $\mathcal{O}(10^2 2\pi r_{1,0}^2/\Gamma_{vor,0})$ downstream from the trailing edge of the wing. Radial profiles of the circulation show the necessity for a two-length-scales trailing vortex model. In such a vortex model, the inner length scale characterizes the viscous decay of the vortex core while the outer length scale characterizes the roll-up of the vortex sheet. Here, we applied the vortex models VM1 and VM2 as introduced by Jacquin et al. (2001).

The values for the VM2 parameters β and r_2/r_1 are found to be higher, respectively lower than those found by Jacquin et al. (2001). This is most likely caused by the rectangular lift distribution of our wing, instead of the more elliptical lift distribution of the wing used by Jacquin et al. (2001). Due to this difference, the axial vorticity is more closely concentrated around the vortex centre and higher, respectively lower values are found for β and r_2/r_1.

Van Jaarsveld (2008) found that the radius r_1 of the inner vortex region decays like that of a Lamb-Oseen vortex. This behaviour is retrieved for $\mathcal{O}(10^2 2\pi r_{1,0}^2/\Gamma_{vor,0})$ downstream from the trailing edge of the wing. According to Van Jaarsveld (2008), the outer region of the vortex with radius r_2 stays approximately constant. This is in contradiction with our results, which suggest an evolution in r_2. Van Jaarsveld (2008) found values of r_2/r_1 constantly around ten, while we observed values evolving from larger than 12 to as small as 3.8. Further analysis is necessary to resolve this discrepancy.

Special care is taken to accurately determine the vortex centre position for each of the 1.000 realizations in one ensemble. A probability distribution function (PDF) is determined for the radial position of the vortex centre from its mean position in the stationary frame of reference. The PDFs show a good agreement with that of a Rayleigh distribution, which suggests that an analogy with a random walk in two dimensions is possible.

The vortex wandering is more intense with grid-generated turbulence for $\mathcal{O}(10^2 2\pi r_{1,0}^2/\Gamma_{vor,0})$ downstream from the trailing edge of the wing. For later times, the vortex wandering was found to be more intense for the cases without grid-generated turbulence. This is remarkable, and needs further investigations. One may think of the flow field in the wind tunnel diffuser being significantly different for the cases with and without grid-generated turbulence. This may influence the vortex wandering as measured close to the diffuser, there where the more intense vortex wandering without grid-generated turbulence is observed.

6.1 Future work

We will end this chapter with providing some suggestions for future work.

- Future work may involve hotwire measurements, since these kind of measurements can capture the small velocities in the outer region of the vortex more accurately. This may solve the discrepancy between this work and that of Van Jaarsveld (2008) about the evolution of the outer region of the vortex with radius r_2. The effects of vortex wandering are believed to be very small in the outer region of the vortex, see Appendix H. Nevertheless, the correction method of Devenport et al. (1996) can be applied, supplemented with a detailed knowledge of the fluctuating vortex centre position as provided in this work.

- The numerical simulation of a vortex with net vorticity in a flow domain with periodic boundary conditions is found to be troublesome, see Appendix A. However, we believe that it is possible to verify the evolution of flow quantities in the inner region of the vortex with the help of the discussed numerical code. One can think of simulating the evolution of the trailing vortex with initial conditions found in the experiments at $\mathcal{O}(10^2 2\pi r_{1,0}^2/\Gamma_{vor,0})$ downstream from the wing. Here, the influence of the roll-up process on the inner region of the vortex is believed to be negligible, so that an axisymmetric initial trailing vortex can be applied.

- We analyzed a single trailing vortex with and without grid-generated turbulence. The grid-generated turbulence is characterized as having a weak turbulence intensity. This means that trailing vortex pair would break-up due to the Crow-instability and the subsequent linking of vortex lines. The break-up of a trailing vortex pair in strong external turbulence is analyzed by Van Jaarsveld (2008), and it would be interesting to analyze the break-up with weak external turbulence. This will give more insight in the complex break-up mechanism as described by Van Jaarsveld (2008).

- Green (1995) reported that the inner region of the vortex becomes approximately axisymmetric within three chord lengths from the trailing edge of the wing. Future 3C-PIV measurement may be performed at multiple streamwise positions within this region. This will give more insight in the complex evolution of a jet-like to a wake-like structure in the inner region of the trailing vortex.

Nomenclature

f	frequency
i	integer
t	time, $t = 0$ corresponds to the trailing edge of the wing and the time increases with downstream distance
j, k	j^{th} grid point in y-direction and k^{th} grid point in z-direction as in the co-moving frame of reference, $j = 1..N_y$ and $k = 1..N_z$
j_s, k_s	j_s^{th} grid point in y-direction and k_s^{th} grid point in z-direction as in the stationary frame of reference, $j_s = 1..N_{s,y}$ and $k_s = 1..N_{s,z}$
x, y, z	streamwise, horizontal, and vertical coordinate in the frame moving with the vortex centre position, $x = 0$ corresponds to the position of the turbulence grid, the vortex centre is located at $y = z = 0$
r, θ, x	radial, azimuthal and axial or streamwise coordinate in the frame of reference co-moving with the vortex centre, $r = 0$ corresponds to the vortex centre

Experimental parameters

α	angle of attack of the wing ($\alpha = 7.5°$)
$\overline{U}_x$	main stream velocity ($\overline{U}_x = (15 \pm 0.5)$ m s^{-1})
$\triangle x$	streamwise distance of the measurement location from x_a
c	chord length of the wing ($c = 7.5 \cdot 10^{-2}$ m)
x_a	streamwise position of measurement location, is defined as the streamwise position of the wings' trailing edge from the position of the turbulence grid

Values of parameters used to make quantities dimensionless

$(\Gamma_{vor,0}/2\pi r_{1,0})^2$	$= 1.9 \cdot 10^2$ m^2 s^{-2}
$2\pi r_{1,0}^2/\Gamma_{vor,0}$	$= 4.2 \cdot 10^{-4}$ s
$\Gamma_{vor,0}$	$= 5.0 \cdot 10^{-1}$ m^2 s^{-1}
$\Gamma_{vor,0}/(2\pi r_{1,0}^2)$	$= 2.4 \cdot 10^3$ s^{-1}
$\Gamma_{vor,0}/2\pi r_{1,0}$	$= 1.4 \cdot 10^1$m s^{-1}
$r_{1,0}$	$= 5.8 \cdot 10^{-3}$ m

Nondimensional quantities

$Re_\lambda = \frac{u_{rms}\lambda}{\nu}$	Taylor Reynolds number based on root-mean-square turbulence velocity and Taylor microscale
$Re_f = \frac{\Gamma_w}{\nu}$	flight Reynolds number based on root circulation of the wing
$Re_{vor} = \frac{\Gamma_{vor}}{\nu}$	trailing vortex Reynolds number based on total circulation of the trailing vortex

Postprocessing parameters

$\mathrm{p}, \mathrm{P}, \mathcal{P}$	realization $\mathrm{p} \in \mathcal{P}$ and $\mathrm{p} = 1..\mathrm{P}$ with $\mathrm{P} = 1.000$
$\triangle r$	size of annular bins in which data is averaged
$\triangle r_{s,c}$	size of annular bins for determining a PDF for the vortex centre positions $r_{c,s}^{\mathrm{p}}$
PDF	probability distribution function
$r_{c,s}^{\mathrm{p}}$	centre of vortex for realization p in the vortex stationary frame of reference with $r_{c,s} = 0$ as the mean vortex cenrtre position in ensemble $\mathcal{P}$
$y_{c,s}^{\mathrm{p}}$,$z_{c,s}^{\mathrm{p}}$	y- and z-coordinate of the vortex centre for realization $\mathrm{p} \in \mathcal{P}$ in the vortex stationary frame of reference with $y_{c,s} = z_{c,s} = 0$ as the mean vortex cenrtre position in ensemble $\mathcal{P}$

Flow quantities

Γ	circulation
ν	kinematic viscosity
Ω	rotation rate of a vortex in solid-body rotation
ω	vorticity
ρ	density
$\triangle H$	viscous contribution to Bernoulli function, $\triangle H \geqq 0$
$\triangle p_{cont}$	pressure drop over contraction, the main stream velocity $\overline{U}_x$ is controlled by $\triangle p_{cont}$
ε	turbulence dissipation rate
E	energy density
p	pressure
p_∞	pressure far upstream from the wing where $\vec{U} = (0, 0, \overline{U}_x)$
q	kinetic energy of turbulence according to $q = \frac{1}{2}(u_{rms,x}^2 + u_{rms,y}^2 + u_z^2)$
s	swirl number $s = U_{\theta,max}/(U_{x,max} - \overline{U}_x)$
U	velocity

Sub- and superscripts

0	flow quantity at $t(\Gamma_{vor,0}/2\pi r_{1,0}^2) = 350.0$, used for making quantities dimensionless
A	CCD camera A
B	CCD camera B
vor	value related to the trailing vortex
w	value related to the wing
θ	θ-component of quantity
a	value at the streamwise location of the wings' trailing edge
max	maximum value of a quantity
r	r-component of quantity
rms	root-mean-square value of fluctuating quantity
x	x-component of quantity
y	y-component of quantity
z	z-component of quantity

Turbulence grid and wind tunnel parameters

σ	solidity of turbulence grid, $\sigma = 0.26$ m
L, W, H	length, width, height of TU/e Goliath wind tunnel test section, $L = 8.00$, $H = 1.05$, $W = 0.70$ m
M	mesh size of turbulence grid, $M = 2.54 \cdot 10^{-2}$ m

Vortex model parameters

β	two-length-scales VM2 fit parameter; $U_\theta = \Omega_{vor} r_1 (r/r_1)^{-\beta}$ approximated in the region $r_1 \lessapprox r \lessapprox r_2$, see Jacquin et al. (2001)
$\hat{r}_1$	two-length-scales VM1 fit parameter; solid-body rotation $U_\theta = \Omega_{vor} r$ in the region $0 < r \leqq r_1$, see Jacquin et al. (2001)
$\hat{r}_2$	two-length-scales VM1 fit parameter; $U_\theta = \Omega_{vor} r_1 (r/r_1)^{-\beta}$ in the region $r_1 < r \leqq r_2$, see Jacquin et al. (2001)
R	vortex core radius of Lamb-Oseen vortex model, $U_\theta(r) = \frac{\Gamma_{vor}}{2\pi r}\left(1 - \exp(-r^2/R^2)\right)$
r_1	two-length-scales VM2 fit parameter; solid-body rotation $U_\theta = \Omega_{vor} r$ approximated in the region $0 < r \lessapprox r_1$, see Jacquin et al. (2001), inner region of vortex is defined by $0 < r < r_1$
r_2	two-length-scales VM2 fit parameter; $U_\theta = \Omega_{vor} r_1 (r/r_1)^{-\beta}$ approximated in the region $r_1 \lessapprox r \lessapprox r_2$, see Jacquin et al. (2001), outer region of vortex is defined by $r_1 < r < r_2$

Appendix A

Numerical Simulation of a Vortex with Net Vorticity

The study as described in this appendix considers the influence of periodic boundary conditions on the numerical simulation of a vortex with net vorticity, of which the trailing vortex is an example of this. A detailed description of the Direct Numerical Simulation code can be found in Kuczaj and Geurts (2006).

Pradeep and Hussain (2004) discussed the influence of boundary conditions in numerical simulations of vortices with net vorticity in turbulence. The effect of periodic boundary conditions are found to be twofold.

First, the flow field related to the infinite array of periodic images exerts a strain field on the flow within the computational domain. This strain field realigns and intensifies the turbulence vortex filaments into vortexlets surrounding the main vortex. These vortexlets have a vorticity with a sign that is opposite to that of the main vortex. There are two effect of these vortexlets on the main vortex that have to be considered. The vortexlets can induce strong bending waves on the main vortex, and they peel away vorticity from the main vortex.

Second, the periodicity implies that the net circulation contained within the domain must be precisely zero. Consequently, an isolated vortex is rendered centrifugally unstable by the Rayleigh criterion, see Rayleigh (1880).

This study is organized as follows. We will first specify the circulation profiles of the vortices that will be simulated. We define three variations of the vortex core size relative to the computational flow domain, and two vortex Reynolds numbers. This means that we have six vortex configurations in total. In the subsequent sections, the influence of the periodic boundary conditions on all six vortex configurations with and without a turbulent background is analyzed. It will become clear that a vortex with net vorticity can only be simulated, with periodic boundary conditions, under certain conditions.

A.1 Initialization of vortex parameters

We will analyse the effect of the periodic boundary conditions on vortices with net vorticity. These vortices are described by the two-length-scales Vortex Model 2 of Jacquin (VM2), see Fabre and Jacquin (2004). The azimuthal velocity profile is given by

$$U_\theta(r) = \frac{\Omega_{vor} r}{[1 + (r/r_1)^4]^{(1+\beta)/4}[1 + (r/r_2)^4]^{(1-\beta)/4}}, \tag{A.1}$$

in which $r_2 > r_1$. The radius r_1 characterizes the inner region of the vortex rotating with angular frequency Ω_{vor}, and the radius r_2 characterizes the outer region of the vortex in which 97% of the total circulation $\Gamma_{vor} = 2\pi\Omega_{vor} r_1^2 \frac{r_2}{r_1}^{1-\beta}$ is contained. The angular velocity decays according to $U_\theta(r) \sim r^{-\beta}$ in the region $r_1 \lessapprox r \lessapprox r_2$, and according to $U_\theta(r) \sim r^{-1}$ for $r \gtrapprox r_2$. The circulation profile of the VM2 is specified by:

$$\Gamma(r) = \Gamma_{vor} \frac{(r/r_1)^2}{\frac{r_2}{r_1}^{1-\beta} \cdot [1 + (r/r_1)^4]^{\frac{1+\beta}{4}} \cdot [1 + (r/r_1)^4]^{\frac{1-\beta}{4}}}. \tag{A.2}$$

Batchelor (1964) considered the axial velocity component of a trailing vortex. The link between the azimuthal and axial components of motion in a steady line vortex is provided by the pressure; the radial pressure gradient balances the centrifugal force. Batchelor (1964) derived that the axial velocity in the vortex core is given by

$$U_{x,vor}^2(r) = \overline{U_x^2} - U_\theta^2(r) + 2\int_r^\infty \frac{U_\theta^2(r)}{r} dr, \tag{A.3}$$

with $\overline{U}_x$ the x-component of the main stream velocity at infinity in which we assumed $\overline{U}_x = \sqrt{\overline{U_x^2}}$. It has to be remarked that Batchelor (1964) applied the Bernoulli theorem in which no loss of total pressure is assumed. In combination with Eq. A.1, one is able to derive the axial velocity profile. Since no analytical solution of the axial velocity profile is available, we determine the axial velocity profile by numerical integration

$$U_{x,vor}^2(r) = \overline{U_x^2} - U_\theta^2(r) + \sum_{i=0}^{N=5000} \frac{U_\theta^2(r + i \cdot \triangle r')}{r + i \cdot \triangle r'} \cdot \triangle r'; \qquad \triangle r' = \frac{1}{50} r_1, \tag{A.4}$$

in which we assume that $r + 7500 \cdot \triangle r'$ is approaching infinity. This means that the maximum radius over which integration takes place for $r = 0$ equals $150 \cdot r_1 = 15 \cdot r_2$ when $r_{2,0}/r_{1,0} = 10$, see Van Jaarsveld (2008) and Fabre and Jacquin (2004).

The vortex Reynolds number is defined by $Re_{\Gamma_{vor,0}} = \Gamma_{vor}/\nu$, and varies in the experimental work of Van Jaarsveld (2008) between $16 \cdot 10^3$ and $48 \cdot 10^3$. In this study, we analyse vortices with $Re_{\Gamma_{vor,0}} = 30 \cdot 10^3$ and $7.5 \cdot 10^3$. Van Jaarsveld (2008) found that the VM2 parameter β is typically 0.8. It is experimentally found that $r_2/r_1 = 10$, see for example Van Jaarsveld (2008) and Fabre and Jacquin (2004). With $\beta = 0.8$ and $r_2/r_1 = 10$, the fixed vortex Reynolds number can be obtained by several combinations of $\Gamma_{vor,0}$ and $r_{2,0}(r_{1,0})$. With the sides of computational domain equal to $L_{box} = 1$, we define for each vortex Reynolds number three cases defined by $r_{1,0}/L_{box} = 0.020$, 0.027 and 0.040, see Figure A.1.

The simulations are performed with a numerical resolution $N^3 = 256^3$. This means that the vortex inner region with radii $r_{1,0}/L_{box} = 0.02, 0.027$, and 0.04 is resolved by $256 \cdot r_{1,0}/L_{box} = 5, 7$, and 10 grid points, respectively. One may ask whether if it is sufficient to resolve the vortex core by only five grid points. To test this, we analyse the Lamb-Oseen vortex

$$U_\theta(r) = \frac{\Gamma_{vor}}{2\pi} \frac{1 - \exp(-r^2/R^2)}{r}, \tag{A.5}$$

with core radius R initially resolved by five grid points. The analytical solution of the Lamb-Oseen vortex tells us that the vortex core radius evolves according to $R^2(t) = R_0^2 + 4\nu t$. This relation can be retrieved in Figure A.2b, which shows the evolution of the core radius R for a Lamb-Oseen vortex with $Re_{\Gamma_{vor,0}} = 30 \cdot 10^3$. Apparently, it is sufficient to resolve the Lamb-Oseen vortex core R by five grid points. Herewith, we assume that the axial velocity profile is sufficiently resolved as well. This is acceptable since the vorticity corresponding to the axial velocity profile is approximately a order lower than that of the main vortex.

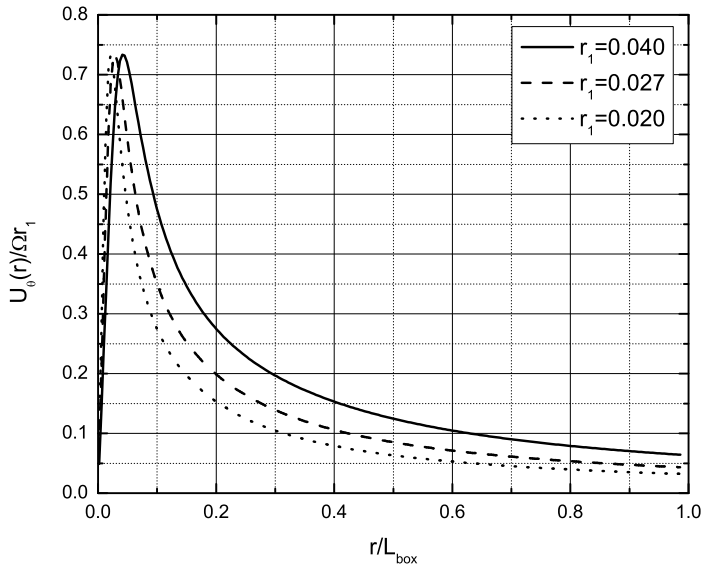

(a) azimuthal velocity profile

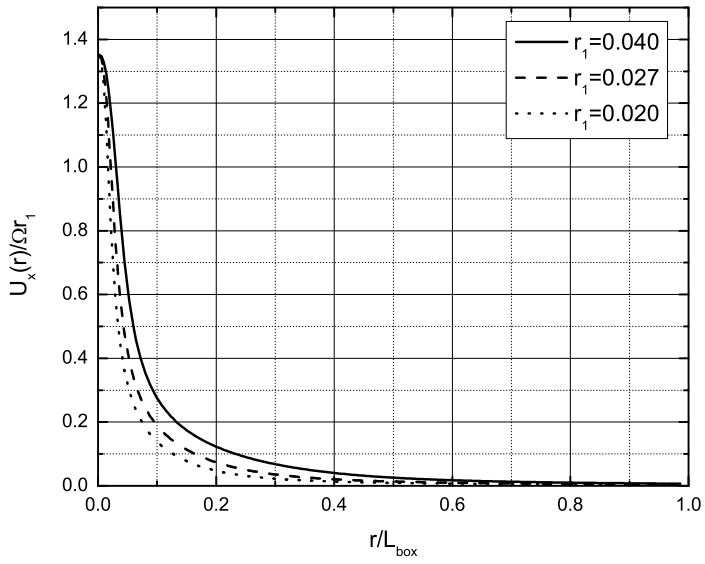

(b) axial velocity profile

Figure A.1: The azimuthal and axial velocity of the VM2 profile. The axial velocity profile is determined by Eq. A.4, in which we set $\overline{U_x^2} = 0$. The inner vortex radius $r_{1,0}/L_{box}$ is set to 0.020, 0.027 and 0.040.

It is sufficient to resolve the core R of a Lamb-Oseen vortex with five grid points only. We will now compare the vorticity distribution of a VM2 vortex at c of which the core $r_{1,0}$ is resolved with ten ($r_{1,0}/L_{box} = 0.04$), seven ($r_{1,0}/L_{box} = 0.027$), and five ($r_{1,0}/L_{box} = 0.02$) grid points. The

evolution of vortex core against the radius nondimensionalized with $r_{1,0}$ is shown in Figure A.3. From this, one can see that the evolution of the inner vortex region with initial radius $r_{1,0}$ resolved with ten ($r_{1,0}/L_{box} = 0.04$) grid points, matches that with seven ($r_{1,0}/L_{box} = 0.027$) and five ($r_{1,0}/L_{box} = 0.02$) grid points. This supports our earlier analysis of a Lamb-Oseen vortex, that it is sufficient to resolve the vortex inner radius $r_{1,0}$ with five grid points only.

A.1.1 Relevant time domain

In the experimental work of Van Jaarsveld (2008), the evolution of the vortex is analyzed only in a limited time domain. This time is determined by the length of the wind tunnel and the main stream velocity. We apply a nondimensional time scale to define the same time domain in the numerical and experimental work. The advection time scale is defined by $2\pi r_1^2/\Gamma_{vor}$, and the diffusion time scale by r_1^2/ν. We will determine these time scales for a trailing vortex that is sufficiently far away from the wing such that remains of the roll-up process can be neglected. With the wing located at $x_a = 1.5$ m, the parameters for a vortex at $\triangle x = 2.25$ m are $t = (L - x_a - \triangle x)/U_a \approx 5/15 \approx 0.3$ s ($L = 8.0$ m), $r_1 \approx 10 \cdot 10^{-3}$ m, $\Gamma_{vor} \approx 0.45$ m^{2}s^{-1}, and $\nu = 1.5 \cdot 10^{-5}$. With these parameters we find a nondimensional advection time domain of $0 < t\Gamma_{vor,0}/(2\pi r_{1,0}^2) \lessapprox 215$ and a nondimensional diffusion time domain of $tnu/r_1^2 \lessapprox 0.15$. This shows the relative importance of advection against diffusion, and therefore we require that the nondimensional advection time domain is the same for the experimental and numerical work. This study addresses the influence of the boundary conditions in the time domain $0 < t\Gamma_{vor,0}/(2\pi r_{1,0}^2) < 225$.

A.1.2 Postprocessing of data

The vortex is analyzed by the evolution of the axial vorticity and the circulation profile. The vorticity field is obtained directly from the numerical code that solves the flow field in spectral space. The circulation profile is obtained by integrating the vorticity field in the same way as discussed in Appendix F. Since the initial vortex centre is located at $y, z = 0.5L_{box}$, we set the maximum radius at which the circulation profile is determined to 0.5 L_{box}.

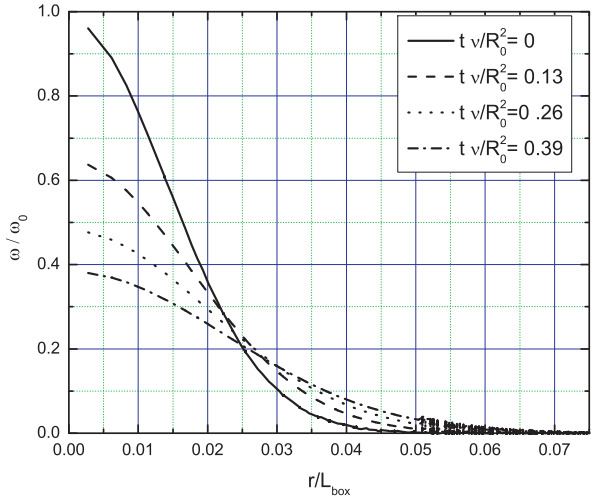

(a) vorticity profile

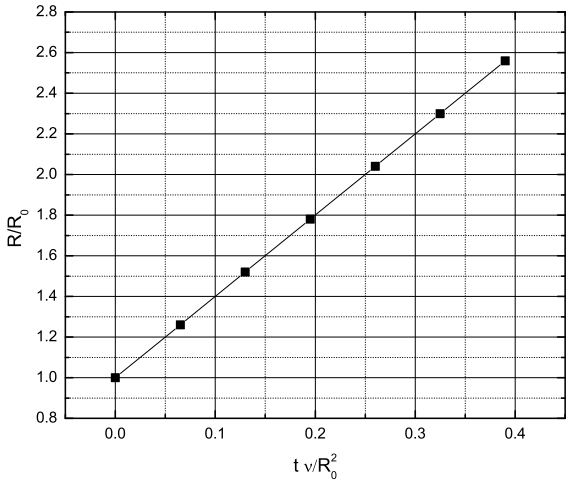

(b) vortex core radius

Figure A.2: Evolution of the vorticity profile and vortex core radius for a Lamb-Oseen vortex which core $R_0/L_{box} = 0.02$ is initially resolved by five grid points. The analytical relation for the evolution of the vortex core R is given by $R(t)^2 = R_0 + 4\nu t$, and can be retrieved in panel b.

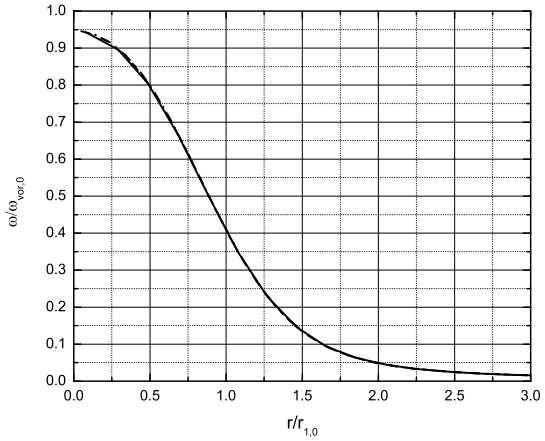

(a) vorticity distribution

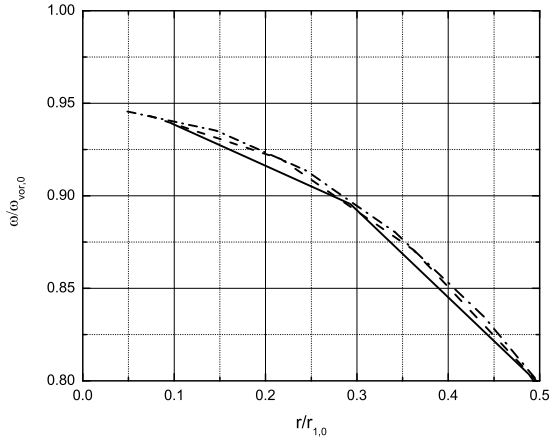

(b) close-up of panel *a*

Figure A.3: Snapshot of the axial vorticity distribution at $t\Gamma_{vor,0}/(2\pi r_{1,0}^2) = 225(tnu/r_1^2 = 0.15)$ *for* $Re_{\Gamma_{vor,0}} = 30 \cdot 10^3$ *and* $r_{1,0}/L_{box} = 0.02$ (———)*,* $r_{1,0}/L_{box} = 0.027$ (- - - -)*, and* $r_{1,0}/L_{box} = 0.04$ (-·-·-)*. The vortex core with initial size* $r_{1,0}$ *is resolved by five, seven, and ten grid points, respectively. The vorticity distributions match each other, which indicates that it is sufficient to resolve the vortex core* $r_{1,0}$ *with five grid points only.*

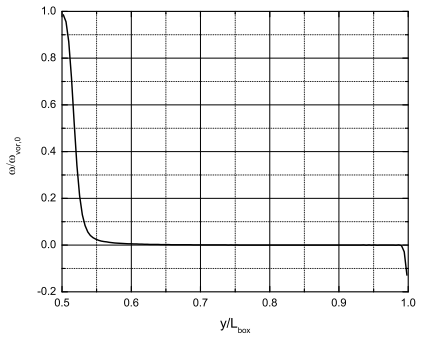

(a) $t\Gamma_{vor,0}/(2\pi r_{1,0}^2) = 20$

Figure A.4: Vorticity distribution for the case $Re_{\Gamma_{vor,0}} = 7.5 \cdot 10^3$, $r_{1,0}/L_{box} = 0.02$ for $t\Gamma_{vor,0}/(2\pi r_{1,0}^2) = 20$. The periodic boundary conditions requires net zero circulation, this is achieved by a vorticity concentration near the boundary, that is at $y/L_{box} = 1$, with a sign opposite to that of the main vortex. The centre of the main vortex is located at $y/L_{box} = 0.5$.

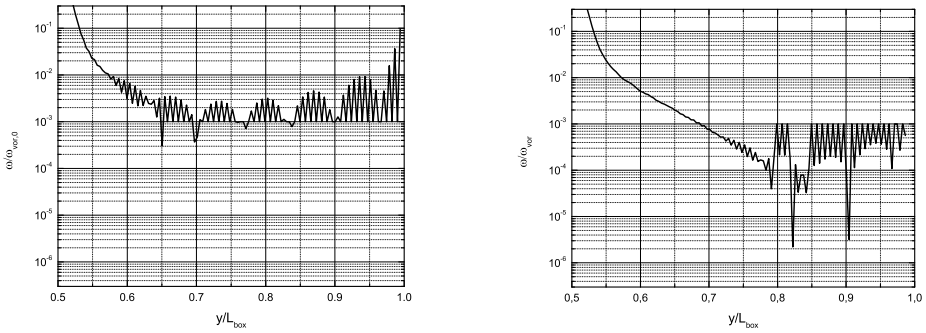

(a) $t\Gamma_{vor,0}/(2\pi r_{1,0}^2) = 0$

(b) $t\Gamma_{vor,0}/(2\pi r_{1,0}^2) = 20$

Figure A.5: Vorticity distribution for the case $Re_{\Gamma_{vor,0}} = 7.5 \cdot 10^3$, $r_{1,0}/L_{box} = 0.02$ for the initial condition $t\Gamma_{vor,0}/(2\pi r_{1,0}^2) = 0$ and $t\Gamma_{vor,0}/(2\pi r_{1,0}^2) = 20$, as is shown in Figure A.4 with linear axes. Initially, the boundary vorticity distribution shows a non-smooth pattern. At $t\Gamma_{vor,0}/(2\pi r_{1,0}^2) = 20$, this pattern has evolved into a smoother profile.

A.2 Vortex without turbulence

The evolution of the circulation and vorticity profiles of the vortices with $Re_{\Gamma_{vor,0}} = 7.5 \cdot 10^3$ and $30 \cdot 10^3$ with initial inner core radius $r_{1,0}/L_{box} = 0.02, 0.027$, and 0.04 are shown in Figures A.6 and A.7, respectively. Here, the vorticity is shown against the radius that is made dimensionless with the box size L_{box}.

The circulation profile goes to a constant value for the circulation for large radii since the main vortex is nonisolated. However, the net circulation of the whole flow domain is zero, as required by the periodic boundary conditions. Note that in Figures A.6 and A.7, we only show the circulation for $r/L_{box} \leqq 0.5$, which is only part of the flow domain. The net circulation is brought

to zero by a concentration of vorticity near the boundaries, with a sign opposite to that of the main vortex. The vorticity concentrated near the boundary can be seen in Figure A.4 which is a profile of the axial vorticity in y-direction. It has to be remarked, that this vorticity concentration near the boundaries is numerically created, and not prescribed: it is a product of the periodic boundary conditions. Initially, the boundary vorticity distribution shows a non-smooth pattern, see A.5. This patterns continues even after $r_{2,0}$ more inwards. However, the amplitude is here $\mathcal{O}(10^{-2})$ which is believed to be negligibly small. After $t\Gamma_{vor,0}/(2\pi r_{1,0}^2) = 20$, the non-smooth pattern has evolved into a smoother profile.

The opposite-signed vorticity concentrations that wrap around the main vortex in ring-like structures are called vortexlets. The vortexlets can induce strong bending waves on the main vortex, and it can merge with the main vortex such that vorticity gets dissipated. Moreover, since the net circulation needs to be zero, centrifugal instability can be initiated. Neither strong bending waves, nor centrifugal instabilities are found to occur in all the analyzed cases. Note that this asymmetric behaviour may occur when the flow is initially perturbed. We therefore analyse the same cases with turbulence in Section A.3.

The evolution of the vorticity distribution in a yz-plane is given for $Re_{\Gamma_{vor,0}} = 7.5 \cdot 10^3$ and $r_{1,0}/L_{box} = 0.02$, and $Re_{\Gamma_{vor,0}} = 30 \cdot 10^3$ and $r_{1,0}/L_{box} = 0.04$ in Figures A.9, and A.10, respectively. Here, one clearly sees that for $Re_{\Gamma_{vor,0}} = 7.5 \cdot 10^3$ and $r_1 = 0.02$, the vortexlets consists of four bands of strong vorticity moving inwards in time. For $Re_{\Gamma_{vor,0}} = 30 \cdot 10^3$ and $r_1 = 0.04$, the vortexlets spread out more quickly and are more equally distributed over a larger region surrounding the main vortex. The vortexlets spread inwards in time primarily due to advection by the main vortex flow field.

The vortexlets affect the circulation profile of the main vortex, as can be seen in Figures A.6 and A.7. The circulation profile diverts from the constant value Γ_{vor} at large radii. The radius at which the circulation starts to decrease, that is the radius at which $d\Gamma_{vor}(r)/dr = 0$, decreases in time $t\Gamma_{vor,0}/(2\pi r_{1,0}^2)$ and is dependent on the initial vortex inner radius $r_{1,0}/L_{box}$, but is virtually independent on the Reynolds number $Re_{\Gamma_{vor,0}}$. For both $Re_{\Gamma_{vor,0}} = 7.5 \cdot 10^3$ and $30 \cdot 10^3$ and at a fixed time $t\Gamma_{vor,0}/(2\pi r_{1,0}^2)$, the circulation profile starts to decrease at a radius that decreases with increasing initial vortex inner radius $r_{1,0}/L_{box}$. At $t\Gamma_{vor,0}/(2\pi r_{1,0}^2) = 225$, the circulation profiles corresponding to the main vortices with $r_{1,0}/L_{box} = 0.02, 0.027$, and 0.04 start to decrease at $r/L_{box} = 0.46, 0.42$, and 0.35, respectively. Note that the outer radius of the vortex equals $r_{2,0}/L_{box} = 10 r_{1,0}/L_{box}$ in our definition. The vortices with $r_{2,0}/L_{box} = 0.2$ and $r_{2,0}/L_{box} = 0.27$ evolve most isolated from the vortexlets, when it is assumed that the outer radius stays approximately constant during the simulation $r_2(t) \approx r_{2,0}$ (note that $t\nu/r_{2,0} \ll 1$). In this case, there is the largest distance between the initial vortex core outer radius $r_{2,0}$ and the point that the circulation starts to decrease $d\Gamma_{vor}(r)/dr = 0$. The vortex with $r_{2,0}/L_{box} = 0.4$ cannot evolve isolated from the vortexlet since the vortex outer core radius $r_{2,0}$ is larger than the radius at which the circulation starts to decrease $d\Gamma_{vor}(r)/dr = 0$.

We also numerically simulated the case $r_{1,0}/L_{box} = 0.02$, $Re_{\Gamma_{vor,0}} = 7.5 \cdot 10^3$ with a resolution of $N^3 = 384^3$. The simulations with $N^3 = 256^3$ and $N^3 = 384^3$ give a better insight in the effect of the resolution on the periodic boundary effects. Therefore we reproduced Figures A.6a,b for the case with a numerical resolution $N^3 = 384^3$, see Figure A.8. Apparently, increasing the resolution from $N^3 = 256^3$ to 384^3 does not significantly influence the evolution of the circulation profile near the boundaries.

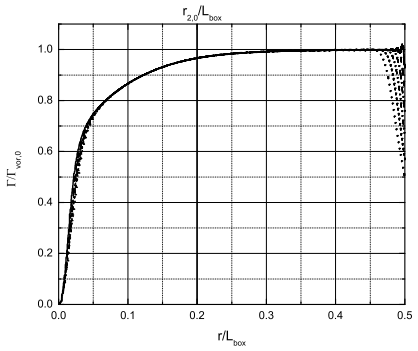

(a) circulation profile, $r_{1,0}/L_{box} = 0.02$

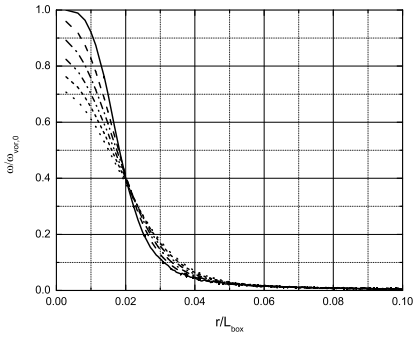

(b) vorticity profile, $r_{1,0}/L_{box} = 0.02$

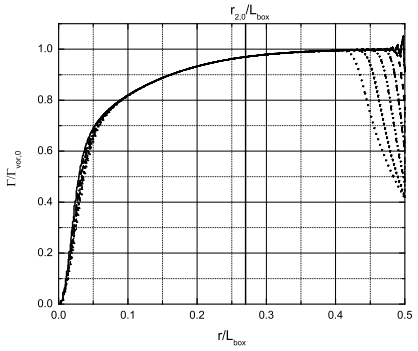

(c) circulation profile, $r_{1,0}/L_{box} = 0.027$

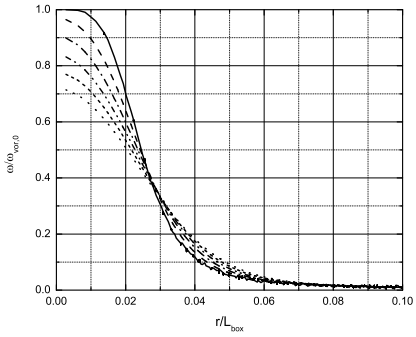

(d) vorticity profile, $r_{1,0}/L_{box} = 0.027$

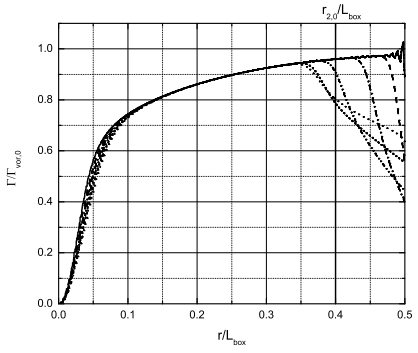

(e) circulation profile, $r_{1,0}/L_{box} = 0.04$

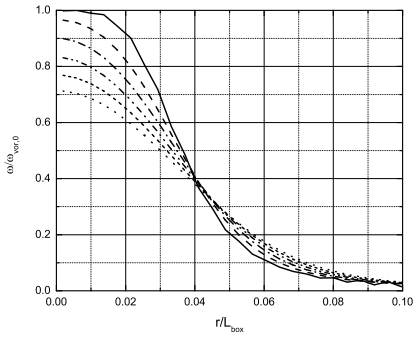

(f) vorticity profile, $r_{1,0}/L_{box} = 0.04$

Figure A.6: Evolution of the circulation and axial vorticity profile for the vortices with $Re_{\Gamma_{vor,0}} = 7.5 \cdot 10^3$*. The smallest radius at which the circulation starts to decrease due to the effects of the periodic boundary conditions is for* $r_{1,0}/L_{box} = 0.04$ *at* $r/L_{box} \approx 0.34$*, see panel e.* $t\Gamma_{vor,0}/(2\pi r_{1,0}^2) =$ 0——— ; 45– – – – ; 90–·–· ; 135–··–·· ; 180- - - - ; 225····· .

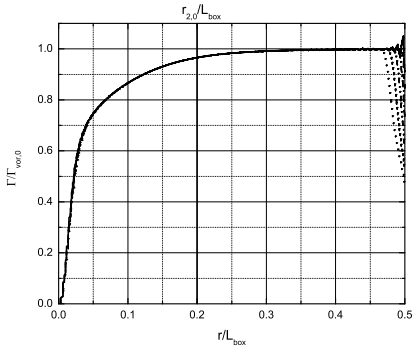

(a) circulation profile, $r_{1,0}/L_{box} = 0.02$

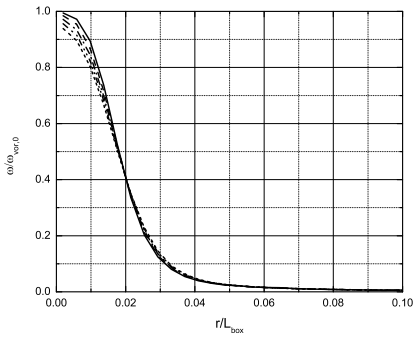

(b) vorticity profile, $r_{1,0}/L_{box} = 0.02$

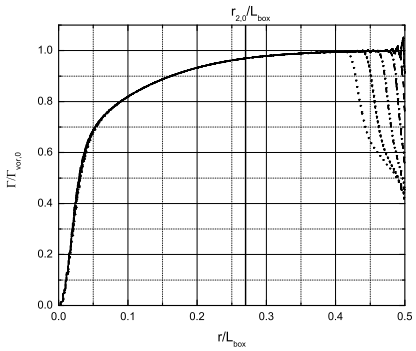

(c) circulation profile, $r_{1,0}/L_{box} = 0.027$

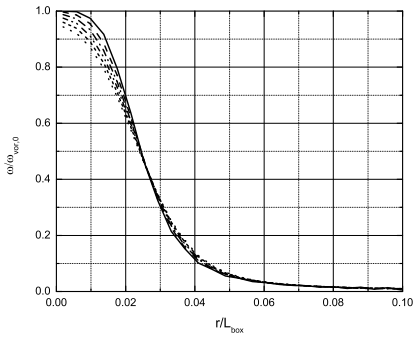

(d) vorticity profile, $r_{1,0}/L_{box} = 0.027$

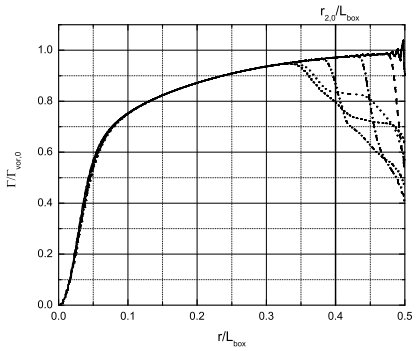

(e) circulation profile, $r_{1,0}/L_{box} = 0.04$

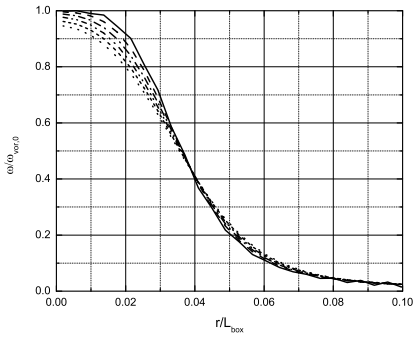

(f) vorticity profile, $r_{1,0}/L_{box} = 0.04$

Figure A.7: Evolution of the circulation and axial vorticity profile for the vortices with $Re_{\Gamma_{vor,0}} = 30 \cdot 10^3$. *The smallest radius at which the circulation starts to decrease due to the effects of the periodic boundary conditions is for* $r_{1,0}/L_{box} = 0.04$ *at* $r/L_{box} \approx 0.32$, *see panel e.* $t\Gamma_{vor,0}/(2\pi r_{1,0}^2) = 0$——— ; 45– – – – ; 90–·–·– ; 135–··–··– ; 180– – – – ; 225····· .

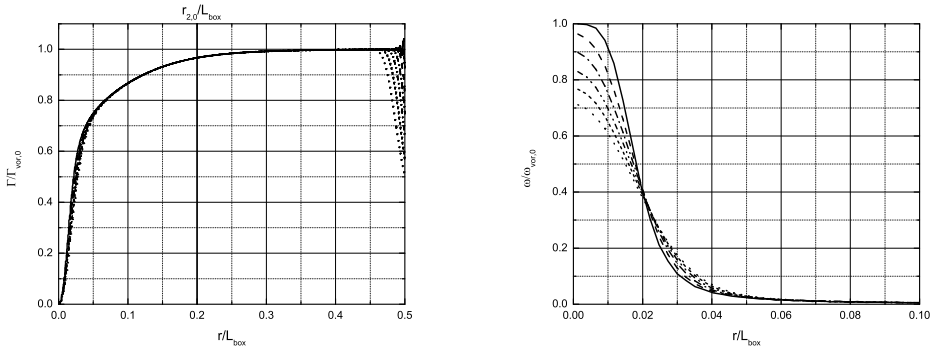

(a) circulation profile, $r_{1,0}/L_{box} = 0.02$

(b) vorticity profile, $r_{1,0}/L_{box} = 0.02$

Figure A.8: Evolution of the circulation and axial vorticity profile for the vortex with $Re_{\Gamma_{vor,0}} = 7.5 \cdot 10^3$, $r_{1,0}/L_{box} = 0.02$, *and with a numerical resolution of* $N^3 = 384^3$. *A close match was found between these profiles and those in Figure A.6. This means that that increasing the numerical resolution from* $N^3 = 256^3$ *to* 384^3 *does not significantly influence the extent in which a vortex specified by* $r_1, Re_{\Gamma_{vor,0}}$, *can evolve isolated from the periodic boundary effects.* $t\Gamma_{vor,0}/(2\pi r_{1,0}^2) = 0$——— ; 45– – – – ; 90–·–· ; 135–··–·· ; 180- - - - ; 225····· .

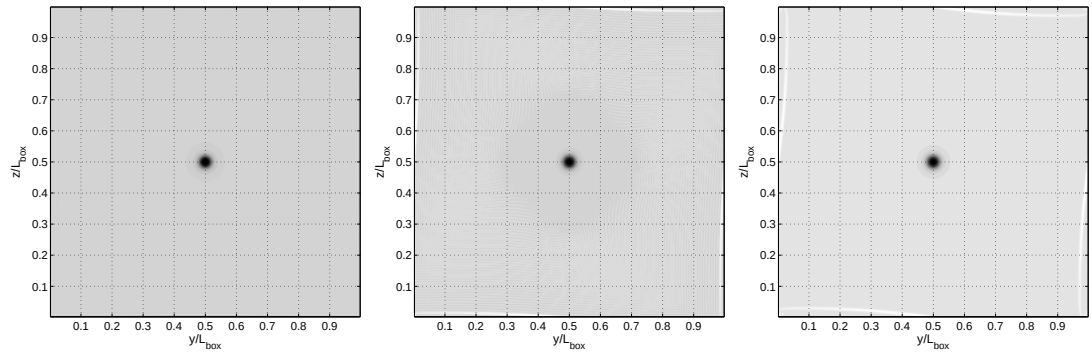

(a) $t\Gamma_{vor,0}/(2\pi r_{1,0}^2) = 0$ (b) $t\Gamma_{vor,0}/(2\pi r_{1,0}^2) = 45$ (c) $t\Gamma_{vor,0}/(2\pi r_{1,0}^2) = 90$

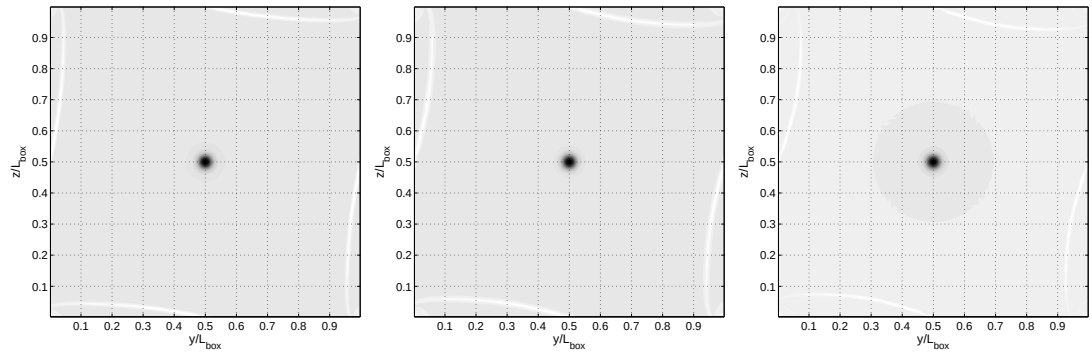

(d) $t\Gamma_{vor,0}/(2\pi r_{1,0}^2) = 135$ (e) $t\Gamma_{vor,0}/(2\pi r_{1,0}^2) = 180$ (f) $t\Gamma_{vor,0}/(2\pi r_{1,0}^2) = 225$

Figure A.9: Evolution of the axial vorticity for the vortex with $Re_{\Gamma_{vor,0}} = 7.5 \cdot 10^3$ and $r_{1,0}/L_{box} = 0.02$, which is rotating counterclockwise. The vortexlets are concentrated in four band near the boundaries. The vortexlets get primarily advected from the boundaries, but stay concentrated in the region $r \gtrapprox 2r_{2,0}$. One can consider this case ($r_{1,0}/L_{box} = 0.02$) as the case in which the vortex can evolve most isolated from the effects of the periodic boundaries. The vortex outer core radius $r_2(t) \approx r_{2,0}$ is smaller than the radius at which vortexlets are present. The color scale varies for the different panels.

A.2.1 Conclusion and discussion

We may conclude the following:

- It is sufficient to resolve the VM2 vortex inner radius $r_{1,0}$ with only five grid points;
- The vortex with net vorticity in a periodic domain, results in a opposite-signed vorticity concentration near the boundaries that are called vortexlets. Initially, the boundary vorticity distribution shows a non-smooth pattern. This patterns continues even after $r_{2,0}$ more inwards. However, the amplitude is $\mathcal{O}(10^{-2})$ which is believed to be negligibly small. The non-smooth pattern has evolved into a smoother profile after typically $t\nu/r_{1,0}^2 = 1.50 \cdot 10^{-2}$.
- Vortexlets are observed near the periodic boundaries. These vortexlets move inward, and affect the circulation profile of the main vortex. The radius at which the circulation profile starts to decrease (the radius at which $d\Gamma_{vor}(r)/dr = 0$) from depends on the time $t\Gamma_{vor,0}/(2\pi r_{1,0}^2)$, and the size of the vortex $r_{1,0}/L_{box}$, but not on the vortex Reynolds number $Re_{\Gamma_{vor,0}}$ and is not significantly dependent on the numerical resolution $N^3 = 256^3$ or 384^3.
- Although the vortexlets are observed, neither strong bending waves, nor centrifugal instability is found to occur.

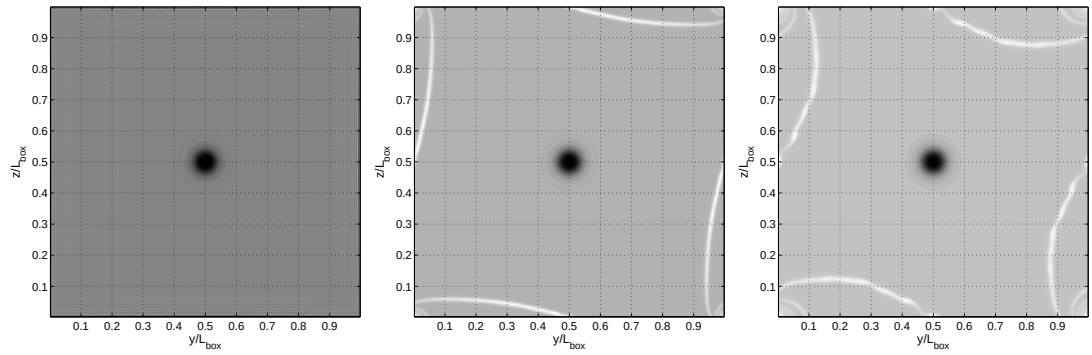

(a) $t\Gamma_{vor,0}/(2\pi r_{1,0}^2) = 0$ (b) $t\Gamma_{vor,0}/(2\pi r_{1,0}^2) = 45$ (c) $t\Gamma_{vor,0}/(2\pi r_{1,0}^2) = 90$

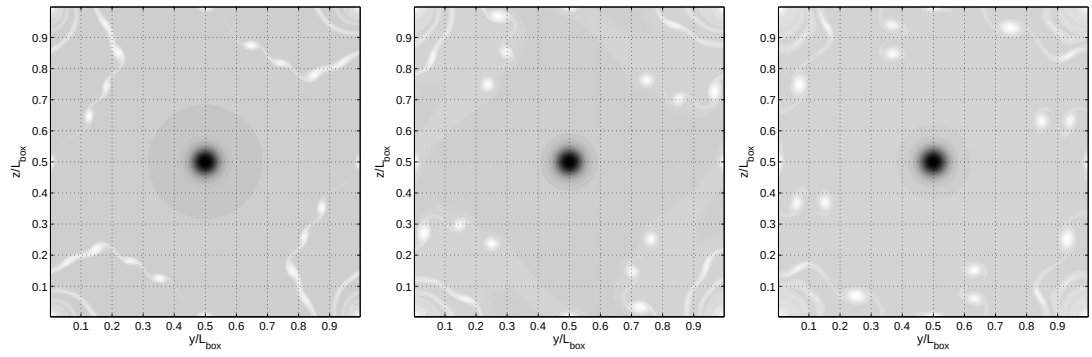

(d) $t\Gamma_{vor,0}/(2\pi r_{1,0}^2) = 135$ (e) $t\Gamma_{vor,0}/(2\pi r_{1,0}^2) = 180$ (f) $t\Gamma_{vor,0}/(2\pi r_{1,0}^2) = 225$

Figure A.10: Evolution of the axial vorticity for the vortex with $Re_{\Gamma_{vor,0}} = 30 \cdot 10^3$ and $r_{1,0}/L_{box} = 0.04$, which is rotating counterclockwise. The vortexlets get primarily advected from the boundaries, but stay concentrated in the region $r \gtrapprox 0.8 r_{2,0}$. One can consider this case ($r_{1,0}/L_{box} = 0.04$) as the case in which the vortex can evolve least isolated from the effects of the periodic boundaries. The vortex outer core radius $r_2(t) \approx r_{2,0}$ is larger than the radius at which vortexlets are present. The color scale varies for the different panels.

- The vortex with $r_{1,0}/L_{box} = 0.02$ is found to be most isolated from the vortexlets in the time domain of $0 < t\Gamma_{vor,0}/(2\pi r_{1,0}^2) < 225$. In other words, there is the largest distance between the initial vortex core outer radius $r_{2,0}$ and the point that the circulation starts to decrease $d\Gamma_{vor}(r)/dr = 0$.

These conclusions may be different for the cases in which the flow field is perturbed with turbulence. This will be analyzed in the next section.

A.3 Vortex with turbulence

Turbulence can change the evolution of the main vortex and the vortexlets. This means that the influence of periodic boundary effects on a vortex with net vorticity can be different from those described in the section above. The case with $Re_{\Gamma_{vor,0}} = 7.5 \cdot 10^3$, $r_{1,0}/L_{box} = 0.02$ and $Re_{\Gamma_{vor,0}} = 30 \cdot 10^3$, $r_{1,0}/L_{box} = 0.02$ were found to be most isolated from the vortexlets in the time domain of $0 < t\Gamma_{vor,0}/(2\pi r_{1,0}^2) < 225$. This means that we should now consider these vortices together with a turbulent background. However, the turbulence field that will to be superimposed on the vortex with $Re_{\Gamma_{vor,0}} = 30 \cdot 10^3$ cannot be resolved by the numerical grid with resolution $N^3 = 384^3$ (this will be elucidated later). Therefore, we will proceed with only considering $Re_{\Gamma_{vor,0}} = 7.5 \cdot 10^3$, $r_{1,0}/L_{box} = 0.02$.

The turbulence that will be added to the flow field of a VM2 vortex defined by $Re_{\Gamma_{vor,0}} = 7.5 \cdot 10^3$, $r_{1,0}/L_{box} = 0.02$, is based on the model spectrum discussed in Pope (2000)

$$E(\kappa) = C\varepsilon^{2/3}\kappa^{-5/3} f_L(\kappa L) f_\eta(\kappa\eta), \tag{A.6}$$

where $f_L(\kappa L)$ and $f_\eta(\kappa\eta)$ are specified non-dimensional functions. The function $f_L(\kappa L)$ determines the shape of the energy-containing range, and tends to unity for large κL. Similarly, $f_\eta(\kappa\eta)$ determines the shape of the dissipation range, and it tends to unity for small $\kappa\eta$. In the inertial subrange both $f_L(\kappa L)$ and $f_\eta(\kappa\eta)$ are essentially unity, so the Kolmogorov spectrum with $\kappa^{-5/3}$ is recovered. The function $f_L(\kappa L)$ is defined by

$$f_L(\kappa L) = \big(\frac{\kappa L}{\sqrt{(\kappa L)^2 + c_L^2}}\big)^{11/3}. \tag{A.7}$$

Clearly $f_L(\kappa L)$ tends to unity for large κL, while the exponent $11/3$ leads to $E(\kappa)$ varying as κ^2 for small κL. The function $f_\eta(\kappa\eta)$ is defined by:

$$f_\eta(\kappa\eta) = \exp -\gamma[((\kappa\eta)^4 + c_\eta^4)^{1/4} - c_\eta]. \tag{A.8}$$

This indicates that the energy-spectrum function decays exponentially for large wavenumbers κ.

The model energy spectrum contains four parameters: the constant C; the exponent γ and constant c_L, both important in the large lengths scales; and a constant c_η important in the the small length scales. The results of experimental and numerical work established that $C = 1.5$ and $\gamma = 5.2$, see for example Saddoughi and Veeravalli (1994). The results of our turbulence experiments suggest that these values are correct. With $C = 1.5$ and $\gamma = 5.2$, we are left with the values of c_η and c_L. These values are indirectly determined by specifying values for the turbulence dissipation rate ε and the integral scale $L(\equiv E_{tot}^{3/2}/\varepsilon)$ since:

$$\varepsilon = \int_0^\infty 2\nu\kappa^2 E(\kappa) d\kappa, \tag{A.9}$$

$$L(\equiv E_{tot}^{3/2}/\varepsilon) = \big[\int_0^\infty E(\kappa) d\kappa\big]^{3/2} / \int_0^\infty 2\nu\kappa^2 E(\kappa) d\kappa. \tag{A.10}$$

We determine the values of c_η and c_L from the turbulence dissipation rate and the integral scale, since we believe that ε and L are the important parameters in the study on turbulence-vortex interaction. The turbulence dissipation rate is found to be important in turbulence and trailing vortices interaction, see for example Van Jaarsveld (2008), while the integral scale represents the scale of the most energetic eddies that interact with the trailing vortex.

It is now still a matter of defining the turbulence dissipation rate and the integral scale. For this, we will apply nondimensional values to relate experimental value with those in the numerical simulations. The nondimensional turbulence dissipation rate for the interaction between turbulence and a single vortex interaction is taken as:

$$\varepsilon^*_{r_{1,0}} \equiv 2\pi \frac{\varepsilon_0^{1/3} r_{1,0}^{4/3}}{\Gamma_{vor,0}}. \tag{A.11}$$

The nondimensional integral length scale $L^*_{r_{1,0}}$ is defined to be:

$$L^*_{r_{1,0}} = \frac{L}{r_{1,0}}. \tag{A.12}$$

The turbulence generated with the $M254$ grid and the vortex generated with the same wing as used by Van Jaarsveld (2008), will result in $\varepsilon^*_{r_{1,0}} = 1.3 \cdot 10^{-2}$, since $\varepsilon = 0.067$ m^{2}s^{-3}, $r_1 = 0.01$ m,

and $\Gamma_{vor} = 0.45$ m^{2}s^{-1}. The same parameters for the $M127$ grid are given by $\varepsilon^*_{r_{1,0}} = 0.9 \cdot 10^{-2}$, since $\varepsilon = 0.032$ m^{2}s^{-3}, $r_1 = 0.01$ m, and $\Gamma_{vor} = 0.45$ m^{2}s^{-1}. The nondimensional integral length scale $L^* = \frac{(\frac{3}{2}u^2_{rms})^{3/2}}{r_{1,0}\varepsilon_0}$ equals 3.5 and 3.2 for the $M254$ and $M127$ grid respectively. These values are based on the turbulence characteristics measured at the position $x/L = x_a/L = 0.44$ and $y, z = 0$, see Chapter C.

It is not possible to perform direct numerical simulations of the turbulence flow field that corresponds to the vortex with $Re_{\Gamma_{vor,0}} = 30 \cdot 10^3$, $r_{1,0}/L_{box} = 0.02$. The nondimensional turbulence dissipation rate goes with the third power of the circulation, see Eq. A.11. When the vortex Reynolds number increases with a factor 4, the dissipation rate increases with a factor 64 (in case that the inner vortex core radius stays fixed with $r_{1,0}/L_{box} = 0.02$). When the dissipation rate increases with a factor 64, the Kolmogorov microscale becomes about 2.5 times smaller since $\eta \sim \varepsilon^{-1/4}$. It was found that the Kolmogorov microscale corresponding to the turbulent flow field for $Re_{\Gamma_{vor,0}} = 7.5 \cdot 10^3$, $r_{1,0}/L_{box} = 0.02$ becomes as small as $2/3N$ for $N^3 = 384^3$, that is 2/3 of the distance between two grid points. This shows that $Re_{\Gamma_{vor,0}} = 7.5 \cdot 10^3$,$r_{1,0}/L_{box} = 0.02$ is already close to the limit for $N^3 = 384^3$. It becomes possible to perform direct numerical simulations of $Re_{\Gamma_{vor,0}} = 30 \cdot 10^3$, $r_{1,0}/L_{box} = 0.02$ with corresponding turbulence when a numerical resolution of $N^3 \geqq 1024^3$ is applied.

With the model spectrum given by Eq. A.6; $C = 1.5$ and $\gamma = 5.2$ fixed; and both $\varepsilon^*_{r_{1,0}}$ and $L^*_{r_{1,0}}$ determining c_η and c_L, the spectrum is completely specified. The turbulence fields are initialized with different values of $\varepsilon^*_{r_{1,0}}, L^*_{r_{1,0}}$ than those corresponding to the trailing vortex in turbulence generated by the $M254$ and $M127$ grids. In this way, the turbulent field is able to relax before the desired values of $\varepsilon^*_{r_{1,0}}, L^*_{r_{1,0}}$ are obtained. To quantify the relaxation process of the turbulence, we consider the total energy E_{tot}, the Taylor Reynolds number Re_{lambda}, and the skewness of S. The resolved kinetic energy is strongly influenced by the larger scales in the flow, whereas Re_{lambda} and S depend on the components of the velocity derivatives and hence characterize the accuracy with which smaller scales are captured. The evolution of these parameters are shown in Figure A.11.

The nondimensional energy spectra $E_{11}(k)\Gamma^2_{vor,0}/r_{1,0}$ obtained in the experiments and applied in the numerical simulation for $L^* = 3.5$, $\varepsilon^*_{r_{1,0}} = 1.3 \cdot 10^{-2}$ ($M254$) and $L^* = 3.2$, $\varepsilon^*_{r_{1,0}} = 0.9 \cdot 10^{-2}$ ($M127$) are shown in Figure A.12. Distributions of the absolute vorticity for the numerical simulations are shown in Figure A.13. The evolution of the circulation profiles of the turbulent flow fields are shown in Figure A.14. These results reveal that the turbulent flow field alters the initial VM2 circulation profile with ten percent at maximum.

The turbulence flow field with $L^* = 3.6$, $\varepsilon^*_{r_{1,0}} = 1.3 \cdot 10^{-2}$ ($M254$) is now added to the flow field of a vortex with $Re_{\Gamma_{vor,0}} = 7.5 \cdot 10^3$, $r_{1,0}/L_{box} = 0.02$. The circulation profiles, as also given in Figure A.6 without turbulence, are shown in Figure A.15. These circulation profiles are obtained by integration of the average axial vorticity distribution. Here the averaging takes place in the axial and azimuthal direction. Apparently, the integral scale of turbulence is too large to obtain averaged circulation profiles according to $\lim_{L\to 0} \Gamma(r) = 0$.

Note that the initial circulation profile of a vortex in turbulence is a superposition of that due to turbulence, see Figure A.14, and due to the vortex, see Figure A.6. The fluctuations between $0.15 \lessapprox r/L_{box} \lessapprox r0.30$ are due to the turbulent flow field, the boundary effect is visible for $r \gtrapprox 0.30$. The evolution of the circulation between a vortex with and without turbulence can be observed by comparing Figures A.15 and A.6. One should note that the negative vorticity concentration near the boundaries gets advected further in the same amount of time. For the case without turbulence, the radius at which the circulation starts to decrease $d\Gamma_{vor}(r)/dr = 0$, moved inwards to $r/L_{box} = 0.46$. In the case with turbulence, this radius is $r/L_{box} \approx 0.35$. However, it is difficult to separate the effect of turbulence and the periodic boundary conditions on the circu-

lation profile.

Distributions of the axial vorticity distribution are given in Figure A.16. Concentrated bands of opposite-signed vorticity, that are vortexlets, are less present than in the case without turbulence, compare Figures A.9 and A.16. The vortexlets are believed to be advected by the turbulent flow field over a wider area, including the area more inwards. The turbulence is in this view responsible for distributing the opposite-signed vorticity quicker inward.

A.3.1 Conclusion and discussion

We may conclude the following:

- The initial circulation profile is influenced by turbulence and the opposite-signed vorticity concentration near the boundaries. The initial turbulence results in a fluctuation on the initial circulation profile of maximal 7% ($M127$) and 10% ($M254$).
- The vortexlets near the periodic boundaries mix with turbulence. Therefore, they get advected quicker and further inwards than in the case without turbulence. The vortex evolves in an isolated way from the periodic boundary effects in the time domain till $t\Gamma_{vor,0}/(2\pi r_{1,0}^2) = 225$. In this time domain, the vortex core outer radius $r_2(t) \approx r_{2,0} = 0.2/L_{box}$ is approximately smaller than the radius at which opposite-signed vorticity is concentrated ($r/L_{box} \gtrapprox 0.35$).
- Although the perturbed flow field is centrifugally unstable, no overturning motion (which is typical for centrifugal instability) is found to occur. Signs of bending waves are visible, but is is unknown if these are caused by the periodic boundary conditions; this needs a more thorough analysis with different kinds of boundary conditions.

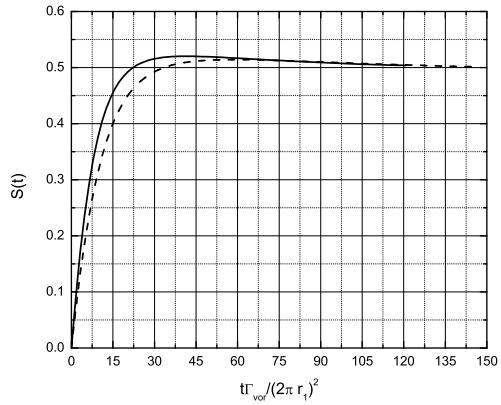

(a) Skewness

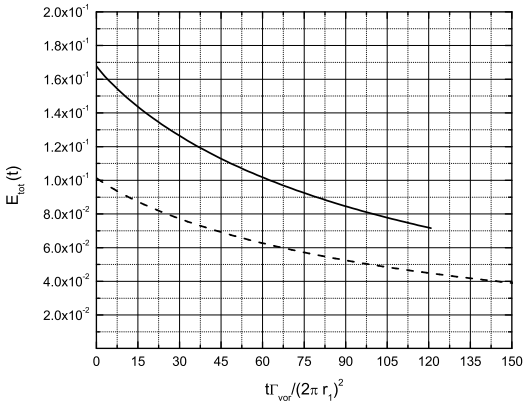

(b) Total Energy

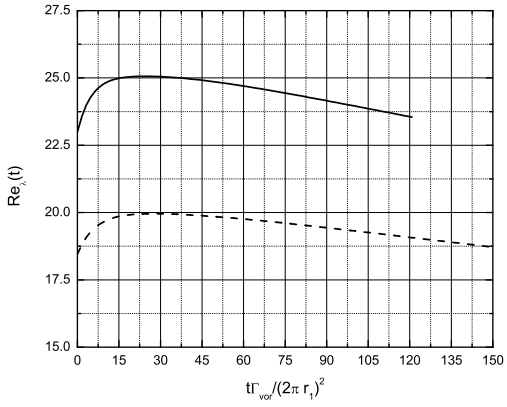

(c) Taylor Reynolds number

Figure A.11: The evolution of the skewness and the Taylor Reynolds number show that initial effect are present. The skewness needs to be typically 0.5, and the Taylor Reynolds number normally decreases in decaying turbulence. Therefore, the turbulence needs to be relaxed for a sufficient amount of time. The turbulence corresponding to $L^* = 3.6$, $\varepsilon^*_{r_{1,0}} = 2 \cdot 10^{-3}$ *(M254) (———) is decayed for* $t\Gamma_{vor,0}/(2\pi r^2_{1,0}) = 150$ *and that of* $L^* = 3.2$, $\varepsilon^*_{r_{1,0}} = 1.5 \cdot 10^{-3}$ *(M127) (- - - -) for* $t\Gamma_{vor,0}/(2\pi r^2_{1,0}) = 120$.

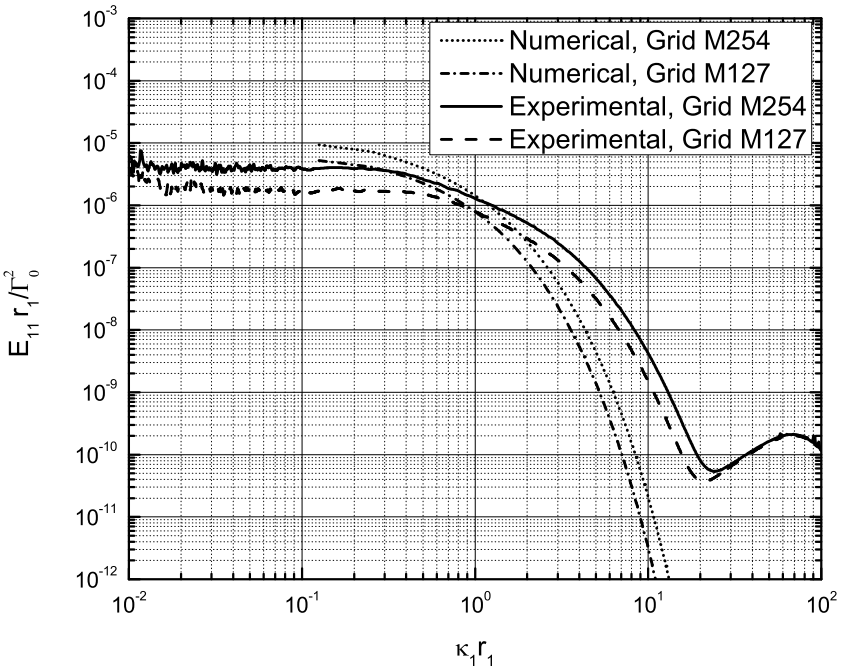

Figure A.12: The longitudinal energy spectrum nondimensionalised with the vortex parameters Γ_{vor} and $r_{1,0}$. It becomes clear that the nondimensional enegy of the turbulence with length scale $r_{1,0}$ corresponds with that of the experiments.

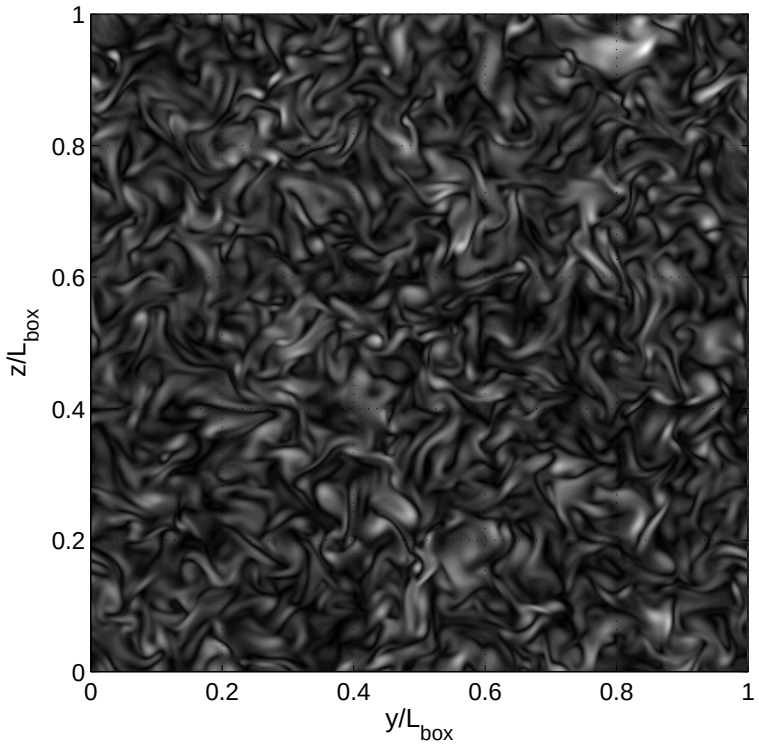

(a) $L^* = 3.5$, $\varepsilon^*_{r_{1,0}} = 2 \cdot 10^{-3}$ (M254)

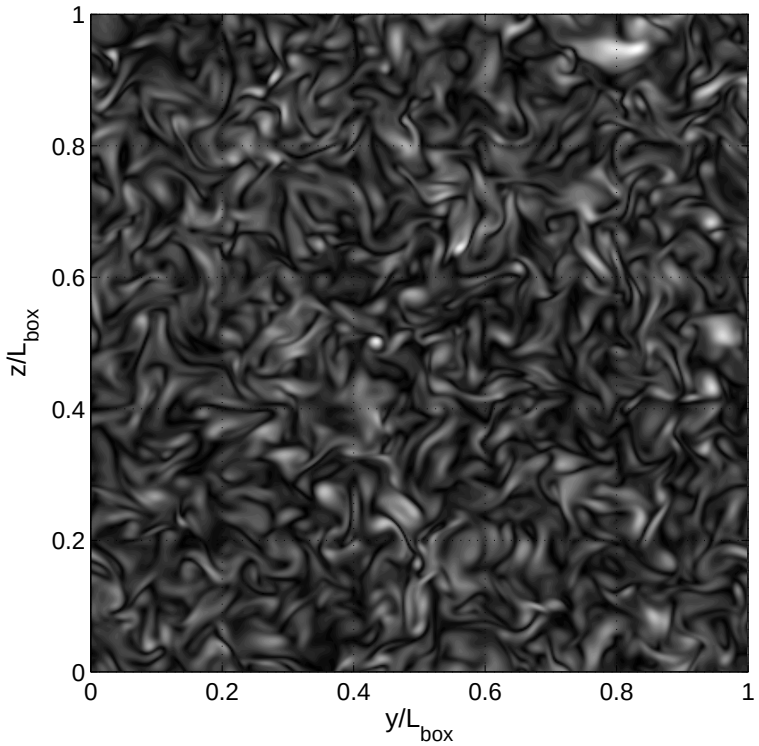

(b) $L^* = 3.2$, $\varepsilon^*_{r_{1,0}} = 1.5 \cdot 10^{-3}$ (M127)

Figure A.13: Distributions of the absolute vorticity are shown for the cases $L^* = 3.6$, $\varepsilon^*_{r_{1,0}} = 2 \cdot 10^{-3}$ (M254) and $L^* = 3.2$, $\varepsilon^*_{r_{1,0}} = 1.5 \cdot 10^{-3}$ (M127).

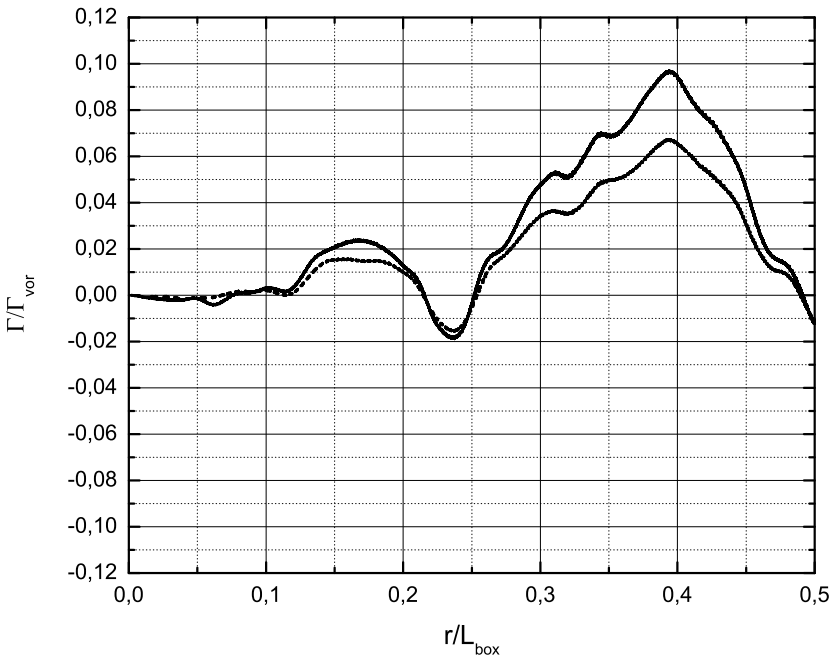

Figure A.14: The circulation profile of the turbulent flow field corresponding to $L^* = 3.6$, $\varepsilon^*_{r_{1,0}} = 2 \cdot 10^{-3}$ *(M254) (———) and* $L^* = 3.2$, $\varepsilon^*_{r_{1,0}} = 1.5 \cdot 10^{-3}$ *(M127) (- - - -). The circulation is normalized with* Γ_{vor} *corresponding to* $Re_{\Gamma_{vor,0}} = 7.5 \cdot 10^3$. *It becomes clear that the turbulent flow field alters the initial VM2 circulation profile with maximal ten (M254) and seven (M127) percent. Apparently, the integral scale of turbulence is too large to obtain averaged circulation profiles according to* $\lim_{L \to 0} \Gamma(r) = 0$.

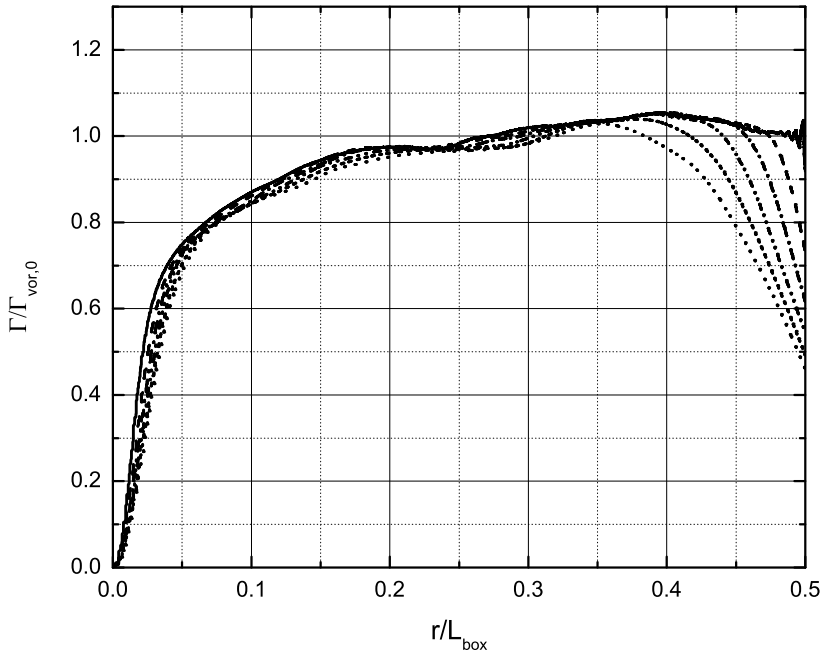

Figure A.15: Evolution of the circulation profile for the vortex with $Re_{\Gamma_{vor,0}} = 7.5 \cdot 10^3$ *and* $r_{1,0}/L_{box} = 0.02$ *with turbulence specified by* $L^* = 3.6$, $\varepsilon^*_{r_{1,0}} = 2 \cdot 10^{-3}$ *(M254). The boundary effect of decreasing circulation is clearly visible. However, it is difficult to separate the effect of turbulence and the periodic boundary conditions on the circulation profile. For the case without turbulence, the radius at which the circulation starts to decrease* $d\Gamma_{vor}(r)/dr = 0$*, moved inwards to* $r/L_{box} = 0.46$*. In the case with turbulence, this radius is* $r/L_{box} \approx 0.35$*. The advective property of turbulence is believed to be responsible for distributing the opposite-signed vorticity quicker inward.* $t\Gamma_{vor,0}/(2\pi r^2_{1,0}) =$ 0——— ; 45– – – – ; 90–·–· ; 135–··–·· ; 180- - - - ; 225····· .

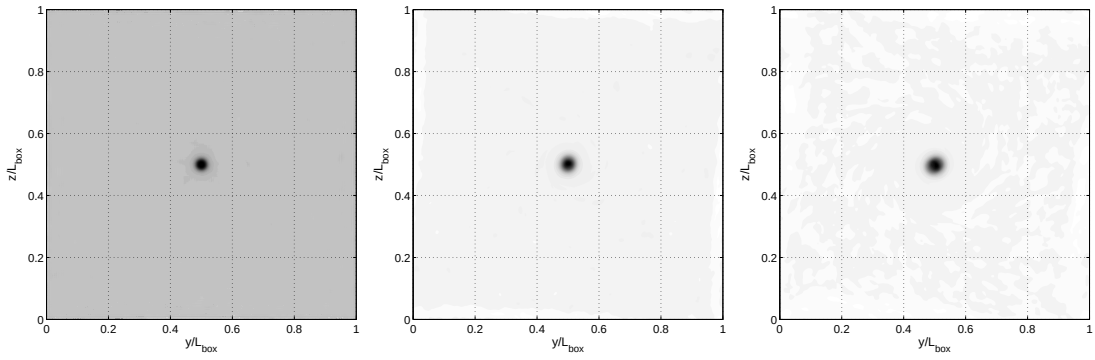

(a) $t\Gamma_{vor,0}/(2\pi r_{1,0}^2) = 0$ (b) $t\Gamma_{vor,0}/(2\pi r_{1,0}^2) = 45$ (c) $t\Gamma_{vor,0}/(2\pi r_{1,0}^2) = 90$

(d) $t\Gamma_{vor,0}/(2\pi r_{1,0}^2) = 135$ (e) $t\Gamma_{vor,0}/(2\pi r_{1,0}^2) = 180$ (f) $t\Gamma_{vor,0}/(2\pi r_{1,0}^2) = 225$

Figure A.16: Evolution of the axial vorticity for the vortex with $Re_{\Gamma_{vor,0}} = 7.5 \cdot 10^3$ and $r_{1,0}/L_{box} = 0.02$ with turbulence specified by $L^* = 3.6$, $\varepsilon^*_{r_{1,0}} = 1.3 \cdot 10^{-2}$ (M254). One can see that negative vorticity, initially concentrated near the boundary, moves inwards in time. The color scale varies for the different panels.

Appendix B

Motivation for Turbulence Grid Design

This work considers the evolution of a single trailing vortex without and with grid-generated turbulence. By applying weak instead of strong external turbulence, it is believed that we will contribute to an enhanced understanding of the observations made by Van Jaarsveld (2008). It has to be remarked that the definition of weak or strong turbulence given by Crow and Bate (1976) depends on the distance between the two trailing vortices, and that we use typical values for these as applied by Van Jaarsveld (2008). Note that experiments on the breakdown of a trailing vortex pair in weak turbulence will be executed in a later stage of the TU/e trailing vortex program. For this, the analysis of a single trailing vortex in weak turbulence will be a good starting point.

This appendix is organized as follows. We first discuss the theory of grid-generated turbulence and some relevant parameters in the decay of a trailing vortex pair in turbulence. With that in mind, we then discuss some alternatives to designing a new turbulence grid. After that, the biplane and perforated turbulence grid configurations are considered. The choice for a biplane grid with specific mesh sizes and solidity, is motivated by streamwise profiles of turbulence quantities, as derived by applying the empirical formulas of grid-generated turbulence. We end this study with some points of discussion and the conclusion.

B.1 Theory

We will first briefly discuss the theory of grid-generated turbulence. This is primarily developed and applied by Comte-Bellot and Corssin (1966). After this, we consider the relevant turbulence quantities in the decay of a trailing vortex pair in turbulence. These quantities are made dimensionless with parameters of the trailing vortex pair.

B.1.1 Theory for grid-generated turbulence

Following Comte-Bellot and Corssin (1966), we use the empirical formula

$$\overline{u^2_{rms,x}} = \overline{U^2_x} A^{-1} \left(\frac{\overline{U}_x t}{M} - \frac{\overline{U}_x t_v}{M} \right)^{-m}, \tag{B.1}$$

with $\overline{u^2_{rms,x}}$ the mean square turbulent velocity in the x-direction; $\overline{U}_x$ the mean main stream velocity ($\overline{U_y} = \overline{U_z} = 0$), M the mesh size of the turbulence grid, and t the time. The streamwise distance from the grid equals $x = \overline{U}_x t$. The parameters m, A, and $\overline{U}_x t_v = x_v$ vary with grid

and flow configurations. $\overline{U}_x t_v = x_v$ corresponds to the virtual origin of turbulence decay such that $u^2_{rms,x}$ decays exponentially with $(\overline{U}_x t/M)^{-m}$. Because isotropy is not guaranteed, one usually makes a distinction between the turbulent velocity components parallel to the main stream velocity, $u_{rms,x}$, and the components perpendicular to this, $u_{rms,y}, u_z$. However, for the sake of the argument, we assume isotropy, $\overline{u^2_{rms,x}} = \overline{u^2_{rms,y}} = \overline{u^2_z}$. The rate of decay of the turbulence intensity is defined by:

$$\varepsilon = -\frac{1}{2}\overline{\frac{d}{dt}(u^2_{rms,x} + u^2_{rms,y} + u^2_z)} = -\frac{3}{2}\overline{\frac{d}{dt}(u^2_{rms,x})}. \tag{B.2}$$

To compare different grid geometries, we need an equation for the dissipation rate similar to Eq. B.1. For this, Friehe and Schwarz (1970) used the expression for the eddy dissipation rate in homogeneous and isotropic turbulence that is related to the Taylor microscale λ by

$$\varepsilon = 15\nu\frac{u^2_{rms}}{\lambda^2}, \tag{B.3}$$

see for example Pope (2000). Furthermore, it is shown by Batchelor (1960) that λ^2 equals $10\nu t/m$ in the case of isotropic turbulence. Combining the latter with Eq. B.3 yields

$$\varepsilon = \frac{3m\overline{U}^3_x}{2MA}\left(\frac{\overline{U}_x t}{M}\right)^{-1-m}, \tag{B.4}$$

where we have ignored the offset parameter $\overline{U}_x t_v/M = x_v/M$, which is found to be in other grid turbulence experiments $\mathcal{O}(5)$, see for example Comte-Bellot and Corssin (1966), Mohamed and Larue (1990), Liu et al. (2007), and Lavoie et al. (2007). Moreover, we have assumed that $\overline{U^2_x} = \overline{U}^2_x$. This may cause slight differences in the values found for A with Eq. B.1 and B.4.

B.1.2 Relevant parameters in the decay of a trailing vortex pair in turbulence

In the trailing vortex society, the turbulence dissipation rate ε is made dimensionless with the help of the tip vortices separation distance b_0 and the downwash velocity $U^{vor}_{z,0} = \Gamma_{vor,0}/2\pi b_0$ (with $\Gamma_{vor,0}$ the circulation of the trailing vortex at time $t = 0$):

$$\varepsilon^*_{b_0} = \frac{(\varepsilon b_0)^{1/3}}{U^{vor}_{z,0}}. \tag{B.5}$$

From Eq. B.4 and B.5, one can deduce the relation $\varepsilon^*_{b_0} \sim M^{\frac{n}{3}}$. The dimensionless time is defined as:

$$t^* = \frac{b_0}{U^{vor}_{z,0}}. \tag{B.6}$$

Van Jaarsveld (2008) considered $\varepsilon^*_{b_0} = \mathcal{O}(10^{-1} - 1)$ which is characterized as strong turbulence by the definition of Crow and Bate (1976). In this work, we are interested in weak turbulence: $\varepsilon^*_{b_0} = \mathcal{O}(10^{-2})$.

B.2 Alternatives to a new turbulence grid

We will first discuss some alternatives that are possible in reducing the dimensionless eddy dissipation rate $\varepsilon^*_{b_0}$ without realizing a new grid. Considering Eq. B.5, one can reduce $\varepsilon^*_{b_0}$ by increasing the root circulation of the wing $\Gamma_w \sim \Gamma_{vor,0}$ or decreasing the wing-tip separation distance $d \sim b_0$. The former is possible by increasing the angle of attack of the current wing design. However, increasing the angle of attack is already applied by Van Jaarsveld (2008) and thus will not result in uncovered values of $\varepsilon^*_{b_0}$. The second option in increasing the circulation, is to construct a new

wing. This option is due to economical and practical reasons not favorable.

Our second alternative is to decrease the wing-tip separation distance d and with that the trailing vortices separation distance b_0. The trailing vortices separation distance is related to the dimensionless eddy dissipation rate by $\varepsilon^*_{b_0} \sim b_0^{4/3}$. Van Jaarsveld (2008) varied the wing-tip separation distance between $b_0 = 10.00, 5.00$, and $3.00 \cdot 10^{-2}$ m. They concluded that $b_0 = 3.00 \cdot 10^{-2}$ m is already the minimum value possible due to overlap of the trailing vortex cores. Therefore, it is not possible to reduce the dimensionless eddy dissipation rate anymore by this method.

To summarize, there are two alternative possible in decreasing the dimensionless eddy dissipation rate. The first one is to construct a new turbulence grid with a smaller mesh size so that the turbulence intensity is lower, and the second one is to construct a new wing design that induces a higher circulation. The former is favorable due to practical and economical reasons.

B.3 Turbulence grid designs and parameters

Turbulence generated by passive grids is extensively discussed in the literature. When grid-generated turbulence is analyzed, one is generally interested in the intensity, homogeneity, and isotropy of the turbulent flow along the longitudinal direction. In general, two types of passive grid configurations can be distinguished in studies of grid-generated turbulence: perforated plates and biplane grids. Biplane grid are built out of two layer, one with horizontal bars and one with vertical bars. Together they form a grid of square openings. Especially the biplane grids are common as a turbulence generator. This is presumably due to the convention and the ease of building a grid as opposed to making a perforated plate. We will first discuss the solidity, that is the parameter that defines the area fraction of the solid portion, which is therefore independent of the grid type. Turbulence that is produced by a grid acquires its energy primarily from the pressure drop across the turbulence generator. The pressure drop, and ultimately the turbulence level, depends essentially on the mesh size but also on the turbulence generator solidity ratio, see Baines and Peterson (1951), Mohamed and Larue (1990), and Liu et al. (2004). Liu et al. (2004) found that the turbulence generated by a passive grid with a fixed mesh size is related to the solidity by:

$$\ln\left(\frac{\sqrt{\overline{u^2_{rms,x}}}}{\overline{U}_x}\right) \sim \ln(p) + q\sigma, \tag{B.7}$$

with the empirical parameter p in the range of 1.0-2.5, and q in the range of 1.6-2.0. The value for q is found to be constant with downstream distance to the grid. This implies that the influence of the plate solidity persists as the turbulence is convected downstream. The value of p decreases in downstream direction, which indicates that the turbulence decays. The influence of the grid solidity σ on the eddy dissipation rate can now be derived by combining Eq. B.3 and Eq. B.7:

$$\varepsilon \sim \overline{u^2_{rms,x}} \sim e^{2q\sigma}. \tag{B.8}$$

A decrease of the grid solidity from 0.36 to 0.26 results in a decrease of ε with approximately 30%, that is approximately a decrease of 10% for $\varepsilon^*_{b_0}$. In other words, the influence of the grid solidity on the turbulence intensity is significant.

An optimal grid solidity depends on more factors. In order to obtain isotropic turbulence, the solidity ratio of the turbulence generator cannot be too high. Otherwise, the uniformity of the mean flow will cease to exist. Moreover, the maximum obtainable wind tunnel speed becomes lower when the solidity increases. In our work, a compromise between the desired turbulence intensity, uniformity of the flow (lower solidity), maximum obtainable wind tunnel speed (solidity of 0.2, to math conditions of Van Jaarsveld (2008)), the robustness of the turbulence generator (higher solidity), and convention in grid-generated turbulence studies (σ varying between 0.30

and 0.45), results in a solidity around 0.25. We will now proceed with discussing the two kinds of passive grid configurations.

B.3.1 Turbulence grids of perforated plates

Perforated plates occur with round openings and square openings, see for example Bailey and Tavoularis (2008), Liu et al. (2004), and Liu et al. (2007). No study has been found that discusses the influence of the hole shape (round or square) on the intensity, isotropy, and homogeneity of the turbulence. The work of Liu and Ting (2007) discusses the difference of turbulence generated by sharp-edged orificed perforated plates and perforated plates that have a finite thickness. With this, the influence of the thickness of the perforated plate on the turbulence generated by the perforated plate is analyzed. Liu and Ting (2007) found that the turbulence generated by sharp-edged orifice perforated plates is relatively more intense and more isotrope.

B.3.2 Biplane turbulence grids

We will now continu with discussing the second type of passive turbulence generator: the biplane grid. The biplane grids can be separated in those built out of square bars, and those built out of round bars, see for example Comte-Bellot and Corssin (1966), Mohamed and Larue (1990), and Lavoie et al. (2007). Furthermore, the grid is defined by the mesh size and solidity. The solidity σ is defined by

$$\sigma = \frac{D}{M}\left(2 - \frac{D}{M}\right), \tag{B.9}$$

in which M is the mesh size and D the diameter of the round bars or length of the sides of the square bars. It was found by Lavoie et al. (2004), that the bar shape exerts a stronger influence on the energy containing scales than the grid solidity, which has little effect on the scales ranging from Kolmogorov length to Taylor microscale. Therefore, we will continue with concentrating on the shape of the bars. Lavoie et al. (2007) showed that round bars result in a more isotropic turbulence distribution, than their square bar counterpart. However, round bar result in a more coherent structure of the large scales, see Lavoie et al. (2005). In other words, square bar are more efficient at destroying their large scale flow coherence. To prevent the coherence of the large scale, Lavoie et al. (2007) analyzed the turbulence generated by a biplane grid with round bar, which have a small helical wire wound around the bars at a pitch of one mesh length. They showed that the helical wire effectively reduces the coherence at the larger scales.

The intensity of the turbulence generated by grids with square bars is found to be higher than that generated by comparable grids with round bars, see Comte-Bellot and Corssin (1966) and Lavoie et al. (2007).

It is believed that both the biplane grid and perforated plates as turbulence generators are able to result in desirable turbulence characteristics as intensity, isotropy, and homogeneity. However, detailed complementary studies of turbulence generated by perforated plates are not present as is the case with biplane grids. Many studies considered the turbulence generated by biplane grid built of square and round bars, with a mesh size of 2.54 cm (1 inch) and 5.08 cm (2 inch) and a solidity varying between 0.30 and 0.45, see for examplwe Comte-Bellot and Corssin (1966), Friehe and Schwarz (1970), Uberoi and Wallis (1976), Mohamed and Larue (1990), Lavoie et al. (2004), Lavoie et al. (2005), Lavoie et al. (2007). This means that the characteristics (intensity, homogeneity, isotropy) are already well investigated for some very specific biplane grid designs, in contrast to that of perforated plates. Therefore, we will apply a biplane grid as turbulence generator in our work. From a practical/economical point of view, there is no significant difference in the ease/cost of producing biplane grids or perforated plates.

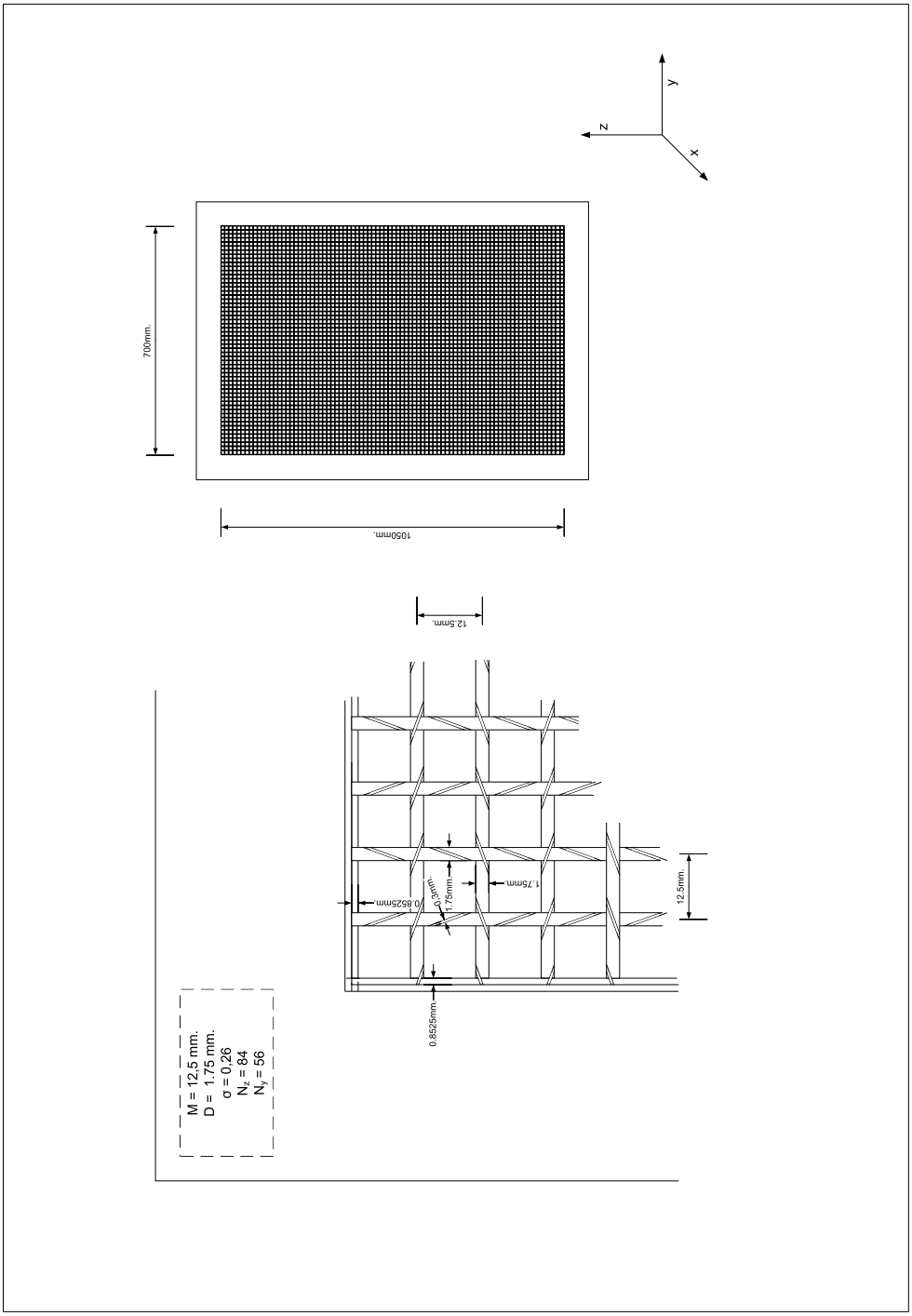

Figure B.1: Design 'M125' of biplane grid with round bars.

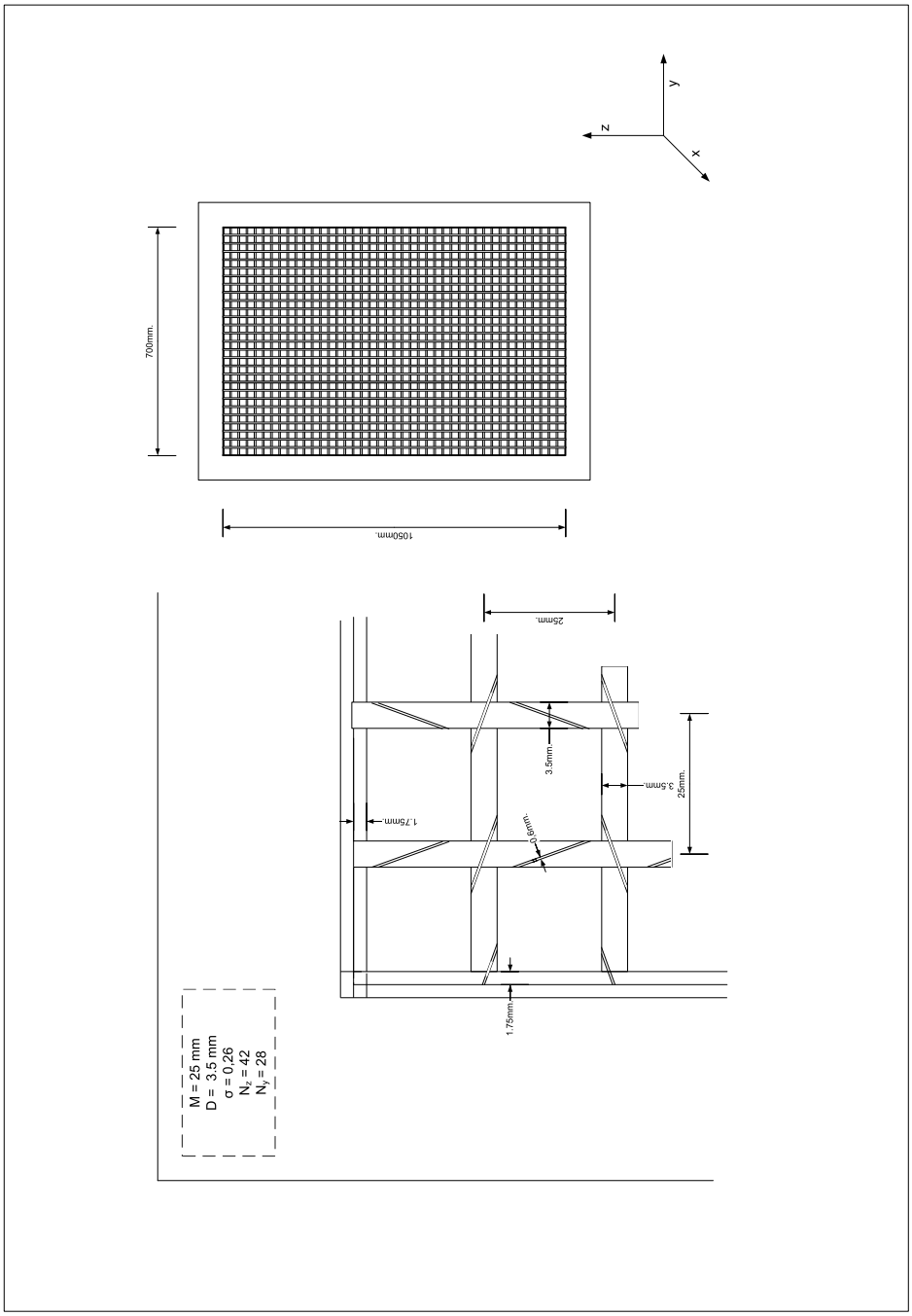

Figure B.2: Design 'M250' of biplane grid with round bars.

B.4 The final turbulence grid

In this work, we will use a biplane grid with round bars as turbulence generator. A biplane grid with round bars is preferred above that with square bars because of a higher expected isotropy and a relatively milder turbulence intensity. To reduce the coherence of the turbulence at large scale as reported by Lavoie et al. (2005), we apply the adapted round bar design of Lavoie et al. (2007). This design includes a small helical wire wound around the bars at a pitch of one mesh length. The turbulence characteristics, besides the reduction of the large scale coherence, are not believed to be significantly different than that generated by comparable round bar designs without this extra feature.

By combining the turbulence data of Van Jaarsveld (2008) ($M = 10 \cdot 10^{-2}$ m) with Eq. B.4, it is possible to deduce values for the empirical parameters A and m. In doing this, we assume that these parameters are independent of the mesh size M. Further analysis showed that turbulence grids with mesh sizes of $M \approx 1.27 \cdot 10^{-2}$ m and $M \approx 2.54 \cdot 10^{-2}$ m combined with a solidity of around 0.25, will result in a grid that generates turbulence with characteristics that cover our desired range of intensities.

With the dimensions of the TU/e wind tunnel Goliath in consideration, our biplane grids M125 and M250 are defined by the combinations $M = 1.25 \cdot 10^{-2}$ m, $D = 1.75 \cdot 10^{-3}$ m and $M = 2.50 \cdot 10^{-2}$ m, $D = 3.50 \cdot 10^{-3}$ m, see Figure B.1 and B.2. In this way, the cross-sectional area of the TU/e wind tunnel Goliath covers an integer number of meshes N_z and N_y. Both grids have a solidity equal to 0.26.

When the bars are made of yellow brass, the resonance frequency ($f_{res} = \sqrt{k/m}/2\pi$) of an individual bar is approximately 281·10^3 (along y-direction, $D = 1.75 \cdot 10^{-3}$ m), 344·10^3 Hz (along z-direction, $D = 1.75 \cdot 10^{-3}$ m), 140·10^3 (along y-direction, $D = 3.50 \cdot 10^{-3}$ m), 172·10^3 Hz (along z-direction, $D = 3.50 \cdot 10^{-3}$ m). The resonance frequency of the whole bar construction is 32·10^3 Hz ($D = 1.75 \cdot 10^{-3}$m) and 23·10^3 Hz ($D = 3.50 \cdot 10^{-3}$m). Here, the modulus of elasticity k is given by $k = 10 \cdot 10^{10}$ N/m^2 and the mass m is determined with a density of yellow brass of $\rho = 8.47 g/cm^3$, see Lide (2006). The Strouhal frequency is determined with $f_{str} = 0.21 \cdot \overline{U}_x/(D/2)$, see Kundu et al. (2008). With $\overline{U}_x = 15$ m/s, this results in $f_{str} = 3.6 \cdot 10^3$ Hz ($D = 1.75 \cdot 10^{-3}$ m) and $1.8 \cdot 10^3$ Hz ($D = 3.50 \cdot 10^{-3}$ m). Resonance is not to be expected. The isotropy, expressed as the ratio of $\sqrt{\overline{u^2_{rms,x}}/\overline{u^2_{rms,y}}}$, is expected to be of order 1.1-1.3. These are typical values for turbulence generated by passive grids, see for example Comte-Bellot and Corssin (1966), Liu et al. (2007), and Lavoie et al. (2007). Comte-Bellot and Corssin (1966) showed that a contraction of the wind tunnel, located after the grid results in a condition of $\sqrt{\overline{u^2_{rms,x}}/\overline{u^2_{rms,y}}}$ approaching unity. However, it is not possible to build a secondary contraction in the TU/e wind tunnel Goliath. We will continue with discussing the turbulence characteristics belonging to our grid.

The maximum main stream velocity is assumed to be $\overline{U}_x = 15$ m/s for a turbulence grid with a solidity of 0.26. This assumption is based on the main stream velocity achieved with a comparable grid with solidity of 0.26 in the TU/e wind tunnel Goliath, see Van Jaarsveld (2008). A mean stream velocity of $\overline{U}_x = 15$ m/s results in $\Gamma_w \approx 0.6$ m^2/s for an angle of attach $\alpha = 7.5°$. We elaborated the evolution of $\varepsilon^*_{b_0}$ and $u/\overline{U}_x$ for $M = 12.5 \cdot 10^{-3}$ m and $M = 25.0 \cdot 10^{-3}$ m, with $b_0 = 10.00, 5.00$, and $3.00 \cdot 10^{-2}$ m. Herewith, we assume dat the wing-tip separation distance is equal to the vortex separation distance; $d = b_0$. In this analysis, we use the values $A = 18$, $m = 1.36$, and $U_0 t_0/M = 0$. Although no study exists with exactly corresponding grid specifications, we found that the values for our empirical parameters are typical for comparable biplane grids and main stream velocities, see for example Comte-Bellot and Corssin (1966). Our profiles of turbulence quantities satisfies those of Beninati and Marshall (2005), who used a grid with $M = 5.0 \cdot 10^{-3}$ m.

It takes about $40M$ before (quasi-)isotropy and (quasi-)homogeneity of the turbulence generated by a grid with round bars are developed, see for example Comte-Bellot and Corssin (1966) and Mohamed and Larue (1990). This is equal to 0.50 m for $M = 12.5 \cdot 10^{-3}$ m, and 1.00 m for $M = 25 \cdot 10^{-3}$ m, see Figure B.4 and B.5. Values of $\varepsilon^*_{b_0}$ that are $\mathcal{O}(10^{-2})$ are well covered with our flow and grid configuration, see Figure B.3. Variations of 0.5% of the main velocity ($u_{rms,x}/\overline{U}_x = 0.005$) can still be measured with the current hotwire measurement technique. Because the variations of the main velocity will drop in stream wise direction eventually below 0.5%, extrapolation of $u_{rms,x}/\overline{U}_x$ may be necessary, see Figure B.6.

The magnitudes of the length scales within the free stream could play an important role in the interaction between the turbulence and the vortex. It is shown in Figure 3 of Bailey and Tavoularis (2008), that the large length scales equal the grid size after 100M. Furthermore, they showed that the large length scales L increase in streamwise direction according to $L \sim x^{0.4}$. With the length of test section of the TU/e wind tunnel Goliath equal to 640M ($M = 12.5 \cdot 10^{-3}$ m) and 320M ($M = 25 \cdot 10^{-3}$ m), the large length scale will be increase to about $1.2M = 2.1 \cdot 12.5 \cdot 10^{-3}m = 26 \cdot 10^{-3}$ m and $1.6M = 1.6 \cdot 25 \cdot 10^{-3}m = 40 \cdot 10^{-3}$ m. The location of the wing x_a will be determined by a compromise between (1) isotropy/homogeinity of the flow (large x_a) (2) intensity of the turbulence (average to large x_a, see Figure B.3) (3) the dimensionless lifespan of the trailing vortex which has to be contained in the test section of the TU/e wind tunnel Goliath (small to average x_a). These conditions are condensed in Figure C.19. From this, it follows that the option to choose for two wing locations, denoted by x_a, is considerable. One may think of $x_a = 3.5$ m and 4.5 m as appropriate wing locations. With the wing location of $x_a = 4.5$ m, it will only be possible to use the wing-tip separation distance of $d = 5.00$ and $3.00 \cdot 10^{-2}$ m.

B.5 Points of discussion

We will end this study on turbulence grid design with some points of discussion:

1. The values of the parameters A and m are based on the work Van Jaarsveld (2008). However, the grid considered in that work is different than our proposed grid. The values for A and m are found to vary between $A = 10, n = 1.40$ and $A = 50, n = 1.25$, see Comte-Bellot and Corssin (1966). Note that A and m are more or less correlated. The variations in the parameters are due to for example different wind-tunnel specifications, solidities, and main stream velocities. The uncertainty in the parameters A and m results in a uncertainty of about 20% in the value of $\varepsilon^*_{b_0}$, and 25% in the value of $\sqrt{\overline{u^2_{rms,x}}}/\overline{U}_x$.

2. The main velocity in the TU/e wind tunnel Goliath without a grid fluctuates about 1% around its mean value with a frequency of about 1 Hz. The turbulent fluctuations expressed in terms of $\sqrt{\overline{u^2_{rms,x}}}$ are of 0.5% of the mean main velocity $\overline{U}_x$, see Van Jaarsveld (2008). It is believed that this low frequency oscillation is not of importance in the turbulence characteristics, since the grid-generated turbulence is contained in higher frequencies. However, the low-frequency oscillations can be important in the turbulence-trailing vortex interaction. We will analyse the the low-frequency contribution in more detail in Appendix C.

3. Besides the low frequency oscillations, the TU/e wind tunnel Goliath contains also a intrinsic turbulence level. This intrinsic level of turbulence is not known since it is equal or below the measurement limit. The problem is that the grid-generated turbulence at large distance can get close to this measurement limit, and therefore possibly to the intrinsic turbulence level of the wind tunnel. This means that the grid-generated turbulence may not be separable from the intrinsic turbulence anymore. Moreover, the turbulence generated by the wing is not known as well. This means that the intrinsic turbulence level of the wing can be comparable to the grid-generated turbulence. Van Jaarsveld (2008) made an approximation of the turbulence level when no grid is installed. This approximation may correspond to

the intrinsic turbulence level of both the wind tunnel and wing. When we assume that this approximation is correct, the grid-generated turbulence is more intense than the intrinsic turbulence level of the wind tunnel and wing together.

4. The proposed grids are composed of bars with a diameter of $D = 1.75 \cdot 10^{-3}$ m and $D = 3.50 \cdot 10^{-3}$ m. The grids have to withstand the pressure force caused by the wind tunnel main velocity of 15 m/s. No mechanical calculation are performed of the stresses on the grids, but a literature study shows that comparable grids under comparable conditions are able to withstand the force. Nevertheless, the grids need to be mounted firmly.

5. The isotropy of turbulence generated by grids with a solidity of around 0.25 is not well investigated in the literature. Most works on grid-generating turbulence are concentrated on grid with a solidity of 0.36 or 0.44. The influence of solidity on the isotropy is not well known as well. This means that the isotropy may deviate from our expectations, based on data obtained with grids characterized by a solidity of 0.36 or 0.44. The influence of solidity on isotropy is possibly significant.

Some points of concern are specifically related to the grid design $M125$ or $M250$. The points 1, 2, and 5 apply to both the $M = 12.5 \cdot 10^{-3}$ m and $25 \cdot 10^{-3}$ m grids. The point of concern described by 3 and 4 are thought to be more relevant for the $M = 12.5 \cdot 10^{-3}$ m grid design. In general, 3 and 5 are thought to be the most relevant.

B.6 Conclusion

The dimensionless eddy dissipation rate can be decreased with two alternatives. Constructing a new grid with a smaller mesh size, or a new wing that induces a higher circulation. The former is favorable due to practical and economical reasons. The proposed grid designs are based on a compromis of demands and limitations. These are based on for example the desired level of grid-generated turbulence, characteristics of the TU/e wind tunnel Goliath, convention in literature, connection with the prior work of Van Jaarsveld (2008). The proposed grids are biplane grids defined by the combinations $M = 1.25 \cdot 10^{-2}$ m, $D = 1.75 \cdot 10^{-3}$ m and $M = 2.50 \cdot 10^{-2}$ m, $D = 3.50 \cdot 10^{-3}$ m, see Figure B.1 and B.2. Both have a solidity of 0.25. An isotropy that deviates from our expectations, and the intensity of the intrinsic turbulence of the wind tunnel and wing are the most relevant points of concern in applying the $M125$ and $M250$ turbulence grids.

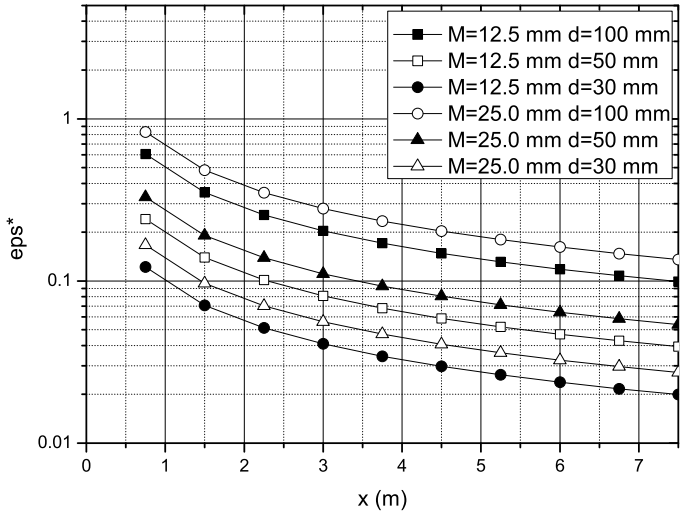

Figure B.3: Graph showing the range of $\varepsilon^*_{b_0}$ that can be obtained by varying the wing-tip separation distance b_0 and the mesh size M. It becomes clear that $\varepsilon^*_{b_0} = \mathcal{O}(10^{-2})$ is well covered.

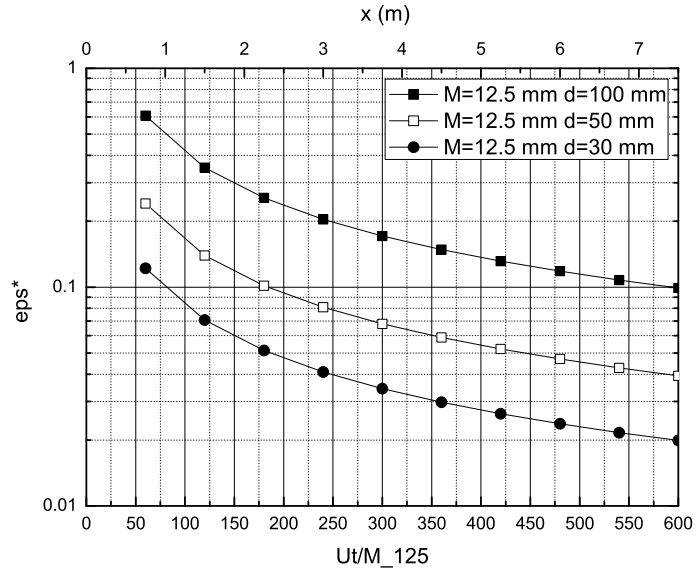

Figure B.4: Graph showing the streamwise evolution of $\varepsilon^*_{b_0}$ as function of $\overline{U}_x t/M$ for $M = 1.25 \cdot 10^{-2}$ m. It takes about 40M for (quasi-)isotropy and (quasi-)homogeneity to develop, see for example Comte-Bellot and Corssin (1966) and Mohamed and Larue (1990).

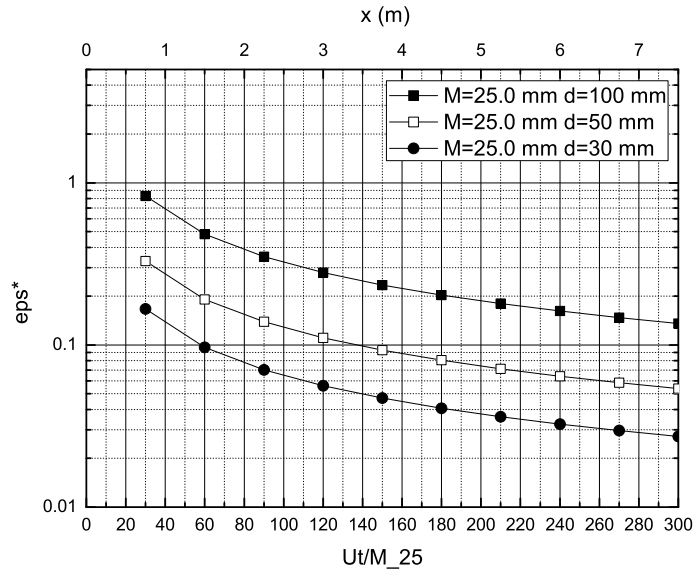

Figure B.5: Graph showing the streamwise evolution of $\varepsilon^*_{b_0}$ as function of $\overline{U}_x t/M$ for $M = 2.50 \cdot 10^{-2}$ m. It takes about 40M for (quasi-)isotropy and (quasi-)homogeneity to develop, see for example Comte-Bellot and Corssin (1966) and Mohamed and Larue (1990).

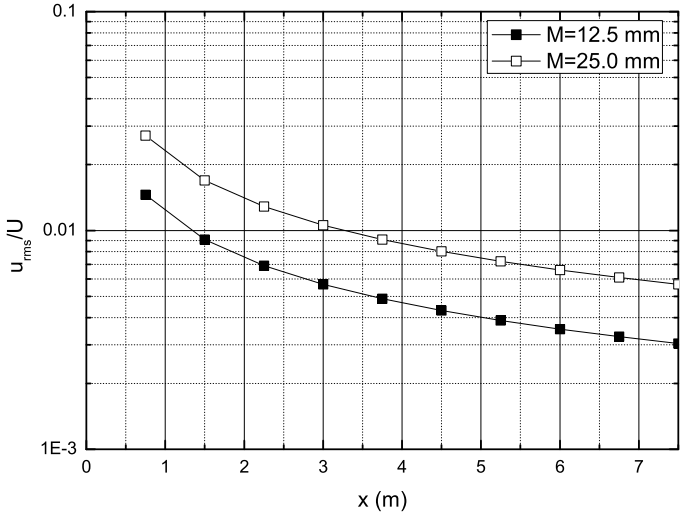

Figure B.6: The streamwise evolution of $\sqrt{\overline{u^2_{rms,x}}}/\overline{U}_x$ is shown as function of x. Variations of 0.005 of the main velocity ($u_{rms,x}/\overline{U}_x = 0.005$) can still be measured with the hotwire measurement technique. This minimum will be approached near the middle of test section of the TU/e wind tunnel Goliath.

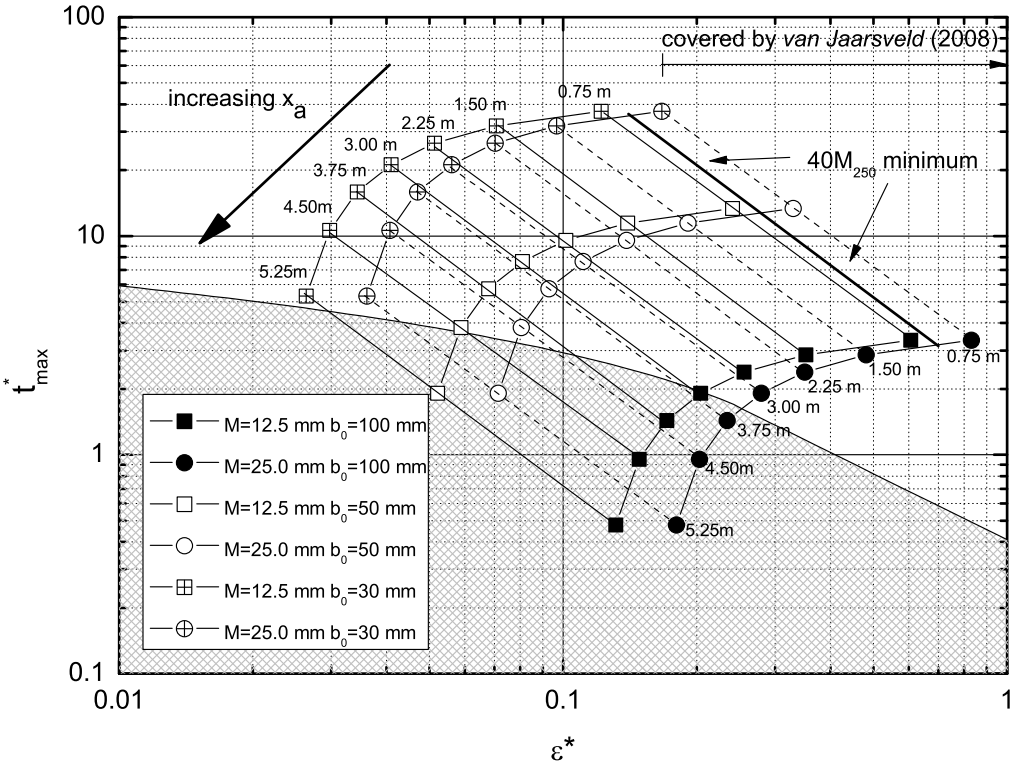

Figure B.7: The values of dimensionless dissipation rate $\varepsilon^*_{b_0}$ and the maximum achievable dimensionless time t^* are presented for two grid configurations and three initial wing-tip separations b_0. The maximum achievable dimensionless time is based on the distance $x_c - x_a$, with x_c the position where an analysis of the trailing vortices is still possible. Here, x_c is set to 6.0 m and is determined by the maximum position at which PIV measurements can be performed in the TU/e wind-tunnel Goliath. For determining the optimal wing location x_a, it is important that the maximum achievable dimensionless time t^* is larger than the lifespan predicted by Crow and Bate (1976). This means that the optimal wing-location lies outside the shaded area. On the other hand, the grid-generated turbulence needs about a distance of 40M before (quasi)-isotropy and (quasi)-homogeneity are developed. In combination with the desired range of $\varepsilon^*_{b_0}$, it can be concluded that two wing locations, $x_a = 3.5$ m and 4.5 m, are appropriate. With the wing location of $x_a = 4.5$ m, it will only be possible to use the wing-tip separation distance of $d = 5.00$ and $3.00 \cdot 10^{-2}$ m.

Appendix C

A Study on the Windtunnel Flow and Grid-Generated Turbulence Characteristics

The study as described in this Appendix considers the characteristics of the TU/e wind tunnel Goliath and the turbulence generated by the turbulence grids with mesh sizes $M = 2.54 \cdot 10^{-2}$ and $1.27 \cdot 10^{-2}$ m. The wind tunnel flow without grid-generated turbulence is denoted by $M000$, and that with the grid-generated turbulence by $M254$ and $M127$ for the turbulence grids with mesh sizes $M = 2.54 \cdot 10^{-2}$ and $1.27 \cdot 10^{-2}$ m, respectively. An extensive motivation for the design of these turbulence grids can be found in Appendix B.

This chapter is organized as follows. We first discuss the experimental setup and the validation of the pressure and turbulence measurement equipment. We then continue with defining a relation between the pressure drop over the contraction and the main stream velocity in the test section. This makes it possible to set the main stream velocity $\overline{U}_x$ in the test section while keeping the test section itself clear of any obstacle that can cause interference with a trailing vortex. In the subsequent section, we discuss the homogeneity of main stream velocity. For this, we analyze the vertical profiles of the main stream velocity at several downstream locations. Turbulence characteristics of grid-generated turbulence ($M254$ or $M127$) and that without grid-generated turbulence ($M000$) are obtained by analyzing the energy spectra. The turbulence intensity, turbulence dissipation rate, and the Taylor Reynolds number are obtained at several downstream locations. We will end this study with a recommendation on the wing location for vortex pair decay in $M254$ or $M127$ grid-generated turbulence. The study of vortex pair decay in turbulence is not performed in this work, but will be executed in a later stage of the TU/e trailing vortex research program.

C.1 Experimental setup

A schematic overview of the TU/e wind-tunnel Goliath is shown in Figure C.1. The equipment used for the measurements is given by apparatus (model number), manufacturer, and serial number:

a) Water manometer, v. Essen Delft, 0154

b) Electronic manometer (1400 1BX), Datametrics Dreser, 310-905

c) Barocel pressure sensor (590D-1kPa-2PI-V1K-4D), Datametrics Dreser, 310-1164

d) Streamline frame (90N10) plus 2 CTA modules (90C10) at pos. 2 and 6, Dantec, 00697

e) Computer, 00728

f) Low noise preamplifier (SR560), Stanford Research Systems, 82093

g) Crosswire signal processing, Parsam

h) Barotron (698A11TRA), MKS, 4XX9-00309954

i) Signal conditioner (760BD81), MKS, 4XX9-00310450

j) Single hotwire, Dantec

k) Temperature sensor, Dantec

The TU/e Goliath wind tunnel has a test section with length $L = 8.00$ m, height $H = 1.05$ m, and width $W = 0.70$ m. An ideal wing location is predicted to be at $x/L = x_a/L = 0.44$ where $x = 0$ corresponds to the entrance of the wind tunnel test section, see Appendix B. We will continue with considering this location as the ideal wing location. The flow field enters the test section after passing the contraction. This contraction is characterized by an area decrease from 18.38 to 0.74 m^2 over a distance of 5.30 m. The pressure drop over this contraction is denoted by $\triangle p_{con}$. This pressure difference is measured with barocel pressure sensor (c) and electronic manometer (b). The electronic manometer is calibrated with water manometer (a).

The velocity is measured with the help of a hotwire. Measurements are performed with a single wire and a crosswire. The crosswire is found to resolve the turbulence scales incompletely, see section C.1.3. Therefore, the crosswire is used for making main stream velocity profiles and determining the isotropy of the turbulence only, see section C.3. All the remaining measurements are performed with the single wire. The Parsam signal processing system is used for the crosswire, while the Dantec system is used for the single wire signal processing. The Parsam signal processing system has a sampling frequency of 20 $\cdot 10^3$ s^{-1}, and is filtered with a low-pass filter of 10 $\cdot 10^3$ s^{-1}. The Nyquist-Shannon sampling theorem is satisfied when the frequency of the low-pass filter equals half of the sampling frequency.

The Dantec system (d) allows one to measure the hotwire signal together with the temperature close to the hotwire. Subsequently, the hotwire signal is filtered by a low noise preamplifier (f). The sampling frequency of the Dantec system equals 100 $\cdot 10^3$s^{-1}. To satisfy the NyquistShannon sampling theorem, the signal is filtered with a low pass filter of 30 $\cdot 10^3$ s^{-1}. The temperature at the hot wire location, the pressure drop over the contraction, and the hotwire signal are monitored with a computer. We did not measure the temperature continuously during a measurement. However, this may be interesting for future measurements since the temperature influences the main stream velocity and the calibration function of the hotwire.

When turbulence is generated, the engine of the wind tunnel fan will experience more resistance. As a result, the engine and therefore the flow through the wind tunnel will warm up. When less turbulence is generated, the engine and the flow through the wind tunnel will cool down. In this way, temperature changes are observed of about one degrees Celcius in one measurement of 600 seconds. The effect of a temperature change is twofold. First, the calibration function becomes incorrect when the temperature deviates from that present during the calibration. When the temperature of the main stream flow decreases, the hotwire cools off more, which is perceived as a velocity increase. The second effect of a temperature change, is that the density of air and therewith the air velocity changes. The density of air increases when the temperature decreases. The velocity $\overline{U_x^2}$ decreases when the density increases, since the pressure drop over the contraction and the dynamic pressure $\rho(T)\overline{U_x^2}/2$ are fixed. It is found that the second effect is stronger than the first effect; the main stream velocity obtained from the hotwire signal decreases, when a decrease in temperature is observed.

It was found that the temperature effect changes the velocity, derived from the hotwire signal, approximately linearly in time. Therefore, a linear correction is applied in obtaining velocity profiles, see section C.3. The averaged main stream velocity is kept constant in all measurements at $\overline{U}_x = 15 \pm 0.5$ m/s.

The total pressure p_t and static pressure p_s in the wind tunnel test section are determined with the help of a pitot tube. The dynamic pressure and therewith the main stream velocity can be derived from the total and static pressure: $\rho\overline{U_x^2}/2 = p_t - p_s$. The pitot tube can be placed at several fixed x-positions with a distance closer than 0.20 m to the hotwire. The main stream flow field is found to be approximately constant close to the hotwire, see section C.3. The pitot tube is aligned parallel to the main stream flow field by finding the maximum value of the dynamic pressure while rotating the pitot tube along its vertical axis. The pressure difference obtained from the pitot tube is processed by signal conditioner (i).

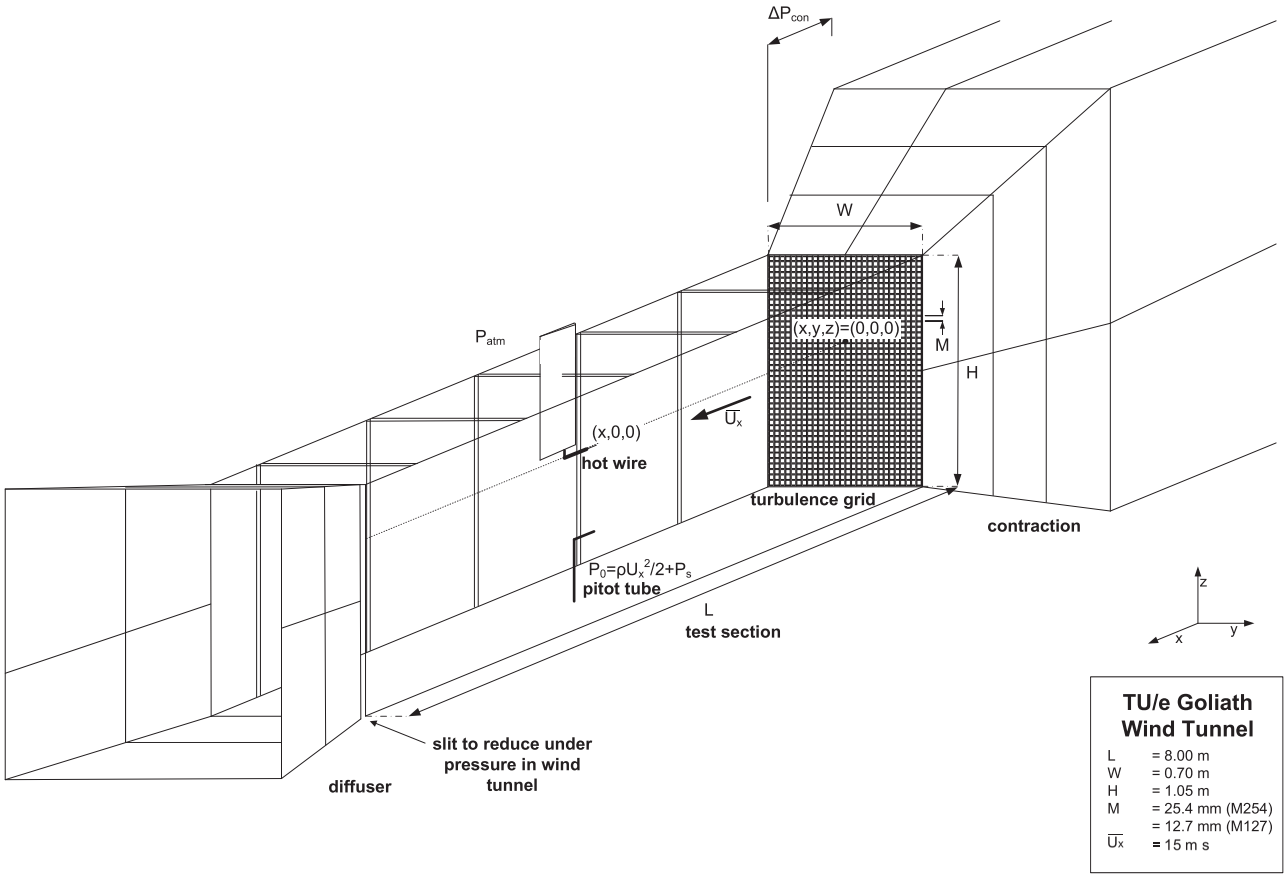

Figure C.1: Schematic view of the TU/e Goliath Windtunnel with the turbulence grid installed. The dimensions of the wind tunnel are given by $L \times H \times W = 8.00 \times 1.05 \times 0.70$ m^3. The contraction is characterized by an area decrease from 18.38 to 0.74 m^2 over a distance of 5.30 m, the relating pressure drop is given by $\triangle p_{con}$. The velocity is determined with the help of the hotwire. The dynamic and static pressure is determined with the help of the pitot tube.

C.1.1 Pressure in the wind tunnel

This work will use the same wind tunnel as Van Jaarsveld (2008) did. However, a slight modification is applied to reduce a severe underpressure in the wind tunnel. A normalized total pressure difference of typically $(p_t - p_{atm})/\triangle p_{con} = -0.30$ for $\triangle p_{con}$ around $200Pa$, was found in the experiments of Van Jaarsveld (2008). The total pressure outside the wind tunnel is equal to the static pressure since there is no velocity, and is denoted by p_{atm}. The total pressure inside the wind tunnel is given by $p_t = p_s + \rho\overline{U_x^2}/2$. The normalized total pressure difference is reduced from -0.30 to -0.05 by applying a sufficiently sized slit at the end of the wind tunnel test section, see Figure C.2. From this, it follows that the normalized static pressure decreases for increasing pressure drop over the contraction. The static pressure also decreases with increasing distance from the grid location. The measurements are performed for the case without grid, that is $M000$.

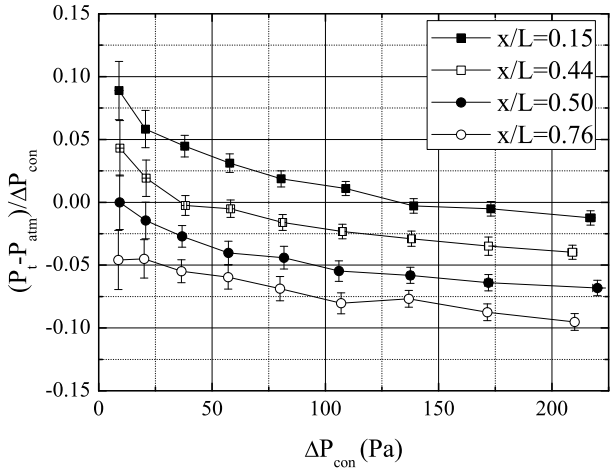

Figure C.2: The normalized total pressure difference $(p_t - p_{atm})/\triangle p_{con} = (p_s + \rho\overline{U_x^2}/2 - p_{atm})/\triangle p_{con}$ obtained at several streamwise positions and a range of pressure drops over the contraction. It can be seen that the typical normalized static pressure level is $(p_t - p_{atm})/\triangle p_{con} = -0.05$ for $\triangle p_{con}$ around 200 Pa.

C.1.2 Validation of electronic manometer

The pressure drop over the contraction is measured with an electronic manometer. The values obtained with the electronic manometer are validated with those obtained with a water-manomenter, see Figure C.3. For every value of the pressure drop over the contraction, a measurement of 60 seconds was performed. The mean pressure and accompanying error are for both the electronic manometer and the water manometer obtained by visual inspection. Four independent series (A,B,C, and D) of increasing pressure drop over the contraction showed that the values obtained with the electronic device and the water manometer are correlated by $\triangle p_{con}^{wat} = (0.990 \pm 0.005)\triangle p_{con}^{elec}$. The offset was found to be 0.0495 ± 0.0002 Pa, which is negligibly small. It is believed that a correlation of 0.990 ± 0.005 is sufficiently accurate, since the intrinsic temporal variations of the pressure drop over the contraction in the wind tunnel is $0.03\overline{\triangle p_{con}}$, see section C.4.1.

C.1.3 Single wire and crosswire

In our experiments, we will measure with a single wire and a crosswire. Both come together with a different experimental setup and signal processing. We will consider the difference between the obtained longitudinal energy spectrum first, see Figure C.4a. The single wire signal is sampled

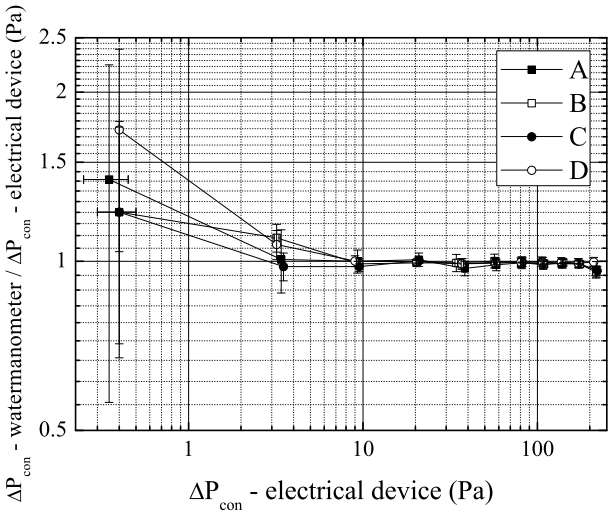

Figure C.3: The values for pressure drop over the contraction as obtained with the electronic manometer are validated against those obtained with the water manometer. For this, we performed four series of measurements A, B, C, and D. These measurements resulted in relation between the values obtained with the water manometer and the electronic manometer of $\triangle p_{con}^{wat} = (0.990 \pm 0.005) \triangle p_{con}^{elec}$*. The offset was found to be* 0.0495 ± 0.0002 *Pa.*

with a frequency of $100{\cdot}10^3$ s^{-1}, while the sampling frequency of the the crosswire setup is limited by 20 $\cdot 10^3$ s^{-1}. The frequency at which noise becomes significant in the longitudinal energy spectrum is found to be $3{\cdot}10^3$ s^{-1} for the crosswire, and $5{\cdot}10^3$ s^{-1} for the single wire. In our case, it means that the turbulence dissipation scales are better covered with the single wire experimental setup, see Figure C.4b. For that reason, we will only use the crosswire experimental setup for making vertical scans of the mean velocity, and for determining the isotropy of the turbulent flow. The single wire is used in the remaining experiment in which velocities are determined.

calibration of single and crosswire

The single and crosswire are both calibrated by defining a fourth order correlation function between the hotwire output voltage and the local air velocity. The local air velocity is derived from the dynamic pressure $\frac{1}{2}\rho(T)\overline{U_x^2}$ and corresponding temperature T. Note that the calibration function depends on the temperature of the flow, and that calibration function becomes invalid when the temperature during a measurements deviates from that used during a measurement.

We will continue with considering two methods that make it possible to determine the main stream velocity at the wing location, without placing a measurement device (hotwire/pitot tube) at that position itself. It is necessary to correlate the main stream velocity at the wing location with a parameter at another position, since it is not desired to place a measurement device close to the wing. First, we will discuss the method of correlating the pressure drop over the contraction with the dynamic pressure at the wing location, from which the main stream velocity can be obtained easily. The second method will be discussed in section C.3.

C.2 Relation between pressure drop over contraction and dynamic pressure

The pressure drop over the contraction $\triangle p_{con}$ can be correlated with the dynamic pressure $(\frac{1}{2}\rho(T)\overline{U_x^2})_a$ in the TU/e Goliath wind tunnel test section at the wing location $x/L = x_a/L = 0.44$.

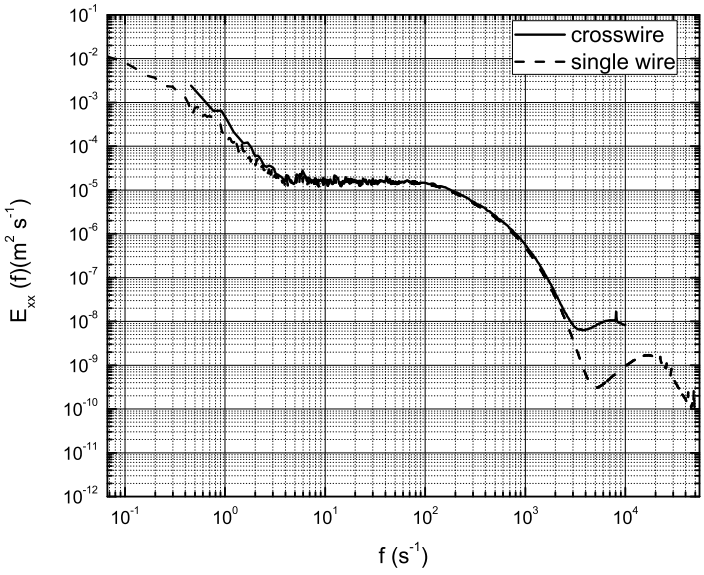

(a) longitudinal energy spectrum

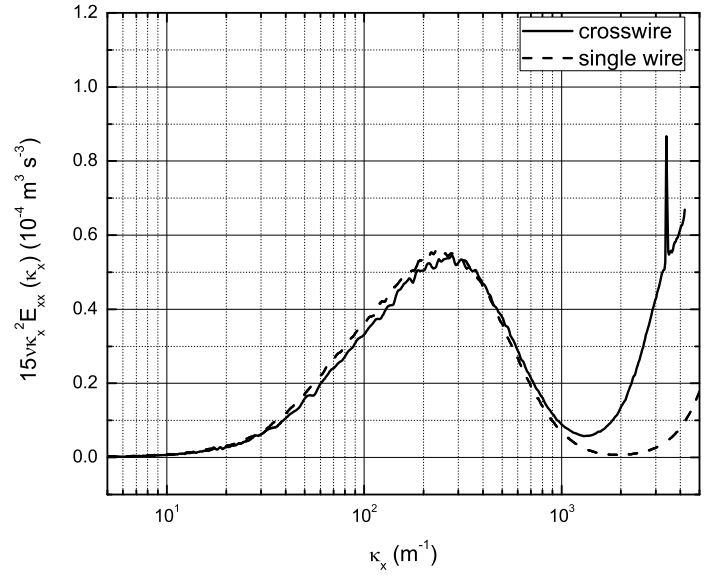

(b) dissipation spectrum

Figure C.4: The longitudinal energy spectrum (a) and dissipation spectrum (b) obtained with the crosswire and single wire for the turbulence at $x/L = x_a/L = 0.44$ generated with the M127 grid. The crosswire has a lower frequency at which noise starts to dominate the dissipation spectrum. From the dissipation spectrum, it can be concluded that the single wire signal processing captures the highest frequencies contained in the turbulence without a significant contribution of noise. The crosswire is only used for making vertical scans of the main stream velocity, and for determining the isotropy of the flow at different streamwise positions.

In this way, the main stream velocity at the wing location can be set by adjusting the pressure drop over the contraction while keeping the test section clear of any main stream velocity measurements devices. To define a relation between the pressure drop over the contraction and the main stream velocity, we have to assume that $\overline{U}_x^2 = \overline{U_x^2}$ which is allowed since the main stream fluctuations are only about 1%. Note that the dynamic pressure does not depend on temperature variations, while the density and therefore the velocity do. The correlation between the pressure drop over the contraction and the dynamic pressure is determined for a specific range of $\triangle p_{con}$ both with grid ($M254$ and $M127$) and without grid ($M000$), see Figure C.5. For every value of the pressure drop over the contraction, a measurement of 60 seconds was performed. The dynamic pressure is determined with the help of the pitot tube:$\rho\overline{U_x^2}/2 = p_t - p_s$. It was found that the correlation between $\triangle p_{con}$ and $(\frac{1}{2}\rho(T)\overline{U_x^2})_a$ is given by:

$$M000: \quad (\tfrac{1}{2}\rho(T)\overline{U_x^2})_a = (1.0572 \pm 0.0004) \cdot \triangle p_{con} - (0.01 \pm 0.02), \tag{C.1}$$

$$M127: \quad (\tfrac{1}{2}\rho(T)\overline{U_x^2})_a = (1.055 \pm 0.001) \cdot \triangle p_{con} + (0.08 \pm 0.05), \tag{C.2}$$

$$M254: \quad (\tfrac{1}{2}\rho(T)\overline{U_x^2})_a = (1.048 \pm 0.001) \cdot \triangle p_{con} + (0.12 \pm 0.03). \tag{C.3}$$

These correlation make it possible to determine the velocity from the pressure drop over the contraction, when the temperature T is known. The offset is very small compared to the levels of dynamic pressure, which are typically of $\mathcal{O}(10^2)$. This supports the correlation between the dynamic pressure and the pressure drop over the contraction. The error in the correlation parameters is negligible, when compared to the intrinsic spatial or temporal variations of the wind tunnel main stream velocity, see section C.4.1 or C.3. The spatial or temporal variations of the main stream velocity are about $0.01\overline{U}_x$.

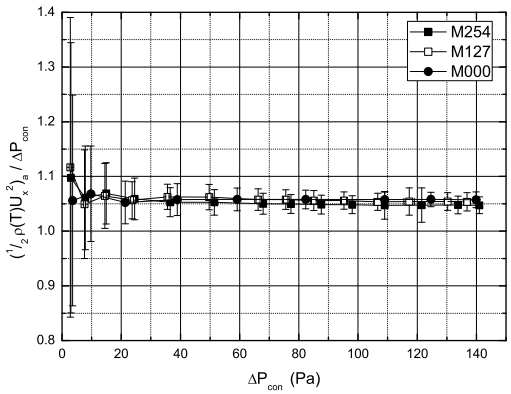

Figure C.5: The relation between $\triangle p_{con}$ and $(\frac{1}{2}\rho(T)\overline{U_x^2})_a$ is linear for the cases with grid (M254 and M127) and without grid (M000). The well defined correlation between the pressure drop over the contraction, and the dynamic pressure makes it possible to set the main stream velocity without a measurement device (pitot tube/ hotwire) at the wing location itself.

C.3 Homogeneity of main stream flow

In this section, we will consider the main stream velocity profiles at several streamwise locations. This will give us information about the homogeneity of the main stream flow field. The profiles are obtained in the z-direction with $y = 0$. The hotwire is transferred every 30 seconds to a new z-positions until the desired range of z-positions is covered. A coarse profile with $\triangle z = 20$ mm is obtained at six downstream positions between $x = /L0.12$ and $0.81L$. Note that $\triangle z = 20$ mm

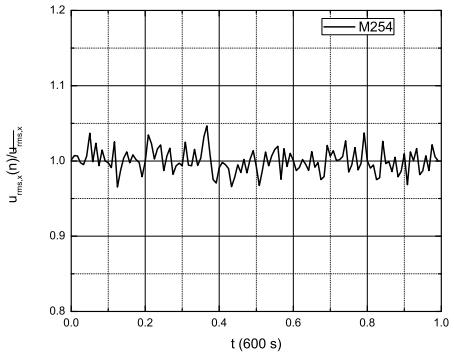

(a) M254, blocks of five s.

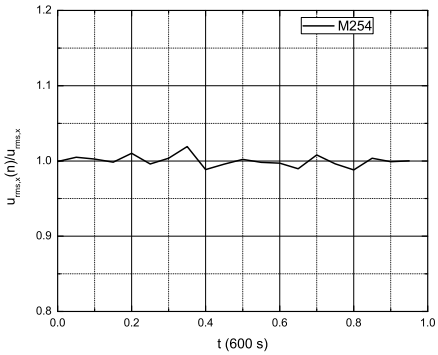

(b) M254, blocks of thirty s.

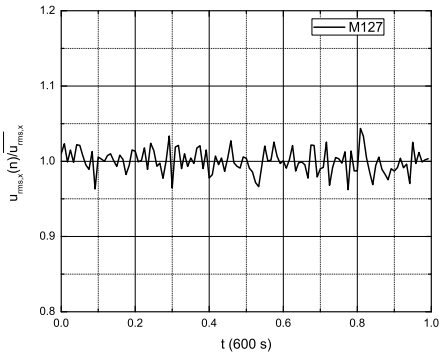

(c) M127, blocks of five s.

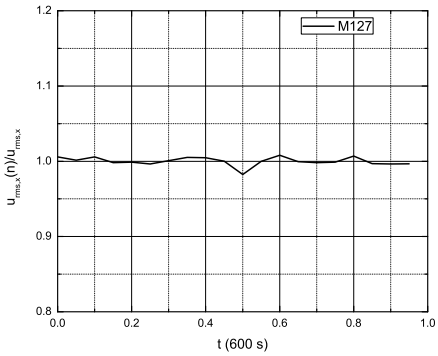

(d) M127, blocks of thirty s.

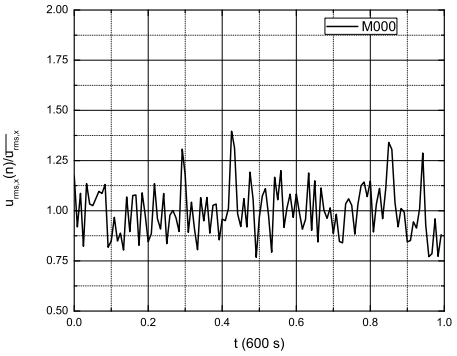

(e) M000, blocks of five s.

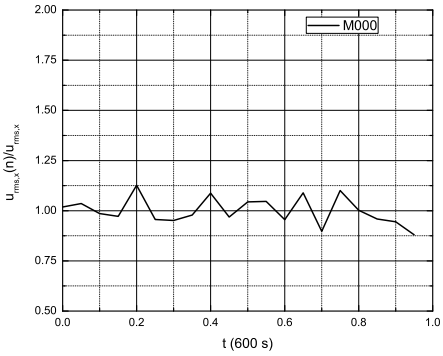

(f) M000, blocks of thirty s.

Figure C.6: The variations of the root-mean-square velocity between blocks of five seconds determined according to Eq. C.16 for the case with (M254 and M127) and without grid-generated turbulence (M000). The measurements are performed at $x_a = 0.44L$ and $y, z = 0$. For the case with grid-generated turbulence, the variation of the root-mean-square velocity between blocks of five seconds is about $0.03\overline{u_{rms,x}}$.

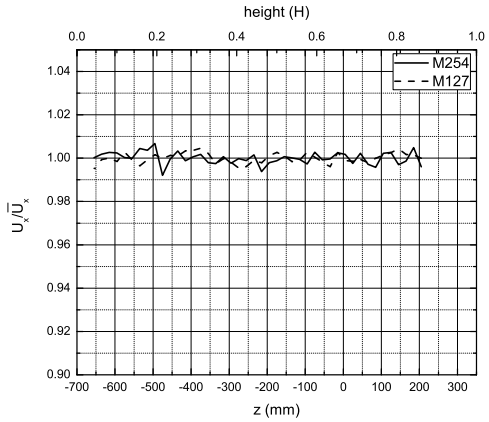

(a) $x/L = 0.19$

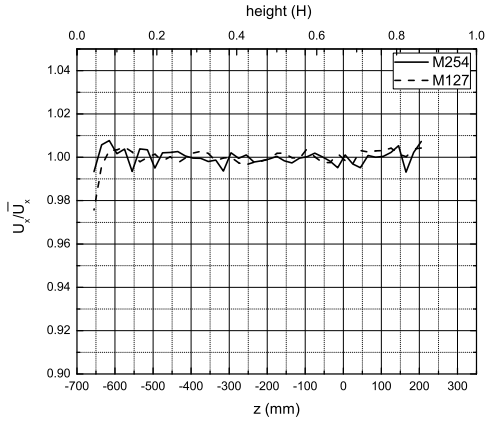

(b) $x/L = x_a/L = 0.44$

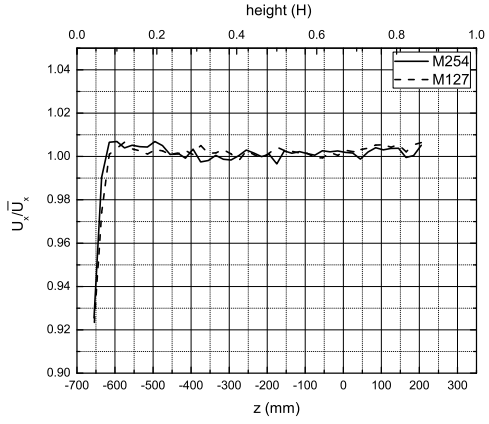

(c) $x/L = 0.69$

Figure C.7: Profiles of the normalized main stream velocity for the M254 and M127 grid, for three different streamwise distances and $y = 0$. The location of the wing equals $z = 0$, and the wind tunnel height H goes from z=-700 till z=350mm. The distance between two scan locations equals $\triangle z-$ 20 mm. One can see that a boundary layer develops in streamwise direction. It is believed that the development of the boundary layer is similar for the top and bottom of the wind tunnel. The velocity increase/decrease due to a temperature change is corrected with a linear correction function.

gives us a resolution of approximately $0.8M$ for the $M254$ and $1.6M$ for the $M127$ grid. The coarse profile gives information about the boundary layer development and the homogeneity of the main stream flow field. The velocity profiles for $x/L = 0.18$, 0.44, and 0.69 are shown in Figure C.7 for the case with $M254$ and $M127$ grid. It can be seen that the thickness of the boundary layer increases from smaller than 50 mm at $x/L = 0.19$, to 75 mm at $x/L = x_a/L = 0.44$, and almost 100 mm at $x/L = 0.69$. The development and thickness of the boundary layer seems to be independent of the grid. It was practically impossible to cover the complete height H of the wind tunnel test section from $z = -700$ till $z = 350$ mm However, we assume that the profiles are symmetric, and that the boundary layers are similar for the top and bottom. The wing location $z = 0$ is believed to be situated far enough from the boundary layer for the whole length of the test section. Outside the boundary layers, the velocity profile is flat with deviations of $0.005\overline{U}_x$ from the average main stream velocity. This is most likely caused temporal variations in the main stream velocity in combination with a limited averaging period per z-position of 30 seconds. The temporal variations in the main stream velocity are namely of U'_x =$0.005\overline{U}_x$.

A fine coarse profile is obtained with a resolution of $\triangle z = 2.5$ mm. This implies a resolution of approximately $0.1M$ for the $M254$ and $0.2M$ for the $M127$ grid. This provides information about the grid footprint on the main stream flow field, or in other words, the extent to which turbulence is developed. If no grid footprint is observed, it is assumed that the turbulence is (quasi-)isotropic and (quasi-)homogeneous. Comte-Bellot and Corssin (1966) and Mohamed and Larue (1990) found that it takes about 40M for grid-generated turbulence is developed. Therefore, the velocity profile is obtained at $x/L = 0.12$ and $x/L = 0.18$, which is about $40M$ and $60M$ for the $M254$ and $80M$ and $120M$ for the $M127$ grid. The range of z-positions is chosen to be from $z = -275$ to -75 mm, covering about $8M$ in case of the $M254$ and $16M$ in case of the $M127$ grid. The z-positions are located around $z = -175$ mm, which equals the centerheight of the wind tunnel test section. It is believed that at the centerheight, the grid-generated turbulence requires the longest distance for its development.

The fine profiles of the main stream velocity at $x/L = 0.12$ for the case with grid ($M254$ and $M127$) and without grid ($M000$) are shown in Figure C.8. From this, it follows that no recognizable grid footprint is present in the main stream velocity profile. This suggests that the grid-generated turbulence is (quasi-)isotropic and (quasi-)homogeneous from $x/L = 0.12$. Turbulence characteristics like the intensity and dissipation rate will be obtained for streamwise positions starting from $x/L = 0.12$. It is reasonable that the turbulence becomes (quasi-)isotropic and (quasi-)homogeneous at a distance closer to the grid, especially for the $M127$ grid. However, due to practical reasons we stay fixed with $x/L = 0.12$ as the closest measurement position from the grid. The velocity profile is flat with deviations of $0.007\overline{U}_x$ from the average main stream velocity. Again, this is most likely caused by a combination of temporal variations in the main stream velocity and a limited averaging period per z-position of 30 seconds. Temporal variations of $U'_x = 0.005\overline{U}_x$ are namely found in the main stream velocity.

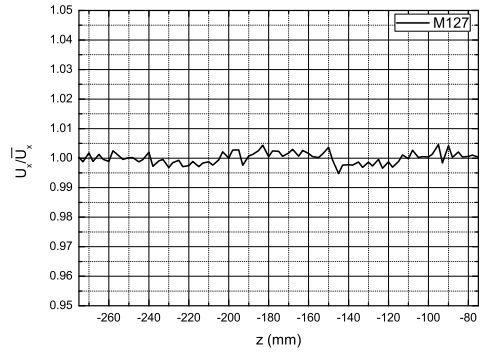

(a) $x/L = 0.12 \approx 80M/L$

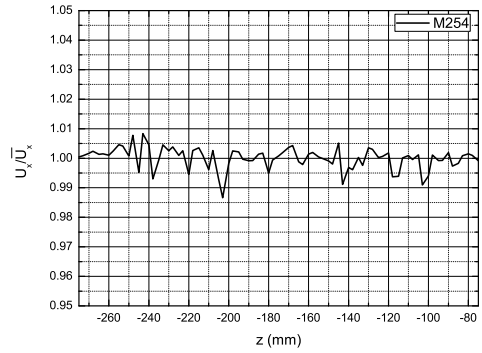

(b) $x/L = 0.12 \approx 40M/L$

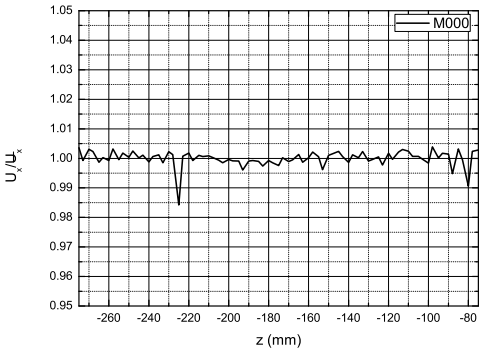

(c) $x/L = 0.12$

Figure C.8: The fine profiles of the main stream velocity for the case with grid (M254 and M127) and without grid (M000) at $x/L = 0.12$ and $y = 0$. The location of the wing equals $z = 0$, and the wind tunnel height H goes from $z = -700$ till $z = 350$ mm. One can see that there is a negligible grid foot print at $x/L = 0.12$. The profile resolution is set to 2.5 mm, which equals approximately $0.1M$ for the M254 and $0.2M$ for the M127 grid. A measurement of 30 seconds is performed at every position. This means that temporal variations of the mean stream velocity, with $U'_x = 0.005\overline{U}_x$, may here be interpreted as spatial variations in the velocity profile. One can prevent this by measuring for a longer period at every position, however, this is not possible due to practical reasons.

C.4 Turbulence characteristics

We will now proceed with discussing the turbulence characteristics. It will become clear that various non-turbulence contributions are present in the energy spectra. The influence of these contributions on the turbulence will be analyzed. After that, we discuss the turbulence intensity, the turbulence dissipation rate, the isotropy of turbulence, and the Taylor Reynolds number.

C.4.1 Energy spectra

An energy spectrum of the flow field gives information about the temporal and spatial scales contained in the flow. With this information, characteristics of the turbulent flow field can be determined. The energy spectrum is obtained at 12 streamwise locations (with $y, z = 0$) for the case without ($M000$), and with ($M127$ or $M254$) grid installed. Here, we will only discuss the spectra obtained at the wing location $x_a = 0.44L = 3.55$ m. All the spectra are obtained by measurements of 600 seconds, in which 20 spectra obtained from blocks of 30 seconds are averaged. In this way, we set the bandwidth of captured frequencies between $6.7{\cdot}10^{-2}$ and $50{\cdot}10^{3}$ s^{-1}. These frequencies are determined by the Nquist theorem in combination with the size of the blocks (lower frequency) and the sampling frequency (upper frequency).

The longitudinal energy spectrum is given for $M000$, $M127$, and $M254$ in Figure C.9. Here, the longitudinal energy $E_{xx}(f)$ is defined by:

$$\overline{u^2_{rms,x}} = u^2_{rms,x} = \int_0^\infty E_{xx}(f)df. \tag{C.4}$$

With this, we use the same definition as Pope (2000). The influence of the grid-generated turbulence in the energy spectrum becomes obvious when $M000$ is compared to $M127$ or $M254$. The turbulent flow field has a significant contribution from 2 s^{-1} and higher. The turbulence bandwidth is found to be between 2 and 4.775 s^{-1}. Note that 4.775 s^{-1} corresponds to a wavenumber of $2 \cdot 10^3 m^{-1}$. This value corresponds to the transition between contributions of turbulence dissipation and high frequency noise in the dissipation spectrum, see Figure C.4. The Taylor hypothesis is used for conversion between the frequency and wavenumber domain

$$\kappa_x = \frac{2\pi f}{\overline{U}_x}, \tag{C.5}$$

which is only valid when $\overline{u'_{rms,x}}/\overline{U}_x \ll 1$. In our experiments, $\overline{u'_{rms,x}}/\overline{U}_x = \mathcal{O}(5 \cdot 10^{-3})$, with $\overline{U}_x \approx 15$ m/s.

The characteristics of the grid-generated turbulence can be compared with literature by non-dimensionalizing the energy spectrum. This will be done in section C.4.1. Besides the presence of turbulence in the energy spectrum, there are three peculiar contributions that need to be considered. The low-frequency contributions below 2 s^{-1}, the mid-low frequency peak around 5 s^{-1}, and the high noise frequency from approximately 4.775 s^{-1} will be discussed in section C.4.1. After that, we will derive some characteristic turbulence parameters like the turbulence intensity and the turbulence dissipation rate as function of the streamwise distance.

Nondimensional energy spectra

According to the first Kolmogorov hypothesis, velocity statistics pertaining to the universal equilibrium range have a universal form that is uniquely determined by the turbulence dissipation rate ε and the kinematic viscosity ν, see Pope (2000). In this way, one can use ε and ν or ε and the wavenumber κ to non-dimensionalize $E_{xx}(\kappa_x)$. Note that κ can be used since $(\nu/\varepsilon^3)^{1/4}$ gives the Kolmogorov length scales, see Pope (2000). With ε and ν, one can non-dimensionalize the

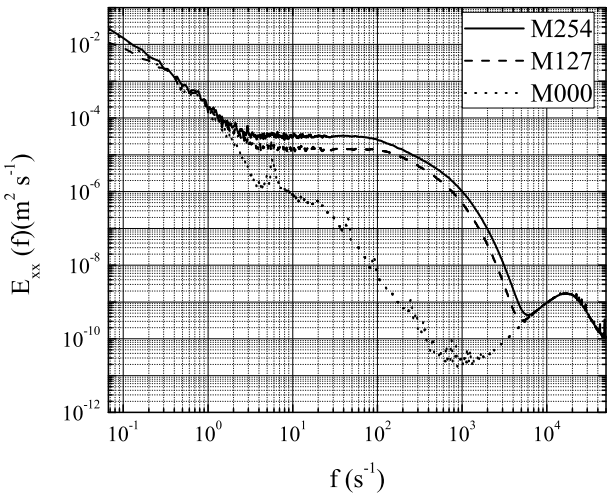

(a)

Figure C.9: The longitudinal energy spectrum is shown for the case with grid (M254 and M127) and without grid (M000). The measurements are performed at the distance $x/L = x_a/L = 0.44$ and $y, z = 0$. The spectrum is obtained by averaging over 20 spectra obtained with a 30 seconds measurement. The turbulence bandwidth is found to be between 2 and 4.775 s^{-1}; note that 4.775 s^{-1} corresponds to a wavenumber of 2 $\cdot 10^3$ m.

longitudinal energy spectrum by

$$E_{xx}(\kappa_x) = \varphi(\kappa_x \eta)(\varepsilon \nu^5)^{1/4}, \tag{C.6}$$

where $\varphi(\kappa\eta)$ is a universal non-dimensional function - the Kolmogorov spectrum function. Using ε and κ to non-dimensionalize $E_{xx}(\kappa_x)$, one obtains

$$E_{xx}(\kappa_x) = \Psi(\kappa_x \eta)\varepsilon^{2/3}\kappa_x^{-5/3}, \tag{C.7}$$

in which $\Psi(\kappa_x\eta)$, the compensated Kolmogorov spectrum function, is nondimensional and universal. The Kolmogorov spectrum function and the compensated Kolmogorov spectrum function for the $M127$ and $M254$ grid are given in Figure C.10 and C.11, respectively. The Kolmogorov length scale and turbulence dissipation rate are found to be $\eta = 5.7 \cdot 10^{-4}$ m and $\varepsilon = 3.2 \cdot 10^{-2}$ m^{2}s^{-3} for the $M127$ grid, and $\eta = 4.7 \cdot 10^{-4}$ m and $\varepsilon = 6.7 \cdot 10^{-2}$ m^{2}s^{-3} for the $M254$ grid. The turbulence dissipation rate is determined by integrating the dissipation spectrum

$$\varepsilon = 15\nu \int_0^\infty \kappa_x^2 E_{xx}(\kappa_x) d\kappa_x, \tag{C.8}$$

in which the kinematic viscosity equals $\nu = 1.5 \cdot 10^{-5}$ m^2/s. The Kolmogorov length scale is determined by Kolmogorov relation $\eta = (\nu^3/\varepsilon)^{1/4}$.

The Kolmogorov spectrum function obtained for the $M127$ and $M254$ grid closely match each other in the inertial subrange and dissipation range, that is $\kappa_x \eta > 3 \cdot 10^{-2}$. The Kolmogorov spectrum functions correspond closely to those found in literature, see Pope (2000) Fig 6.14. The second Kolmogorov hypothesis states that the motions in the inertial subrange are dominated by inertial effects, and that viscous effects are negligible. This means that in the inertial subrange, $E_{xx}(\kappa_x)$ has a universal form uniquely determined by ε, independent of ν. As a consequence, the compensated Kolmogorov spectrum function, tends to a constant value in the inertial subrange. This constant is empirically found to be approximately 0.49, see Pope (2000). In our experiments, a value of 0.40 for the $M127$ grid and 0.45 for the $M254$ grid is found, see Figure C.11. Note

that the inertial subrange has a very small bandwidth. This is characteristic for low intensity turbulence, that is turbulence with a low Taylor Reynolds number. A plateau in the compensated Kolmogorov spectrum function, indicating a larger bandwidth of the inertial subrange, can be found for more intense turbulence, see Pope (2000) Figure 6.17.

The compensated Kolmogorov spectrum function obtained from the $M127$ and $M254$ grid, closely match for $\kappa_x \eta > 2 \cdot 10^{-1}$ which represents the dissipation range. This emphasizes the universal character of the compensated Kolmogorov spectrum function for high wavenumbers, that is the dissipation range.

Comparison with the nondimensional energy spectra functions found in literature, see Pope (2000), shows no abnormalities. However, the longitudinal energy spectrum given for $M000$, $M127$, and $M254$ show some peculiar non-turbulent contributions, see Figure C.9. We will continue with discussing these contributions and the influence of these on turbulence.

Non-turbulence contributions to the energy spectrum

The turbulence bandwidth is found to be between 2 and 4.775 s^{-1}. We will discuss three non-turbulent contribtions to the energy spectrum. These are the low-frequency contributions below 2 s^{-1}, the mid-low frequency peak around 5 s^{-1}, and the high noise frequency from 4.775 s^{-1}, see Figure C.9.

high-frequency noise at $f >$ 4.775 s^{-1}: noise of experimental setup

The high frequency noise at $f >$ 4.775 s^{-1} (note that $f = 4.775 \cdot 10^3$ s^{-1} corresponds to a wavenumber of $2 \cdot 10^3 m^{-1}$) is caused by the noise of the experimental setup that comes together with the hotwire. It is important to ensure that high significant frequencies in the turbulence spectrum are not dominated by this noise. This can be tested by analyzing the dissipation spectrum. The dissipation range contains namely the highest frequencies, and if the high frequency noise significantly contaminates the turbulence spectrum, it can be seen in the dissipation spectrum $15\nu\kappa_x^2 E_{11}(\kappa)$. We determine the eddy dissipation rate by integrating the dissipation spectrum, see Eq. C.8. The dissipation spectrum is shown in Figure C.12. It can be seen that the high frequency noise does not significantly contaminate the dissipation range of the turbulence.

midlow-frequency noise around $f = 5$ s^{-1}

The longitudinal energy spectrum of the flow field as obtained without grid ($M000$) at the distance $x/L = x_a/L = 0.44$ and $y, z = 0$ is given in Figure C.9. At about 5 s^{-1} there is a peak which can be noted in the longitudinal energy spectrum of the flow field as obtained with the $M127$ and $M254$ grid installed. This contribution is more obvious in the case of the $M127$ grid.

It was hypothesized that the origin of the contribution had to be found in the mechanical vibration of the wind tunnel. It may be the case that the hotwire is vibrating together with the wind tunnel (the hotwire setup is positioned on the wind tunnel), or that the wind tunnel passes the vibration towards the flow field. In other words, there may be a direct or indirect contamination of the hotwire signal.

Our hypothesis is tested by determining the energy spectrum of the vibrating wind tunnel. This is done with the help of a laser distance meter, directed from a fixed position towards a wooden wall or window of the vibrating wind tunnel. An energy spectrum is derived from the signal from the laser distance meter. In this way, the dominant frequencies of the vibrating wind tunnel are retrieved, see Figure C.13. Here, the energy spectrum of the grid-generated turbulence, the flow field of the wind tunnel without a grid, and the window is shown. All measurements are performed at the distance $x/L = x_a/L = 0.44$. This means that the laser distance meter was

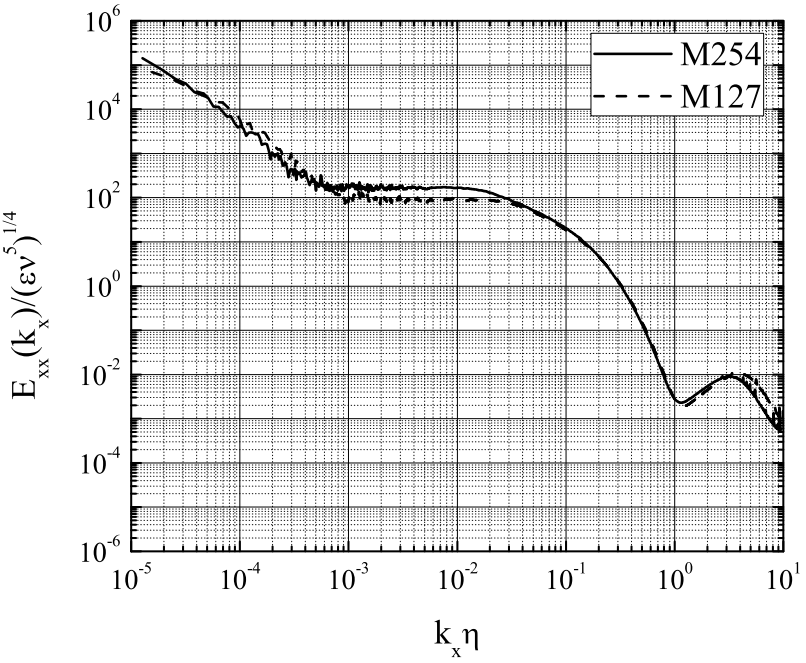

(a)

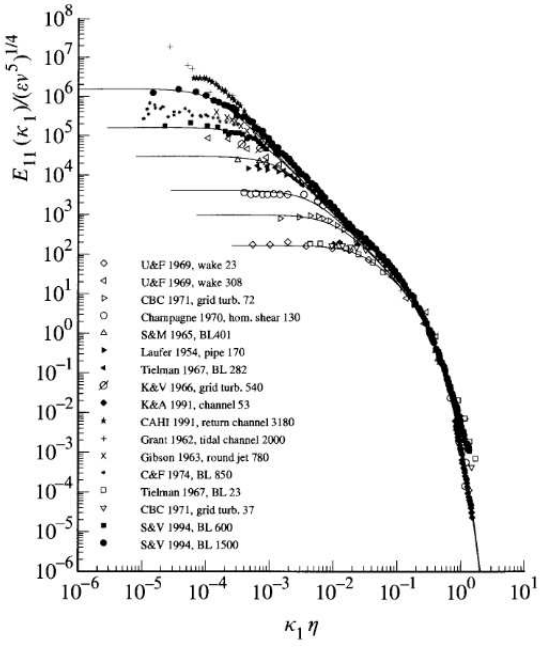

(b)

Figure C.10: a) One-dimensional Kolmogorov spectrum function $\varphi(\kappa_x\eta)$ is shown for the M127 and M254 grid at the distance $x/L = x_a/L = 0.44$ and $y, z = 0$. A close match of the M127 and M254 data for $\kappa_x\eta > 3 \cdot 10^{-2}$ indicates the universal character of the dissipation range. The contribution to the spectrum for $\kappa_x\eta > 1$ is due to high frequency noise, see C.4.1. b) Figure 6.14 of Pope (2000) is shown for comparison with one-dimensional Kolmogorov spectrum function obtained in other turbulence experiments. The final number in the legend is the value of the Taylor Reynolds number. Our data closely matches the data of the experiments performed by U&F, 1969 with Taylor Reynolds number of 23.

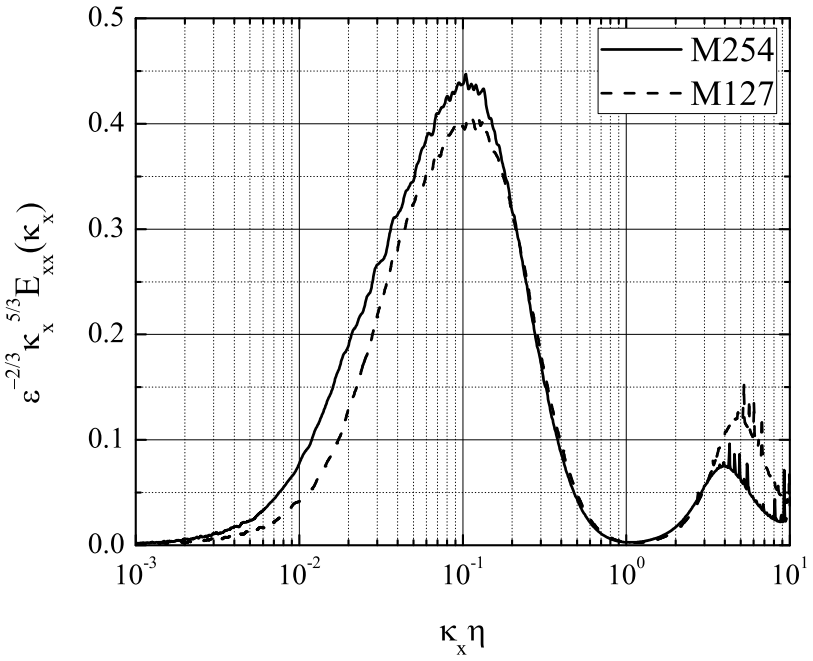

(a)

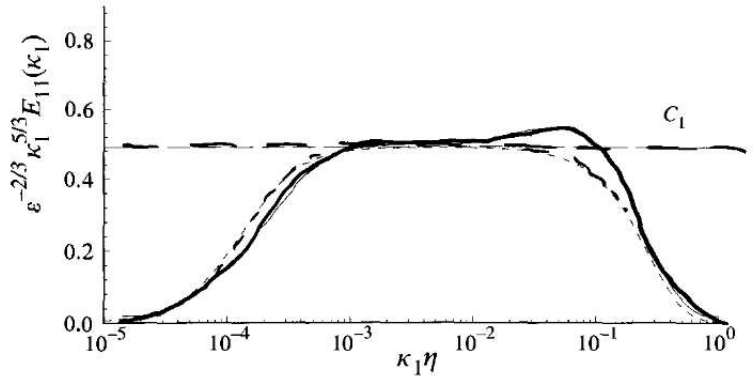

(b)

Figure C.11: a) Compensated one-dimensional Kolmogorov spectrum function $\Psi(\kappa_x\eta)$ is shown for the M127 and M254 grid at the distance $x/L = x_a/L = 0.44$ and $y, z = 0$. The universal character of the dissipation range is emphasized by the close match for $\kappa_x\eta > 2 \cdot 10^{-1}$ between the spectrum of M127 and M254. The contribution to the spectrum for $k_x\eta > 1$ is due to high frequency noise, see C.4.1. b) Figure 6.17 of Pope (2000) is shown for comparison with one-dimensional compensated Kolmogorov spectrum function obtained in a turbulent boundary layer at a Taylor Reynolds number of 1,450. The data is originally from experiments performed by Saddoughi and Veeravalli (1994). In our experiments, the spectrum does not show a plateau at the level of 0.49, which represents the inertial subrange, see Pope (2000). This is due to a very low Taylor Reynolds number, which means that the inertial subrange is contained in a smaller bandwidth.

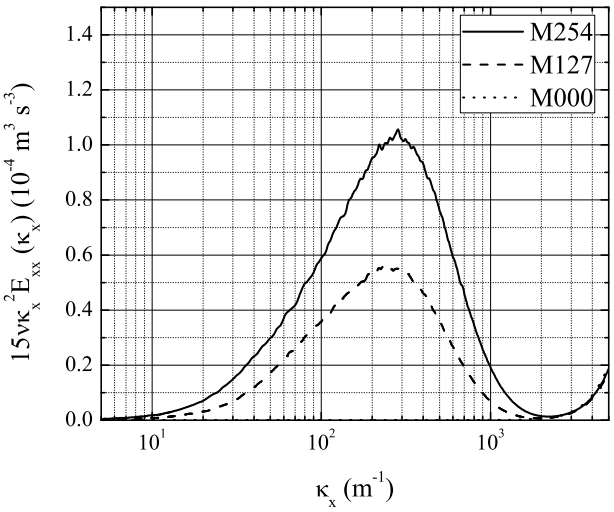

(a)

Figure C.12: The dissipation spectrum $15\nu\kappa_x^2 E_{11}(\kappa)$ is shown for the case with grid (M254 and M127) and without grid (M000). The measurements are performed at $x_a = 0.44L$ and $y, z = 0$. It can be seen that the high frequency noise does not significantly contaminates the dissipation range of the turbulence.

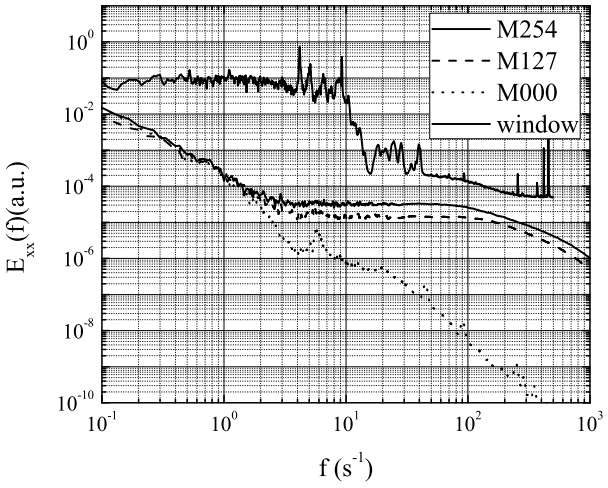

(a)

Figure C.13: The peaks present around $f = 5s^{-1}$ may be caused by the vibration of the wind tunnel itself. The vibration of the wind tunnel is measured by scanning the distance from a fixed point to a vibrating window of the wind tunnel, and transforming that time-varying signal to an frequency spectrum.

directed at a window of the wind tunnel test section. Note that an arbitrary scale is applied at the vertical axis. The laser distance meter is also placed at different locations, including the wooden walls and other windows of the test section. It was found that the energy spectra obtained at different locations, contain the same characteristics.

While the energy spectrum of the flow field shows a peak at 6 s^{-1}, the window spectrum shows several peaks around 5 s^{-1}, but not at 6 s^{-1} itself. This makes the vibration of the wind tunnel as cause for the midlow frequency noise debatable. There may be an underlying process that is the cause for the midlow frequency noise, for example periodic vortex shedding in the diffuser.

The wind tunnel test section is succeeded by the diffuser. The diffuser consists of a diverging flow channel in which the flow slows down. Ideally, the flow keeps attached to the diverging walls and slows down in a laminair fashion. This is not the case in our wind tunnel. The angle under which the walls diverge is too big. An adverse pressure gradient arises and the flow detaches and forms a vortex. At the moment that his vortex is created, the reason for its existence disappears. The vortex breaks down and it all starts again from the beginning. The frequency of the vortex shedding is unknown but is estimated by visual inspection to be $\mathcal{O}(10\ \mathrm{s}^{-1})$. Visual inspection is performed by placing little pennons on the diffuser wall where vortex shedding takes place. A contamination of the upstream flow field in the test section is likely. Further analysis has to retrieve the frequency of the vortex shedding, and determine its contribution to the energy spectrum and its influence on turbulence characteristics.

low-frequency noise for f$< 2\mathrm{s}^{-1}$

The low frequency noise from f <2 s^{-1} is the third non-turbulent contribution to the longitudinal energy spectrum that will be discussed. Starting from 2 s^{-1}, the contribution to the energy spectrum increases for decreasing frequencies, see Figure C.9. This means that slow fluctuations are present in the flow field. When the main stream velocity is written as:

$$U_x(t) = \overline{U}_x + U'_x(t) + u'_{rms,x}(t), \tag{C.9}$$

we identify the non-turbulence fluctuations with $U'_x(t)$ and the turbulence fluctuations with $u'_{rms,x}(t)$. The low frequency noise from $f < 2\ \mathrm{s}^{-1}$ corresponds to non-turbulence variations $U'_x(t)$. When the main stream velocity is sampled with a frequency of 1 s^{-1}, we may assume that $u'_{rms,x}(t) = 0$ since frequencies of $f > 2\mathrm{s}^{-1}$ are filtered out. In this way, $U_x(t) = \overline{U}_x + U'_x(t)$ is given in Figure C.14a, c, and e. The main stream velocity is measured during 600 seconds at the distance $x/L = x_a/L = 0.44$ and $y, z = 0$ with grid ($M254$ and $M127$) and without grid ($M000$). The mean main stream velocity is in all measurements kept between $\overline{U}_x = 15 \pm 0.5$ m/s. Variations in the main stream velocity U'_x are believed to occur in two ways. First, the main stream velocity changes due to a changing temperature during a measurement. The temperature change has an influence on the main stream velocity, but not on the pressure drop over the contraction. In the second place, the main stream velocity and the pressure drop over the contraction can change sporadically but suddenly. This may be caused by the flow through the diffuser. It was found that vortex shedding occurs for most of the time. However, when the flow keeps suddenly attached to the diffuser wall, no vortex shedding will occur, which will suddenly influence the main stream velocity. The other way around is also possible. When the extent of vortex shedding suddenly increases, it will suddenly influence the main stream velocity as well. These changes in the main stream velocity occur sporadically but suddenly. This means that it will contribute to the full bandwidth of the energy spectrum. Since these fluctuations are not recognized as turbulence, we need to ensure that these fluctuations do not influence the turbulence characteristics. This will be considered in the next section.

To summarize, we discussed three frequency ranges of the energy spectrum in which non-turbulence contribution are found. We believe that the non-turbulence contributions are caused by different processes:

- The high frequency noise at $f > 4.775\ \mathrm{s}^{-1}$ is caused by noise of the experimental setup;
- It was hypothesized that the midlow frequency noise around $f = 5\ \mathrm{s}^{-1}$ is caused by mechanical vibrations of the wind tunnel. Although the wind tunnel vibrates with a frequency around $f = 5\ \mathrm{s}^{-1}$, no exact match in the energy spectrum is found. The periodic vortex shedding may be the reason for the midlow frequency noise around $f = 5\ \mathrm{s}^{-1}$. Further analysis is necessary to confirm this hypothesis;

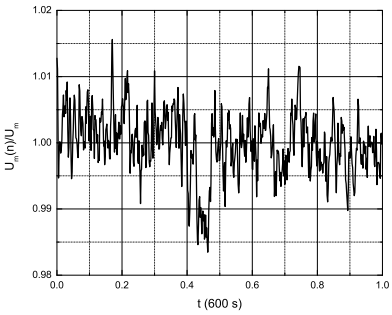

(a) main stream velocity for M254 case

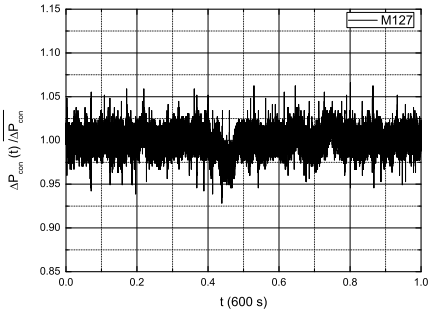

(b) pressure drop over contraction for M254 case

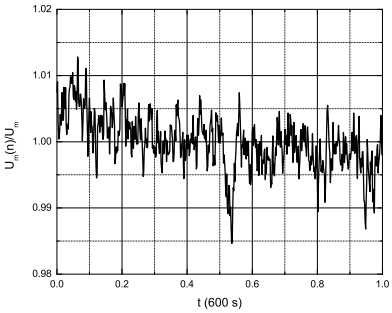

(c) main stream velocity for M127 case

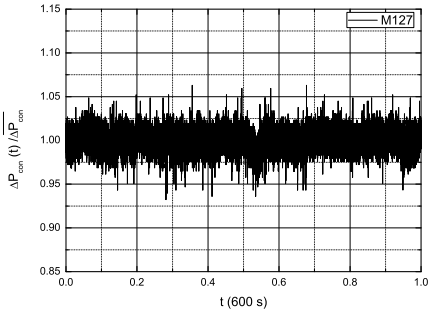

(d) pressure drop over contraction for M127 case

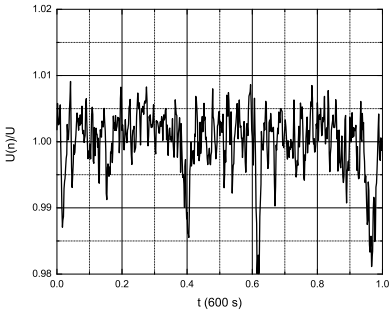

(e) main stream velocity for M000 case

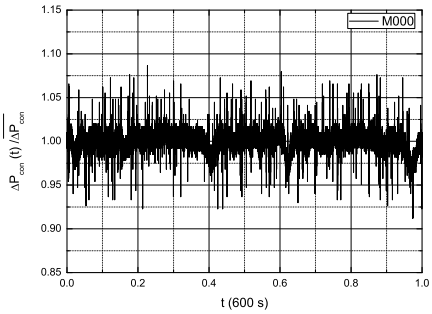

(f) pressure drop over contraction for M000 case

Figure C.14: The main stream velocity and the pressure drop over the contraction for the M127 grid are plotted as function of the time. The main stream velocity is measured at $x_a/L = 0.44$ and $y, z = 0$. The averaged main stream velocity is kept constant in all measurements at $\overline{U}_x = 15 \pm 0.5$ m/s. Variations in the main stream velocity of $U'_x = \mathcal{O}(0.01\overline{U}_x)$ are found to occur suddenly. The influence of these main stream fluctuations may influence the turbulence. In case of M127, the main stream velocity decreases in time while the pressure drop over the contraction stays around a constant value. This is caused by a temperature change in the main stream flow.

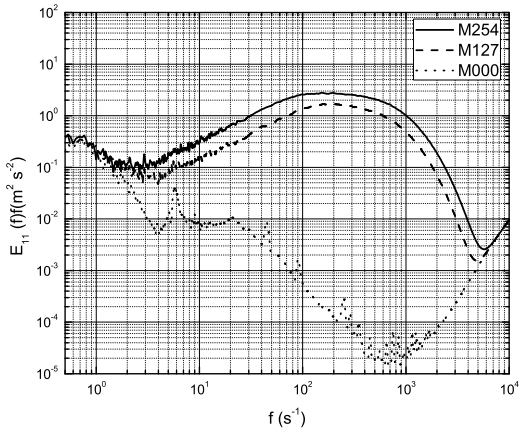

Figure C.15: The root-mean-square velocity is determined by $u_{rms,x} = \sqrt{\int_{f_1}^{f_2} E_{xx}(f)df}$, with f_1 =2 to f_2 =f4.775 s^{-1}. The energy spectrum of M000 between 2 and 20 s^{-1} shows that the non-turbulence fluctuations $U^2_{rms,x}(t)$ are only about $\mathcal{O}(10)$ smaller than the turbulence fluctuations $u^2_{rms,x}(t)$. This means that non-turbulence fluctuations contaminate the turbulence fluctuations.

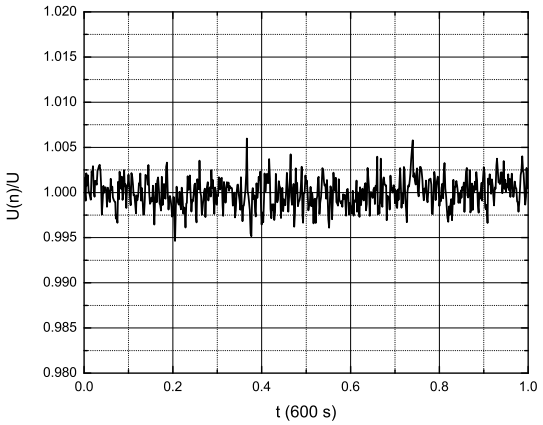

Figure C.16: The main stream velocity as measured in the TU/e David wind tunnel. This wind tunnel is a smaller version of the TU/e Goliath wind tunnel. Here, sudden variations in the main stream velocity are found in a lesser extent than in the TU/e Goliath Windtunnel, see for comparison Figure C.14.

- The low frequency noise for $f < 2$ s^{-1} can be identified with two possible processes. First, the main stream velocity changes due to a temperature change during a measurement. This may cause the low frequency contributions in the energy spectrum. This may also be caused by the observed sporadic but sudden main stream velocity fluctuations. It is hypothesized that these velocity fluctuations are caused by changes in the diffuser flow field.

influence of non-turbulence contributions

We will continue with considering the influence of the non-turbulence contributions discussed in Section C.4.1, C.4.1, and C.4.1. For this, we will analyse the root-mean-square velocity $u_{rms,x}$

which can be determined in two ways. In the first method, the root-mean-square velocity is determined directly from $\overline{U_x^2(t)}$ and $\overline{U_x(t)}^2$:

$$
\begin{aligned}
u_{rms,x}^2 &= \overline{U_x^2(t)} - \overline{U_x(t)}^2 && \text{(C.10)}\\
&= \overline{(\overline{U}_x + U_x'(t) + u_{rms,x}'(t))^2} - \overline{(\overline{U}_x + U_x'(t) + u_{rms,x}'(t))}^2 && \text{(C.11)}\\
&= \overline{\overline{U}_x^2 + U_x'(t)^2 + u_{rms,x}'(t)^2 + 2(\overline{U}_x U_x'(t) + \overline{U}_x u_{rms,x}'(t) + U_x'(t)u_{rms,x}'(t))} - \overline{\overline{U}_x}^2 && \text{(C.12)}\\
&= \overline{U'^2_x(t)} + \overline{u'^2_x(t)} + 2\overline{U_x'(t)u_{rms,x}'(t)} && \text{(C.13)}
\end{aligned}
$$

However, to obtain the root-mean-square velocity related to the turbulent flow field $u_{rms,x}^2 = \overline{u_x'(t)}^2$, the slow fluctuations in the main stream velocity $U_x'(t)$ need to be zero. One can achieve this by performing the averaging procedure over a sufficiently small block size. By setting the block size to 5 seconds, one artificially filters for fluctuations with a frequency below 2.5 s^{-1}. However, it is found virtually impossible to obtain a situation in which $U_x'(t)$ is filtered out properly. Therefore, we prefer the spectral method since it is more versatile with respect to the possibilities of filtering frequencies and defining a sufficient averaging period.

Integration of the energy spectrum is the second method to obtain the root-mean-square velocity $u_{rms,x}$. This makes use of the longitudinal energy spectrum function $E_{xx}(f)$

$$u_{rms,x} = \sqrt{\int_{f_1}^{f_2} E_{xx}(f)df}, \tag{C.14}$$

in which f_1 and f_2 are the lower and upper frequencies of the bandwidth in which turbulence is found to act. In this way, one is able to filter the low frequency fluctuations and the high frequency noise directly. However, it is not known if the slow velocity fluctuations contaminate the energy spectrum in the bandwidth between f_1 and f_2. This considers the question if non-turbulent contributions contaminate the turbulent contribution. For example, sporadic but sudden variations in the main stream velocity are found which indicate the presence of high frequency components, see Figure C.14a, c, and d. We assume that the high frequency noise, that is $f > 4.775$ s^{-1}, contaminates the turbulence energy spectrum to a negligible extent. To get an better insight in the non-turbulent contributions to the turbulence intensity, $E_{xx}(f)f$ is plotted against $\ln(f)$ for the case with ($M254$ and $M127$) and without ($M000$) grid-generated turbulence, see Figure C.15. Note that $E_{xx}(f)df = E_{xx}(f)fd\ln(f)$. This gives an alternative way to write Eq. C.14, and to obtain the root-mean-square velocity by integration:

$$u_{rms,x} = \sqrt{\int_{\ln(f_1)}^{\ln(f_2)} E_{xx}(f)fd\ln f}. \tag{C.15}$$

We assume that the energy spectrum obtained for the case with $M254$ and $M127$ grid is based on the non-turbulence fluctuations $U_x'(t)$ plus the turbulence fluctuations $u_{rms,x}'(t)$, and the energy spectrum obtained for the case $M000$ only on the non-turbulence fluctuations $U_x'(t)$. The energy spectrum of $M000$ shows that the energy contained in $U_x'(t)$ for 2 $s^{-1} < f < 20$ s^{-1} is significant compared to that in $u_{rms,x}'(t)$, see Figure C.15. This means that this part of the turbulence bandwidth is contaminated with non-turbulence contributions. We will continue with discussing the extent of non-turbulence contamination in the turbulence bandwidth. We will consider the variation of the root-mean-square velocity in time. The variation of the root-mean-square velocity in time is determined by the spectral method

$$\frac{u_{rms,x}(n)}{\overline{u_{rms,x}}} = \frac{\sqrt{\int_{f_1}^{f_2} E_{xx}(f,n)df}}{\frac{1}{N}\sum_{n=1}^{N}\sqrt{\int_{f_1}^{f_2} E_{xx}(f,n)df}}, \tag{C.16}$$

in which n corresponds to a block of 5 s, and the average is taken over the total of $N = 120$ blocks. The spectral method is chosen since it combines the possibility of measuring long enough to obtain a reliable energy spectrum (a block size of 5 s), and to relate the root-mean-square velocity only to a specific bandwidth ($f_1 = 2$ to $f_2 = 4.775$ s^{-1}). A block size of 5 s is believed to be long enough for obtaining reliable energy spectra, but short enough to capture individual main stream fluctuations. In other words, the block sizes are short enough so that the average main stream velocity $\overline{U_x(n)}$ in one block equals the average main stream velocity $\overline{U}_x$ for the total number of blocks plus a fluctuation U'_x in the mean stream velocity:

$$\overline{U_x(n)} \approx \overline{U}_x + U'_x. \tag{C.17}$$

The variation of the root-mean-square velocity in time as determined by Eq. C.16, is given in Figure C.6. This shows that variations of $0.03\overline{u_{rms,x}}$ exist in the root-mean-square velocity between blocks of 5 s for the case with grid-generated turbulence. We also determined the exent of these variations for blocks with a size of 30 seconds. For this, we found variations of $0.01\overline{u_{rms,x}}$. However, we believe that the data obtained with block sizes of 5 s are more informative. These show namely the variations in the root-mean-square velocity during individual sporadic but sudden fluctuations of the main stream velocity itself. The variations of the root-mean-square velocity between blocks of 5 s is larger for the case without grid-generated turbulence, that is the case $M000$. Note that the root-mean-square velocity is now related to the fluctuations U'_x in the bandwith f_1 =2 to f_2 =4.775 s^{-1}. Although the average root-mean-square velocity is about an order ten smaller, the fluctuations are larger.

C.4.2 Turbulence intensity and dissipation rate

In this section, we will discuss the turbulence intensity and dissipation rate as function of the distance from the grid. Comte-Bellot and Corssin (1966) used the following empirical formula for the turbulence intensity in grid-generated turbulence:

$$\frac{u^2_{rms}}{\overline{U^2_x}} = A^{-1}\left(\frac{x}{M} - \frac{x_v}{M}\right)^{-m}. \tag{C.18}$$

From this, one can derive a similar equation for turbulence dissipation rate as function of the distance from the grid

$$\varepsilon = \frac{3m\overline{U}^3_x}{2MA}\left(\frac{x}{M} - \frac{x_v}{M}\right)^{-1-m}, \tag{C.19}$$

see Appendix B for the derivation. The empirical parameters m, A, and x_v/M will be determined for the turbulence generated by the $M254$ and $M127$ grid. The measurements are performed at 12 streamwise locations with $y, z = 0$ and x between $x/L = 0.12$ and 0.81. It takes about 40M for (quasi-)isotropy and (quasi-)homogeneity to develop, see for example Comte-Bellot and Corssin (1966) and Mohamed and Larue (1990). For that reason, the closest measurement position was set at $x/L = 0.12$, that is $40M/L$ for the $M254$ grid and $80M/L$ for the $M127$ grid. In section C.3, no grid footprint was found in the flow field at $x/L = 0.12$, which suggests (quasi-)isotropy and (quasi-)homogeneity. The averaged main stream velocity is in all measurements kept between $\overline{U}_x = 15 \pm 0.5$m s^{-1}. All the energy spectra are obtained by measurements of 600 seconds, in which 20 spectra obtained from blocks of thirty seconds are averaged.

The turbulence intensity is determined by the spectral method

$$q(x) = \frac{u^2_{rms,x}(x)}{\overline{U^2_x(x)}} = \frac{\int_{\kappa_{x,1}}^{\kappa_{x,2}} E_{xx}(\kappa_x, x)d\kappa_x}{\overline{U^2_x(x)}}, \tag{C.20}$$

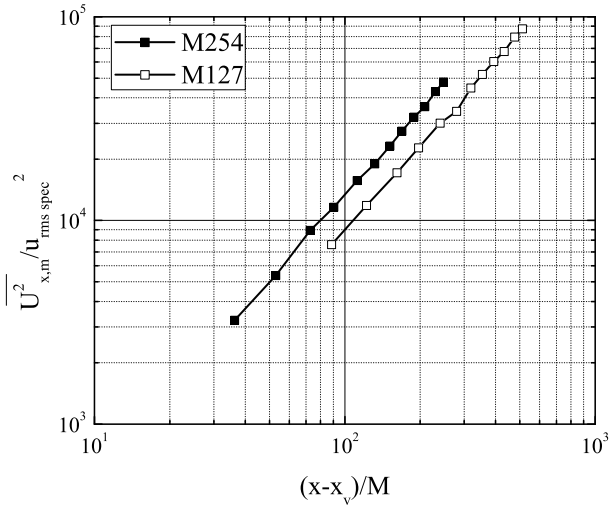

(a) inverse turbulence intensity

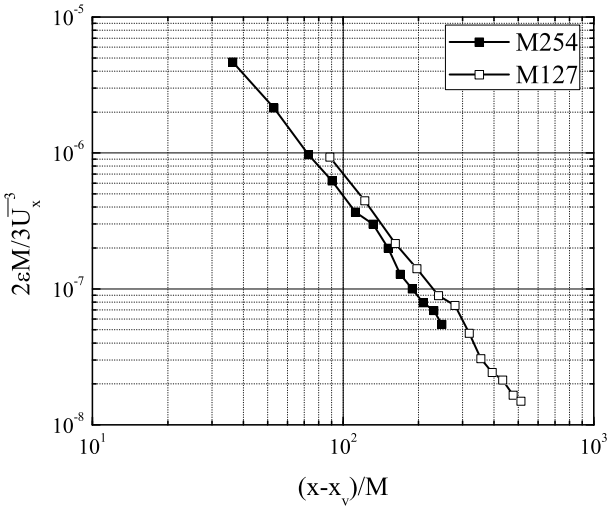

(b) turbulence dissipation rate

Figure C.17: The turbulence intensity is determined by Eq. C.20, and the turbulence dissipation rate by Eq. C.21 for the case with turbulence generated by the M254 and M127 grid. The measurements are performed at 12 streamwise positions between $x/L = 0.12$ and 0.81. Note that L corresponds to 315M in case of the M254 grid, and 630M in case of the M127 grid. The estimated profile of the turbulence intensity and the turbulence dissipation rate as applied in Appendix B, that is with $A = 18$, $n = 1.36$, and $x_v = 0$, is given by the line without symbols. The deviation between the estimate profile and that obtained by the wind tunnel measurements are negligible.

in which $\kappa_1 = 1$ and $\kappa_1 = 2.000$ correspond to the turbulence bandwidth f_1 =2 to f_2 =4.775 s^{-1}. The turbulence dissipation rate is determined from the dissipation spectrum:

$$\varepsilon(x) = 15\nu \int_{\kappa_{x,1}}^{\kappa_{x,2}} \kappa_x^2 E_{xx}(\kappa_x, x) d\kappa_x. \tag{C.21}$$

Again, the turbulence bandwidth is defined to be between $\kappa_1 = 1$ and $\kappa_1 = 2.000$.

The turbulence intensity and dissipation rate as function of the streamwise distance for the tur-

bulence generated by the $M254$ and $M127$ are shown in Figure C.17. The parameter x_v/M corresponds to the virtual origin of the turbulence generated by the grid. The logarithmic turbulence intensity and dissipation rate is plotted for a range of values for he virtual origin x_v/M. The value of x_v/M is sought for which the data obeys the best linear relation. Subsequently, the parameter m is determined from the incline of this line, while the ordinate level determines A.

The parameters A, m and x_v/M for the turbulence intensity are found to be $A = 60 \pm 8$, $m = 1.34 \pm 0.04$ and $x_v/M = 8$ for the $M254$ grid and $A = 32 \pm 7$, $m = 1.40 \pm 0.04$ and x_v/M for the $M127$ grid. The same parameters for the turbulence dissipation rate are found to be $A = 21 \pm 1$, $m = 1.39 \pm 0.01$ and $x_v/M = 8$ for the $M254$ grid and $A = 14 \pm 1$, $m = 1.39 \pm 0.01$ and $x_v/M = 0$ for the $M127$ grid. Deviations of the values obtained for the turbulence intensity and dissipation rate may be caused by anisotropy of the turbulence, while isotropy is assumed in deriving Eq. C.21 from C.20. It was not possible to find a reliable optimum value for x_v/M in case of the $M127$ grid. For that reason, we chose to set $x_v/M = 0$.

The parameters A, m and x_v/M are for a number of turbulence experiments reported in Comte-Bellot and Corssin (1966). Our values fall in the range reported in there. The values for A, m and x_v/M that were used for predicting the evolution of turbulence quantities in Appendix B are $A = 18$, $m = 1.36$ and $x_v/M = 0$. The values obtained in the turbulence measurements, correspond to these estimated values; deviations are negligible.

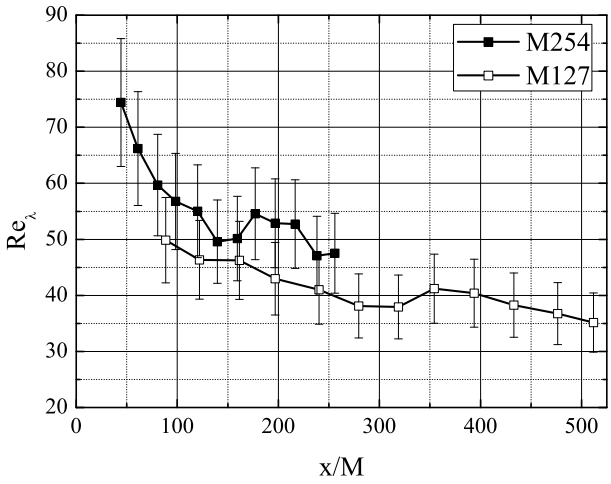

Figure C.18: The Taylor Reynolds number is determined for 12 streamwise positions for the case with the $M254$ and $M127$ grid. The streamwise positions are located between $x/L = 0.12$ and 0.81. Note that L corresponds to 315M in case of the $M254$ grid, and 630M in case of the $M127$ grid.

Isotropy of turbulence

The isotropy $u_{rms,x}/u_{rms,y}$ of the turbulence is measured at six streamwise locations between $x/L = 0.12$ and 0.81. The isotropy is determined at $y, z = 0$ with a measurement of 600 seconds, and for a range of z-positions and $y = 0$ with a measurement at each position of 30 seconds. In this way, an accurate value for the isotropy at $y, z = 0$ is obtained, and an indication for the isotropy distribution for a range of z-positions. It was found that the values for the isotropy vary as much as 5% between different measurements locations. We assume that this is a result of the measurement accuracy or the influence of main stream fluctuations $U'_{x,y}$, see section C.4.1. The isotropy is determined at 1.05 ± 0.05 for the $M254$ grid, and 1.15 ± 0.07 for the $M127$ grid. These values correspond to typical values found in literature, see for example Comte-Bellot and Corssin (1966).

C.4.3 Taylor Reynolds number

An important turbulence parameter is the Taylor Reynolds number defined by:

$$Re_\lambda = \frac{u_{rms}\lambda}{\nu}. \tag{C.22}$$

The Taylor Reynolds number is determined at 12 streamwise locations with $y, z = 0$ and x varying between $x/L = 0.12$ and 0.81. All the energy spectra are obtained by measurements of 600 seconds, in which 20 spectra obtained from blocks of 30 s are averaged. The root-mean-square velocity is determined by the spectral method

$$u^2_{rms,x}(x) = \int_{\kappa_{x,1}}^{\kappa_{x,2}} E_{xx}(\kappa_x, x) d\kappa_x, \tag{C.23}$$

in which $\kappa_1 = 1$ and $\kappa_1 = 2.000$ correspond to the turbulence bandwidth $f_1 = 2$ to $f_2 = 4.775$ s^{-1}. The Taylor microscale is determined by the relation:

$$\lambda^2 = 15\nu \frac{u^2_{rms}}{\varepsilon}. \tag{C.24}$$

The streamwise evolution of the Taylor Reynolds number in case of the $M254$ and $M127$ grid is shown in Figure C.18. The characteristic value of the Taylor Reynolds number corresponds to values found in literature for similar grids, see for example Mohamed and Larue (1990) or Lavoie et al. (2007).

C.5 Optimal Wing Location for Vortex Pair Decay with Weak Grid Generated Turbulence

In Appendix B, we discussed the dimensionless dissipation rate $\varepsilon^*_{b_0} = \frac{(\varepsilon b_0)^{1/3}}{U^{vor}_{z,0}}$ and the maximum achievable dimensionless time $t^*_{max} = \frac{b_0}{U^{vor}_{z,0}}$ in the wind tunnel test section. Here, we will present the graph again with data obtained from the measurements performed in Chapter C. In this way, we can define a optimal wing location when the Crow instability is going to considered for vortex pair decay in weak turbulence. The data shows little deviation from the predicted values as discussed in Appendix B. Therefore, we can consider $x_a = 3.5$ m still as the optimal wing location when both the turbulence grids $M254$ and $M127$ will be used.

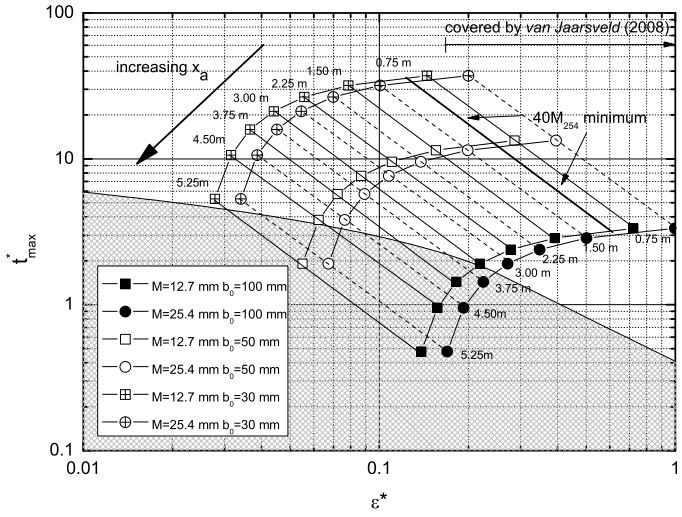

Figure C.19: The values of dimensionless dissipation rate $\varepsilon^*_{b_0}$ and the maximum achievable dimensionless time t^* are presented for two grid configurations M254 and $M127$, and three initial wing-tip separations b_0. The maximum achievable dimensionless time is based on the distance $x_c - x_a$, with x_c the position where an analysis of the trailing vortices is still possible. Here, x_c is set to 6.0 m and is determined by the maximum position at which PIV measurements can be performed in the TU/e wind-tunnel Goliath. For determining the optimal wing location x_a, it is important that the maximum achievable dimensionless time t^* is larger than the lifespan predicted by Crow and Bate (1976). This means that the optimal wing-location lies outside the shaded area. On the other hand, the grid-generated turbulence needs about a distance of 40M before (quasi)-isotropy and (quasi)-homogeneity are developed, see section C.3. In combination with the desired range of $\varepsilon^*_{b_0}$, it can be concluded that two wing locations, $x_a = 3.5$ m and 4.5 m, are appropriate. With the wing location of $x_a = 4.5$ m, it will only be possible to use the wing-tip separation distance of $d = 5.00$ and $3.00 \cdot 10^{-2}$ m. Therefore, we will consider $x_a = 3.50$ m as the optimal wing location.

Appendix D

A Comparison of 3C-PIV and Hotwire Measurement Results

This appendix considers the results obtained with 3C-PIV and hotwire measurements of the trailing vortex at location $x/c = 7.5$ behind the wing. The experimental procedure of the 3C-PIV measurement is elucidated in Chapter 3, and we will now discuss the experimental procedure of the hotwire measurements.

With help of the crosswire technique, it is possible to obtain the $x-$ and $y-$ components of the time-averaged velocity and root-mean-square velocity (rms-velocity) at a certain position, that are $U_x(x_s, y_s, z_s)$, $U_y(x_s, y_s, z_s)$, $u_{rms,x}(x_s, y_s, z_s)$, $u_{rms,y}(x_s, y_s, z_s)$, respectively. Note that the velocities are obtained in the stationary frame of reference. We assume that the flow is incompressible, and that local temperature variations are negligible. Corrections of the crosswire signal due to local temperature variations are not applied, but correction due to changes in the temperature of the mean flow are. In deriving the velocity components U_x and U_y, it is necessary that the time-averaged velocity in the $z-$direction is zero, i.e. $U_z = 0$. We assume that the axis of symmetry of the trailing vortex is parallel to the x-axis, and that $U_z = 0$ along the y-axis. First, the position of the vortex core ($y_s = z_s = 0$) is retrieved, and then, profiles of U_x and U_y along the $z-$axis are obtained.

The position of the vortex centre is obtained in three steps. First, U_x and U_y profiles along the $z-$axis are obtained. The $z-$position where U_y crosses zero is believed to be $z = 0$. Second, U_x and U_y profiles along the $y-$axis are obtained. The position where U_x is a maximum, is believed to be position of the vortex core, i.e. $y = 0$. Third, step one is repeated to obtain the exact position of the vortex core $y, z = 0$. The stepsize in the $z-$direction $\triangle_{step} z/r_{1,0}$ is 0.17 and is controlled by the hotwire traversing system. The $y-$position is controlled by adjusting the wing-tip location. By moving the wing in- or outwards, a stepsize of about $\triangle_{step} y/r_{1,0} = 0.4$ is achieved. Finally, in the postprocessing of the scans in $z-$direction, we introduce an offset in the $z-$positions in such a way that the linear interpolation of U_y in a small region around $U_y = 0$ is exactly zero at $z = 0$. This offset is typically smaller than $0.17 r_{1,0}$.

When the position of the vortex centre is retrieved, we performed scans along the $z-$axis of both the velocity, U_x and U_y, and the rms-velocity, $u_{rms,x}$ and $u_{rms,y}$. The outer region of the trailing vortex is covered by $-12 \leq z_s/r_{1,0} \leq 12$ in steps of $\triangle_{step} z/r_{1,0} = 0.8$, and the inner region by $-3 \leq z/r_{1,0} \leq 1/3$ which is resolved with $\triangle_{step} z/r_{1,0} = 0.2$.

The velocity and rms-velocity as obtained with the 3C-PIV and hotwire measurements are shown in Figures D.1 and D.1, respectively. In the case of the 3C-PIV measurements, both the profiles in the stationary and co-moving frame of reference are presented. There are a few points that need

to be considered:

- There is a significant difference in the velocities in the inner region as obtained with the 3C-PIV and hotwire measurements. In the case of the velocity in the $y-$direction, the magnitude of the velocity peak from the 3C-PIV measurement is about two times that from the hotwire measurements. Moreover, the distance of the velocity peak from the vortex centre is about two times as that from the hotwire measurements. An even bigger difference is observed in the axial velocity component U_x. While the 3C-PIV measurements result in a wake with amplitude $(U_x - \overline{U}_x)(2\pi r_{1,0}/\Gamma_{vor,0}) \approx -0.18$, the hotwire measurements result in a jet with amplitude $(U_x - \overline{U}_x)(2\pi r_{1,0}/\Gamma_{vor,0}) \approx 0.42$.

  The discrepancy can be caused by several reason. A variation in the total temperature may be important since the hotwire measurements are not corrected for this. However, it is not believed that these variations are large enough to cause such a discrepancy. We will give an estimation of change in temperature from $r = r_{1,0}$ to $r = 0$. Inside the vortex core region, it is assumed that vortex is in solid-body rotation $U_\theta = \Omega r$, and that a balance between the centrifugal and pressure force is present:

$$\frac{U_\theta^2}{r} = -\frac{1}{\rho}\frac{\partial p}{\partial r}, \tag{D.1}$$

$$\frac{(\Omega r)^2}{r} = -\frac{1}{\rho}\frac{\partial p}{\partial r}, \tag{D.2}$$

$$\int_0^{r_{1,0}} \Omega^2 r = -\frac{1}{\rho}(P|_{r=r_{1,0}} - P|_{r=0}), \tag{D.3}$$

$$-\frac{1}{2}\rho(\Omega r_{1,0})^2 = (P|_{r=r_{1,0}} - P|_{r=0}). \tag{D.4}$$

  Together with the adiabatic gas relation

$$\frac{T|_{r=r_{1,0}}}{T|_{r=0}} = \frac{P|_{r=r_{1,0}}}{P|_{r=0}}^{(\gamma-1)/\gamma}, \tag{D.5}$$

  and $\Omega r_{1,0} = 10$ m s^{-1}, $\rho = 1.2$ kg m^{-3}, $\gamma = 1.4$, $P|_{r=r_{1,0}} = P|_{r\to\infty} = 10^5$ kg m^{-1} s^{-2}, one obtains a temperature decrease of about 0.02%. Clearly, a change in the temperature in- and outside the vortex core region cannot cause a bias in the hotwire measurement. Moreover, a temperature decrease would result in a larger measured velocities, which is the case for U_x but not for U_y.

  At this stage, it is unknown what the reason for the discrepancy between the hotwire and the 3C-PIV measurements is.

- The profiles of U_x as obtained from the 3C-PIV and hotwire measurements show at $z_s - z_{s,c}/r_{1,0} = -7.5$ both a decrease in velocity. This is caused by a remnant of the wing flow boundary layer, see the figures in Chapter 5.

- The profiles of the rms-velocities are shown in Figure D.2. The values of the rms-velocities as obtained from the 3C-PIV measurements in the stationary frame, and those from the hotwire measurements do not show significant discrepancies. However, a bias can be recognized in the outer region. This bias is most likely a manifestation of the difference in measurement limitations between the 3C-PIV and hotwire technique.

- Both the 3C-PIV results are shown for the stationary and co-moving frame of reference. From visual inspection of Figure D.1, it becomes clear that the deviation in profiles of U_x and U_y are negligible small. However, the measured rms-velocities in the stationary frame are as large as 300% of those in the co-moving frame of reference. For a more thorough analysis of the flow quantities obtained in the stationary and co-moving frame of reference, the reader is referred to Chapter 5.

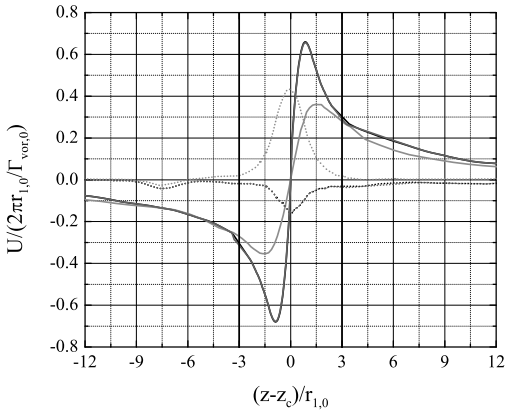

Figure D.1: Vertical profiles of $U_x - \overline{U}_x$ (·····) and U_y (———) obtained from 3C-PIV and hotwire measurements. Both the 3C-PIV results are shown for the co-moving frame (black lines), and those for the stationary frame of reference (gray lines). The hotwire results are shown in the stationary frame of reference (light gray lines).

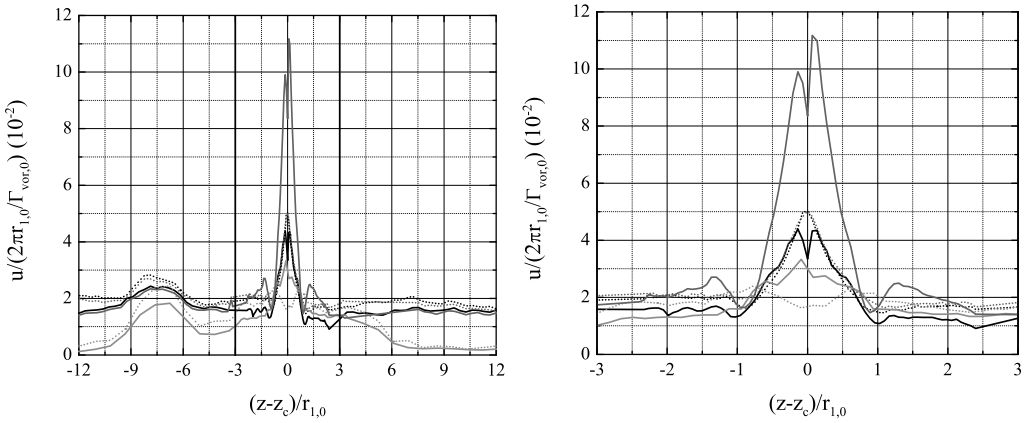

(a) rms-velocity

(b) rms-velocity, close up of panel a

Figure D.2: Vertical profiles of rms-velocities $u_{rms,x}$ (·····) and $u_{rms,y}$ (———) obtained from 3C-PIV and hotwire measurements. Both the 3C-PIV results are shown for the co-moving frame (black lines), and those for the stationary frame of reference (gray lines). The hotwire results are shown in the stationary frame of reference (light gray lines).

Appendix E

Circulation Profiles of the Inner and Outer Region Measurements

Separate 3C-PIV measurements are performed for the inner and outer region of the vortex. The circulation profiles obtained from measurements in the inner and outer region are connected at that radial position such that the derivative $d\Gamma_{vor}/dr$ becomes as smooth as possible. This process is performed with the help of visual inspection. The range in radial position at which both circulation profiles are connected is restricted to $2.5 < r/r_{1,0} < 3.0$. In this way, sufficient positions are available for correctly connecting the inner and outer region, while enough high resolution data of the inner core region is maintained. The circulation profiles of the inner and outer region are shown for the case with and without turbulence grid in Figures E.1 and E.2, respectively.

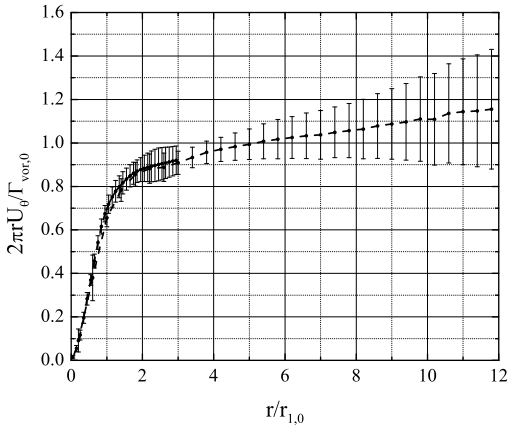

(a) $r_{con}/r_{1,0} = 2.95, t(\Gamma_{vor,0}/2\pi r_{1,0}^2) = 17.5$

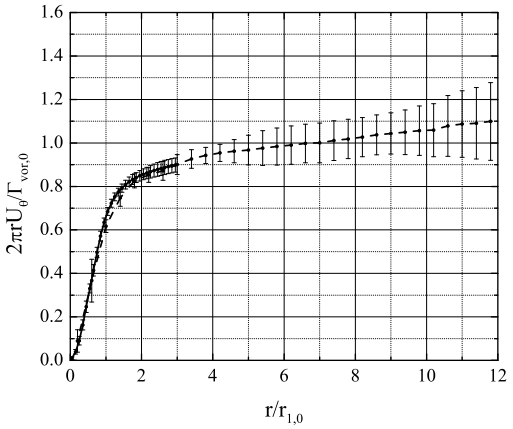

(b) $r_{con}/r_{1,0} = 2.95, t(\Gamma_{vor,0}/2\pi r_{1,0}^2) = 87.5$

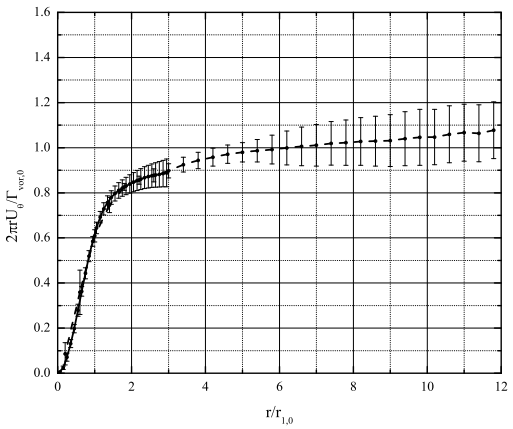

(c) $r_{con}/r_{1,0} = 2.55, t(\Gamma_{vor,0}/2\pi r_{1,0}^2) = 175.5$

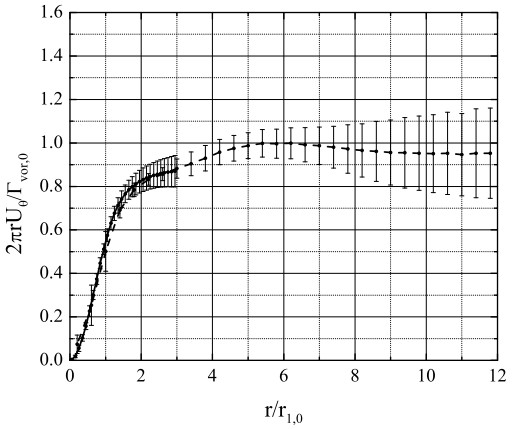

(d) $r_{con}/r_{1,0} = 2.65, t(\Gamma_{vor,0}/2\pi r_{1,0}^2) = 350$

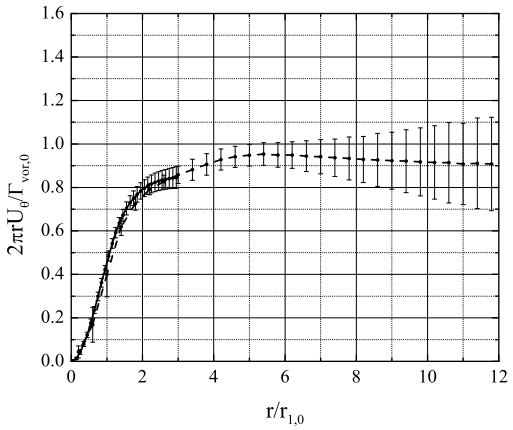

(e) $r_{con}/r_{1,0} = 2.55, t(\Gamma_{vor,0}/2\pi r_{1,0}^2) = 662.5$

Figure E.1: Circulation profiles of the inner region (———) and outer region (- - - -) measurements for the case without grid-generated turbulence. The circulation profiles as shown in Chapter 5 are connected to each other at position r_{con}.

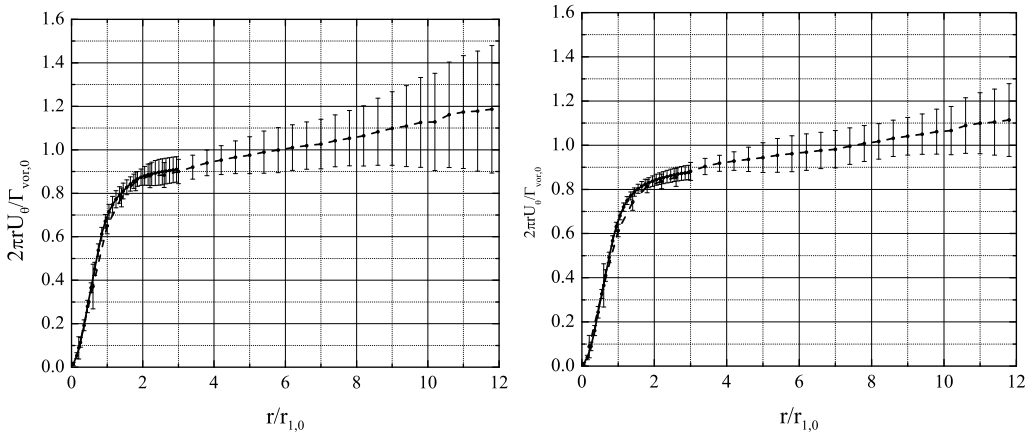

(a) $r_{con}/r_{1,0} = 2.95, t(\Gamma_{vor,0}/2\pi r_{1,0}^2) = 17.5$

(b) $r_{con}/r_{1,0} = 2.65, t(\Gamma_{vor,0}/2\pi r_{1,0}^2) = 87.5$

(c) $r_{con}/r_{1,0} = 2.55, t(\Gamma_{vor,0}/2\pi r_{1,0}^2) = 175.5$

(d) $r_{con}/r_{1,0} = 2.95, t(\Gamma_{vor,0}/2\pi r_{1,0}^2) = 350$

Figure E.2: Radial profiles of the circulation for the inner region (———) and outer region (- - - -) measurements in the case with grid-generated turbulence. The circulation profiles as shown in Chapter 5 are connected to each other at position r_{con}.

Appendix F

Circulation Profiles by Velocity and Vorticity Integration

In the appendix we compare the radial profiles of the circulation as determined by path integration of the azimuthal velocity, see Eq. 4.22, and by area integration of the axial vorticity. With the radial profile of the axial vorticity determined by Eq. 4.22, the radial profile of the circulation by area integration of the axial vorticity is determined by

$$\Gamma(r = i\triangle r \leqq r_{con}/\triangle r) = \sum_{l=1}^{l=i} \omega_x(r = l\triangle r) 2\pi l(\triangle r)^2 \quad i = 1, 2, 3...r_{con}/\triangle r, \tag{F.1}$$

for the inner measurement region, combined with

$$\Gamma(r = i\triangle r > r_{con}/\triangle r) = \sum_{l=r_{con}/\triangle r+1}^{l=i} \omega_x(r = l\triangle r) 2\pi l(\triangle r)^2 + \Gamma(r_{con}); \tag{F.2}$$
$$i - r_{con}/\triangle r = 1, 2, 3...N_{\triangle r} - r_{con}/\triangle r$$

for the outer measurement region. The circulation profiles as shown are connected to each other at position r_{con} as motivated in Appendix E. From Figure F.1, it becomes clear that the radial profiles of the circulation as determined by both methods, are in good approximation similar.

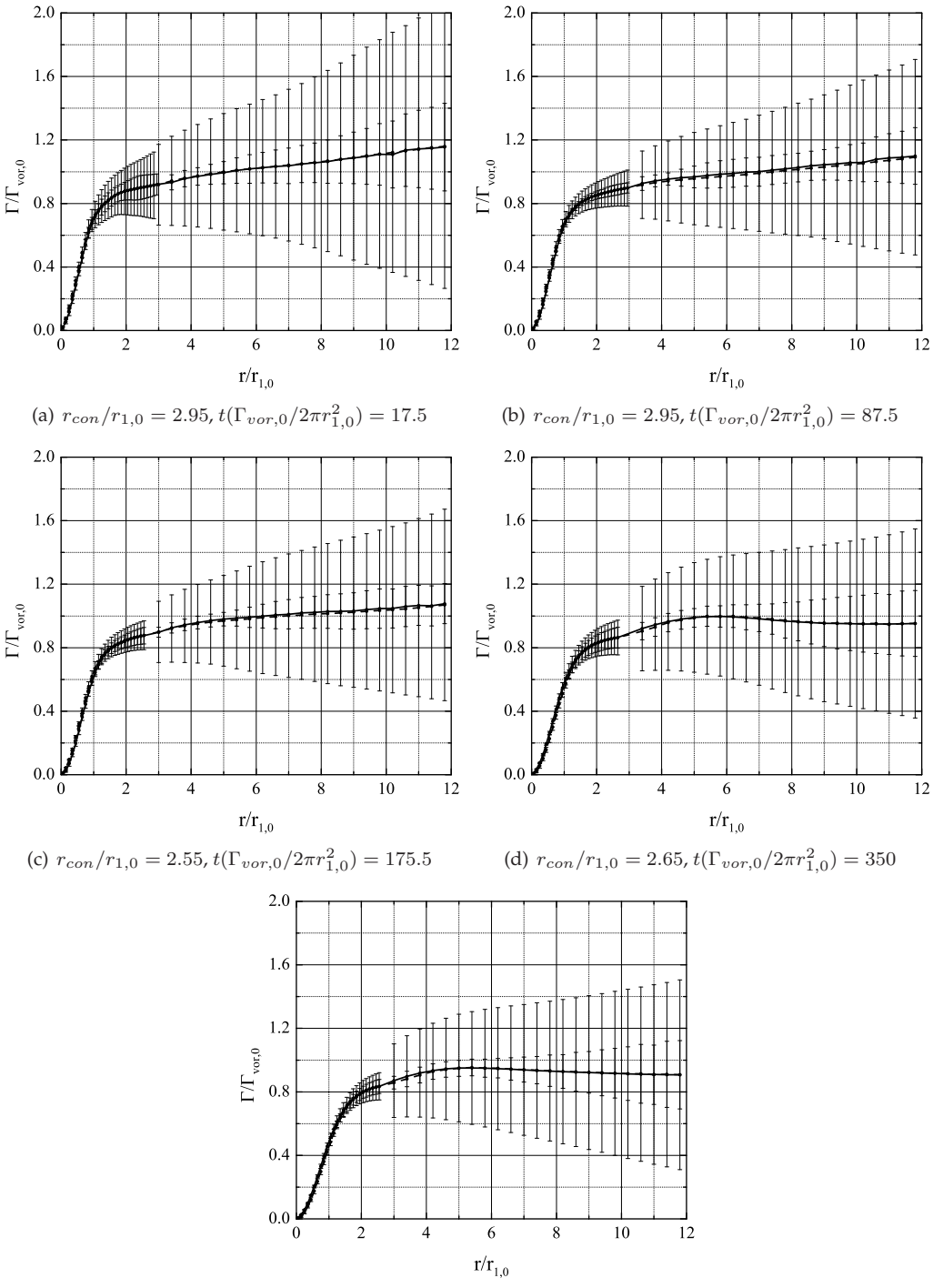

(a) $r_{con}/r_{1,0} = 2.95, t(\Gamma_{vor,0}/2\pi r_{1,0}^2) = 17.5$

(b) $r_{con}/r_{1,0} = 2.95, t(\Gamma_{vor,0}/2\pi r_{1,0}^2) = 87.5$

(c) $r_{con}/r_{1,0} = 2.55, t(\Gamma_{vor,0}/2\pi r_{1,0}^2) = 175.5$

(d) $r_{con}/r_{1,0} = 2.65, t(\Gamma_{vor,0}/2\pi r_{1,0}^2) = 350$

(e) $r_{con}/r_{1,0} = 2.55, t(\Gamma_{vor,0}/2\pi r_{1,0}^2) = 662.5$

Figure F.1: Radial profiles of the circulation for the inner region and outer region measurements and for the case without grid-generated turbulence. The profiles as determined by area integration of the axial vorticity (———), see Eq. F.1 and F.2, and path integration of the azimuthal velocity (– – – –) , see Eq. 4.22, are in good approximation similar. The profiles of the inner and outer measurement region are connected to each other at position r_{con} as motivated in Appendix E, see also Eq. F.1 and F.2.

Appendix G

SPIV Measurements of Flow in Empty Windtunnel: On the Limitations of SPIV

SPIV measurements are performed for the flow in an empty wind tunnel. With an empty wind tunnel, we mean a wind tunnel in which no turbulence grid or wing is installed. The flow is therefore highly uniform and stable, see Appendix C. The flow consists only of an axial velocity component $\overline{U}_x$, and the remaining flow quantities as vorticity, circulation, and kinetic energy of the turbulence are believed to be negligible small.

One may expect that the uniform conditions are retrieved by the 3C-PIV measurements. However, deviations can be caused by measurement noise and limitations in measurement accuracy. For a thorough discussion of the limitations of 3C-PIV the reader is referred to Raffel et al. (2007). The limitations of our 3C-PIV measurements are retrieved by empty wind tunnel measurements. The profiles of the most important flow quantities are given in Figure G.1, and contour plots are presented in Figure G.2 and G.3. Note that separate 3C-PIV measurements are performed for the inner and outer region of the vortex. The circulation profiles as shown in Chapter 5 are connected at the positions motivated in Appendix E. In al cases, the origin equals that of the co-moving frame of reference.

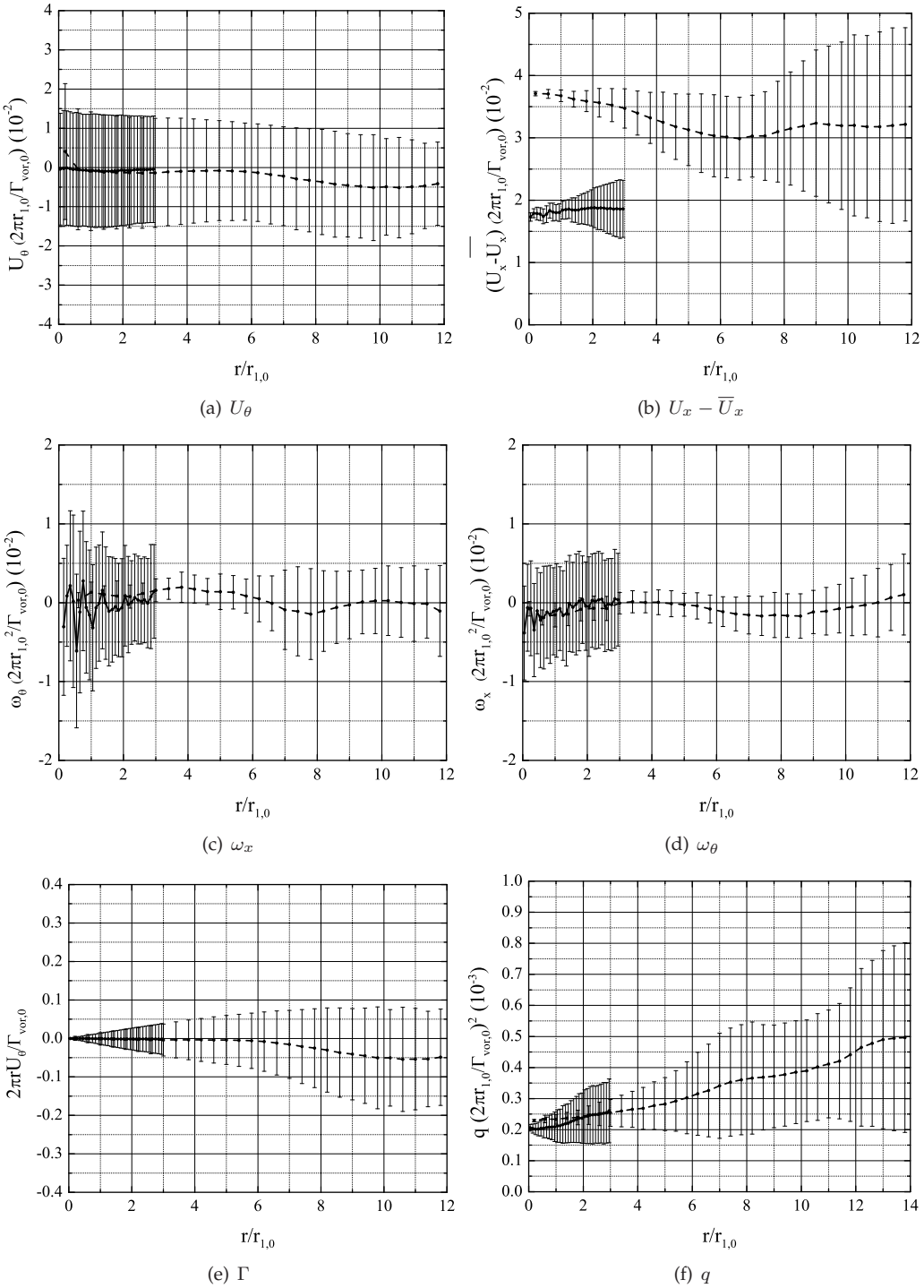

(a) U_θ (b) $U_x - \overline{U}_x$

(c) ω_x (d) ω_θ

(e) Γ (f) q

Figure G.1: Profiles of flow quantities obtained with a 3C-PIV measurement for the inner and outer region in an empty wind tunnel. The deviations from the uniform and stable empty wind tunnel flow with $U_x - \overline{U}_x = 0$ gives an indication of the 3C-PIV measurement limitation. Note that the deviation between $U_x - \overline{U}_x$ observed for inner region measurement and the outer region measurement indicates the uncertainty with which the main stream velocity can be set.

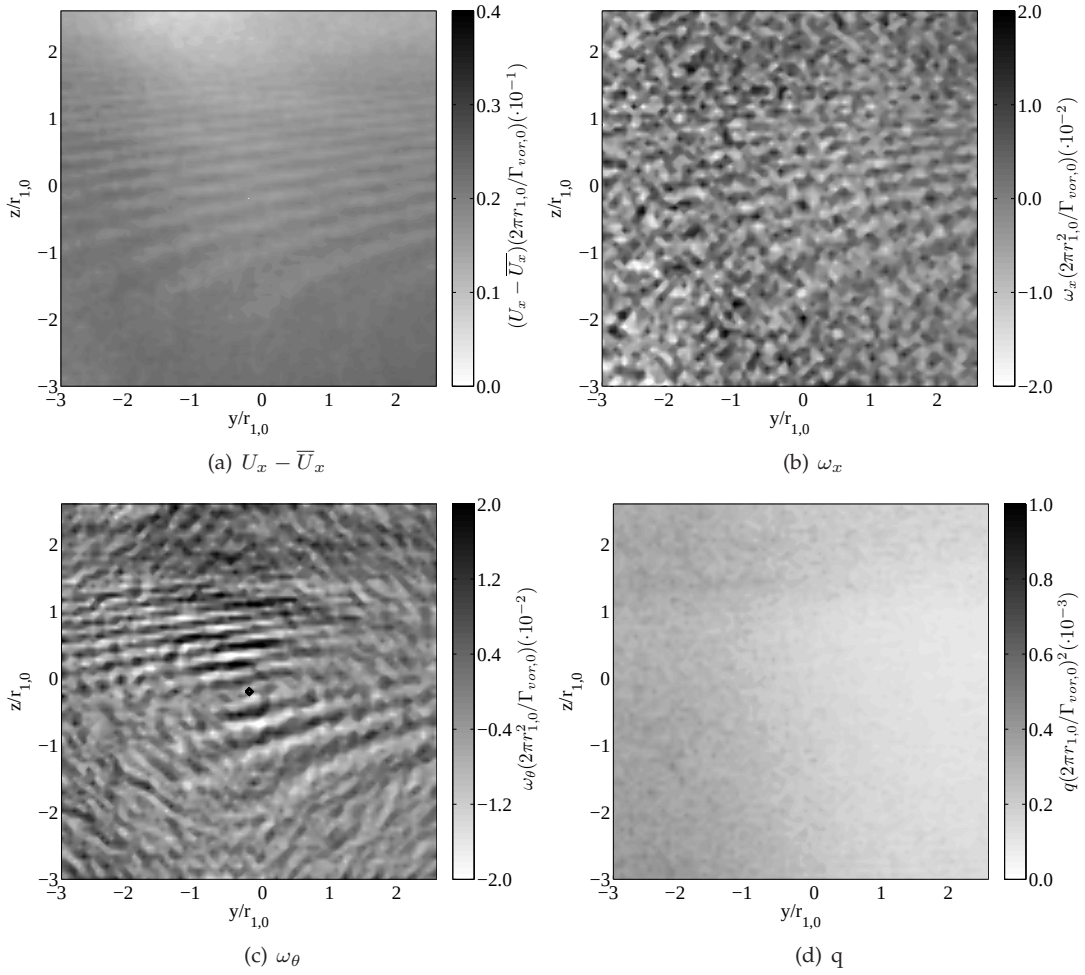

(a) $U_x - \overline{U}_x$ (b) ω_x

(c) ω_θ (d) q

Figure G.2: Distributions of flow quantities obtained with a 3C-PIV measurement for the inner region in an empty wind tunnel. The artificial shapes are a manifestation of the 3C-PIV measurement limitations.

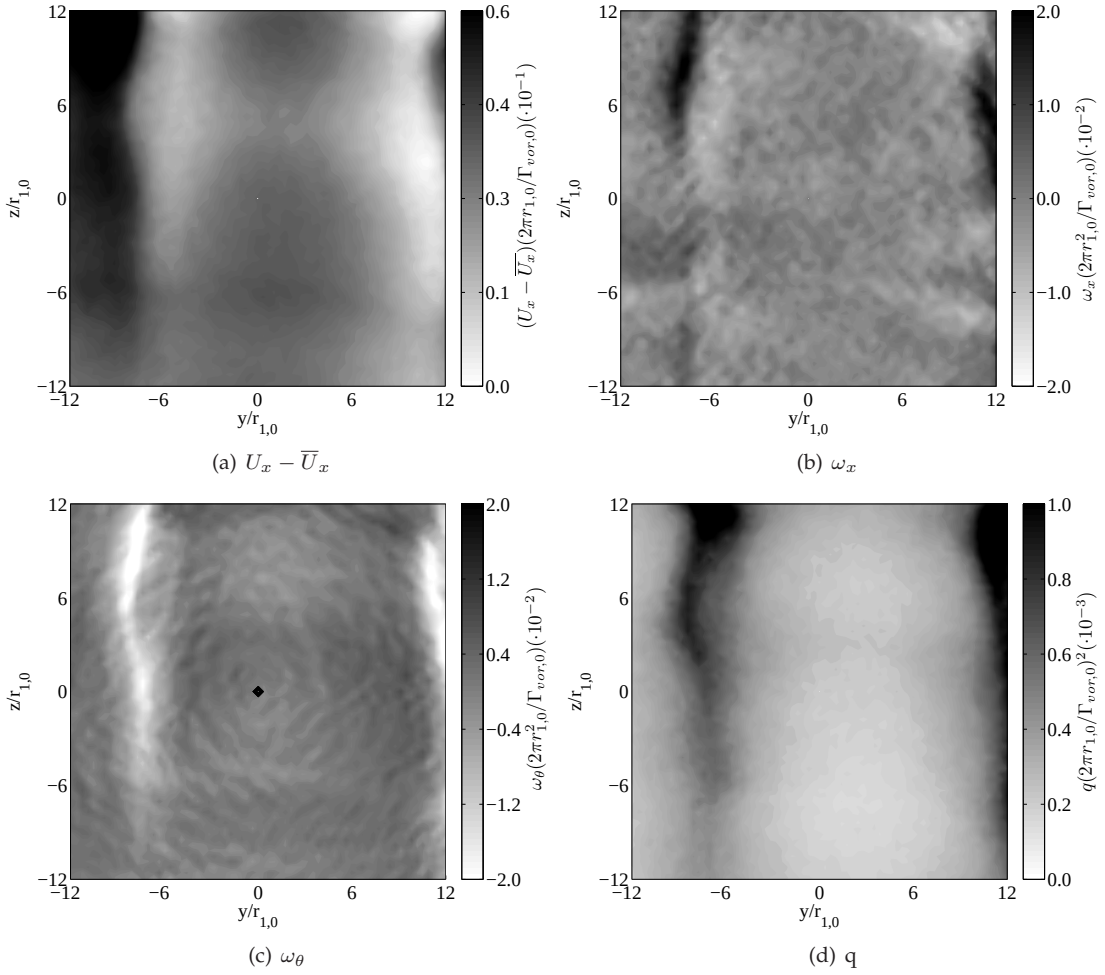

(a) $U_x - \overline{U}_x$ (b) ω_x

(c) ω_θ (d) q

Figure G.3: Distribution of flow quantities obtained with a 3C-PIV measurement of the outer region in an empty wind tunnel. The artificial shapes are a manifestation of the 3C-PIV measurement limitations.

Appendix H

Velocity and Vorticity Profiles for Different Frames of Reference

The discussion of kinetic energy of turbulence considered the importance of determining the vortex centre position correctly. An incorrect vortex centre position in combination with high levels of vorticity are inherent to large velocity fluctuations. This is elucidated by comparing the kinetic energy of turbulence determined in the frame of reference co-moving with vortex centre, in the frame of reference co-moving with grid-point vortex centre frame, and in the stationary frame of reference. The influence of the applied frame of reference for the radial profiles of axial and azimuthal components of the velocity and vorticity is shown in Figure H.1. The difference between the grid-point vortex centre and the vortex centre determined by a least-squares fit of a second-order polynomial through the streamfunction for $r/r_{1,0} < 0.5$ is illustrated in Figure H.2. The shown data corresponds to $t(\Gamma_{vor,0}/2\pi r_{1,0}^2) = 175$ and for the case without grid-generated turbulence. It becomes clear that the difference between the frame of reference co-moving with vortex centre and that co-moving with the grid-point vortex centre is negligible for the radial profiles of velocity and vorticity. However, lower levels of velocity and vorticity are obtained when the stationary frame of reference is applied. This difference is as much as 10% in regions of high level vorticity.

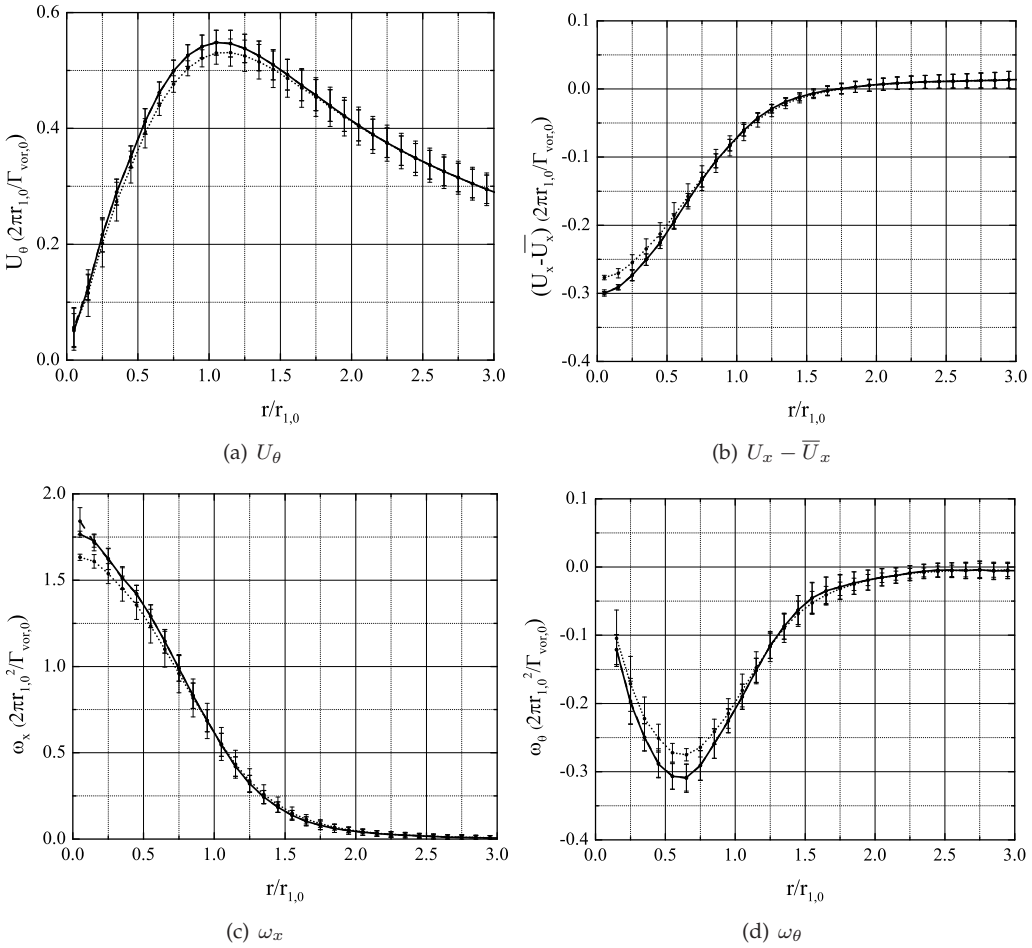

(a) U_θ (b) $U_x - \overline{U}_x$

(c) ω_x (d) ω_θ

Figure H.1: Radial profiles of azimuthal and axial components of velocity and vorticity as obtained in the frame of reference co-moving with the vortex centre (———), and that co-moving with the grid-point vortex centre (– – – –), and that obtained in the stationary frame of reference (·····). The data corresponds to $t(\Gamma_{vor,0}/2\pi r_{1,0}^2) = 350.0$ *and without grid-generated turbulence.*

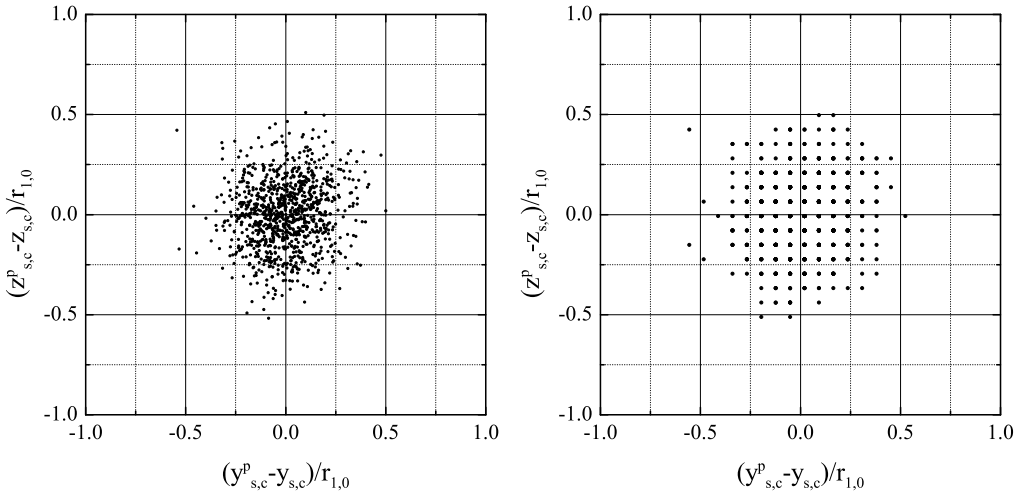

(a) vortex centre position

(b) grid-point vortex centre

Figure H.2: The vortex centre determined by a least-squares fit of a second-order polynomial through the streamfunction for $r/r_{1,0} < 0.5$ and the grid-point vortex centre for $\mathbf{p} = 1..\mathbf{P}$ are shown for $t(\Gamma_{vor,0}/2\pi r^2_{1,0}) = 350.0$ and the case without grid-generated turbulence.

Bibliography

S. C. C. Bailey and S. Tavoularis. Measurements of the velocity field of a wing-tip vortex, wandering in grid turbulence. *J. Fluid Mech.*, 601:281 – 315, 2008.

W. D. Baines and E. G. Peterson. An investigation of flow through screens. *J. Appl. Mech.*, 73:467 – 478, 1951.

G. K. Batchelor. Axial flow in the trailing line vortices. *J. Fluid Mech.*, 20:645 – 658, 1964.

G.K. Batchelor. *The Theory of Homogeneous Turbulence*. Cambridge University Press, 1960.

M. L. Beninati and J. S. Marshall. An experimental study on the effect of free-stream turbulence on a trailing vortex. *Exp. Fluids*, 38:244 – 257, 2005.

B. Cantwell and N. Rott. The decay of a viscous vortex pair. *Phys. Fluids*, 31(3213 – 3224), 1988.

and Zilliac G. G. Bradshaw P. Chow, J. S. Mean and turbulence measurements in the near field of a wingtip vortex. *AIAA Journal*, 35:1561 – 1567, 1997.

G. Comte-Bellot and S. Corssin. The use of a contraction to improve the isotropy of grid-generated turbulence. *J. Fluid Mech.*, 25:657 – 682, 1966.

S. C. Crow. Stability theory for a pair of trailing vortices. *AIAA Journal*, 8:2172 – 2179, 1970.

S. C. Crow and E. R. Jr. Bate. Lifespan of trailing vortices in a turbulent atmosphere. *J. Aircraft*, 13:476 – 482, 1976.

W. J. Devenport, M. C. Rife, S. I. Liapis, and G. J. Follin. The structure and development of a wing-tip vortex. *J. Fluid Mech.*, 312:67 – 106, 1996.

D. Fabre and L. Jacquin. Short-wave cooperative instabilities in representative aircraft vortices. *Phys. Fluids*, 16:1366 – 1378, 2004.

C. A. Friehe and W. H. Schwarz. Grid-generated turbulence in dilute polymer solutions. *J. Fluid Mech.*, 44:173 – 193, 1970.

S. I. Green. Correlating single phase flow measurements with observations of trailing vortex cavitation. *J. Fluid Eng.*, 113:125 – 129, 1991.

S. I. Green, editor. *Fluid Vortices*. Kluwer, Dordrecht, 1995.

S. I. Green and A. J. Acosta. Unsteady flow in trailing vortices. *J. Fluid Mech.*, 227:107 – 134, 1991.

J. D. Iversen. Correlation of turbulent trailing vortex decay data. *J. Aircraft*, 13:338 – 342, 1976.

L. Jacquin, D. Fabre, P. Geffroy, and E. Coustols. The properties of a transport aircraft wake in the extended near field: an experimental study. *AIAA Journal*, 2001-1038, 2001.

E. Kreyszig. *Introductory Functional Analysis with Applications*. John Wiley and Sons. Inc, New York, 1st edition, 1978.

A. K. Kuczaj and B. J. Geurts. Mixing in manipulated turbulence. *J. Turbul.*, 7:67 – 101, 2006.

A. M. Kuethe and J. D. Schetzer. *Foundations of Aerodynamics*. John Wiley and Sons, Inc., New York, 2nd edition, 1959.

P. K. Kundu, I. M. Cohen, and P. S. Ayyaswamy. *Fluid Mechanics*. Academic Press, Inc., 525 B Street, Suite 1900, San Diego, California 92101-4495, U.S.A., fourth edition edition, 2008.

H. Lamb. *Hydrodynamics*. Cambridge University Press, Cambridge, 6th edition, 1932.

F. W. Lanchester. *Aerodynamics*. Constable and Company Ltd, London, 2nd edition, 1907.

P. Lavoie, R. A. Antonia, and L. Djenidi. Effect of grid geometry on the scale-by-scale budget of decaying grid turbulence. In *15th Australasian Fluid Mechanics Conference*, Sydney, 2004. The University of Sydney.

P. Lavoie, P. Burattini, L. Djenidi, and R. A. Antonia. Effects of initial conditions in decaying turbulence generated by passive grids. *Exp. Fluids*, 39:865 – 874, 2005.

P. Lavoie, L. Djenidi, and R. A. Antonia. Effects of initial conditions in decaying turbulence generated by passive grids. *J. Fluid Mech.*, 585:395 – 420, 2007.

D. R. Lide, editor. *CRC Handbook of Chemistry and Physics*. CRC press, 87th edition, 2006.

H. T. Liu. Effects of ambient turbulence on the decay of a trailing vortex wake. *J. Aircraft*, 20:255 – 263, 1992.

R. Liu and D. S. Ting. Turbulent flow downstream of a perforated plate: sharp-edged orifice versus finite-thickness holes. *J. Fluids Eng.*, 129:1164 – 1171, 2007.

R. Liu, D. S. Ting, and G. W. Rankin. On the generation of turbulence with a perforated plate. *Exp. Therm. Fluid Sci.*, 28:307 – 316, 2004.

R. Liu, D. S. Ting, and M. D. Checkel. Constant reynolds number turbulence downstream of an orificed perforated plate. *Exp. Therm. Fluid Sci.*, 31:897 – 908, 2007.

M. S. Mohamed and J. C. Larue. The decay power law in grid-generated turbulence. *J. Fluid Mech.*, 219:195 – 214, 1990.

D. R. Moore and P. G. Saffman. Axial flow in laminair trailing vortices. In *Proceedings of the Royal Society of London*, volume 333 of *Series A, Mathematical and Physical Sciences*, pages 491 – 508, 1973.

S. B. Pope. *Turbulent Flows*. Cambridge University Press, Cambridge, 1st edition, 2000.

D. S. Pradeep and F. Hussain. Effects of boundary conditions in numerical simulations of vortex dynamics. *J. Fluid Mech.*, 516:115 – 124, 2004.

M. Raffel, C. E. Willert, S. T. Wereley, and J. Kompenhans. *Particle Image Velocimetry; A Practical Guide*. Springer, Berlin, 2nd edition, 2007.

Lord Rayleigh. On the stability, or instability, of certain fluid motions. *Proc. London Math. Soc.*, 9: 57 – 70, 1880.

S. G. Saddoughi and S. V. Veeravalli. Local isotropy in turbulent boundary layers at high reynolds number. *J. Fluid Mech.*, 258:333 – 372, 1994.

P.G. Saffman. Vortex dynamics. In *Cambridge Monographs on Mechanics and Applied Mathematics*. Cambridge University Press, Cambridge, 1992.

T. Sarpkaya. Decay of wake vortices of large aircraft. *AIAA Journal*, 36:1671 – 1679, 1998.

T. Sarpkaya and J. Daly. Effect of ambient turbulence on trailing vortices. *J. Aircraft*, 24:399 – 404, 1987.

P. Spalart. Airplane trailing vortices. *Annu. Rev. Fluid Mech.*, 30:107 – 138, 1998.

I. Tombach. Observations of atmospheric effects on vortex wake behaviour. *J. Aircraft*, 10:641 – 647, 1973.

C. Tropea, A. L. Yarin, and J. F. Foss, editors. *Springer Handbook of Experimental Fluid Mechanics*. Springer, 2007.

M. S. Uberoi and S. Wallis. Effect of grid geometry on turbulence decay. *Phys. Fluid*, 10:1216 – 1224, June 1976.

J. P. J. Van Jaarsveld. Wind tunnel experiments on wake-vortex decay in external turbulence. Master's thesis, Eindhoven University of Technology, 2008.

Acknowledgement

First of all, I would like to thank Ruben Trieling. Your logical thinking helped me with problems I encountered during this project. I highly appreciate the freedom you gave me in the interpretation of this project. Your sense of priorities and planning were of great value in this.

I want to express my gratitude to GertJan van Heijst and Bernard Geurts for encouraging me to start a PhD study. You recognize your role in motivating students to excel in academics. GertJan, many thanks for providing all kinds of support during my masters in fluid dynamics.

I would like to thank Bram Elsenaar for thoroughly reviewing my work and providing illuminating discussions on the theory of airfoils. You motivated me to examine my analyses more carefully. This has been, and will be, of great value to the quality of my work.

The quality of the 3C-PIV and hotwire measurements is greatly contributed by the technical support of Ad Holten. I highly appreciate your commitment to my project.

Ergün Çekli, many thanks for patiently helping me with the cross wire measurements. I enjoyed the discussions we had beyond the scope of this thesis.

I would like to sincerely thank Bernard Geurts and Arek Kuczaj for helping me out with the numerical simulations.

I want to express my gratitude to Willem van de Water en Gerald Oerlemans for their contributions to my project.

The Fluid Dynamics Department served as an excellent place to perform my study. I would like to thank all the people of the Fluid Dynamics Department for providing both a stimulating and pleasant environment to work in. I really enjoyed the table tennis matches I played against many of the Fluid Dynamics Department. Berend, I didn't make it to the final of the table tennis tournament, but if I did, I would have beaten you.

Last but certainly not least, I would like to thank my parents, friends, housemates, and family, for providing all kinds of support during the whole course of my study.

Daan van Sommeren
December 2009